

https://dspace.org/

Design, Construction and Evaluation of a Modified Tubular Linear Synchronous Motor

Van Zyl, Andre Willem

2006-11-14T07:06:04Z
http://hdl.handle.net/10539/1657

Downloaded from a DSpace repository. https://dspace.org/

Design, Construction and Evaluation of a Modified Tubular Linear Synchronous Motor

André Willem van Zyl

A thesis submitted to the Faculty of Engineering and the Built Enviroment, University of the Witwatersrand, Johannesburg, in fulfilment of the requirements for the degree of Doctor of Philosophy.

Johannesburg, March 2006

Declaration

I declare that this thesis is my own, unaided work, except where otherwise acknowledged. It is being submitted for the degree of Doctor of Philosophy in the University of the Witwatersrand, Johannesburg. It has not been submitted before for any degree or examination in any other university.

Signed this ___ day of _____ 20___

André Willem van Zyl.

Abstract

This thesis describes the design, construction and evaluation of a prototype modified tubular linear synchronous motor. The linear motor has a long static primary and a short permanent magnet mobile secondary. The design is unique in that a tubular topology has been modified to allow access to the moving secondary section. This modification means that this design can be used in long distance applications. The application for this research is the use of linear motors in rope-less vertical transportation systems in ultra deep level mines. The design of the linear motor has been analysed from an electrical, magnetic, mechanical and thermal perspective. Finite Element Analysis was used to predict the performance of the linear motor. The design of the secondary section has been optimised to produce the greatest possible thrust force while reducing the effects of the cogging forces. The linear motor has been tested extensively and the results correlate with theoretical predictions from the Finite Element Analysis. This project proves that the modified tubular linear synchronous motor is a viable technology that can be used in rope-less vertical transportation systems.

Acknowledgements

First I would like to thank my supervisor, Prof. Charles Landy, for the support both academically and financially. His support has contributed to the success of this project. This project has taken a while to succeed and his trust and faith in me was greatly appreciated. I would also like to thank Mr Rupert Cruise for his time. He has been an inspiration and a solid sounding board to bounce off ideas, concepts and thoughts. His constructive criticism has kept me on the right path towards the completion of this project. I would also like to thank Ms Lorraine Marais for her help with the construction drawings that are found in the appendix. Her time and patience with me is greatly appreciated. Lastly, but definitely not least, I would like to thank the workshop staff for their help in the construction of the linear motor, especially, Mr Eddie Jackwitch. The linear motor was a very difficult machine to construct mechanically, and with Mr Eddie Jackwitch's brilliance, the linear motor is not only mechanically sound, but it is a work of art. The precision and accuracy of the construction is a tribute to his expertise.

This section would not be complete without acknowledging the financial support that industry has provided. In particular I would like to thank the DEEPMINE Collaborative Research Programme, especially Dr Ray Durrheim, for the support they have offered to this project. Without their support this project would not have come close to the success it has achieved. It is their support that enabled the linear motor, not only to be built with the best materials available, but also to be built by the expertise of Mr Eddie Jackwitch. On a further note, I would also like to thank ESKOM's Tertiary Education Support Programme (TESP). The support from TESP has made it possible for me to do my research and to allow me to make a valuable contribution to the field of knowledge in linear motors for their application in ultra deep level mines in South Africa.

To my family and Lorraine for their continual support and encouragement.

Contents

Declaration i

Abstract ii

Acknowledgements iii

Contents v

List of Figures x

List of Tables xx

List of Symbols xxi

List of Definitions xxvi

1 Introduction 1

1.1 Background to the Development of the Modified Tubular Linear Synchronous Motor 2

1.1.1 Background to Rope Hoists 2

1.1.2 Limitations of Rope Hoists 3

1.1.3 Background on Linear Motors 5

1.1.4 Benefits and Limitations of Linear Motors Compared to Rope Hoists . . . 10

1.2 Research Objectives . . . 15

1.2.1 The Modified Tubular Topology . . . 15

1.2.2 Optimisation of the Secondary Section . . . 17

1.3 Summary . . . 18

1.4 Outline of Report . . . 19

2 The Design **20**

2.1 Primary . . . 21

2.2 Secondary . . . 26

2.3 Summary . . . 27

3 Design of the Electrical System **28**

3.1 Approximate Equivalent Circuit Per Coil . . . 28

3.1.1 Fluxes Generated in the Linear Motor . . . 33

3.2 Calculation of the Required Applied Voltage . . . 35

3.2.1 Induced Voltage for One Coil, E_{f1} . . . 35

3.2.2 Voltage Phasor for the Coil Resistance, R_{a1} . . . 38

3.2.3 Voltage Phasor for the Coil Synchronous Reactance X_{s1} . . . 39

3.2.4 Applied Voltage, V_{t1} . . . 41

3.3 Required Applied Voltage for a Full Scale Motor . . . 47

3.4 Summary . . . 48

4 Design of the Magnetic System **49**

4.1 Secondary Excitation Source 50
4.1.1 DC winding 50
4.1.2 Permanent Magnets and their Properties 50
4.2 Magnet Arrangements 59
4.2.1 Optimisation Approach for the Conventional Tubular LSM . 60
4.2.2 Optimisation Approach for the Modified Tubular LSM 75
4.2.3 Split-Pole Surface Mounted Magnet Arrangement 80
4.2.4 Reduction of the Cogging Forces 83
4.3 Summary 92

5 The Design of the Mechanical System 94

5.1 Primary Construction 94
5.2 Secondary Construction 98
5.3 Summary 103

6 Evaluation of the Thermal System 104

6.1 Thermal Model for the Outside Surface of the LSM 105
6.1.1 Values for the Thermal Model 108
6.2 Thermal Model for the Primary Winding 112
6.3 Practical Temperature Measurements 117
6.4 Temperature Effects on the $NdFeB_{N-35}$ Magnets 119
6.5 Duty Cycle 119
6.6 Loading Bays 121
6.7 Summary 122

7 Finite Element Modelling **123**

7.1 Executive Commands 126

7.2 Summary 133

8 Results **135**

8.1 Predicted Forces Using FEM 135

8.2 Testing Procedure 136

8.2.1 AC test 138

8.2.2 DC test 139

8.3 Discussion of Results 141

8.4 Summary 149

9 Conclusion **151**

9.1 Design Aspects 152

9.2 Results 154

9.3 Viability 155

References **156**

A Correlating the Physical Model to the Finite Element Model **163**

B Required Applied Voltage for a Full Scale Motor **167**

C Electric Circuit Analogy for the Split Pole Magnet Arrangement **173**

D Construction Drawings **176**

E Friction Force on the Guidance System **185**

F Voltage and Current Waveforms **187**

G Efficiency Calculations for a Full Scale Model **195**

List of Figures

1.1 The conversion from rotary to linear motor. 5

1.2 The two basic linear motor configurations. (a) Long primary and short secondary. (b) Short primary and long secondary. 7

1.3 The three different linear motor topologies from the left: single-sided; double-sided; tubular. 8

1.4 Flux concentration towards the centre of the tubular topology 9

1.5 Graphical representation of tubular, single-sided and double-sided topologies 10

1.6 A hybrid hoisting system. 15

1.7 The conventional and modified tubular topologies. 16

2.1 On the left is an axial cross-sectional view of a totally enclosed tubular motor. On the right is the cross-sectional view of the modified tubular motor. 21

2.2 Hoisting system for a mine shaft. The conveyance is attached to the secondary sections of two modified tubular LSM's. 22

2.3 Block arrangement of primary laminations for a modified tubular LSM. 23

2.4 Primary laminations and coils shown during the winding of the modified tubular LSM. 23

2.5 Primary lamination with semi-closed slots. 24

2.6 Primary lamination with open slots. 24

2.7 Shape of one coil inside the primary section. 25

3.1 The flux pattern developed by: (a) the LSM with the coils un-energised and with the magnets present; (b) the LSM with only the coils energised. The properties of the objects representing the magnets have been changed to that of a vacuum; (c) the LSM with the coils energised and with the magnets present. 29

3.2 Equivalent circuit representing equation 3.1 30

3.3 Phasor diagram of Figure 3.4 31

3.4 Equivalent circuit per coil with the reactances X_{ar_1} and X_{al_1}. 31

3.5 Final equivalent circuit per coil. 32

3.6 The phasor diagram for the LSM operating as a motor. 32

3.7 The equivalent circuit per coil without the secondary section. 33

3.8 The phasor diagram for the LSM operating without the secondary. . 33

3.9 The phasor diagram for the LSM operating with the secondary. This shows that the resistance volt drop dominates. 33

3.10 A sample section of the primary winding. All three phases are shown. A indicates a 'go' conductor and A′ the 'return' conductor. 36

3.11 The phasor diagram from Figure 3.9 with $\delta = 90^o$ 42

3.12 The phasor diagram from Figure 3.9 with $\delta = -90^o$ 42

3.13 The phasor diagram from Figure 3.9 with $\delta = 0^o$ 42

3.14 The phasor diagram combining Figures 3.11, 3.12 and 3.13 43

3.15 Primary winding connections. 45

3.16 Voltage and current waveforms measured on the modified tubular LSM 46

3.17 Phasor diagram of voltage and current measurements 47

4.1 Demagnetisation curves and maximum energy product grid for a $NdFeB_{N-35}$ magnet. 52

4.2 Demagnetisation curves for a $NdFeB_{N-35}$ magnet 53

4.3 P_c lines for two magnet arrangements superimposed on the demagnetisation curves for a $NdFeB_{N-35}$magnet 54

4.4 Cross-sectional view of the SMMA. 56

4.5 Cross-sectional view the flux in a tubular LSM with buried magnets. 57

4.6 B-H curve for a $NdFeB_{N-35}$ showing both the demagnetisation quadrant and the energy product, BH, as a function of B. (B_r = residual flux density and H_c = coercive force.) 58

4.7 Cross-sectional view of the tubular LSM with surface mounted magnets. The gray areas represent the permanent magnet and the white areas represent the steel sections. 63

4.8 Cross-sectional view of the flux in a tubular LSM with surface mounted magnets. 63

4.9 Graphical view of the cross-sectional areas through which the flux flows. 64

4.10 Cross-sectional view of the tubular LSM with surface mounted magnets that have been adjusted to reduce the effects of the cogging forces. 65

4.11 Cross-sectional view the flux in a tubular LSM with surface mounted magnets that have been adjusted to reduce the effects of the cogging forces. 65

4.12 Cross-sectional view of the tubular LSM with buried magnets. 66

4.13 Cross-sectional view the flux in a tubular LSM with buried magnets. 67

4.14 Cross-sectional view of the tubular LSM with a combined surface mounted and buried magnet arrangements - ***Design One***. 68

4.15 Cross-sectional view of the tubular LSM with a combined surface mounted and buried magnet arrangements - ***Design Two***. 68

4.16 Magnet volume versus the ratio of the lengths of the surface mounted and buried magnets - with a fixed r_2 (***Design One***) 70

4.17 Magnet volume versus the ratio of the lengths of the surface mounted and buried magnets - with a fixed τ (***Design One***) 71

4.18 Flux density plot of the CMA - ***Design One***. The darker colours are areas of low flux density. 72

4.19 Magnet volume versus the ratio of the lengths of the surface mounted and buried magnets - with a fixed r_2 (***Design Two***) 73

4.20 Magnet volume versus the ratio of the lengths of the surface mounted and buried magnets - with a fixed τ (***Design Two***) 75

4.21 Thrust force with the change in permanent magnet volume in a surface mounted magnet arrangement (12 A per coil). 77

4.22 Thrust force with the change in permanent magnet volume in a buried magnet arrangement (12 A per coil). 78

4.23 Thrust force with the change in permanent magnet volume in a surface mounted and buried magnet arrangements (12 A per coil). . . . 79

4.24 A four pole rotary motor 80

4.25 A four pole linear motor with the cut made at Line 1. 81

4.26 A four pole linear motor with the cut made at Line 2. 81

4.27 Conventional magnet arrangement with flux lines 82

4.28 Conventional magnet arrangement with saturation effects 82

4.29 Split-pole magnet arrangement with flux lines 83

4.30 Cogging forces produced by both the leading and trailing edge of a pole shoe. 84

4.31 A skewed magnet for cogging force reduction 84

4.32 A skewed primary for cogging force reduction 84

4.33 A semi-closed slots for cogging force reduction 85

4.34 Cross-sectional view of the tubular LSM with surface mounted magnets. 87

4.35 Cross-sectional view of the tubular LSM with buried magnets. 87

4.36 Cogging forces for a permanent magnet length of $57mm-60mm$. This small range is used to emphasise the difference between the magnet lengths. 90

4.37 Cogging forces for a permanent magnet length of $77mm - 80mm$. . . 90

4.38 Cogging forces for a varying pole shoe lengths in a BMA. 91

4.39 Cogging forces for a varying pole shoe lengths in a SMMA. 91

4.40 Cross-sectional view the flux in a tubular LSM with buried magnets. The areas of magnetic field distortion are highlighted. The flux is forced to enter/exit from the sides of the buried magnets. 92

5.1 The frame of the motor with primary sections only in the bottom half. 95

5.2 A close-up of the motor showing 4 of the 5 primary sections. 96

5.3 Diagram indicating the use of small pieces of angle-iron to connect the primary sections to the frame. 96

5.4 The modified tubular LSM from above showing the arrangement of the primary sections 97

5.5 The primary section with the copper windings. 97

5.6 A close-up of the motor windings. 98

5.7 Top view of the secondary 99

5.8 The magnet length, y, is made up of three individual magnets 100

5.9 Construction of the secondary section for the buried magnet arrangement 100

5.10 The completed secondary section for the buried magnet arrangement 101

5.11 Normal forces in the modified tubular linear motor 101

5.12 Secondary section attached to the guidance system. 102

5.13 Diagram of the guidance system. 102

5.14 The complete model 103

6.1 The heat generated in the primary section is dissipated through the surface area shown in red 111

6.2 Close up of Figure 6.1 111

6.3 Surface temperature model. 112

6.4 Experimental temperature curves of the surface and coil temperatures for a current of 5A per coil. The difference in the two temperatures reaches a steady state value after a short period of time. 113

6.5 Experimental temperature curves of the surface and coil temperatures for a current of 8A per coil. The difference in the two temperatures reaches a steady state value after a short period of time. 113

6.6 Linear model of the temperature difference between the coil temperature on the primary winding and the temperature on the surface of the linear motor 114

6.7 The final model of temperature rise for both the primary winding and the surface temperature. The above graphs are for the case when the linear motor has class F insulation. 116

6.8 The temperature of the primary winding (coils) and the surface of the linear motor (surface) for a current level of $5A$ per coil. Both the theoretical model and practical measurements are plotted. 118

6.9 The temperature of the primary winding (coils) and the surface of the linear motor (surface) for a current level of $8A$ per coil. Both the theoretical model and practical measurements are plotted. 118

6.10 Reduction of thrust force in the SMMA due to the increase in temperature of the $NdFeB_{N-35}$ permanent magnets. The current decreases with time as the temperature of the primary winding increases. . . . 120

6.11 Reduction of thrust force in the BMA due to the increase in temperature of the $NdFeB_{N-35}$ permanent magnets. The current decreases with time as the temperature of the primary winding increases. . . . 120

6.12 Cooling at loading bays with the use of fans. 121

7.1 Procedure for setting up, solving and analysing a model 124

7.2 Diagram showing both the primary and secondary sections. Each set of coloured coils represents either a "go" or "return" current for one phase. 125

7.3 B-H curve for 'Steel 1010'. 128

7.4 Diagram showing the reference block and constraint. 128

7.5 A close up showing sufficient number of triangles in the air gap for a model with 7224 triangles. 132

8.1 The graph of the force versus position of the secondary relative to the reference block for a current with the value of $12A(rms)$ per coil in the SMMA 136

8.2 The FEM predicted force versus the rms current applied to each coil 137

8.3 The maximum air gap flux densities for a given probe position for the AC and DC tests 138

8.4 AC test with the scale attached between the secondary and the floor of the test bed 139

8.5 Graphical representation of the AC test 140

8.6 Graphical representation of the DC test 141

8.7 Measured and predicted forces for the surface mounted magnet arrangement 142

8.8 Measured and predicted forces for the buried magnet arrangement . 143

8.9 Predicted thrust forces for both magnet arrangements 144

8.10 Measured thrust forces for both magnet arrangements 145

8.11 Predicted FWRs for both magnet arrangements 145

8.12 Measured FWRs for both magnet arrangements 146

8.13 Forces measured during the AC tests for both magnet arrangements 146

8.14 Forces measured during the DC tests for both magnet arrangements 147

8.15 Mechanical output power of the modified tubular linear synchronous motor 148

8.16 Electrical input power to the modified tubular linear synchronous motor 148

8.17 Force produced compared with the electrical input power 149

A.1 Block arrangement of primary laminations for a tubular LSM. 164

A.2 Block arrangement of primary laminations for a modified tubular LSM. 164

A.3 The grey areas represent the difference between the FEM model and the physical model. 165

B.1 The phasor diagram from Figure 3.6 with a larger E_{f1} and for $\delta > 0^o$ 169

B.2 The phasor diagram from Figure 3.6 with a larger E_{f1} and for $\delta < 0^o$. 169

B.3 The phasor diagram showing the range of angle δ. 170

B.4 The phasor diagram for maximum δ, such that the LSM will operate as a motor. 170

B.5 The phasor diagram for $\delta = 0^o$. 170

B.6 The phasor diagram for unity power factor: $\phi = 0^o (\delta = -2.59^o)$. . . 170

C.1 Circuit analogy representing the magnetic circuit for the conventional magnet arrangement (without saturation effects). 174

C.2 Circuit analogy representing the magnetic circuit for the conventional magnet arrangement (with saturation effects). 174

C.3 Circuit analogy representing the magnetic circuit for the split-pole magnet arrangement (without saturation effects). 175

C.4 Circuit analogy representing the magnetic circuit for the split-pole magnet arrangement (with saturation effects). 175

D.1 The support plate 176

D.2 Close-up of the connection between the support plate and the primary 177

D.3 Position of the guidance system 178

D.4 The assembly of the linear motor as seen from above. 179

D.5 Side view of the linear motor. The shaded areas show the location of the primary section. The position of the secondary section is indicated with a dashed outline 180

D.6 Close up view of the connection between the support plates and the connecting rods. 181

D.7 Front view of the linear motor. The lighter shading shows the location of the primary section. The darker shading shows the position of the secondary section. 182

D.8 Side view of the linear motor with the surface mounted magnet arrangement. 183

D.9 Side view of the linear motor with the buried magnet arrangement. . 184

E.1 Moment of force for the AC test. 186

E.2 Moment of force for the DC test. 186

F.1 Custom $\frac{V}{f}$ pattern setting 188

F.2 Voltage and current waveforms with an inverter setting of n014 = $9.0Hz$. Surface mounted magnet arrangement. 189

F.3 Voltage and current waveforms with an inverter setting of n014 = $6.0Hz$. Surface mounted magnet arrangement. 189

F.4 Voltage and current waveforms with an inverter setting of n014 = $4.0Hz$. Surface mounted magnet arrangement. 190

F.5 Voltage and current waveforms with an inverter setting of n014 = $3.5Hz$. Surface mounted magnet arrangement. 190

F.6 Voltage and current waveforms with an inverter setting of n014 = $2.5Hz$. Surface mounted magnet arrangement. 191

F.7 Voltage and current waveforms with an inverter setting of n014 = $2.0Hz$. Surface mounted magnet arrangement. 191

F.8 Voltage and current waveforms with an inverter setting of n014 = $9.0Hz$. Buried magnet arrangement. 192

F.9 Voltage and current waveforms with an inverter setting of n014 = $6.0Hz$. Buried magnet arrangement. 192

F.10 Voltage and current waveforms with an inverter setting of n014 = $4.0Hz$. Buried magnet arrangement. 193

F.11 Voltage and current waveforms with an inverter setting of n014 = $3.5Hz$. Buried magnet arrangement. 193

F.12 Voltage and current waveforms with an inverter setting of n014 = $2.5Hz$. Buried magnet arrangement. 194

F.13 Voltage and current waveforms with an inverter setting of n014 = $2.0Hz$. Buried magnet arrangement. 194

G.1 Power and speed diagram for a winder cycle. 196

G.2 Standard form of hoisting cycle 197

G.3 Power and speed diagram for a LSM hoisting cycle. 200

G.4 Power flow in the modified tubular LSM. 201

G.5 Core loss curve for the steel used in the primary laminations. 202

List of Tables

1.1 Peak power comparison. 12

2.1 Winding Parameters 26

3.1 Flux values in the LSM 34

4.1 Comparison of $NdFeB$ and $SmCo$ Magnets 51

4.2 Comparison between SMMA and BMA Pc gradients 57

4.3 Secondary Design Parameters 79

6.1 Insulation Classes 115

6.2 Continuous current ratings for each class of insulation 117

A.1 Percentages of material used 165

F.1 Descriptions of the inverter settings shown in Figure F.1 188

G.1 Shaft systems in South Africa 199

List of Symbols

α	ratio of tooth width to slot pitch
β	span of the coil in electrical degrees
δ	angle between V_{t1} and E_{f1}
η_{LSM}	efficiency of the modified tubular LSM
η_{rope}	efficiency of the rope hoist
γ	span in electrical degrees between coils
μ_0	$4\pi \times 10^{-7}$ magnetic permeability of free space
ϕ	angle between V_{t1} and I_{a1}
ϕ_a	armature flux
ϕ_{al}	armature leakage flux
ϕ_{ar}	armature reaction flux
ϕ_f	field flux
ϕ_r	air gap flux
Φ	flux per pole
ρ	resistivity
ρ_{cu}	mass density of copper
ρ_{fe}	mass density of iron
τ	pole pitch
θ	temperature rise

θ_{coil}	coil temperature
θ_k	gradient of the constant slope in Figure 6.6
θ_o	ambient temperature
θ_{ss}	steady state temperature response
$\theta_{surface}$	surface temperature
A	cross-sectional area of the copper wire
A	surface area
A_g	cross-sectional area of the air gap
A_m	cross-sectional area of the magnet
a	acceleration/deceleration rate
B	flux density
B_g	flux density in the air gap
B_i	intrinsic magnetic flux density
B_m	flux density at the operating point
B_r	residual flux density
C_p	specific heat
d	length of wind (depth of shaft)
E_a	voltage induced due to the armature flux
E_{al}	voltage induced due to the armature leakage flux
E_{ar}	voltage induced due to the armature reaction flux
E_f	voltage induced due to the field flux
E_r	voltage induced due to the air gap flux
F_T	thrust force
F_f	friction (of the guidance system)

F_w	weight of secondary
f	frequency
g	gravity
H	magnetic field intensity
H_c	coercive force
H_g	magnetic field intensity in the air gap
H_m	magnetic field intensity at the operating point
h	number of coils per group
h	length of the pole shoe in the SMMA, BMA and CMA
h	heat transfer coefficient
I_a	primary current
K_e	chording factor
K_m	distribution factor
k	constant which accounts for the poorer ventilation at standstill
L_g	air gap length
L_{ar}	armature reaction inductance
L_{al}	leakage inductance
L_{ar}	armature reaction inductance
L_g	actual air gap length
L'_g	effective air gap length
L_m	magnet length (along the magnetised axis of the magnet)
l	length of the copper wire
M	mass
m_c	mass of the motor moving components (active material)

m_p	mass of payload
N_c	number of turns per coil
P_c	permeance coefficient
P_c	constant power losses (iron, friction and windage losses)
P_{cu}	copper losses
P_{in}	input electrical power
$P_{in(rms)}$	rms input electrical power
P_m	mechanical power converted from electrical power (thrust force)
P_{out}	output mechanical power
$P_{payload}$	average power required to lift the payload from the bottom to the top of the shaft
Q	Electrical loading
q	heat source
R_a	coil resistance
r	radius to the middle of the air gap
r_1	inside radius of the secondary (only applicable for SMMA and CMA)
r_2	outside radius of the secondary
t_a	time taken during acceleration and deceleration
t_c	time during creep
t_f	time at full speed
t_s	slot pitch
t_t	tooth width
t_t	total cycle time from shaft bottom to headgear tip and vice versa
t_u	time to load/unload the skips when the winder is stationary
V_a	voltage between phase a and the star point

V_b	voltage between phase b and the star point
V_{bc}	voltage between phase b and phase c
V_{cu}	volume of copper
V_{fe}	volume of angle iron
V_t	applied voltage
$V_{t_{group}}$	applied voltage for the coil group
$V_{t_{phase}}$	applied voltage for the phase
v_c	creep speed
v_f	full winding speed
v_s	secondary velocity
X_{al}	armature leakage reactance
X_{ar}	armature reaction reactance
X_s	synchronous reactance
y	length of the buried magnet in the BMA and CMA

List of Definitions

BMA	Buried Magnet Arrangement
CMA	Combined Magnet Arrangement
FEA	Finite Element Analysis
FEM	Finite Element Modelling
FWR	Force to Weight Ratio
LIM	Linear Induction Motor
LSM	Linear Synchronous Motor
MMF	Magneto Motive Force
$NdFeB$	Neodymium Iron Boron rare earth permanent magnets
$NdFeB_{N-35}$	$NdFeB$ magnets with an energy product of $35MGOe$
PWM	Pulse Wave Modulation
$SmCo$	Samarium Cobalt rare earth permanent magnets
SMMA	Surface Mounted Magnet Arrangement

Chapter 1

Introduction

This thesis describes the design, construction, testing and evaluation of a modified tubular linear synchronous motor (LSM). This project had two main research objectives, namely:

- to design, construct and evaluate the modified tubular LSM and assess its viability for use in rope-less vertical transportation systems in ultra deep level mines;
- to develop and verify design optimisation criteria for the modified tubular LSM.

This project had two defined stages which followed these research objectives. The first stage was the development and construction of a prototype modified tubular LSM. This stage had a very strong practical approach as it made extensive use of finite element analysis (FEA)[1] for the development of the linear motor instead of the usual design equations. As will be described, this approach proved itself in that, not only was a full working prototype developed, but also a complete optimisation procedure was formulated with the aid of FEA.

This first stage proved successful and an indepth understanding of the modified tubular LSM design was attained. This allowed the project to move into the second stage, which was the optimisation of the linear motor design. The construction of the linear motor occurred in the first stage and the primary section of the LSM was the major part of the mechanical structure. Thus, it was decided to keep the primary structure the same for the second stage and the optimisation of the linear motor design would focus on the secondary section.

[1] FEA is an analytical process which uses finite element modelling (FEM) as a tool.

1.1 Background to the Development of the Modified Tubular Linear Synchronous Motor

The reason for this research into LSM's is to find an alternative means of transportation which would be quicker, cheaper and more efficient than existing elevators or rope hoists [1]. The next part of this chapter will give some background to existing rope hoists and describe their limitations. Thereafter, a brief history and a description of linear motors is given. The various linear motor topologies are compared, showing that the tubular topology has some advantages over other topologies. This section will also introduce the benefits than can be achieved if rope hoists are replaced with linear motors. Finally, the research objectives will be discussed in more detail.

1.1.1 Background to Rope Hoists

Gold was discovered on the Witwatersrand in the 1880's. The gold reef discovered was exposed at the earth's surface and gently sloped southwards deeper underground. This exposed reef led to a gold rush and inevitably the establishment of the town, Johannesburg, in 1886. Eventually, the exposed gold reef was over exploited, forcing miners to go deeper and deeper into the surface for the elusive gold.

Mining houses were formed, and these companies had the financial support to sink shafts into the ground in order to reach the deeper and richer reserves of gold. The advancements of rope hoist technology allowed these companies to go deeper still into the earth and the shafts now extend approximately $2800m$ into the earth's surface, at their deepest point. These shafts are now located approximately $70km$ south from where gold was first discovered. To the present day, all gold mines use rope hoists to transport men and materials into and out of the deep level mines. However, these rope hoists have both depth and capacity limitations. With gold now being discovered at levels of $5000m$, new means of transportation need to be investigated to make mining more cost effective.

One of these large mining houses investigated the feasibility of using linear motors in a mine shaft [2]. This study concluded that the linear motor based hoisting system was technically feasible. However, it found that the R&D and industrialisation costs were prohibitively expensive. Thus, the Machines and Drives Research Group at the University of the Witwatersrand saw this as an opportunity to become involved as the development costs can be reduced significantly in an university environment.

1.1.2 Limitations of Rope Hoists

Underground mines that require a vertical transportation system to access the deep levels of the mine, use rope hoists. The limitations of using a rope hoist are emphasised to show that there are significant advantages to using a linear motor in a rope-less hoisting system.

The limitations to rope hoists are as follows:

- The rope itself is a major restricting factor. The mass of the rope limits the depth of a mine shaft.
- Large peak powers are required to accelerate hoists. Thus, large expensive electrical machines are needed.
- Sub-vertical shafts are used to attain greater depths, but they add to transportation times and reduce mine productivity.

Due to these limiting factors mentioned here, the costs per ounce of gold mined increases with depth. An overall cost analysis showed that the costs increase substantially for depths below $2000m$ and even more so for depths beyond $2500m$ [3]. All the limitations discussed are due to the use of thick diameter ropes. To further improve on hoisting technology, the rope diameter has to be reduced dramatically or be removed completely to make way for a linear motor.

The rope

At present no single rope hoist goes beyond $3000m$ [4]. As a hoist goes deeper, the mass of the rope increases. This limits the mass of the payload and hence the hoisting capacity of the mine. Also, the deeper the mine, the greater the duration of the hoisting cycle. This further reduces the hoisting capacity and productivity of the mine [5].

Another aspect to a rope hoisting system is that it requires considerable maintenance and time for both inspections and rope replacements. There are large costs involved in terms of the capital and maintenance expenditure for the ropes and drums used in a rope hoisting system.

Safety factors are incorporated into the size of the ropes. Aspects, like dynamics during acceleration and deceleration, have to be accounted for, so ropes have large

diameters and large masses. Due to the stringent safety requirements in the mining industry, a safety factor of between five and ten is incorporated in the hoisting rope selection [6]. This safety factor means that the rope selected must be designed to take five to ten times the maximum static load that it would experience. This factor is calculated depending on the depth of the wind, the capacity of the hoist and the accelerations that the hoist will experience. This factor also takes various conditions into account, including dynamic loading, fatigue of the steel in the rope, corrosion of the steel and size variations in the rope.

Peak power requirements

All mine hoists use a counterweight when hoisting, hence a lot of the energy goes into lifting the unbalanced weight of the hoisting system. Even though the conveyances[2] are counterbalanced with either another conveyance or counterweight, there is always an imbalance in the weight of the whole system due to the varying rope lengths as the conveyances travel in the shaft[3]. The deeper the mine shaft, the larger the weight imbalance and hence, the larger the peak power requirements to accelerate the load conveyance. Thus, large expensive electrical machines are needed to meet this demand.

Sub-vertical shafts

With the gold bearing reef at $3500m$, an additional subterranean shaft is sunk to obtain the gold. This shaft has its own electric drive and rope hoist assembly situated underground. Having sub-vertical shafts, the travel time of both men and material increases, reducing the productivity of the mine [8]. Along with reduced productivity, there are extra costs involved in terms of the capital expenditure for the equipment and installation of the conveyances in these sub-vertical shafts.

[2]Cages are used for man winders and skips are used for rock winders. Thus the word, *conveyance*, is used to represent either a cage or a skip.

[3]The only hoisting system that does not have rope weight imbalances is a Koepe winder with a tail-rope. These systems, however, are not generally used as they have other disadvantages, such as the possibility of rope slip and creep. Also, with two conveyances in balance, hoisting can only be done from one level [7].

1.1.3 Background on Linear Motors

A linear machine stems from the idea of cutting open a rotary motor and lying it out flat. With this simple conversion from rotary to linear motion, many applications are possible. This conversion can be seen in Figure 1.1.

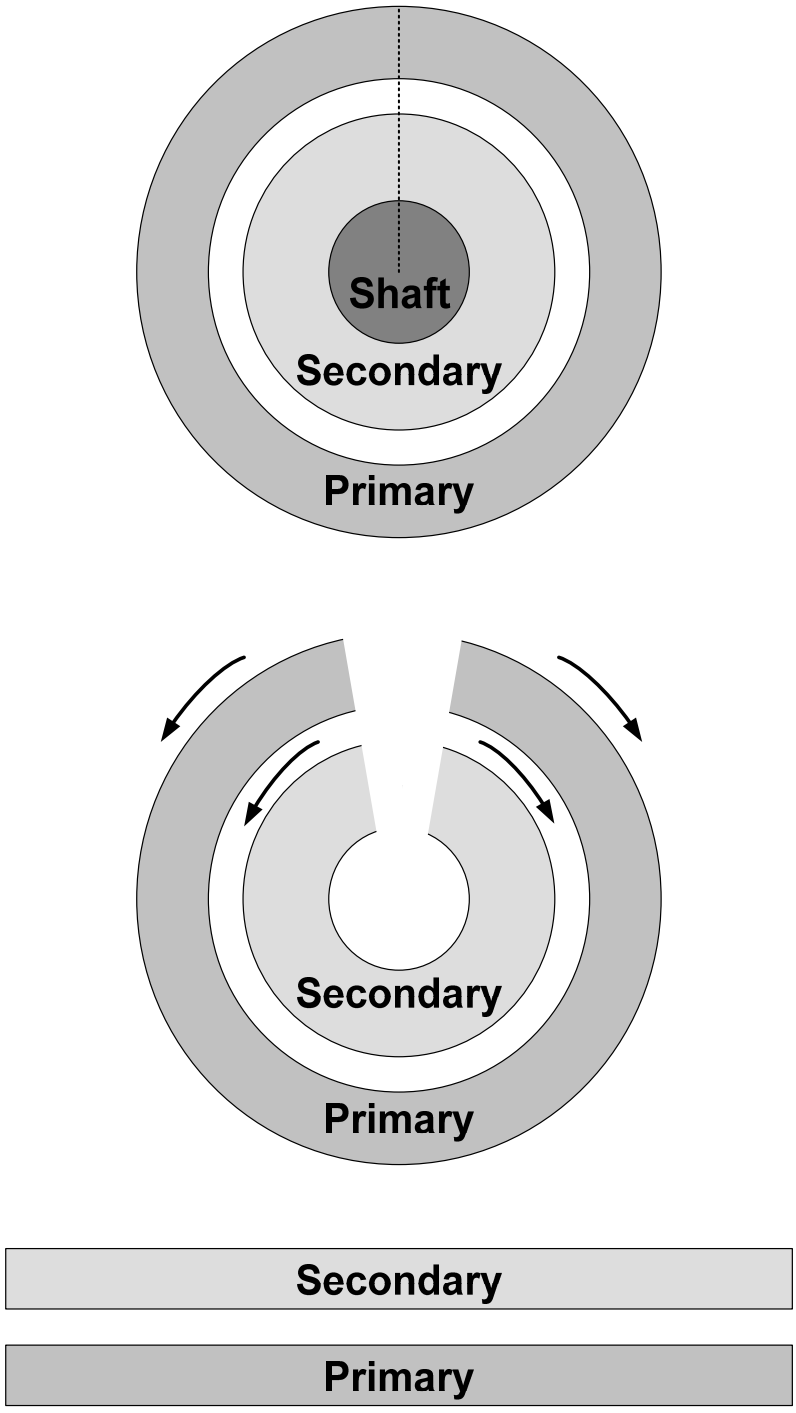


Figure 1.1: The conversion from rotary to linear motor.

Wheatstone designed the first linear motor in 1841, just 10 years after Faraday's discovery of the Laws of Induction [9]. Since then, until the 1960's, there has been relatively little development in the field of linear motors compared to that of the rotary motor. This was mainly due to the perception of engineers, that rotary motion was the most efficient way to convert electrical energy to mechanical energy or vise versa [10]. Also, linear motors generally aren't able to achieve the same power factors and efficiencies that the equivalent rotary motors can achieve [11].

With the increased interest of linear motors in the latter half of this century, linear induction motors (LIM) found more applications. Linear motors can eliminate the need for gears, ball screw drives or belts connected to a rotary motor for particular applications, as direct linear motion could be used. An example is an industrial printer. Instead of belts connected to rotary motors positioning the ink cartridges, the linear motor can be used to position them. Thus, the convenience of direct linear motion, in some applications, can make up for the reduction in performance compared to the rotary motor [11].

With advances in magnet technology in the 1990's, LSM's are becoming more popular. Along with improved performance, there is an ever increasing number of applications for LSM's. LSM applications vary in size from large requirements like a Maglev transportation system [12], to small precise applications like point to point sample testing in biomedical equipment [13]. Linear motors are also utilised for positioning with incremental changes in the order of nanometres.

For this project, it was decided that a LSM be chosen, as it produces a better efficiency and power factor compared with that of a LIM [11] [14]. Additionally, with the advances in rare earth magnet technology, magnets are now more powerful and can produce higher forces, compared with magnets 10 years ago. With the objective of attempting to produce the greatest force possible with a certain input power, the synchronous motor option was selected. Thirdly, an added advantage of using the synchronous motor, instead of an induction motor, is the inherent ability to allow for dynamic braking should there be an electrical power failure. This gives enhanced safety features to the linear motor.

There are two basic configurations of a linear machine (Figure 1.2):

- A long stator or primary section and a short rotor or secondary section.
- Or the converse of the first, with a short primary section and a long secondary.

Each of these configurations have two options in that either the primary or the

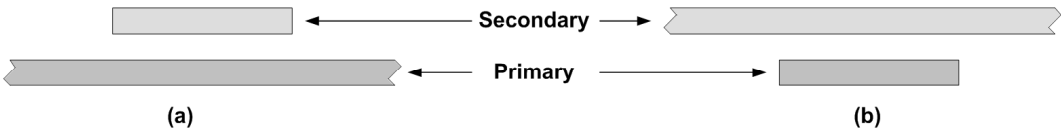


Figure 1.2: The two basic linear motor configurations. (a) Long primary and short secondary. (b) Short primary and long secondary.

secondary can be fixed, with the other being the mobile section. The stator windings are usually associated with the primary section. In the case of a LIM, an aluminium or copper plate forms the secondary. Permanent magnets or another set of coils would form the secondary for a LSM. For this project, a long stationary primary and a short mobile secondary with permanent magnets was used. This is the most convenient arrangement for this particular application and the reasons are discussed in Section 4.1.1.

There are three different linear motor topologies, namely (Figure 1.3):

- **Single-sided.** This consists of one primary section and one secondary section.
- **Double-sided.** Usually, consists of two primary sections, which are positioned on both sides the secondary.
- **Tubular.** A tubular linear motor is formed by rolling up a flat linear motor around the longitudinal axis. In general, the primary completely encircles the secondary.

Each topology in Figure 1.3 has a permanent magnet secondary. The decision to use a tubular topology rather than either the single- or double-sided topologies is discussed after a brief background on tubular linear motors is given.

Background on Tubular Linear Motors

In general, most tubular linear motors are used for short stroke applications [15–17]. The reason are:

- **for a long primary, short secondary,** the secondary section can only be accessed from the two ends of the primary.
- **for a short primary, long secondary,** the secondary needs to be supported. The secondary cannot be too long as it can only be supported at the two ends.

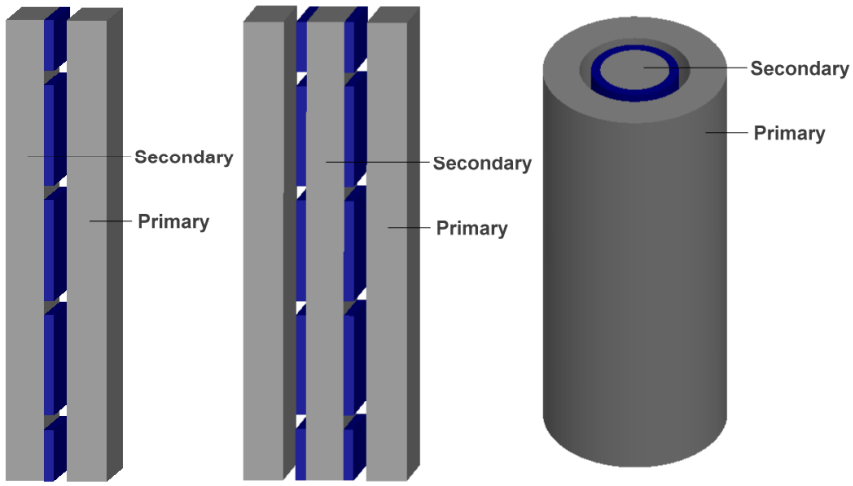


Figure 1.3: The three different linear motor topologies from the left: single-sided; double-sided; tubular.

Tubular linear motors are designed and used in various applications. Those listed below are for short stroke applications:

- As an electromagnetic hammer for the manufacture of gold foils [18] or hammers which have greater performance characteristics compared to oil and air pressure types [19].
- As pumps for artificial hearts [20, 21].
- As a finger supporter which enables the wearer to bend and straighten their finger if, through injury, they have lost the ability to do so themselves [22].
- As the direct drive for a positive displacement diaphragm air-compressor [23].
- As a cryocooler compressor [24].

Advantages of the Tubular Design

The tubular design has a few advantages over that of single and double-sided LSM:

- It has high force densities due to its cylindrical topology [25]. Due to the geometry of the tubular topology, the flux is concentrated towards the centre of the motor. As the flux flows radially from the primary to the secondary, the air gap flux density increases, as shown in Figure 1.4. This increase in air gap flux density towards the centre is proportional to the ratio of the primary

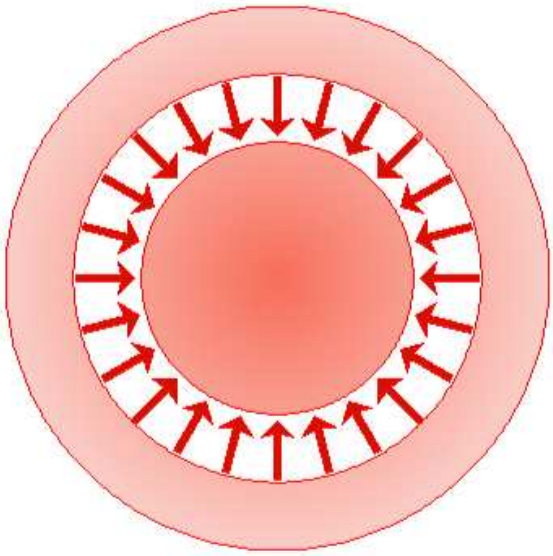


Figure 1.4: Flux concentration towards the centre of the tubular topology

surface area to the secondary surface area. Since the lengths of the poles on both the primary and secondary are the same, this increase in flux density is then proportional to the ratio of the respective circumferences and hence radii. Using the dimensions of this project as an example:

The primary inner radius = $60.00mm$
The secondary outer radius = $47.50mm$
Ratio of primary to secondary radii = 1.26

Thus, the area of the primary is 26% greater than the secondary, and the air gap flux density increases by 26% from the primary to the secondary. In a single or double-sided LSM, there is no flux concentration as the primary and the secondary have the same surface areas.

- It has a compact design and makes effective use of space. The tubular and double-sided topologies are more compact and use space more effectively compared to the single-sided topology. This can be seen in Figure 1.5 where all three topologies have the same cross-sectional area and equivalent active surface area. This is crucial in a mine shaft, as space is limited and must be used effectively.

- The normal or radial forces are negligible. As long as the air gap is kept constant, the normal forces are balanced. This is as a result of an equal radial force around the circumference of the tubular motor. For a single or double-sided LSM, the normal forces generated make the control of a constant air gap more difficult.

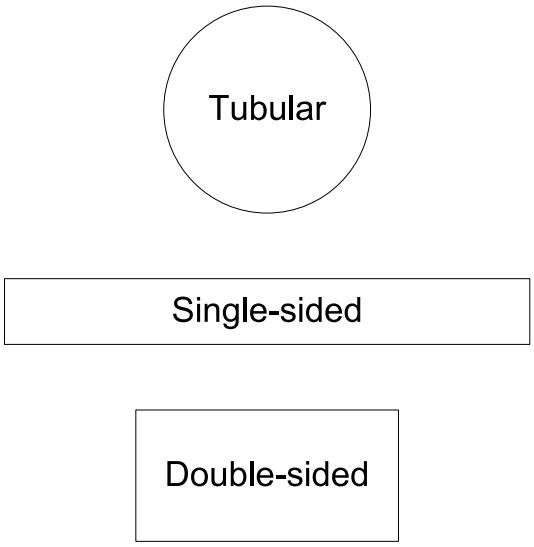


Figure 1.5: Graphical representation of tubular, single-sided and double-sided topologies

- The coils are also completely cylindrical so there is no overhang. This ensures optimum use of the copper and stored energy [26]. In a complete tubular topology, the primary windings encircle the secondary. There is one primary section and no overhangs. The single-sided topology also has one primary section, but has overhangs on its two sides. The double-sided topology, however, has two primary sections and hence overhangs on four sides. In the modified tubular topology, which will be explained in the next chapter, there are two sides that have overhangs with one primary section. The number of primary sections and overhangs can have cost implications for a very long linear motor.

1.1.4 Benefits and Limitations of Linear Motors Compared to Rope Hoists

Linear motors are seen as a viable alternative to rope hoisting technology. The major benefits are:

- Improved mechanical efficiency which reduces the operating costs of the system.
- An important safety feature when there is a loss of the electric power supply.
- Increased speed and acceleration capability.

- Increased productivity. There is no depth limitation along with increased transport capacity and reduction of transportation times.

The limitations of linear motor system are:

- High development and capital costs. However, a hybrid hoisting system[4] can reduce the overall length of the required linear motor and substantially reduce the capital costs.
- The human factor. The psychology of people travelling in a cage without a rope. Again, the linear motors can be used in a hybrid hoisting system.

Efficiency

The benefit for the linear motor technology, at ultra deep levels, is that the operating costs will be considerably less than that of the rope hoist, due to the improved efficiency. The reason being that no energy is consumed to correct for the rope weight imbalances that exist in a rope hoisting system.

An important parameter used in the design of a linear motor, that describes its performance and efficiency, is the Force to Weight Ratio (FWR).

The FWR is defined as:

$$FWR = \frac{F_T}{m_c g} \tag{1.1}$$

- F_T = thrust force
- m_c = mass of the motor moving components (active material)
- g = gravity

The greater the FWR, the better the efficiency of the system as more of the thrust force is used to lift the payload and the non-active material mass of the conveyance compared to the mass of the motor moving components, m_c.

The improved efficiency of the linear motor technology over the conventional rope hoist results in a lower input power requirement. Table 1.1 [27] gives the comparison of the peak power input required[5]. Clearly, with a much smaller peak power

[4] A hybrid hoisting system has a separate rope hoisting system operating together with the linear motor.

[5] A more detailed comparison of the two hoisting systems is given in Chapter 8.

Table 1.1: Peak power comparison.

Description	**Conventional Hoist**	**Rope-less Hoist**
Peak power	20MW	2.2MW

requirement, the operating costs of a linear motor system will be less than that of a large rotary motor used in a conventional rope hoist. It is not only the costs of the rotary motor on the surface that have to be taken into account, but also the costs of the electric drives situated underground for the sub-vertical shafts. There can be two separate sub-vertical shafts, depending on the depth of the mine.

Safety Feature

Another major advantage is the safety aspect of the whole system. If the electric power supply to the linear motor fails, the hoist will not drop at terminal velocity to the bottom of the shaft. Instead, due to the dynamic braking characteristic that can be employed in a linear synchronous motor, the hoist would travel slowly down the mine-shaft [28].

This steady state speed of the hoist travelling down the mine-shaft is dependent on various design aspects of the LSM. These include:

- The number of poles in the secondary section
- The pole pitch
- The strength of the magnets
- The air gap area
- The air gap length
- The number of coils in the primary sections
- The impedance of the coils
- The weight of the hoist

Under normal conditions, the coils of the primary winding will be short-circuited. The winding is only energised in the parts of the primary that are near or adjacent to the hoist. This has the added advantage that the energy costs can be optimised, as

there is no need to energise the whole length of the primary winding simultaneously. Once the hoist has passed, the coils are de-energised and again short-circuited.

Under a fault condition (loss of the electrical power supply) the coils of the primary winding will remain short-circuited. With the application of Faraday's Law of Induction and Lenz's Law, a free-falling cage passing these short-circuited coils would feel a force opposing its motion. This dynamic braking characteristic then slows the cage substantially such that the reduced speed at which the cage will hit the bottom of the shaft will be in no way life threatening. At the reduced speeds a mechanical brake could also be applied.

Another safety feature is that there is no risk of an overwind as there is no rope. An overwind is an expensive occurrence as the cage and or the rope can be damaged. There is also the downtime involved to get the cage back into operation.

Speed and Acceleration

In a rope hoisting system, the steady state speed is limited by the shaft steelwork and conveyance design [29]. In a linear motor the design of the guidance system could be investigated to increase the steady state speed of the cage, since the linear motor would have different requirements when it comes to these limitations. The major limiting factor would be that of passenger comfort.

The strength and size of the rope determines the acceleration of the conveyance in a rope hoisting system. In a linear motor, the major factor limiting the acceleration rate would again be passenger comfort.

Productivity

To mine effectively, a single shaft must be sunk to the full depth of a mine [30]. This can be achieved using a linear motor as there is no depth limitation. As there is no need for sub-vertical shafts, the productivity of the mine would increase with the work force getting to the work areas faster. By eliminating the rope, the operating costs would be reduced as there is no longer a need to use any energy to lift the rope up and down the shaft.

Using a linear motor, the diameter of a shaft can also be decreased, reducing the cost and time of sinking a shaft. The reason for decreasing the diameter of the shaft

is that multiple cages can operate simultaneously in the same shaft. Each of these cages will be smaller than the conventional cages and will take smaller loads. With many cages the overall transport capacity will be greater than the conventional rope hoist. Using one shaft for upward travel and another for downward travel, transportation becomes a continuous process instead of a batch process [31].

The Development and Capital Costs

A full-scale implementation of a linear motor in a mine-shaft would be very expensive. An investigation by a leading gold mining company concluded that the technology was viable, but shelved the project in 1992 for economic reasons [2]. Due to the reduced development costs at the University of the Witwatersrand, investigations into this technology continue.

Linear motors require a large capital outlay for the installation of the motor. The system would have a long stationary primary section and a short secondary section. This system would need the copper and steel for the primary section of the motor, and this would be expensive if the motor extends $5000m$ underground. It is however, envisaged that with the savings in the operating costs, as well as the profits made with the increased productivity, that the system would pay for itself in a few years.

Using a hybrid hoisting system would reduce the capital costs considerably. The hybrid hoisting system is a combination of a conventional rope hoist and a linear motor, as shown in Figure 1.6 [32]. The linear motor sections would be used at the bottom of a mine shaft as well as at each level. These linear motors would be used to accelerate and decelerate the conveyances. The use of a hybrid hoisting system combining a rope hoist and a linear motor can reduce the dynamics in the rope dramatically [33]. With the dynamics being reduced, the safety factor can also be reduced. This will lead to thinner ropes and greater depths being attained for single shafts [5]. The reduction in the safety factor with the use of thinner ropes means that hoisting capacity can be increased [5]. Also with the thinner ropes, the operating costs can be reduced as the rope imbalances are smaller, thus improving the efficiency of the system.

The Human Factor

This deals with the psychology of people. If mine workers refuse to get into a cage as there is no rope, it could prevent this project being implemented. This would

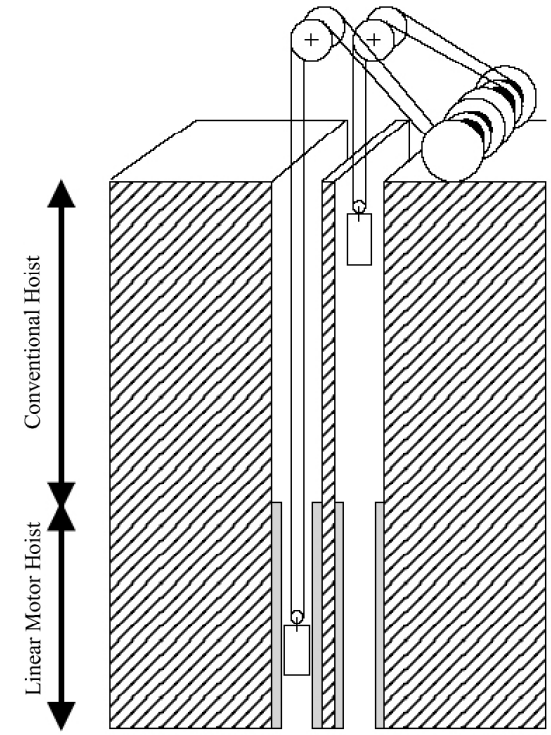


Figure 1.6: A hybrid hoisting system.

require an investigation in itself. Hopefully, this technology should be able to sell itself and convince anyone that it is a safe option which is far more convenient than the present rope hoists. However, if this is not the case, then these linear motors can be used in a hybrid hoisting system or operate alone in a rock hoist.

1.2 Research Objectives

The objectives of this research were stated in the beginning of this chapter. This section describes these objectives in more detail and outlines the contribution that the objectives make to the field of knowledge in linear motors.

1.2.1 The Modified Tubular Topology

As described earlier, conventional tubular motors are generally used only for short distance applications. The modified tubular LSM has been designed for long distance applications.

The modified tubular LSM is a unique linear motor and, as far as the author is

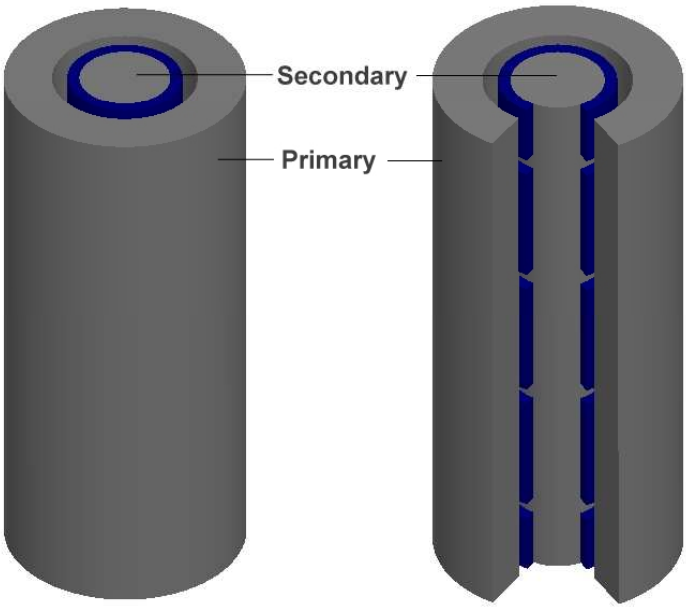


Figure 1.7: The conventional and modified tubular topologies.

aware, it is original in terms of its design and construction. It is a tubular linear motor with a gap in the primary along the length of the linear motor to allow access to the secondary section. This is shown in Figure 1.7. Due to the modification, this type of linear motor is not restricted in terms of its length and is seen as an ideal model for linear motors in long distance applications, such as ultra deep-level mines. The modified tubular topology uses the advantages of a tubular linear motor for long distance applications.

The literature does indicate that two other tubular motors have been built with a gap or a slit. However, these motors are used for short distance applications. Nasar et al. [34] states that a gap or slit can be used in the primary of a tubular linear motor, however, this is not to gain access to the secondary, but rather to reduce the eddy-currents in a transversely laminated primary. *The coils are still completely cylindrical.* Using a similar approach to [34], Roy et al. [35] also uses a slit in a tubular linear motor. This slit prevents eddy currents, in a conducting plate, to flow completely around the tubular linear motor. The magnetic fields resulting from the eddy currents in the plate are used to reduce the leakage flux of the linear motor. The result is a concentration of flux in the air gap. Once again, this slit or gap is not used as a means to access the secondary section of the tubular linear motor.

1.2.2 Optimisation of the Secondary Section

Another major objective of this project was the optimisation of the secondary section. This is necessary in order to increase the linear motor's force density, or FWR. There is limited space in a mine shaft, therefore the linear motor needs to produce as large a thrust force as possible, while keeping it's dimensions to a minimum.

The second stage of the project looked at optimising the modified tubular LSM, without changing the primary section. There are two ways to improve the performance of the linear motor, particularly when looking at increasing the overall output power or force. For this case, where there is a long primary and a short secondary, either the current can be increased in the primary or a greater magnet volume (stronger magnets) can be used in the secondary design. Increasing the current may lead to overheating of the linear motor, so a new secondary design would be a more viable option.

There are presently three different magnet arrangements commonly used for permanent magnet linear synchronous motors. They are the surface mounted magnet arrangement (SMMA), buried magnet arrangement (BMA) and Halbach array. Also, mention should be made of a novel design using magnets in a pulse wave modulation (PWM) arrangement [36][6].

The Halbach array was not analysed for this modified tubular topology. The structure of a Halbach array would make it difficult to implement practically for this modified tubular LSM. In a tubular topology, the Halbach array requires half the the number of magnets to be magnetised in the radial direction. This would be impossible for a disc magnet, therefore ring or doughnut shaped magnets would have to be used. Using ring shaped magnets would reduce the volume of the magnet material in the tubular topology. Manufacturing of these magnets could also be problematic as highlighted by Wang et al. [37][7]. The Halbach array has been practically implemented in a tubular linear motor before. Kim et al. [38] built a linear motor with a short mobile secondary section and primary on the inside of the motor. The magnet arrangement on the secondary encircled the primary and this made the use of the Halbach array a lot more practical.

Surface mounted magnets were used during the first stage of the project as part of the investigation into the feasibility of the modified tubular LSM. This surface

[6]The PWM design uses a similar form to the conventional surface mounted magnet arrangement.

[7]Wang et al. presented an analytical approach to a long secondary and a short stationary primary which encircled the secondary.

magnet arrangement is described in this thesis along with the new optimised design of the secondary section, which was built during the second stage of the project. The optimisation of the secondary focused on the commonly used magnet arrangements, excluding the Halbach array. The optimisation also included a new type of magnet arrangement. The magnet arrangements investigated were as follows:

- Surface mounted magnet arrangement (SMMA).
- Buried magnet arrangement (BMA).
- Combined magnet arrangement using both surface and buried magnets (CMA).

Parameter equations were developed for each arrangement. The optimisation involved shaping the flux paths in the secondary of a linear motor to prevent saturation of the steel sections. The geometry of the secondary was optimised and equations relating to the tubular linear motors dimensions were determined. These equations related all the dimensions of the secondary with respect to both the outside radius as well as the pole pitch. Generally, it is either of these two variables that are known and around which the rest of the dimensions need to be related. The analysis was aided with the use of FEA.

Another unique aspect to the optimisation of the modified tubular LSM is the development of a split pole magnet arrangement for the SMMA. Again, as far as the author is aware, this aspect of design optimisation is also original. This new variation to the SMMA is not restricted to the modified tubular LSM and can be applied to any type of linear synchronous motor, whether it is single-sided, double-sided or tubular in form. It is however, only applicable to surface mounted magnet arrangements. This split-pole magnet arrangement is described in more detail in Section 4.2.3.

1.3 Summary

The two main research objects of this thesis have been defined. These are to assess the viability of using a modified tubular LSM for rope-less vertical transportation systems and to develop design optimisation criteria for the LSM. The modified tubular topology was introduced within these research objects and it's contribution to the field of knowledge was highlighted. The background to existing rope hoists along with their limitations was discussed to emphasise the distinct advantages that linear motors can offer as a replacement to these rope hoists.

1.4 Outline of Report

The next chapter gives an overview of the whole design and justifies the use of the modified tubular topology. Included in the chapter are brief descriptions of both the primary and secondary designs.

From Chapter 3 onwards, the design and design optimisation criteria of the motor are described, as well as the construction and experimental results obtained. In the design of any motor there are four main aspects. Each of these aspects has an influence on the others, so careful consideration must be given to each. These are the electrical, magnetic, mechanical and thermal aspects and are considered in detail in Chapters 3, 4, 5 and 6 respectively. The optimisation of the secondary is described in the design of the magnetic system; Chapter 4.

FEA was used for the design of the linear motor and Chapter 7 describes this process in detail. FEA is a computer based application tool, which enables a designer to quickly analyse different design topologies and investigate their properties.

In Chapter 8, the results from the FEA are presented along with the experimental results. The experimental setup is summarised and the test procedure is outlined. The experimental and FEA results are then compared. The linear motor hoisting system is also compared with the conventional rope hoisting system.

In Chapter 9, conclusions are presented on the merits and drawbacks of the new motor topology. The research is summarised and its contribution to the field of linear motors is re-stated.

Chapter 2

The Design

Before this project could commence, certain design constraints were defined. These constraints gave the basic framework for the design to evolve into a working linear motor and are outlined in this chapter. The primary section design has more predefined constraints compared to the secondary section and these are described in more detail below.

The essence of the overall project is to investigate the feasibility of using a tubular linear synchronous motor for hoisting applications. Since men and materials are to be lifted, the conveyance cannot be contained within the motor. Thus, the tubular linear motor design has been altered to accommodate the conveyance on the outside of the motor. This modified design was shown in Figure 1.7. The actual conveyance carrying the men and materials would be attached to the moving secondary section, thus making the modified tubular LSM so unique. This configuration is illustrated in Figure 2.1.

This modified design no longer has all the advantages associated with conventional tubular linear motors as listed in the previous chapter. The advantages change as follows:

- There are still high force densities due to its cylindrical topology. The modified tubular LSM attempts to maintain this advantage even though the model is not completely cylindrical. The advantage remains in that there is still a flux concentration towards the centre of the modified tubular topology and it is for this reason that this topology was investigated for this project.
- The modified tubular topology still makes effective use of space. The modified tubular topology is still compact and would make effective use of space in a mine shaft.

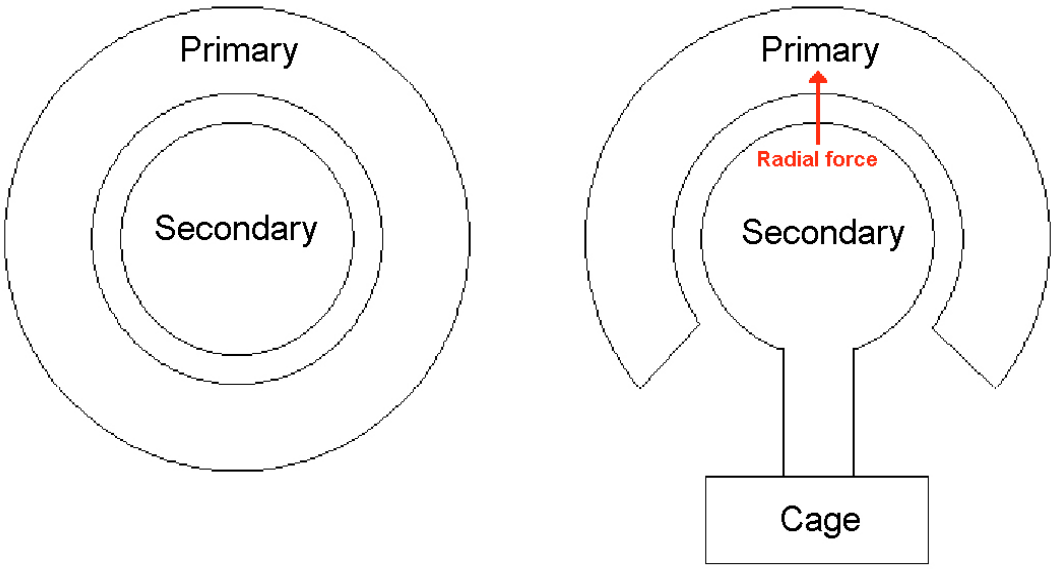


Figure 2.1: On the left is an axial cross-sectional view of a totally enclosed tubular motor. On the right is the cross-sectional view of the modified tubular motor.

- *The normal or radial forces are no longer negligible.* With a part of the primary removed there will be a large normal or radial force on the side opposite the conveyance as shown in Figure 2.1. However, this radial force would be balanced by another modified tubular linear motor which is placed on the open side of the conveyance as shown in Figure 2.2. Thus, there would be two linear motors, either side of the conveyance in a hoisting system. For the prototype, only one side was built to limit the costs of the project as well as to simplify the construction. The radial forces were then balanced mechanically by the guidance system. This is explained in more detail in Chapter 5.

- *The coils are not completely cylindrical.* Another advantage lost is that the primary coils do not encircle the secondary. The coils have overhangs on the open ends of the primary section.

2.1 Primary

For small tubular motors, solid steel sections or Soft Magnetic Composites could be used for the construction [39]. For larger machines, such as this one, it is suggested that laminations be used [11]. The positioning of the primary laminations against one another should be such that they do not fan-out on the outer edge of the primary section. If placed together, the thickness of the laminations would have to vary

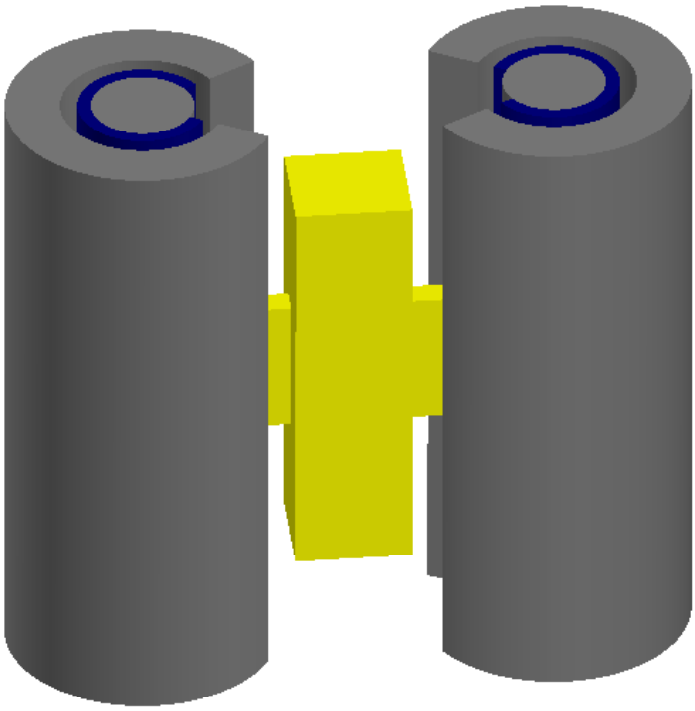


Figure 2.2: Hoisting system for a mine shaft. The conveyance is attached to the secondary sections of two modified tubular LSM's.

from the tooth area to the back of the primary. Either triangular or trapezoidal shaped laminations could be used, however, this would be difficult and costly to manufacture [40]. Therefore, a block arrangement was used, as shown in Figure 2.3 and Figure 2.4. This arrangement is described in further detail in Appendix A. The primary encircles the secondary by $\frac{5}{6}$ of a complete circle.

The design of the primary lamination is a set parameter. This is based on a design by E.R. Laithwaite [40] and was used for the first linear motor built at the University of the Witwatersrand. The dimensions of the lamination can be seen in Figure 2.5. This first linear motor was a twin single-sided LSM. With the previous projects and those running concurrently in the research group, it was decided to have one die made for the manufacture of all the laminations. This was an economic consideration as the cost of one tool is expensive and it is not viable to have numerous designs.

Initially the linear motor was constructed with semi-closed slots. However, it was found that once the first part of the linear motor was built with these semi-closed slots that the task of winding the machine would be extremely difficult. A thinner lamination strip was then used, such that the laminations would have open slots as shown in Figure 2.6 (The semi-closed portion of the laminations were not punched). This had implications on the air gap, as it was now $5mm$ longer.

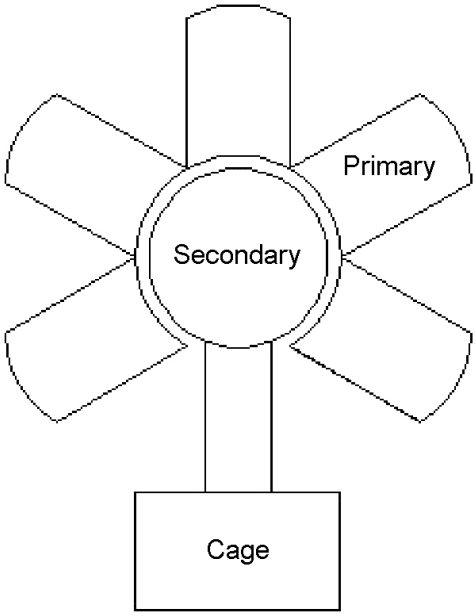


Figure 2.3: Block arrangement of primary laminations for a modified tubular LSM.



Figure 2.4: Primary laminations and coils shown during the winding of the modified tubular LSM.

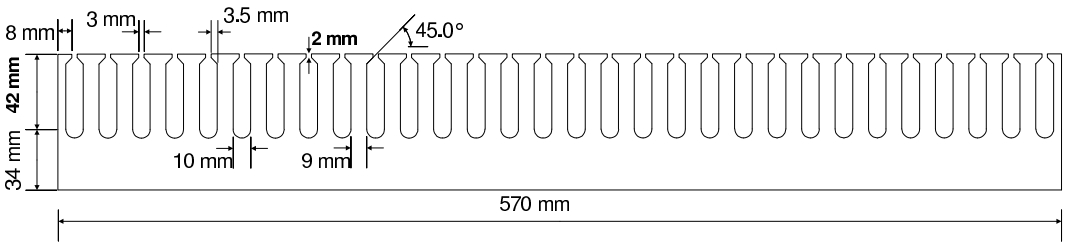


Figure 2.5: Primary lamination with semi-closed slots.

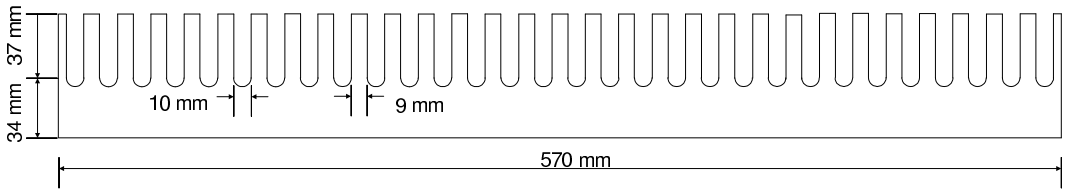


Figure 2.6: Primary lamination with open slots.

Since the lamination tooth height was reduced from $42mm$ to $37mm$, there would be a gap between each stack of laminations, so extra laminations were added to each stack. Therefore, each stack did not fit into the original design and thus had to be welded to the support frame, rather than bolted (See Section 5.1).

An important aspect of the project is to determine the maximum force that a modified tubular motor can generate. From a practical point of view, the linear motor needs to be long enough to facilitate these force measurements. The primary laminations have a length of $570mm$, which accommodate five poles using Laithwaite's design (pole pitch = $114mm$). So the length of two laminations would result in an overall length of $1140mm$ or ten poles. This would be long enough to fit a suitably sized secondary and allow the secondary to traverse several pole pitches. The design by Laithwaite used a narrow phase spread, double layer winding, with short chording. Thus, for a ten pole winding some of the return conductors of the coils would extend beyond the ends of the lamination stacks. In order to contain all the coils within the active length of the linear motor, the primary winding therefore consisted of nine poles[1].

Round copper wire with a diameter of $0.9mm$ was bought in bulk for the various ongoing projects at the University of the Witwatersrand. With the slot size as shown

[1]An odd number of poles is possible in a linear motor with a narrow phase spread winding. Unlike in the case of a rotary motor, an odd number of poles in a linear motor does not mean that two adjacent poles would be the same. In a linear motor the two end poles are the same, but the rest of the poles still alternate every pole pitch.

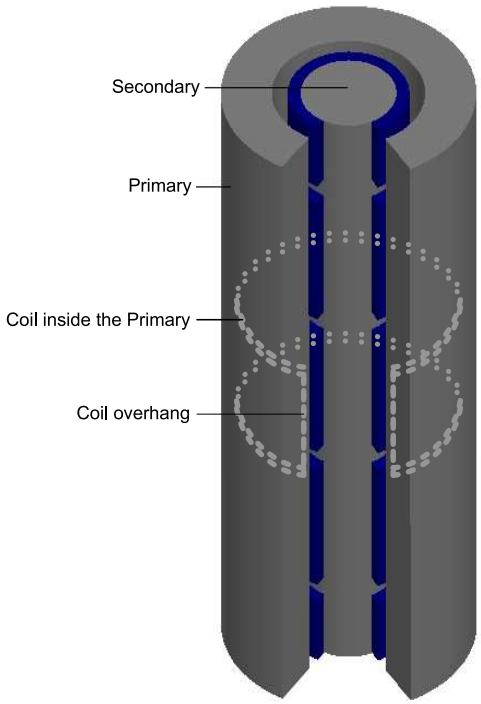


Figure 2.7: Shape of one coil inside the primary section.

in Figure 2.6, this copper wire would be suitable and was available for this project. Even though the diameter of the copper wire is a set parameter, one could still use a different number of turns, and/or a different coil span. However, the same winding configuration of the twin single-sided LSM has been used for the modified tubular linear motor. Subsequently, this winding configuration has also been used in a double-sided LSM built in the same laboratory. This winding configuration is a design proposed by Laithwaite [40]. The winding configuration is double layered, with 2 slots/pole/phase and is short chorded by one slot to reduce the negative effects of space harmonics. Using the same winding configuration allows for the comparison of the performance of the modified tubular LSM to that of motors with different topologies. The winding parameters for the linear motor are given in Table 2.1.

Figure 2.7 shows that the coils of the primary winding have a horse shoe shape. The overhangs run along the axial length of the linear motor and the return coil sides are placed in slots 5 slot pitches further on.

Table 2.1: Winding Parameters

Number of phases	3
Number of poles	9
Number of slots	60
Number of slots/pole/phase	2
Chording	$\frac{5}{6}$
Number of coils	54
Number of turns/coil	45 (2 parallel wires per turn)
Wire size	$0.9mm$ diameter

2.2 Secondary

The number of poles on the secondary had to be chosen such that it would produce a large enough force, but still be able to travel the length of the primary to demonstrate it's functionality. As mentioned, the primary consisted of nine poles, thus a secondary of four poles would allow the secondary to travel more than half a metre. This would be sufficient to test and demonstrate the linear motor.

For the diameter of the linear motor, the thickness of the magnets in the twin single-sided LSM was considered. That LSM prototype was built with $10mm$ thick magnets, so for the first stage of the project it was decided to build the modified tubular LSM with magnets of the same thickness for comparative purposes. FEA was used to determine the optimum diameter, such that the greatest FWR would be achieved.

As the diameter of the secondary increases, the force increases linearly as it is proportional to the surface area, $4\tau \times 2\pi r$ (See Equation 2.1).

$$F = BQ \times 4\tau \times 2\pi r \tag{2.1}$$

- B = average flux density
- Q = electrical loading
- τ = pole pitch
- 4τ = length of secondary
- r = radius to the middle of the air gap

However, the mass of the secondary increases with the square of the radius. So the FWR decreases. On the other side, if the secondary section is too small, the solid steel tube, on which the magnets are mounted, would saturate with flux and the force would reduce. So the FEA sought the optimum diameter to produce the greatest FWR.

Before the construction of the primary section, the FEA simulations were conducted with an air gap of $7.5mm$ and a primary with semi-closed slots. This air gap was chosen to be larger than a conventional rotary motor to account for the radial force that exists in the modified tubular motor (Figure 2.1). Using the FEA results and taking into account the available sizes for the aluminium tubes from the local manufacturers, the final outside diameter of the magnets were chosen to be $95mm$. The aluminium tube is there to protect the permanent magnets from physical damage[2]. However, due to the problems encountered with the semi-closed slots, the laminations were modified which resulted in an air gap of $12.5mm$. As it turned out, even the $12.5mm$ air gap proved to be troublesome as the large radial forces in the modified tubular LSM made the assembly a difficult task. With an air gap of $12.5mm$, the inside diameter of the primary section was $120mm$.

2.3 Summary

The modified tubular topology and it's proposed implementation for a rope-less vertical transportation system was introduced. The differences between the modified and conventional tubular topologies were compared to emphasised the advantages gained and lost with the introduction of the modified topology. However, this chapter's main focus was to give an overview of the modified tubular LSM design and design constraints. The modified tubular LSM was based on a design by Laithwaite [40] for both economic considerations and comparative reasons as there were multiple linear motor viability studies being conducted at the University. The main design constraints were focused around the primary with the lamination and winding designs being similar between projects. The area of greatest flexibility was in the secondary design which was one of the research objectives to develop and verify design optimisation criteria for the modified tubular LSM.

[2]The aluminium tube also acts as an eddy current shield and to some extent it acts as damper bars [41].

Chapter 3

Design of the Electrical System

The winding configuration for the modified tubular LSM is a set parameter. Therefore, this motor has been designed around a current rating rather than a voltage rating. With the winding configuration set, the number of parallel paths, for each phase, can be calculated such that the required supply is practically realisable. Depending on this configuration, the applied voltage can be determined. The LSM can be modelled on the basic equivalent circuit of the rotary synchronous motor.

It will be shown that due to the low operating frequency as well as the large air gap of the LSM, the reactance component of the LSM is negligibly small. Thus, the equivalent model of LSM is mainly resistive and the LSM runs at close to unity power factor. However, the full electrical analysis is presented in this chapter for a full understanding of the LSM. This analysis will also be used when the full scale motor operating at higher frequencies is considered.

3.1 Approximate Equivalent Circuit Per Coil

The permanent magnets on the secondary section produce a flux, ϕ_f, in the air gap (Figure 3.1 (a)). The three-phase primary windings also produces a flux, ϕ_a (Figure 3.1 (b)). This flux, ϕ_a, has two components to it. The first is a *leakage flux*, ϕ_{al}, which links with the primary winding only. The second is the *armature reaction flux*, ϕ_{ar}, and is established in the air gap. This latter component of flux ϕ_{ar} together with ϕ_f forms the air gap flux, ϕ_r (Figure 3.1 (c)). If saturation is neglected then each component of flux may be assumed to induce its own voltage in the primary winding. For example, E_f is induced by ϕ_f.

This modified tubular LSM has a long primary and a short secondary. There are

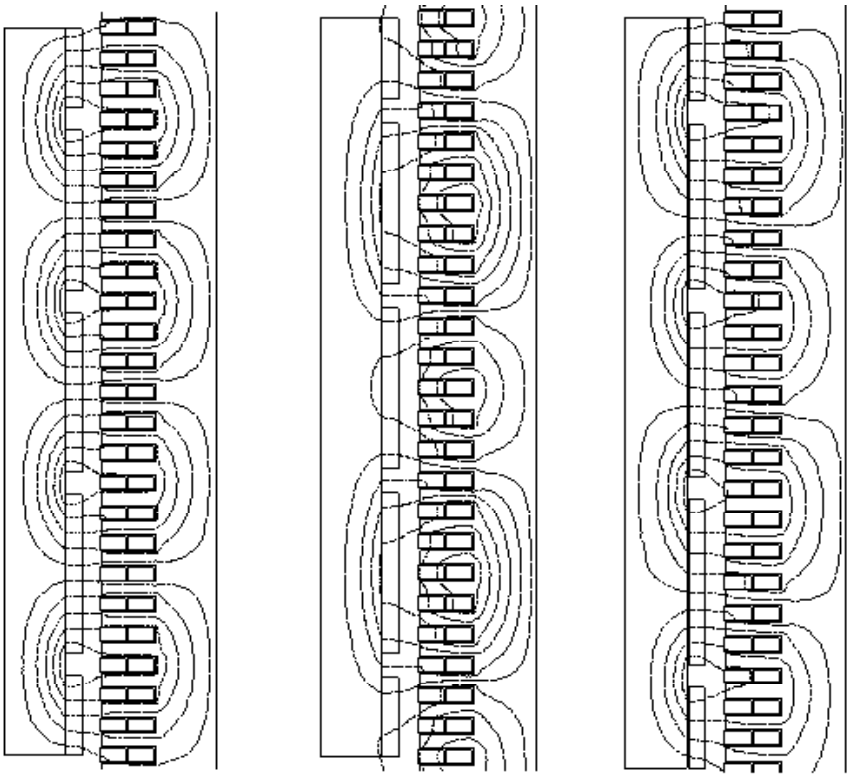


Figure 3.1: The flux pattern developed by: (a) the LSM with the coils un-energised and with the magnets present; (b) the LSM with only the coils energised. The properties of the objects representing the magnets have been changed to that of a vacuum; (c) the LSM with the coils energised and with the magnets present.

nine poles on the primary and four poles on the secondary. The development of a per phase equivalent circuit would have to take into account the number of parallel paths per phase and the position of the secondary relative to the primary. It is for this reason that the equivalent circuits presented here are per coil rather than per phase.

The induced voltages can be represented by the equation[1]:

$$E_{r1} = E_{ar1} + E_{f1} \tag{3.1}$$

The circuit representing this equation is given in Figure 3.2.

Using the motor conventions and referring to the phasor diagram of Figure 3.3, the voltage, E_{ar1}, leads the flux ϕ_{ar1} by 90^0 (This diagram is not to scale.). Therefore,

[1]The subscript 1 indicates that the quantities presented are per coil.

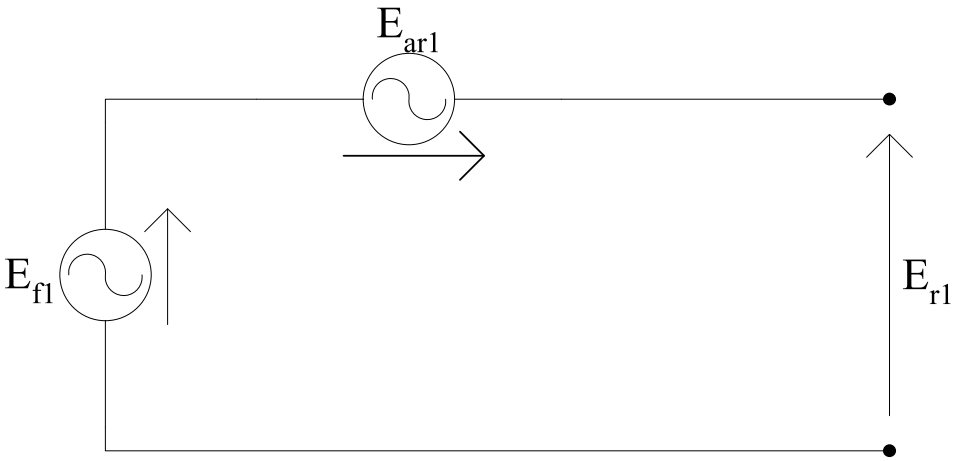


Figure 3.2: Equivalent circuit representing equation 3.1

the current, I_{a1}, lags E_{ar1} by 90^0 and hence this relationship between I_{a1} and E_{ar1} can be represented by the reactance X_{ar1}. This reactance is known as the *reactance of armature reaction*. The effect of the leakage flux, can also be described in terms of a volt drop with I_{a1} flowing through the leakage reactance X_{al1}. If the winding resistance is included, the equivalent circuit can now be represented by Figure 3.4.

If the reactances X_{al1} and X_{ar1} are combined they form X_{s1}, which is called the *synchronous reactance*. The final equivalent circuit per coil is as shown in Figure 3.5. This equivalent circuit shows the voltage drops across the winding resistance and synchronous reactance per coil. The phasor diagram of the equivalent circuit per coil for the LSM, operating as a motor, is shown in Figure 3.6.

With the whole primary energised, there are five poles where the circuit only consists of the primary winding. There will be no E_{f1} or E_{r1} components. The equivalent circuit per coil for these five poles, will consist only of the primary resistance (R_{a1}) and leakage reactance (X_{al1}), as shown in Figure 3.7. The leakage reactance will be much smaller than the coil resistance due to the low applied frequency and large reluctance path. A phasor diagram is shown in Figure 3.8 for the equivalent circuit in Figure 3.7.

As will be shown in the Section 3.2, the volt drop due to the resistance will dominate the equivalent circuit and phasor diagrams with or without the secondary section present. The phasor diagram with the secondary present is shown in Figure 3.9. This is the same phasor diagram as Figure 3.6, but with a comparatively large resistive component. As Figures 3.8 and 3.9 are similar, it will be assumed for the calculation of the applied voltage per coil, V_{t1}, that the secondary spans the whole nine poles of the primary.

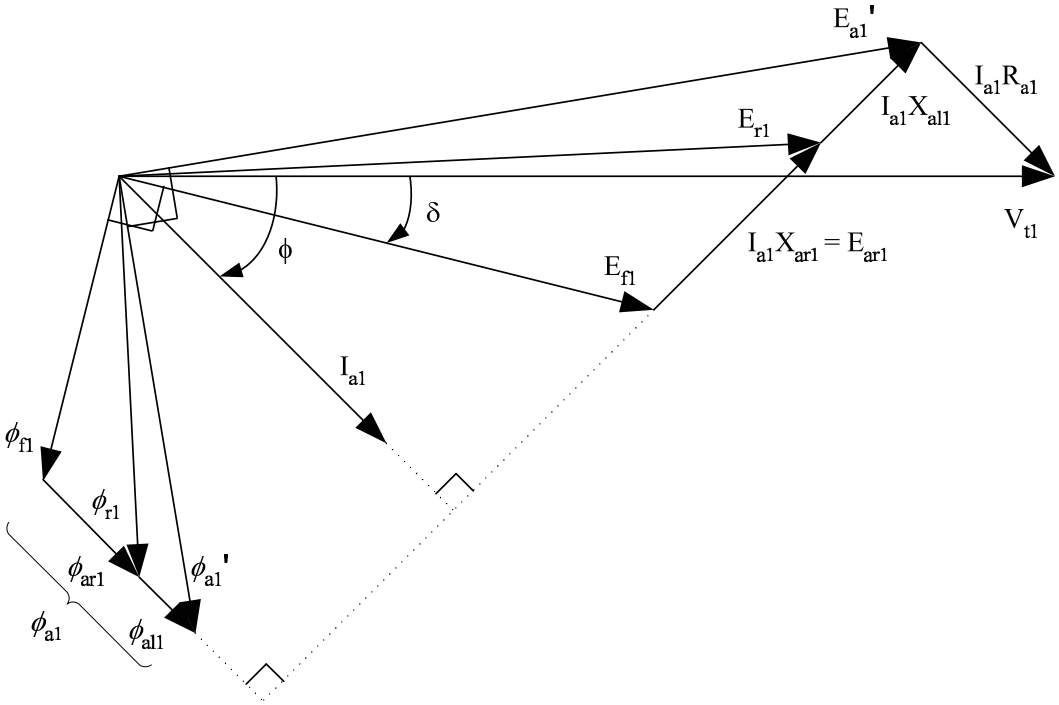


Figure 3.3: Phasor diagram of Figure 3.4

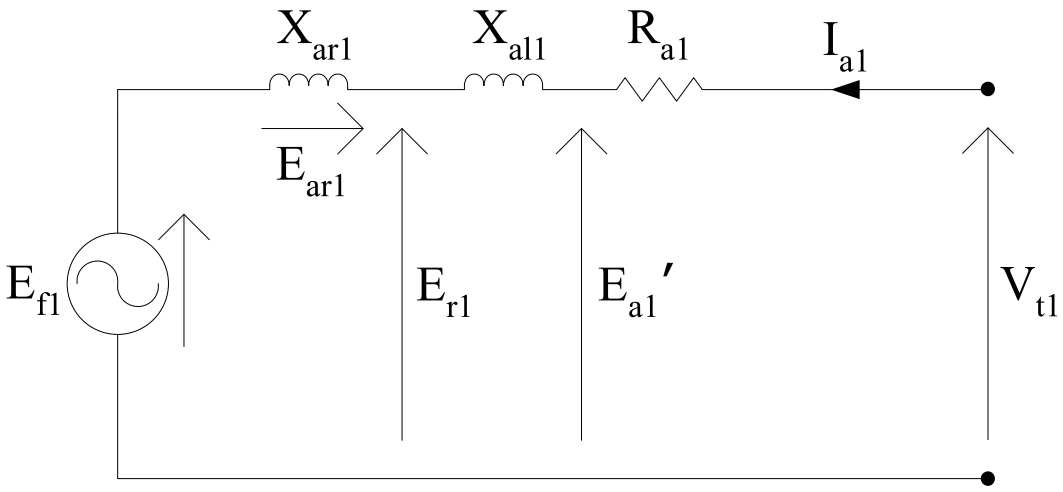


Figure 3.4: Equivalent circuit per coil with the reactances X_{ar_1} and X_{al_1}.

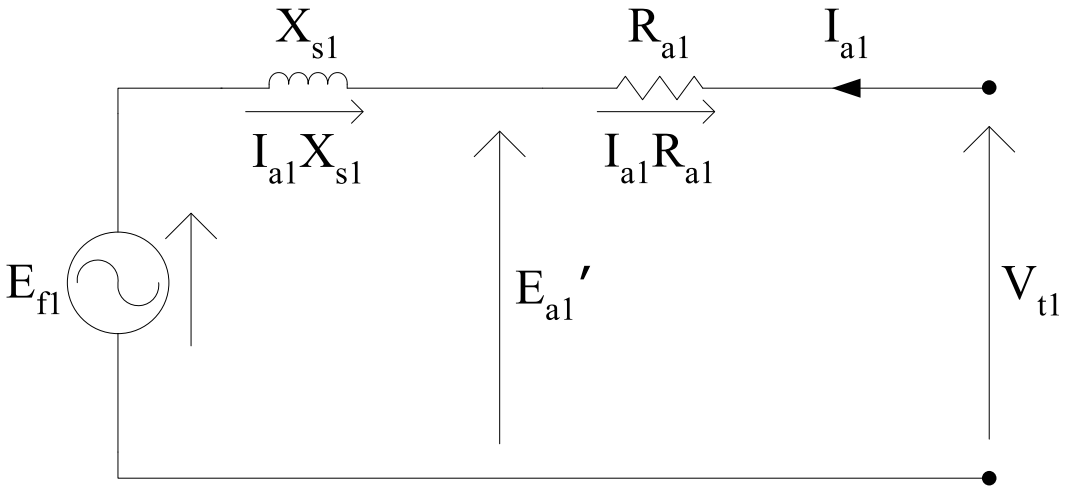


Figure 3.5: Final equivalent circuit per coil.

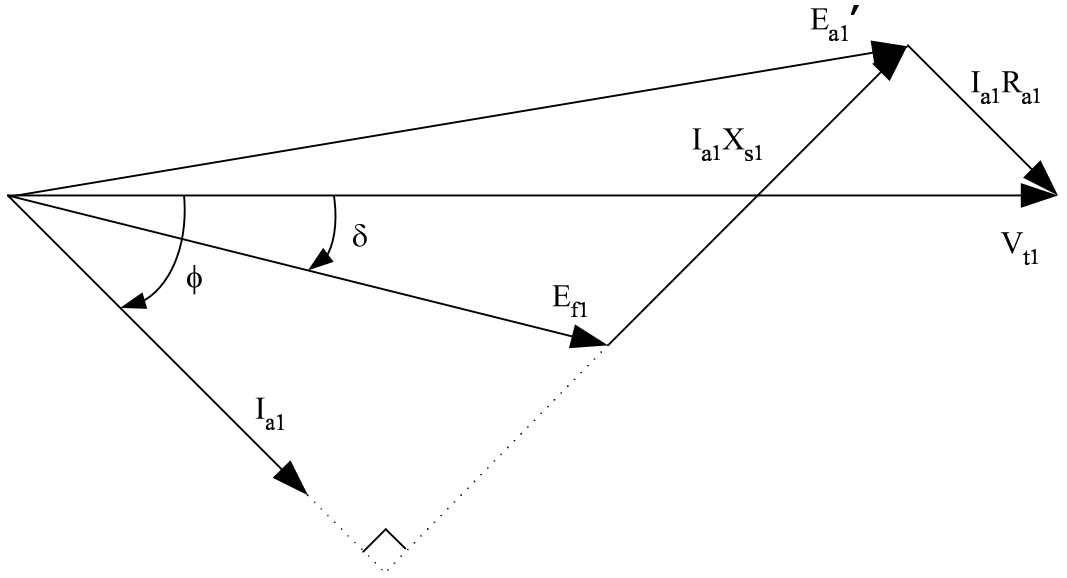


Figure 3.6: The phasor diagram for the LSM operating as a motor.

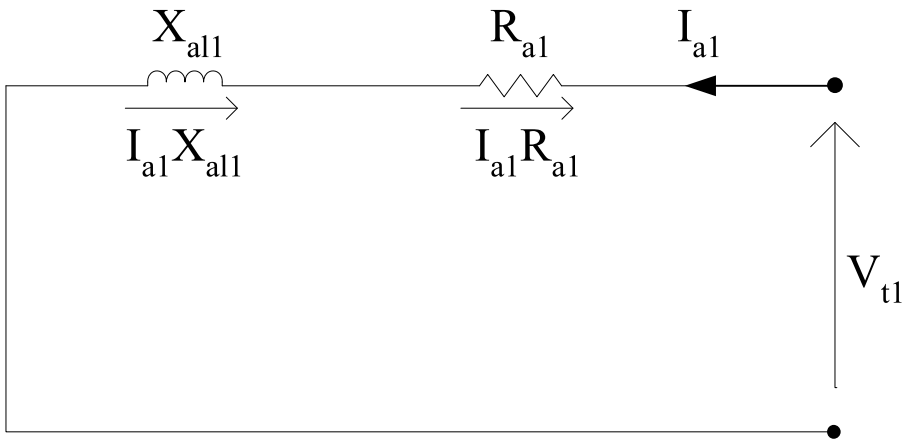


Figure 3.7: The equivalent circuit per coil without the secondary section.

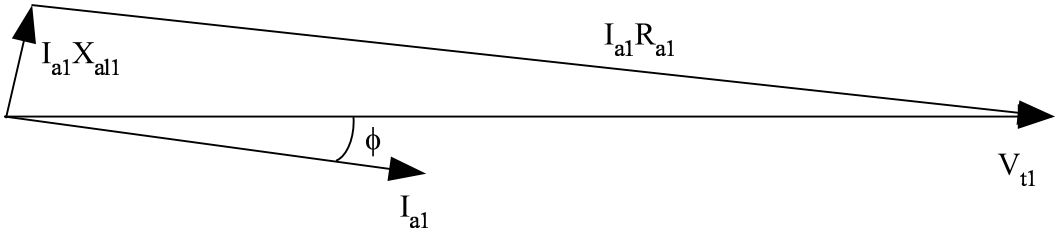


Figure 3.8: The phasor diagram for the LSM operating without the secondary.

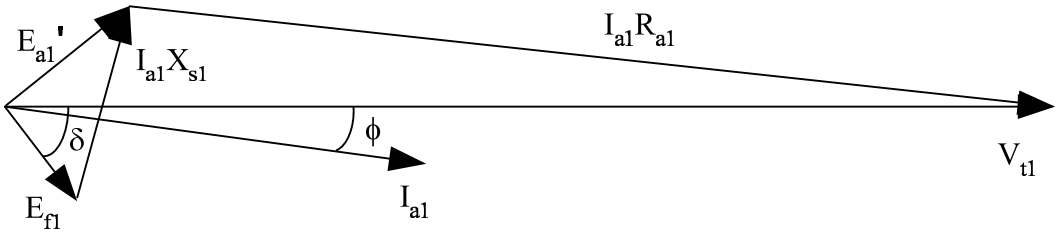


Figure 3.9: The phasor diagram for the LSM operating with the secondary. This shows that the resistance volt drop dominates.

For a full scale model, where the speeds and associated frequencies are a lot higher, the whole LSM must be modelled using both the two equivalent circuits, taking into account the number of parallel paths per phase and the position of the secondary relative to the primary. In this case, the equivalent circuits for the LSM with and without the secondary cannot be assumed to be similar.

3.1.1 Fluxes Generated in the Linear Motor

Powerful rare earth magnets ($NdFeB_{N-35}$) are used in this LSM. The field generated by these magnets is significantly greater than the field generated by the primary

Table 3.1: Flux values in the LSM

Permanent magnets and the coils un-energised (0A) - Figure 3.1 (a)	**Flux**
Top of the slots	$13.41mWb$
Bottom of the slots	$12.77mWb$
Permanent magnets and the coils energised (8A) - Figure 3.1 (c)	
Top of the slots	$13.40mWb$
Bottom of the slots	$12.21mWb$

winding and it follows that E_f will be larger than E_a in magnitude. This will be shown during the calculation of the induced voltages further on in this chapter. A FEA confirms the domination of the flux generated by the permanent magnets.

The fluxes generated within the linear motor can be seen by analysing the FEA plots in Figure 3.1. The surface mounted magnet arrangement has been used for this analysis. Figure 3.1 (b) shows the flux pattern developed by the LSM with only the primary winding energised (8A per coil). In this case, because the field flux is not present, the properties of the objects representing the magnets were set to those of a vacuum. Figure 3.1 (a) shows the flux pattern developed by the LSM with the primary winding un-energised (0A per coil) and with the magnets present. This figure is similar to Figure 3.1 (c) where the flux pattern developed by the LSM having the primary winding energised (8A per coil) and with the magnets present, is shown. These three figures show that the dominating flux in the LSM is the flux developed by the permanent magnets because the patterns shown in Figure 3.1 (a) and (c) are similar, rather than those of Figure 3.1 (b) and (c).

Examining the flux values using FEA confirms the visual analysis that the dominating flux in the LSM is the flux from the permanent magnets. In the FEM model two lines are defined. The first is along the top of the slots for one pole pitch, and the other is along the bottom of the slots[2]. The amount of normal flux passing through each line can be calculated using the "Post Processor" of the FEM program. See Table 3.1 for the results.

[2]Using two lines and the top and the bottom of the slots allows for the slot leakage flux to be evaluated.

3.2 Calculation of the Required Applied Voltage

The required applied voltage per coil is the phasor V_{t1} in the phasor diagram in Figure 3.9. In order to calculate its magnitude, the values of the other three phasors (E_{f1}, R_{a1} and X_{s1}) that sum up to produce V_{t_1}, need to be determined.

3.2.1 Induced Voltage for One Coil, E_{f1}

The induced voltage for one coil in the primary, produced by the magnets, can be determined from the following fundamental equation:

$$E_{f1} = 4.44\Phi f N_c K_e \tag{3.2}$$

- E_{f1} = induced voltage for one coil
- Φ = flux per pole
- f = frequency
- N_c = number of turns per coil
- K_e = chording factor

Each of the five components of Equation 3.2 were evaluated as follows:

Chording Factor, K_e

A sample section of the primary winding can be seen in Figure 3.10. The total number of slots for the primary section is 60. In these slots there are 18 coils for each phase. Thus, the total number of coils is 54.

There are 9 groups of coils for each phase, so there are also 2 coils per group. Each pole spans 6 slots, and thus 180^0 electrical degrees. So the angle between each slot is 30^0 electrical degrees.

$$K_e = \sin\left(\frac{\beta}{2}\right) = 0.966 \tag{3.3}$$

- β = span of the coil in electrical degrees = $\left(\frac{5}{6} \times 180^0\right) = 150^0$

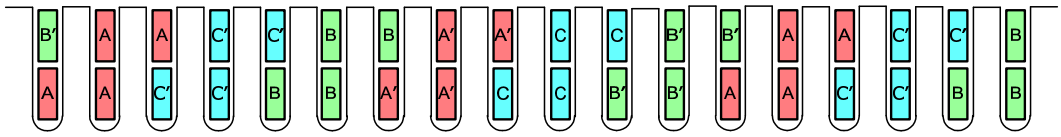


Figure 3.10: A sample section of the primary winding. All three phases are shown. A indicates a 'go' conductor and A′ the 'return' conductor.

Number of Turns, N_c

N_c is the number of turns per coil, which equals 45.

Frequency, f

The frequency of the electrical power supply is another parameter of Equation 3.2. Its value is chosen depending on the required velocity of the linear motor.

The velocity of the secondary, is determined from the equation:

$$v_s = 2\tau f \tag{3.4}$$

- v_s = secondary velocity
- τ = pole pitch ($114mm$)
- f = frequency

The primary section has a total length of $1140mm$.

Therefore, the velocity for a frequency of $10Hz$ is $2.28m/s$. This means that the secondary will cover the length of the primary in approximately half a second. Practically, this is too fast for the short length of this motor, so a frequency of $0.5Hz$ was chosen, allowing the secondary to cover the distance in 10 seconds. This low speed was chosen so that meaningful and reliable measurements could be taken during the AC tests (The AC test is described in Chapter 8).

Flux per Pole, Φ

This is determined from the flux density acting on the primary windings for one pole pitch multiplied by the pole area. The flux is generated by the permanent magnets.

$$\Phi = B \times area \tag{3.5}$$

- B = average flux density
- $area$ = length of a pole pitch $\times$ circumferential width of the motor.
  - length of a pole pitch = $114mm$
  - circumferential width of the motor = $\frac{5}{6} \times 2 \times \pi \times r = 288mm$ $(r = 60mm)$

The reason for the $\frac{5}{6}$ factor in the area calculation is that the modified tubular linear motor covers 300^o of the tubular topology. (See Figure 2.1)

The flux density can be determined analytically [42–47]. However, the flux per pole can also be determined using FEA. The results from the FEA approach were used for this project as the non-linearity associated with the magnetic steel can be easily accounted for when doing predictions.

In the FEM model two lines are defined as described in Section 3.1. The first is along the top of the slots for one pole pitch, and the other is along the bottom of the slots. The amount of normal flux passing through each line is then calculated. Unless there is a large amount of leakage flux or the flux direction changes drastically such that the normal component reduces significantly, these two values should be similar. This simulation was performed with the coils unexcited, so that only the influence of the magnets on the coils themselves could be analysed. The results obtained are the same as those in Table 3.1.

The two values of flux per pole are:

Top of slots: $13.41mWb$

Bottom of slots: $12.77mWb$

From these two values, the average value of normal flux passing through the coils can be calculated. This value is $13.09mWb$ and is the amount of normal flux over one pole pitch.

The flux value used is that for the surface mounted magnet arrangement. The same approach can be used for the buried magnet arrangement. The buried magnet arrangement is the optimised secondary design which is described in Section 4.2. It is anticipated that the flux value for the buried magnet arrangement would be slightly higher as the magnet operates along a steeper *permeance coefficient* line (Section 4.1.2).

Induced Voltage for One Coil, E_{f1}

From Equation 3.2, using a frequency of $0.5Hz$, the induced voltage should be:

$$\begin{aligned} E_{f1} &= 4.44\Phi f N_c K_e \\ &= 4.44 \times 0.01309 \times 0.5 \times 45 \times 0.966 \quad V \\ &= 1.26 \quad V \end{aligned} \tag{3.6}$$

The above result gives the value for the voltage produced in one coil.

3.2.2 Voltage Phasor for the Coil Resistance, R_{a1}

The resistance for one coil R_{a1} is:

$$R_{a1} = \frac{\rho l}{A} \tag{3.7}$$

- ρ = resistivity (copper = $1.78 \times 10^{-8} \quad \Omega m$ at 20^oC)
- l = length of the copper wire
- A = cross-sectional area of the copper wire

The average length of one turn of a coil is $1.2m$. Each turn is made of two strands of $0.9mm$ wire. The cross-sectional area for each strand is $6.36 \times 10^{-7} m^2$.

For one coil:

$$R_{a1} = 0.755 \quad \Omega \tag{3.8}$$

This is the DC resistance value. Since the frequency used is $0.5Hz$, any skin effect is negligible and hence the DC resistance will be modified only for temperature. With full rated current of $8A$ flowing through the coil[3], the volt drop across the coil is $6.04V$ at 20^oC and is only due to the resistance of the copper wire.

3.2.3 Voltage Phasor for the Coil Synchronous Reactance X_{s1}

This is the third phasor which completes the voltage triangle in the phasor diagram. This reactance is made up of the leakage reactance, X_{al1} and the armature reaction reactance, X_{ar1}. The leakage reactance can be calculated from the equation:

$$X_{al1} = 2\pi f L_{al1} \tag{3.9}$$

- f = frequency = $0.5Hz$
- L_{al1} = leakage inductance for one coil

This leakage reactance, X_{al1}, is made up of the slot leakage and the overhang leakage. The overhang leakage reactance is dependant on the overhang arrangement and on the proximity of metal masses, such as end-covers [48]. For this linear motor, the overhangs are, to a certain extent, out in the open and are not near any other metallic objects except for the primary stacks. Detailed pictures are shown in Chapter 5 (Figures 5.5 and 5.6). Also, the length of the coil inside the primary is approximately two times the length of the overhang. Thus, it is assumed that the overhang leakage reactance will be a negligibly small and X_{al1} will only be the slot leakage reactance.

[3]The initial full rated current of $8A$ per coil is based on a current density of just over $6A/mm^2$. This may seem high, but for the application, the duty cycle of the linear motor is expected to be small (See Section 6.5). The continuous rating of the linear motor is less than $8A$ and was based on the thermal capacity of the linear motor using Class F insulation (See Table 6.2)

Since the primary laminations have open slots, it is assumed that the slot leakage flux paths do not saturate. Thus, a linear relationship exists between the leakage flux and the current. The leakage inductance becomes:

$$X_{al1} = 2\pi f N \frac{\phi_{al1}}{I_{a1}} \tag{3.10}$$

The leakage flux is determined by using FEA. The leakage flux, is the flux generated by the coils which does not pass through the air gap. Two lines are defined in the FEM model and over one pole pitch. These lines are used to determine the flux generated by the primary winding which interact only with itself. The lines are defined at the top and bottom of the primary slots. The magnets have been assigned the same properties as that of a vacuum in the FEM model, so that the simulated result will be that of only the magnetic field generated by the current in the primary winding. The rated current of $8A$ per coil is used for the FEM simulation. The normal flux to these defined lines are as follows:

Top of slots: $2.55mWb$

Bottom of slots: $4.85mWb$

There is a difference of $2.30mWb$. However, this is the flux generated over one pole pitch with the whole primary winding energised. Since there are 4 coils per phase per pole, effectively 12 coils generate the total flux per pole. So the average contribution for each coil is $\frac{1}{12}$ of the total flux per pole.

Thus, there is a average difference of $0.19mWb$ per coil and this value is used to calculate the leakage reactance X_{al1} for one coil.

$X_{al1} = 2\pi \times 0.5 \times 45 \times \frac{0.19\times10^{-3}}{8}$ Ω
$X_{al1} = 3.39$ $m\Omega$

With full rated current of $8A$ flowing through the coil, the volt drop across the leakage reactance, X_{al1}, of the copper wire is $27mV$.

The armature reaction reactance can be calculated from the amount of flux that exits at the top of the slots (near the air gap) and crosses the air gap

to the secondary section. The FEA gave a flux value of $2.55mWb$. Using the same approach for the leakage reactance, the armature reaction reactance is:

$X_{ar1} = 2\pi \times 0.5 \times 45 \times \frac{0.21\times10^{-3}}{8} \quad \Omega$
$X_{ar1} = 3.76 \quad m\Omega$

With full rated current of $8A$ flowing through the coil, the volt drop across the armature reaction reactance, X_{ar1}, of the copper wire is $30mV$. This gives a total volt drop of $57mV$ for the coil synchronous reactance, X_{s1}. This value is much smaller than the volt drop across the coil resistance ($6.04V$).

3.2.4 Applied Voltage, V_{t1}

The low voltage values for the induced emf, E_{f1}, and the volt drop across the synchronous reactance, X_{s1}, indicates that at low frequencies the motor is mainly resistive and has a relatively good power factor. The range of power factors in which the motor will operate is determined from the phasor diagram. From the phasor diagram the power factor and V_{t1} are calculated. This would be the applied voltage for one coil, so that the motor would operate at rated current of $8A$ per coil.

By examining the phasor diagram in Figure 3.9 the angle δ cannot be greater than 90^o or less than -90^o. This can be explained as follows. When a sinusoidal voltage is applied to the coil, the secondary section moves relative to the primary. The magnets induce a back emf, E_f, in the coil which opposes the applied voltage. Therefore, if the magnitude of δ is greater than $|90^0|$, it implies that E_f has a component in phase with V_t, rather than out of phase with it (taking E_f as a voltage rise). This is also coupled with a reversal of the force.

From the phasor diagram in Figure 3.9 and taking V_{t1} as the reference, the voltage equation is:

$$V_{t1} \angle 0^o = E_{f1} \angle -\delta + I_{a1} \angle -\phi \, (R_{a1} + jX_{s1}) \tag{3.11}$$

There are three unknowns in equation 3.11. They are the two angles, δ and ϕ, and the applied voltage, V_{t1}. For the reasons stated above, this equation will be solved by making angle δ a known quantity. V_{t1} and the corresponding angle ϕ will be solved for the conditions when angle δ is 90^o, -90^o and 0^o. This will give the range of values required for V_{t1} and the associated power factor.

- When δ is 90^o, -90^o the value of V_{t1} will be the same minimum value. The difference between the two, is the solution to $\phi|_{\delta=\pm 90^o}$. The corresponding phasor diagrams are shown in Figures 3.11 and 3.12 (These phasor diagrams are not drawn to scale).
- For δ equal to 0^o, V_{t1} will be a maximum, and the angle $\phi|_{\delta=0}$ will be between the two solutions from when δ is either 90^o, -90^o. The corresponding phasor diagram is shown in Figure 3.13.

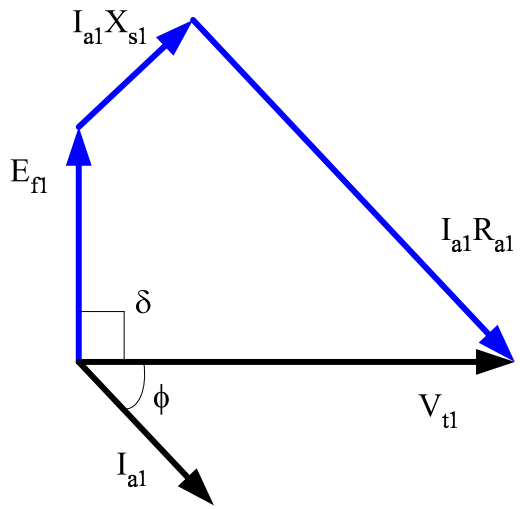


Figure 3.11: The phasor diagram from Figure 3.9 with $\delta = 90^o$

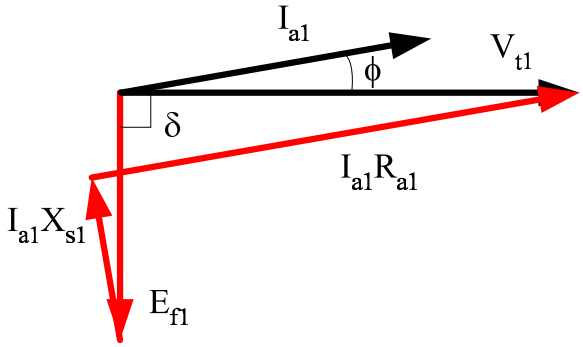


Figure 3.12: The phasor diagram from Figure 3.9 with $\delta = -90^o$

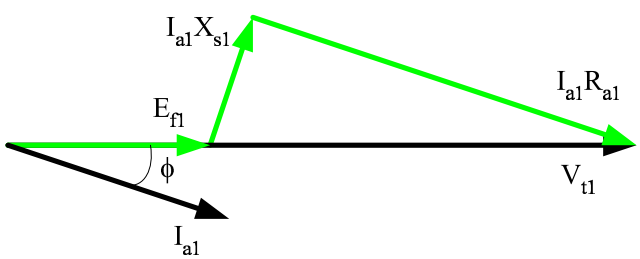


Figure 3.13: The phasor diagram from Figure 3.9 with $\delta = 0^o$

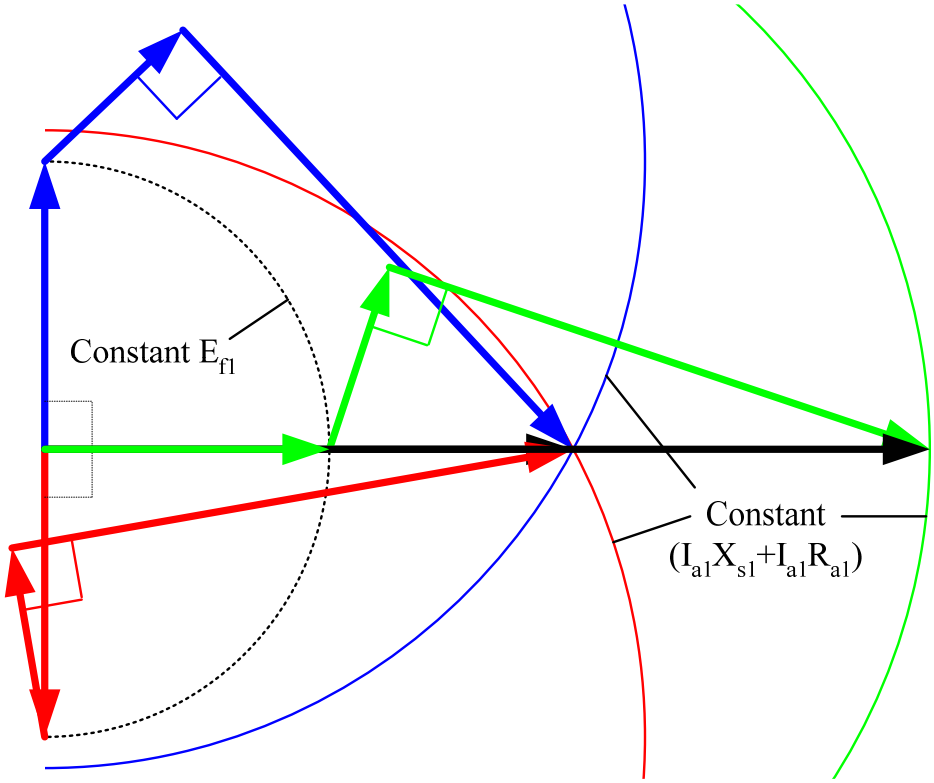


Figure 3.14: The phasor diagram combining Figures 3.11, 3.12 and 3.13

Figure 3.14 combines all three phasor diagrams together and gives an overview of the range of operation for the modified tubular LSM. For this project, with the very low operating frequency, $I_{a1}X_{s1}$ is very small compared to $I_{a1}R_{a1}$. However, it has been included in this analysis as $I_{a1}X_{s1}$ would play a significant role if the modified tubular LSM was operating at much higher frequencies.

Equation 3.11 can be written as:

$$V_{t1}(cos(0^o)+jsin(0^o)) = E_{f1}(cos(\delta)+jsin(\delta))+I_{a1}(cos(\phi)+jsin(\phi))(R_{a1}+jX_{s1}) \tag{3.12}$$

Equating real and imaginary parts:

Reals:

$$V_{t1} = E_{f1}\,cos(\delta) + I_{a1}\,cos(\phi)R_{a1} - I_{a1}\,sin(\phi)X_{s1} \tag{3.13}$$

Imaginaries:

$$0 = E_{f1}\,sin(\delta) + I_{a1}\,sin(\phi)R_{a1} + I_{a1}\,cos(\phi)X_{s1} \tag{3.14}$$

- For $\delta = 90^o$

  $V_{t1} = 5.91V$
  $\phi = -12.58^o$ or $cos(\phi) = 0.98$

- For $\delta = -90^o$

  $V_{t1} = 5.91V$
  $\phi = 11.50^o$ or $cos(\phi) = 0.98$

- For $\delta = 0^o$

  $V_{t1} = 7.30V$
  $\phi = 0.54^o$ or $cos(\phi) \approx 1.00$

It must be noted that these values are for one coil only. The actual applied voltage to the linear motor will depend on:

- the number of coils per group.
- the manner in which the coil groups are connected. (Series or parallel)
- the number of coil groups per phase.
- whether the linear motor is star or delta connected.

The primary winding connections are shown in Figure 3.15. The thicker coils are adjacent to the secondary and are represented by the equivalent circuit in Figure 3.5. The thinner coils are outside the influence of the secondary and are represented by the equivalent circuit in Figure 3.7. Figure 3.15 indicates that the secondary is in the middle of the primary along its length. The details of the primary winding connections are as follows:

- There are two coils per group, which are series connected.
- There are 27 groups of coils; 9 for each phase.
- There are 3 parallel paths for each phase, thus 6 coils in series.
- The primary winding is star connected.

With these details the required phase voltage can be calculate.

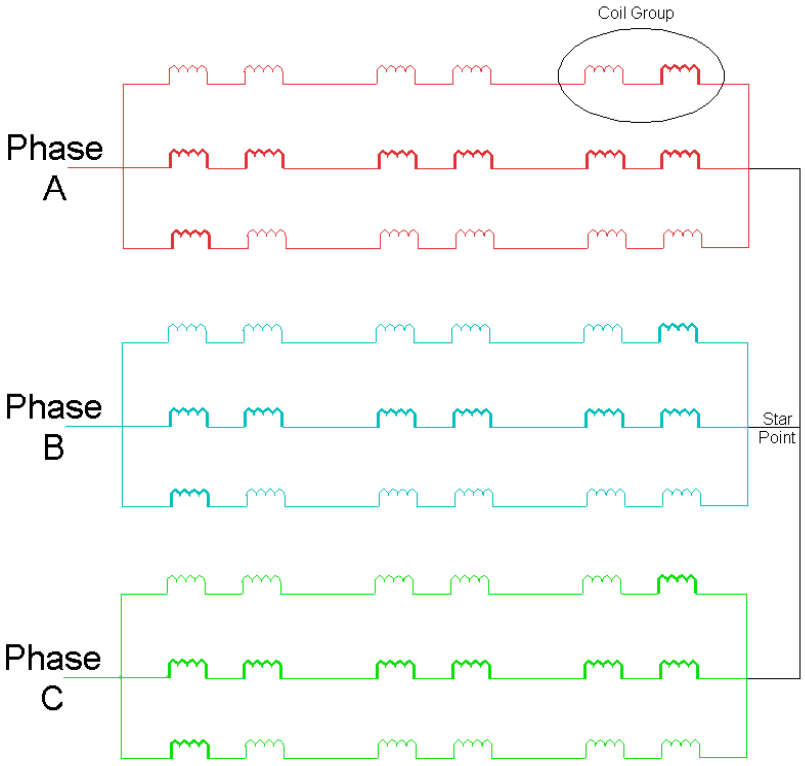


Figure 3.15: Primary winding connections.

Now

$$K_m = \frac{\sin\frac{h\gamma}{2}}{h\sin\frac{\gamma}{2}} \tag{3.15}$$

- $h = 2$ number of coils per group
- $\gamma = 30^o$ span in electrical degrees between coils

Therefore:

$$K_m = \frac{\sin\left(\frac{2\times 30^0}{2}\right)}{2\sin\left(\frac{30^0}{2}\right)} = 0.966 \tag{3.16}$$

Thus, the required voltage per coil group is:

$$V_{t_{group}} = 2 \times V_{t_1} \times K_m$$

There are three groups in series for each phase:

$$V_{t_{phase}} = 3 \times V_{t_{group}}$$

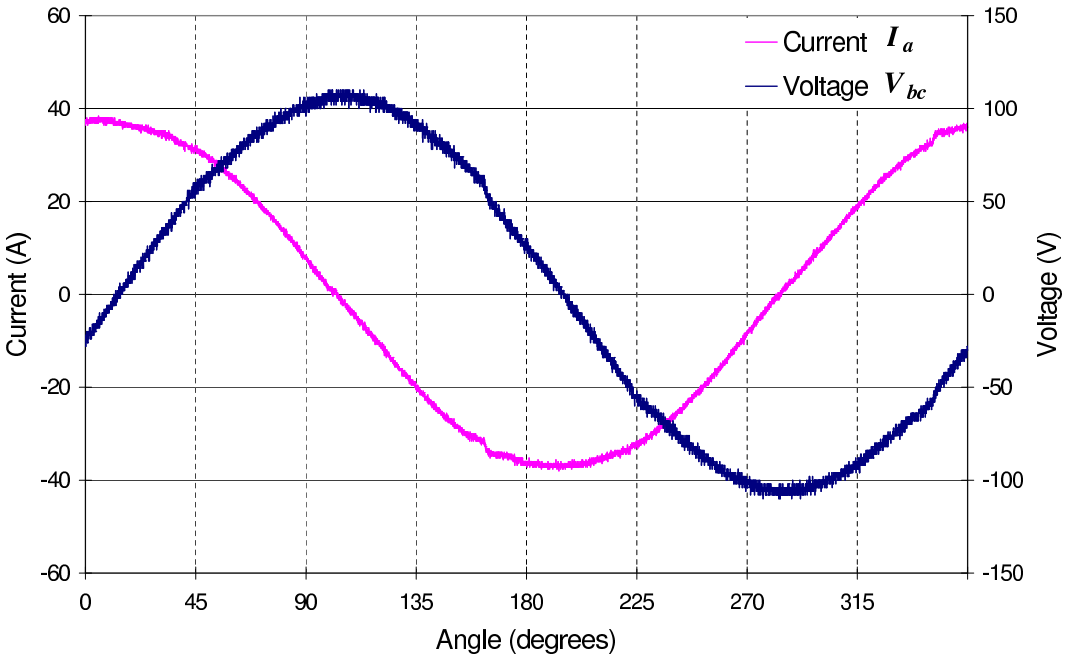


Figure 3.16: Voltage and current waveforms measured on the modified tubular LSM

With rated current flowing in the primary winding, the required line voltage is in the range of $59.33V - 73.28V$, depending on the size of the angle δ. The power factor of the motor has a range between $0.98 - 1.00$; again depending on the size of angle δ.

Typical voltage and current waveforms, measured on the modified tubular LSM running on no load, are shown in Figure 3.16. The current is close to the rated value and was measured in phase A. The line voltage was then measured across the remaining two phases. From the graph it can be seen that the voltage peaks at $105V$. This gives an rms value of $74.2V$, which is in good agreement with the analytically calculated value. Figure 3.16 verifies that the practical measurements correlate with the analytical prediction.

For a power factor of 1.00, the current waveform from the one phase (phase a) must lead the line voltage waveform of the other two phases (phases b and c) by 90^o. This is seen in Figure 3.17, where I_a leads V_{bc} by 90^o. The phase currents are in phase with the phase voltages for unity power factor (i.e. I_a is in phase with V_a). Since the system is balanced, for a star connection, the magnitudes of the line and phase voltages are related by $\sqrt{3}$.

$$i.e. \quad V_{bc} = \sqrt{3}V_b \tag{3.17}$$

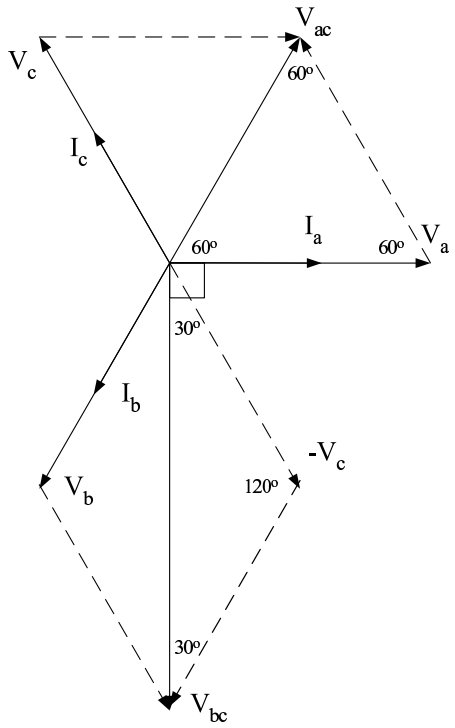


Figure 3.17: Phasor diagram of voltage and current measurements

Figure 3.16 shows that the current waveform in the one phase leads the line voltage waveform of the other two phases by 90^o. This confirms that the linear motor has a power factor of close to 1.00 under no load conditions.

The inverter used can produce a voltage of up to $380V$. If further tests are required to run the motor at higher frequencies than the $0.5Hz$ currently being used, then a greater voltage would be required. The inverter used would have ample capacity to handle the required voltage at the same current rating.

3.3 Required Applied Voltage for a Full Scale Motor

The same analysis presented in this chapter can be used to determine the required applied voltage for a full scale motor. Assuming that the full scale motor has the same dimensions as the prototype model, except that the primary is sufficiently long and operates at a speed[4] of $18m/s$, the required applied voltage is in the range of $1157.98V - 1218.90V$. For a detailed analysis see Appendix B.

[4]The value of $18m/s$ was chosen so that the speed of the linear motor would be similar to the speeds used in conventional rope hoists.

3.4 Summary

This chapter presented the equivalent circuit analysis for the modified tubular LSM. Due to the number of poles on the primary and secondary not being equal, the per phase equivalent circuit can not account for the varying positions of the secondary relative to the primary. Thus, the equivalent circuit has been developed on a per coil rather than on the conventional per phase basis. This analysis has been performed for both the prototype model as well as for a theoretical full scale motor. For the prototype the analysis showed that due to the low operating frequency along with the large air gap of the motor, the equivalent circuit is mainly resistive and the motor runs at close to unity power factor. With an operating current of $8A$, the required voltage for the prototype is in the range of $59.33V - 73.28V$, depending on the size of the angle between the applied and induced voltages. For the full scale model at the same operating current, the required voltage range is $1157.98V - 1218.90V$ with a full range of power factors due to the higher operating frequency.

Chapter 4

Design of the Magnetic System

This chapter gives an overview of the permanent magnet secondary of the modified tubular LSM. The first section describes the properties of the permanent magnets used in this project. An understanding of the permanent magnet properties is essential when optimising the secondary design. This optimisation forms part of the second section of this chapter which aims to improve the total thrust force that can be produced in the linear motor.

The optimisation involves shaping the flux paths in the secondary to prevent saturation of the steel sections. The geometry of the secondary is optimised and equations relating to the tubular linear motor's dimensions are presented. Three different permanent magnet arrangements are discussed, each with their own optimised parameter equations.

One of the permanent magnet arrangements was the surface mounted magnet arrangement, which was used in the first stage of the project. A split-pole magnet arrangement was implemented to reduce the flux per pole in both the primary and secondary sections compared to a conventional surface mounted magnet arrangement. This split-pole magnet arrangement is discussed in further detail in this chapter.

As part of the optimisation process, the cogging forces are investigated in order to reduce the effects these force have on the LSM. The cogging forces are undesirable particularly if smooth travel or precise positioning is required. The cogging forces can be reduced by various techniques with this project focusing on the technique of permanent magnet or pole shoe size optimisation of the secondary section.

4.1 Secondary Excitation Source

The modified tubular linear synchronous motor has a long stationary primary and a short mobile secondary section. As it is a synchronous motor, the secondary needs an excitation source. The various options are:

- DC winding on the secondary
  - with a trailing cable
  - with "overhead" cables
  - with a battery source on board
- Permanent magnets

4.1.1 DC winding

As the purpose of the project is to have a free moving secondary, with no rope connected, having a trailing electrical cable attached to the secondary section would defeat this purpose. This cable would require its own winder. The other option is to have "overhead" cables like that of an electric locomotive. However, it would be dangerous to have exposed high voltage cables through the length of the mine shaft. Another alternative is to have a battery source on the secondary. However, this increases the weight of the secondary and would require continuous maintenance. For these reasons a DC winding on the secondary was not considered to be a viable option.

4.1.2 Permanent Magnets and their Properties

With advances in permanent magnet technology, the strengths of the magnets make them more practical to use, as they require less space within an electric motor. The cost of these magnets is decreasing with time, which makes them more economically viable [49]. With these two factors LSM's are becoming more popular. Along with increased performance, there is an increasing number of applications for LSM's. This section describes some of the properties associated with the chosen permanent magnets for this project[1].

[1]Most of this information used in this section has come from reference [50]. It is an extensive guide to permanent magnets and describes the performance of Rare Earth magnets in detail.

Table 4.1: Comparison of $NdFeB$ and $SmCo$ Magnets

Material	*NdFeB*	*SmCo*
Energy Products	*10 to 48*	15 to 32
Mechanical Strength	*medium*	low
Corrosion Resistance	low	*medium*
Temp Stability	low to medium	*high*
Cost	*lower*	higher

Rare Earth Magnets

For a passive source of MMF, instead of a MMF generated by a DC winding, permanent magnets have been used. The magnets used for this project are Neodymium Iron Boron ($NdFeB$) magnets. It is an alloy made from the elements in the Lanthanide group. Both $NdFeB$ and Samarium Cobalt ($SmCo$) magnets are made from elements in this group which are collectively known as Rare Earths. These Rare Earth magnets are the most powerful available per cubic volume of material and their discovery has largely been credited to Karl Strnat [51]. A comparison between $NdFeB$ and $SmCo$ magnets is shown in Table 4.1.

From Table 4.1, it can be seen that each type of magnet has particular advantages. $SmCo$ magnets can operate at temperatures up to 350^oC and are more resistant to corrosion. The two major advantages of $NdFeB$ magnets are that they can produce a higher energy product and are cheaper. It is for these reasons that the $NdFeB$ magnets were chosen for this project. Figure 4.1 shows the demagnetisation curves supplied by the manufacturer for the chosen permanent magnets, $NdFeB_{N-35}$ [52].

Demagnetisation Curves

Figure 4.1 shows both demagnetisation curves as well as the maximum energy product grid for $NdFeB_{N-35}$ magnets. The maximum energy product will be discussed later.

The flux density produced by a permanent magnet is made up of two components and is described by the following equation [47, 49]:

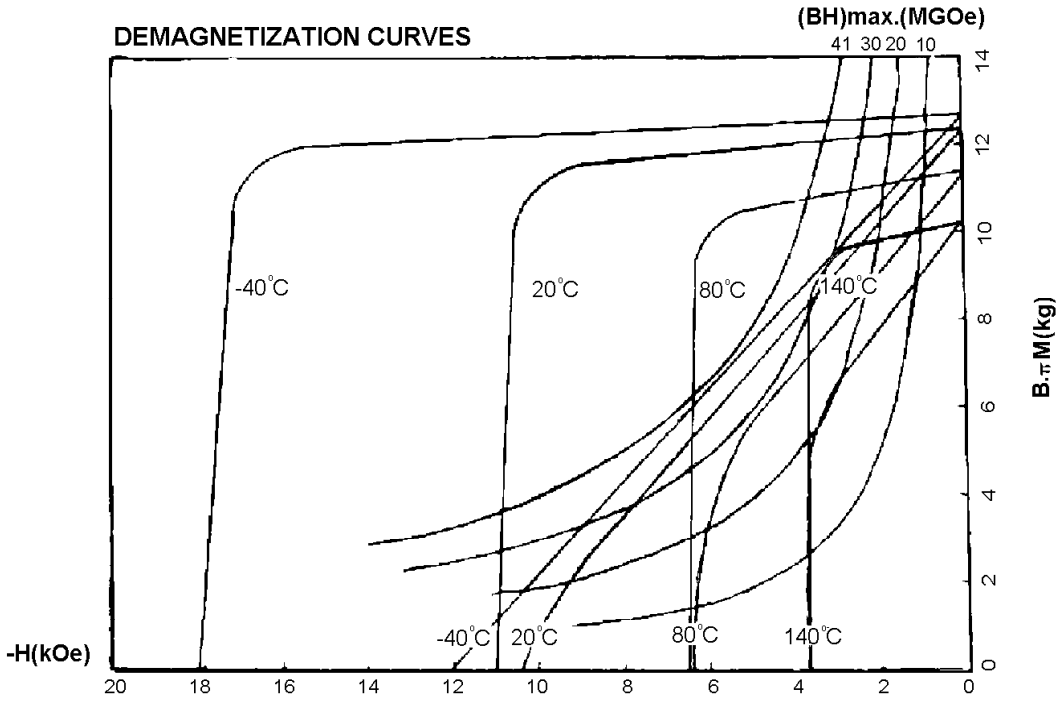


Figure 4.1: Demagnetisation curves and maximum energy product grid for a $NdFeB_{N-35}$ magnet.

$$B = \mu_0 H + B_i \tag{4.1}$$

- B = magnetic flux density
- $\mu_0 = 4\pi \times 10^{-7}$ magnetic permeability of free space
- H = magnetic field intensity
- B_i = intrinsic magnetic flux density

The flux density, $\mu_0 H$, is the flux density that would be produced by a magnetic field intensity, H, in free space, if the ferromagnetic core was not in place. The intrinsic magnetic flux density, B_i, is the intrinsic ability of the ferromagnetic core to produce flux. It is the vector difference between the magnetic flux density in the permanent magnet material, B, and the magnetic flux density that would exist in free space under the same field strength ($B_i = B - \mu_0 H$). The intrinsic flux density is a function of the magnetic field strength, H, as shown in Figure 4.2 and is the contribution of the ferromagnetic core to the overall magnetic flux density, B, in the permanent magnet.

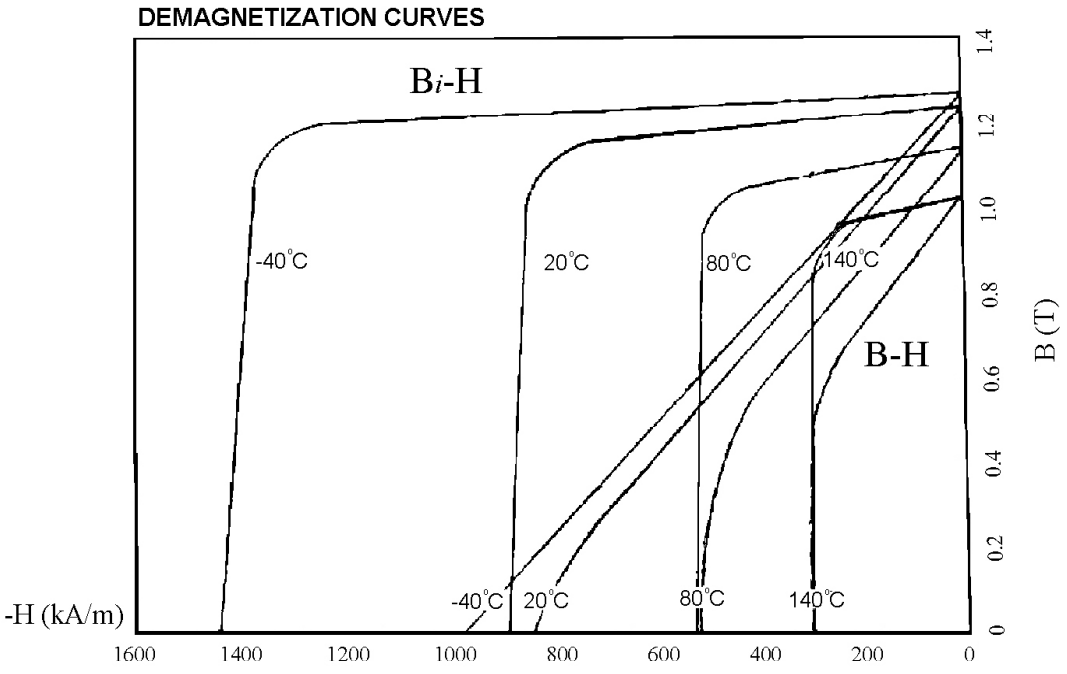


Figure 4.2: Demagnetisation curves for a $NdFeB_{N-35}$ magnet

The relationships $B - H$ and $B_i - H$ are shown for different temperatures in Figure 4.2[2]. The $B - H$ curves are the actual operating curves for the $NdFeB_{N-35}$ magnets. Depending on the reluctance of the magnetic circuit as well as the influence of any external magnetic fields, the operating point of the permanent magnet can be determined.

Permeance Coefficient

The effect of the reluctance in a magnetic circuit on a permanent magnet, is represented by the *permeance coefficient*, P_c. The magnet's operating point is the intersection of the P_c line and the B-H curve. The P_c lines for the SMMA and BMA as well as the B-H curves for various temperatures can be seen graphically in Figure 4.3.

$$P_c = \frac{B_m}{\mu_0 H_m} \tag{4.2}$$

- B_m = flux density at the operating point
- H_m = magnetic field intensity at the operating point

[2]This figure is the same as Figure 4.1, except the maximum energy product grid has been removed and the axes have been converted to SI units.

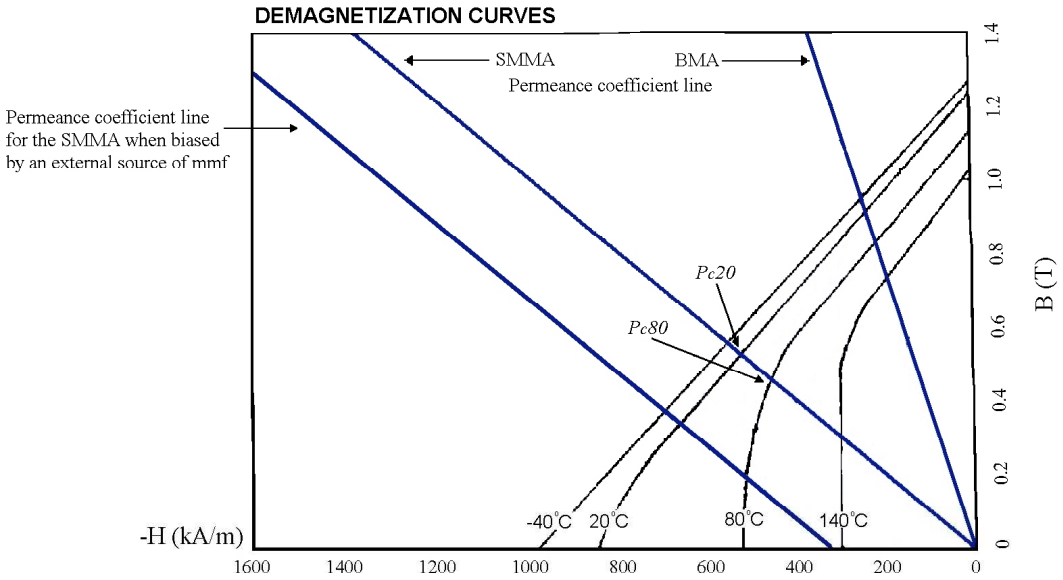


Figure 4.3: P_c lines for two magnet arrangements superimposed on the demagnetisation curves for a $NdFeB_{N-35}$magnet

With the knowledge that:

$$\begin{aligned} H_m L_m &= H_g L'_g = \frac{B_g L'_g}{\mu_0} \\ \text{and} \quad B_m A_m &= B_g A_g \end{aligned}$$

- L_m = magnet length (along the magnetised axis of the magnet)
- H_g = magnetic field intensity in the air gap
- L'_g = effective air gap length
- B_g = flux density in the air gap
- A_m = cross sectional area of the magnet
- A_g = cross sectional area of the air gap

the permeance coefficient, P_c may be determined as follows:

$$\begin{aligned} P_c &= \frac{B_m}{\mu_0 H_m} \\ &= \frac{A_g L_m}{A_m L'_g} \end{aligned}$$

The cross sectional areas of the magnet and air gap, through which the flux flows, are similar. Thus, a first order approximation of the value for P_c can be represented in terms of the magnet length and the effective air gap length.

$$P_c = \frac{B_m}{\mu_0 H_m} \approx \frac{L_m}{L'_g} \tag{4.3}$$

The effective air gap length, L'_g, is used in the calculation of P_c due to the slotted nature of the primary section. The effective air gap length takes into account the varying air gap length over one slot pitch as the air gap is not smooth and continuous.

Using Carter's coefficient [48], the effective air gap length is defined as follows [45]:

$$L'_g = L_g \left[\frac{5L_g + (1-\alpha)t_s}{5L_g + (1-\alpha)t_s - (1-\alpha)^2 t_s} \right] \tag{4.4}$$

- L_g = actual air gap length = $12.5mm$
- t_s = slot pitch = $19mm$
- $\alpha = \frac{t_t}{t_s}$
- t_t = tooth width = $9mm$

For the SMMA, the linear motor has an effective air gap $L'_g = 13.48mm$ and magnet length $L_m = 10mm$ (considering one magnet and one air gap), giving a permeance coefficient of 0.74 (See Figure 4.4 for the flux path of the SMMA). Referring to the 20^oC demagnetisation curve in Figure 4.3, the magnet would operate at a single point on that curve. The point, marked Pc_{20}, would be approximately $H_m = 5.35 \times 10^6 A/m$ and $B_m = 0.5T$. For a temperature of 80^oC the magnet would produce a flux density of approximately $0.43T$ (Point marked Pc_{80}). Therefore, a permeance coefficient line can be drawn on the graph from the origin with a negative slope of $0.74\mu_0$. Where this line intersects the temperature curves, this is then the operating point of the magnet. This P_c line can be seen superimposed on the graph in Figure 4.3. Thus, for the SMMA, small changes in temperature results in a large reduction in the flux

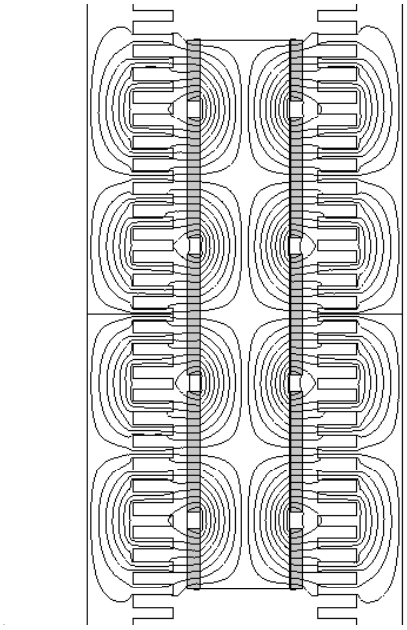


Figure 4.4: Cross-sectional view of the SMMA.

density that the permanent magnet can produce. This is a problem, since the P_c line has a small gradient and the P_c line shifts when an external source of MMF is applied, for example, by the primary winding. If the primary winding produces a MMF of $320kA/m$, the P_c line will start at $-320kA/m$ (Figure 4.3). This reduces the operating flux density at higher temperatures as the $B-H$ curve drops away steeply at high temperatures for small gradients of the P_c line.

From equation 4.3, it can be seen, that as the air gap is reduced and/or the thickness of the magnet increases, the gradient of the superimposed P_c line in Figure 4.3 becomes steeper. Thus, the magnet will be able to operate at comparatively higher flux densities for any temperature.

If the flux path generated for the buried magnet arrangement (BMA)[3] is observed (See Figure 4.5 for the flux path of the BMA), then:

- $L_m = 78.5mm$
- $L'_g = 26.96mm$

[3]The buried magnet arrangement is used in the optimised secondary design described in Section 4.2

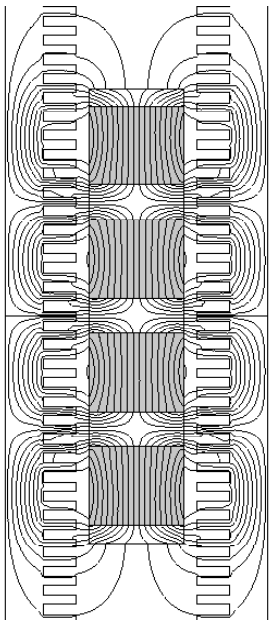


Figure 4.5: Cross-sectional view the flux in a tubular LSM with buried magnets.

Thus, the gradient of the P_c line is 2.91, which results in a steeper P_c line as shown in Figure 4.3 (Table 4.2 shows the comparison between the SMMA and the BMA). Therefore, in the BMA case, changes in temperature will affect the flux generation of the permanent magnets less than for the SMMA. These temperature effects on the performance of the LSM will be discussed further in Chapter 6.

Table 4.2: Comparison between SMMA and BMA Pc gradients

Description	L_m	L'_g	P_c
SMMA	$10.00mm$	$13.48mm$	0.74
BMA	$78.50mm$	$26.96mm$	2.91

Energy Product

The energy product is an indication of the energy that the magnet can supply to a magnetic circuit. It is the product of the flux density, B, and the value of H in the demagnetisation quadrant (Figure 4.6 [50]). Generally, the maximum energy product of the magnet is given in the specifications as well as in the name of the magnet. For instance, the $NdFeB_{N-35}$ magnet has a maximum energy product of $35MGOe$ $(279kTA/m)$[4].

[4]The energy product is generally quoted in $MGOe$.

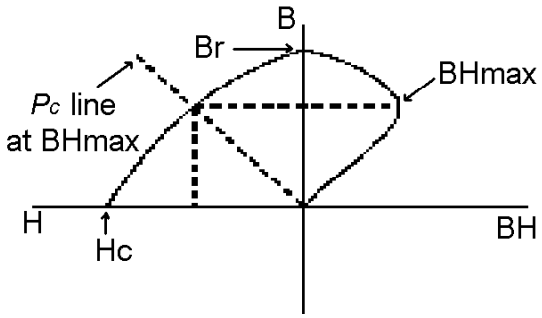


Figure 4.6: B-H curve for a $NdFeB_{N-35}$ showing both the demagnetisation quadrant and the energy product, BH, as a function of B. (B_r = residual flux density and H_c = coercive force.)

The energy product is used to compare different magnet strengths. To obtain a required flux at a certain fixed distance from the magnet surface, the volume of a weaker magnet must be greater than the volume of a stronger magnet. The ratio of larger to smaller volume, is the same as the ratio of the stronger to weaker magnets' energy products. For this project, the higher the energy product, the stronger the magnet will be and the greater the forces the LSM will be able to produce.

Temperature Effects on Magnets

Rare-earth magnets operate along different $B - H$ curves depending on the temperature (See Figure 4.1). The cooler it is, the stronger the magnet. $NdFeB$ permanent magnets are more sensitive to high temperatures compared to $SmCo$ permanent magnets. Thus, care must be taken when using the $NdFeB$ magnets within electrical motors. The $NdFeB$ magnets can only operate up to a maximum temperature of 150^oC [52]. However, this maximum temperature is based on the assumption that the magnetic circuit is stable and that the reluctance of the magnetic circuit is very low. Hence, the actual operating point of any magnet will depend on temperature as well as the reluctance of the magnetic circuit which is determined by the P_c line. Temperature has three defined effects on magnets.

- Reversible losses
- Recoverable losses
- Unrecoverable losses

For reversible loss of magnetic strength, increasing temperature negatively affects the performance of a permanent magnet. This can be seen in Figure 4.2 by comparing the demagnetisation curves for increasing temperature. However, once the magnet has reverted to its original temperature (room temperature), the magnet returns to its normal strength.

Recoverable loss is where the magnet has been partially demagnetised by high temperature effects. The temperature increases are greater than for reversible losses. These losses occur when the magnet operates below the knee of the $B - H$ curve. For example, this can be seen in Figure 4.3 at point P_{c80}. Once the magnet reverts to room temperature, it does not return to its normal strength. However, the slight reduction in flux density improves the magnet's stability as the domains with low commitment to orientation are first to lose their orientation. With the magnet being more stable it will be able to handle the same high temperatures without any further reduction in magnetic flux. If required, the magnet can be re-magnetised to its normal strength.

In unrecoverable losses it is the same as above but only up to a certain temperature. At even higher temperatures the magnet has been damaged to such an extent that the loss in magnetic strength is irretrievable. Thus, the magnet is permanently damaged and should be discarded.

4.2 Magnet Arrangements

As described in the first stage of the project, Section 1.2.2, the modified tubular LSM was built with a $10mm$ thick surface mounted magnet arrangement so that comparisons with other LSM's built at the university could be made. The second stage of the project looked at the optimisation of the secondary design. In redesigning the secondary section, a greater volume of magnet material could be added to produce a desired increase in force and power. However, the drawback is that the steel sections used in the secondary could saturate due to the extra magnet volume. Thus, the new design would have to reduce the saturation effects encountered when the magnet volume is increased.

The optimisation first looks at a conventional tubular LSM. This general approach develops the foundations to the optimisation procedure. Thereafter, the optimisation focuses on the modified tubular LSM. The optimisation is

only concerned with the secondary section for two reasons. The first is that the primary section is a fixed structure and cannot be modified easily. The second is that it is the more likely to saturate with flux before the primary due to the flux concentration towards the centre of the linear motor. Since the focus is on the secondary section this section attempts to give optimised parameters for the design in two cases:

- Optimised design parameters when the outside radius, r_2, of the secondary is known.
- Optimised design parameters when the pole pitch, τ, is known.

Three different designs were investigated for the optimisation. They are:

1. Surface mounted magnet arrangement (SMMA).
2. Buried magnet arrangement (BMA).
3. Combined surface and buried magnet arrangment (CMA).

4.2.1 Optimisation Approach for the Conventional Tubular LSM

Background to the Optimisation

Design optimisation forms part of every electrical motor design. Various aspects of a design can be optimised depending on the objectives and constraints of the project. A few examples of LSM optimisation procedures previously implemented are presented here. The differences between these optimisation procedures and the one used for the modified tubular LSM are highlighted to emphasise the contribution this optimisation procedure makes to the field of knowledge.

Wang et al. [37] did a thorough analysis of the SMMA, BMA and Halbach arrays for a tubular LSM. However, these results cannot be compared directly with the optimisation for this project. The reasons are, firstly, the optimisation by Wang et al. was for a short primary and long secondary. This has implications with the flux distribution of the permanent magnets depending

on the relative position of the secondary to the primary (ignoring the variations produced due to a slotted primary). Since, the modified tubular LSM has a long primary and a short secondary, the flux distribution does not change with position. The second reason is that the optimisation by Wang et al. was for a slot-less primary section. This meant that the effective air gap length is assumed to be large and it is unlikely that saturation will occur in the steel sections of the LSM. Thus, the primary and secondary sections are assumed to be infinitely permeable. For the modified tubular LSM, the dimensions of the secondary were optimised to prevent saturation of the steel sections. Furthermore, the optimisation ratios presented by Wang et al. depend on the coil depth of the primary winding. This is not applicable to the modified tubular LSM, which has a slotted primary.

Eastham et al. [45] also developed an optimisation procedure for a short primary and long secondary section. This has implications with the flux distribution of the permanent magnets depending on the relative position of the secondary to the primary. However, Eastham et al. uses a slotted primary section. The focus of their procedure is to optimise the relationship between the pole pitch and the slot depth on the primary. This differs from the approach for the modified tubular LSM, where just the dimensions of the secondary are optimised.

Bianchi et al. [53] compared the performance of SMMA and BMA for tubular linear permanent magnet motors. However, the approach by Bianchi et al. differs from the optimisation presented for this project for two reasons. The first, is that Bianchi et al. assumes that the steel portions in the linear motor are infinitely permeable and the second is that the optimisation focused on the ratio of the inner and outer diameters of the primary section. This differs from the optimisation presented in this chapter as the permeability of the steel portions for the modified tubular linear motor is taken into account. The reason is that the optimisation for the modified tubular linear motor depends on the outside radius of the secondary section. If the outside radius of the secondary section is small, then there is a possibility that the steel portions may saturate with flux if the pole pitch is too large.

Other researchers have also investigated the difference between the SMMA and BMA, but for single-sided topologies. A case study by Gieras et al. [47] showed that the SMMA produced slightly higher forces compared to the BMA, but at a smaller efficiency. Previous research done at the University of the

Witwatersrand by Jeans et al. [54] has also shown that the SMMA for single-sided topologies produces slightly higher forces compared to the BMA (This investigation only focused on thrust force results obtained from FEA). The investigation presented here for SMMA and BMA looks at a tubular topology, focusing on the geometrical dimensions to obtain an optimised secondary design.

The CMA analysis presented in this section is believed to be a new approach to the optimisation of the magnet arrangements and as far as the author is aware, it has not been previously recorded in the literature.

Surface Mounted Magnet Arrangement

For this permanent magnet design a split-pole magnet arrangement was used (Section 4.2.3 describes this split pole arrangement in more detail.). This can be seen in the longitudinal cross sectional area of the linear motor (Figure 4.7). Half length magnets are placed at the two ends of the secondary section. This arrangement ensures an even distribution of the flux as shown in Figure 4.8.

To ensure an optimal flux pattern, so that no one area saturates with flux before any other area, the design had to follow one concept:

- The cross-sectional areas of the steel section in the secondary, through which the flux flows, must be constant.

This is shown graphically in Figure 4.9 and the equation representing the above concept is:

$$\begin{aligned} \pi r_1^2 &= 2\pi r_1 \times \frac{h}{2} \\ r_1 &= h \end{aligned} \tag{4.5}$$

In Figure 4.7, $h = \tau$, where τ is the pole pitch.

For the first case where the outside diameter, r_2, is known, the pole pitch, τ, can be any value as it is independent of r_2.

Conversely, for the second case where the pole pitch, τ, is known, the outside diameter, r_2 can be any value as it is independent of τ.

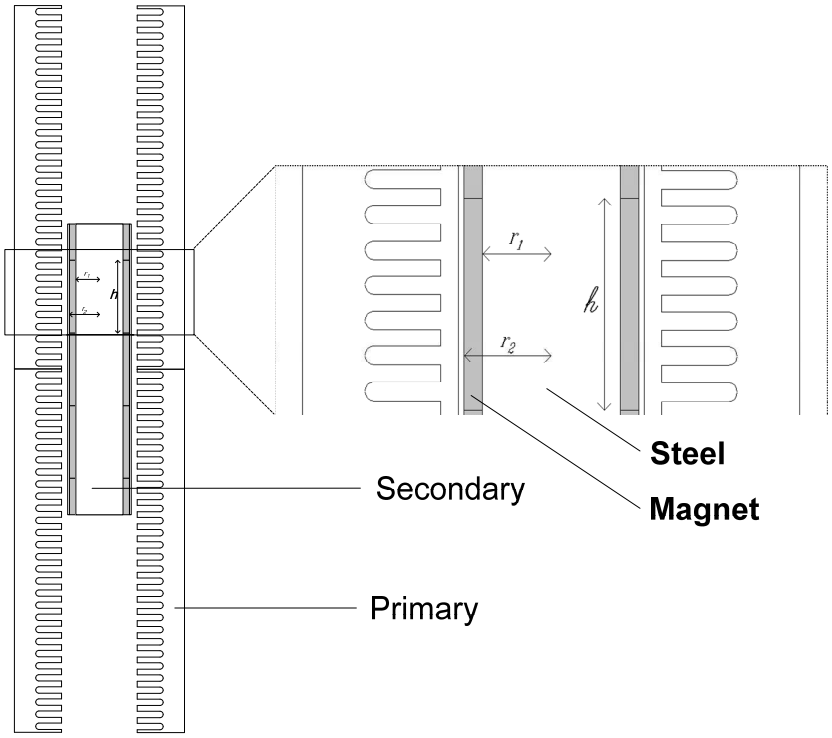


Figure 4.7: Cross-sectional view of the tubular LSM with surface mounted magnets. The gray areas represent the permanent magnet and the white areas represent the steel sections.

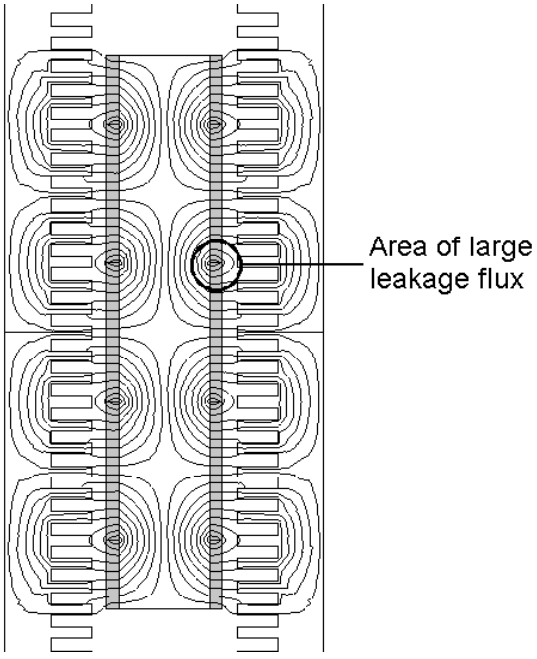


Figure 4.8: Cross-sectional view of the flux in a tubular LSM with surface mounted magnets.

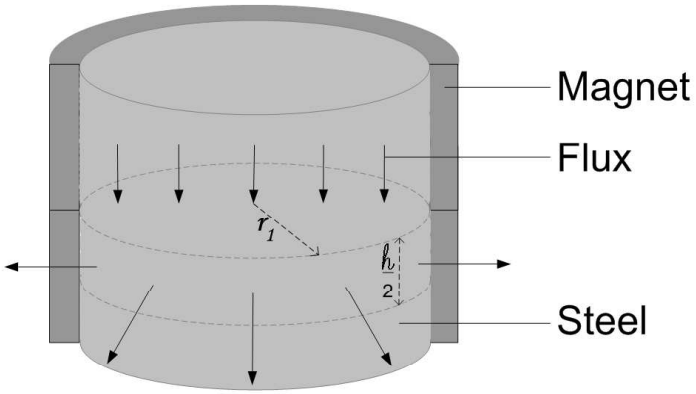


Figure 4.9: Graphical view of the cross-sectional areas through which the flux flows.

For both cases FEA could determine the optimum dimensions of the secondary, by examining the force and flux saturation within the steel sections as either r_2 or τ are varied.

This arrangement has two disadvantages. The first is that there is a large amount of leakage flux between adjacent magnets. Secondly, the length of the magnets have not been optimised to reduce the effects of the cogging forces that will occur in the LSM. The reduction of the cogging forces is explained in further detail in Section 4.2.4.

The SMMA design can be adjusted to reduce the effects of the cogging force and this model is shown in Figure 4.10. Even though there is less magnet volume, there is a reduction in the amount of leakage flux between adjacent magnets. This can be seen in Figure 4.11.

Once again, r_2 and τ are independent of each other and FEA is suggested to determine the optimum dimensions for the secondary section.

Buried Magnet Arrangement (BMA)

The next option to optimise the secondary design would be the use of buried permanent magnets. It must follow the same concept as that of the surface mounted magnet arrangement, namely:

- The cross-sectional areas of the steel sections in the secondary, through which the flux flows, must be constant.

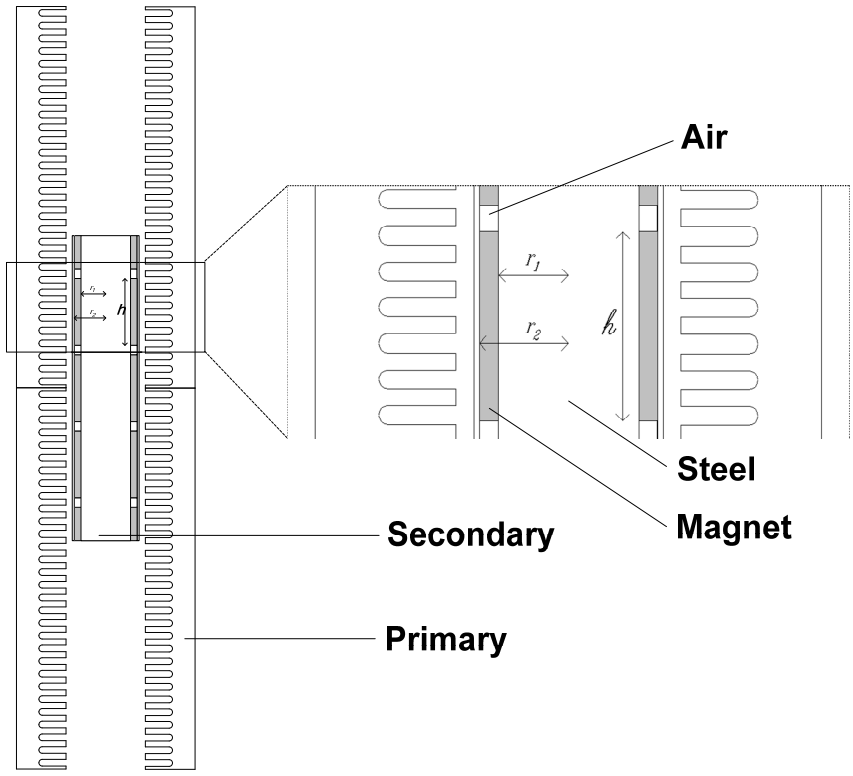


Figure 4.10: Cross-sectional view of the tubular LSM with surface mounted magnets that have been adjusted to reduce the effects of the cogging forces.

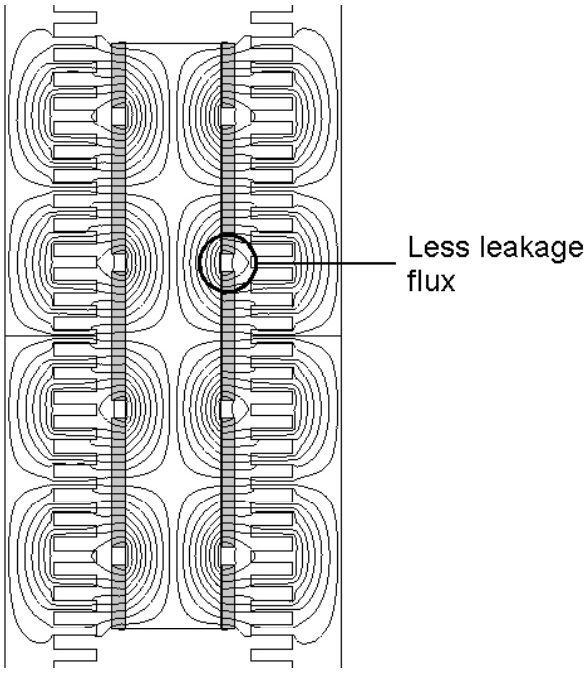


Figure 4.11: Cross-sectional view the flux in a tubular LSM with surface mounted magnets that have been adjusted to reduce the effects of the cogging forces.

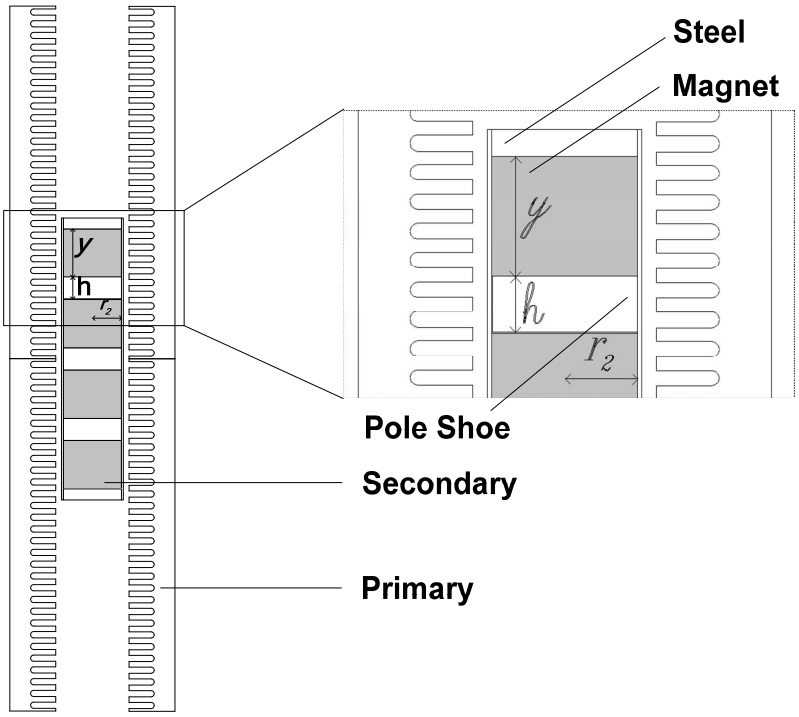


Figure 4.12: Cross-sectional view of the tubular LSM with buried magnets.

This concept for the buried magnet arrangement can be represented mathematically:

$$\begin{aligned} \pi r_2^2 &= 2\pi r_2 \times \frac{h}{2} \\ \therefore \quad r_2 &= h \end{aligned} \tag{4.6}$$

The buried magnet arrangement with its dimensions can be seen in Figure 4.12. The steel sections at either end of the secondary section are $\frac{h}{2}$ in length. This arrangement produces a flux pattern seen in Figure 4.13.

The pole pitch of this buried magnet design is:

$$\begin{aligned} \tau &= h + y \\ \tau &= r_2 + y \end{aligned} \tag{4.7}$$

In the first case, if there is a set outside radius, r_2, for the secondary, then the pole pitch, τ, can be any value as it depends on the length of the buried magnets, y. The pole pitch will always be larger than r_2.

In the second case, if the pole pitch is fixed, then the outside radius cannot be larger than τ:

$$r_2 = \tau - y \tag{4.8}$$

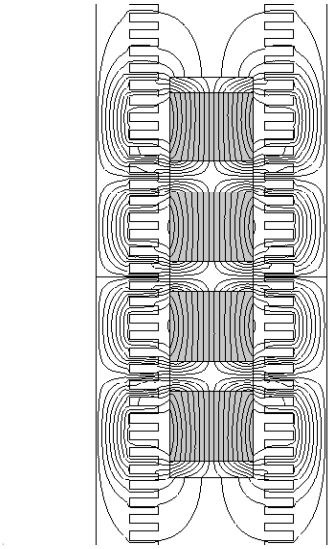


Figure 4.13: Cross-sectional view the flux in a tubular LSM with buried magnets.

Combined Magnet Arrangement

The combined magnet arrangement has both surface mounted and buried magnets. There are two possible designs for this arrangement. They are shown in Figures 4.14 and 4.15.

Both combined magnet arrangements had to follow two design concepts:

- The cross-sectional areas of the steel sections in the secondary, through which the flux flows, must be constant (Concept One).
- For an optimised solution, the volume of the surface mounted magnets must be equal to the volume of the buried magnets (Concept Two). This ensures that the magnets are of equal strength and contribute equally to the flux produced by the secondary. This concept is not applicable for the SMMA and BMA.

The two design concepts can be represented mathematically for ***Design One*** as follows:

Concept One:

$$\begin{aligned} \pi r_1^2 &= 2\pi r_1 \frac{h}{2} \\ r_1 &= h \end{aligned} \tag{4.9}$$

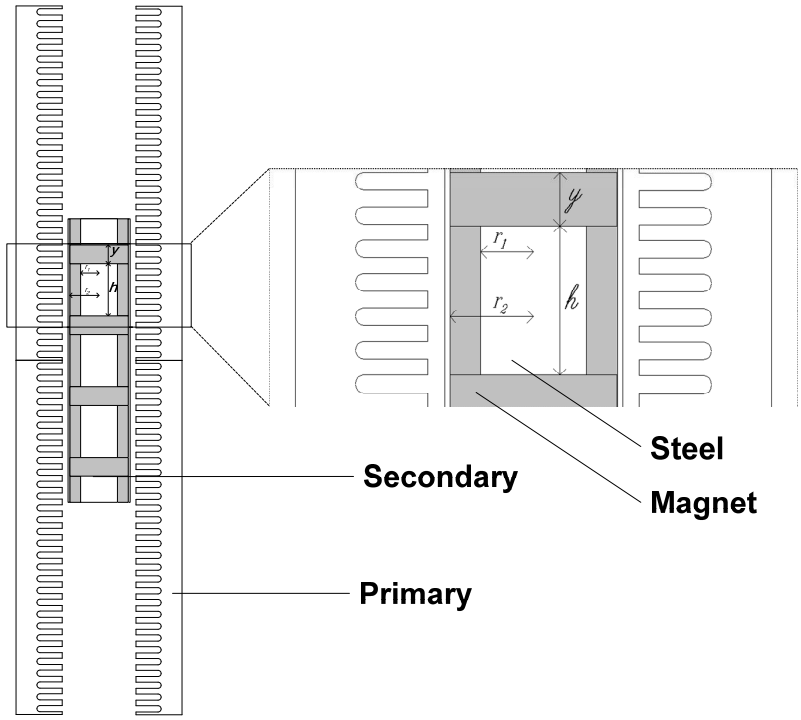


Figure 4.14: Cross-sectional view of the tubular LSM with a combined surface mounted and buried magnet arrangements - ***Design One***.

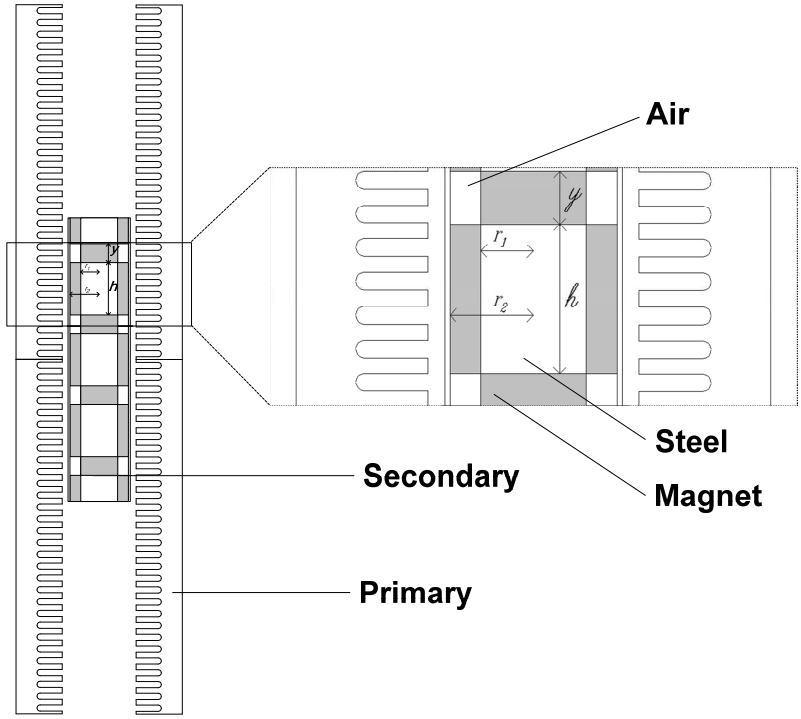


Figure 4.15: Cross-sectional view of the tubular LSM with a combined surface mounted and buried magnet arrangements - ***Design Two***.

Concept Two:

$$\begin{aligned} \pi r_2^2 y &= (\pi r_2^2 - \pi r_1^2)h \\ r_2^2 y &= (r_2^2 - r_1^2)h \end{aligned} \tag{4.10}$$

For ***Design One***, $y < h$, otherwise the volume of the buried magnet would be greater than the volume of the surface mounted magnet. Thus:

$$\frac{y}{h} < 1$$

Let $\frac{y}{h} = x$. Equation 4.10 becomes:

$$\begin{aligned} r_2^2 x &= r_2^2 - r_1^2 \\ x &= 1 - \Big(\frac{r_1}{r_2}\Big)^2 \qquad (4.11) \\ \Big(\frac{r_1}{r_2}\Big)^2 &= 1 - x \qquad (4.12) \end{aligned}$$

Thus, the relationship between r_1 and r_2 is:

$$r_1 = r_2\sqrt{1-x} \tag{4.13}$$

So,

$$h = r_1 = r_2\sqrt{1-x} \tag{4.14}$$

$$\text{and} \quad y = xh = xr_2\sqrt{1-x} \tag{4.15}$$

The pole pitch is:

$$\begin{aligned} \tau &= y + h \\ \tau &= (x+1)\Big(r_2\sqrt{1-x}\Big) \end{aligned} \tag{4.16}$$

All the dimensions of the secondary are now solved in terms of r_2 and x. Thus, for the first case with a given outside radius, r_2, the total magnet volume per pole can be plotted for $0 < x < 1$. This is shown in Figure 4.16. The maximum value can be determined mathematically as follows:

The equation for the permanent magnet volume per pole is:

$$\text{Volume} = \pi r_2^2 y + (\pi r_2^2 - \pi r_1^2)h \tag{4.17}$$

Simplifying Equation 4.17 in terms of r_2 and x gives:

$$\text{Volume} = 2\pi r_2^3 x\sqrt{1-x} \tag{4.18}$$

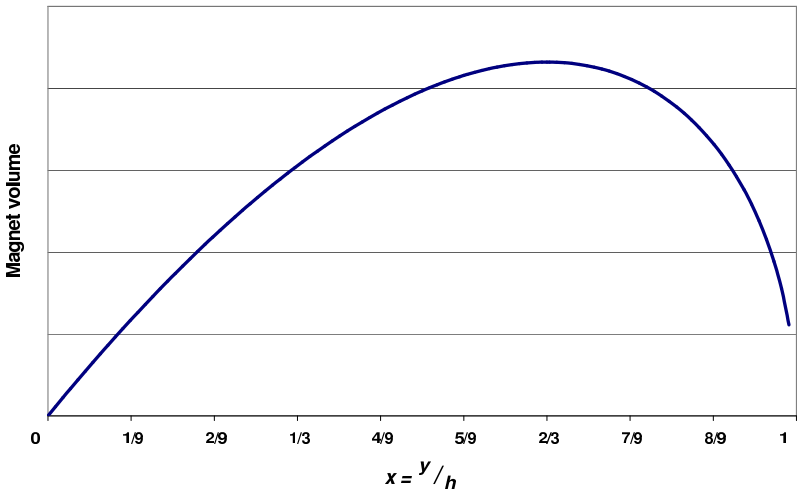


Figure 4.16: Magnet volume versus the ratio of the lengths of the surface mounted and buried magnets - with a fixed r_2 (***Design One***)

With r_2 being a constant, Equation 4.18 can be differentiated with respect to x and made equal to zero in order to determine the value of x where the magnet volume will be a maximum. The maximum volume occurs at $x = \frac{2}{3}$, which is also shown in Figure 4.16.

In the second case, if the pole pitch is a fixed value, then the parameters of the secondary can be described in terms of τ and x as follows:

Firstly, r_1 can be found in terms of τ and x as follows:

$$\begin{aligned} x &= \frac{y}{h} \\ x &= \frac{\tau - h}{h} \\ x &= \frac{\tau - r_1}{r_1} \\ \therefore \quad r_1 &= \frac{\tau}{(1+x)} \end{aligned} \tag{4.19}$$

From Equation 4.13:

$$\begin{aligned} r_2 &= \frac{r_1}{\sqrt{1-x}} \\ r_2 &= \frac{\tau}{(1+x)} \times \frac{1}{\sqrt{1-x}} \end{aligned} \tag{4.20}$$

So,

$$h = r_1 = \frac{\tau}{(1+x)} \tag{4.21}$$

$$\text{and} \quad y = xh = x\frac{\tau}{(1+x)} \tag{4.22}$$

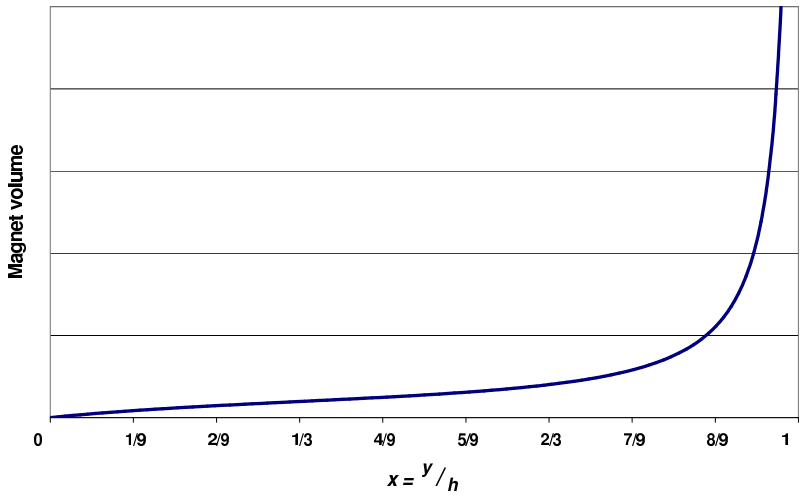


Figure 4.17: Magnet volume versus the ratio of the lengths of the surface mounted and buried magnets - with a fixed τ (***Design One***)

With the primary having a set pole pitch, an optimised magnet volume is not possible. Figure 4.17 shows the change in magnet volume and suggests that the largest possible outside diameter must be used.

FEA of ***Design One*** showed that there was a distinct reduction in the flux density on the buried magnets in the area between r_1 and r_2 (Figure 4.18). This could be attributed to the high reluctance path of the magnetic circuit that the flux from this part of the magnet would encounter. The boundary between the surface mounted and buried magnets creates this situation as the designated flux directions are 90^o apart. This portion of the magnet does not operate at it most efficient level due to the higher reluctance path. It effectively operates on a permeance coefficient line which has a smaller gradient compared to the other parts of the magnet arrangement. Thus, ***Design One*** would be discarded as an option.

The second combined arrangement, ***Design Two***, removed this section of the buried magnets between r_1 and r_2 and was optimised on the new structure. The two design concepts mentioned above can also be applied to this modification and is represented mathematically as follows:

Concept One as before:

$$\begin{aligned} \pi r_1^2 &= 2\pi r_1 \frac{h}{2} \\ r_1 &= h \end{aligned} \tag{4.23}$$

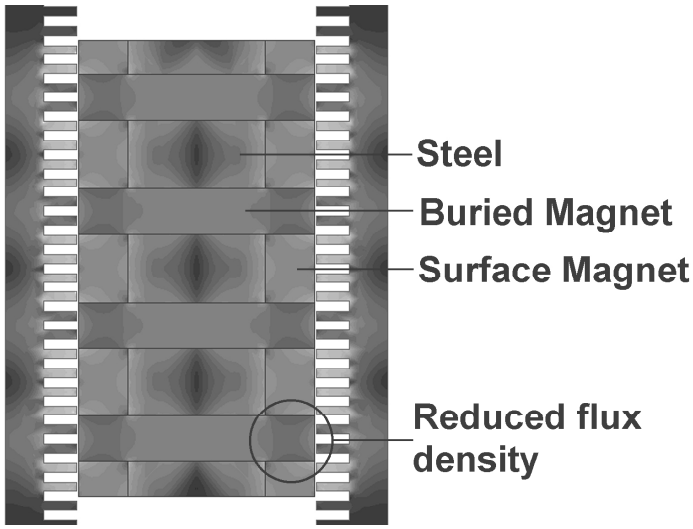


Figure 4.18: Flux density plot of the CMA - ***Design One***. The darker colours are areas of low flux density.

Concept Two:

$$\begin{aligned} \pi r_1^2 y &= (\pi r_2^2 - \pi r_1^2)h \\ r_1^2 y &= (r_2^2 - r_1^2)h \end{aligned} \tag{4.24}$$

Once again let $\frac{y}{h} = x$. Equation 4.24 becomes:

$$\begin{aligned} r_1^2 x &= (r_2^2 - r_1^2) \\ x &= \left(\frac{r_2}{r_1}\right)^2 - 1 \qquad (4.25) \\ \left(\frac{r_2}{r_1}\right)^2 &= 1 + x \qquad (4.26) \end{aligned}$$

Thus, the relationship between r_1 and r_2 is:

$$r_1 = \frac{r_2}{\sqrt{1+x}} \tag{4.27}$$

So,

$$h = r_1 = \frac{r_2}{\sqrt{1+x}} \tag{4.28}$$

$$\text{and} \quad y = xh = x\frac{r_2}{\sqrt{1+x}} \tag{4.29}$$

The pole pitch is :

$$\begin{aligned} \tau &= y + h \\ \tau &= r_2\sqrt{1+x} \end{aligned} \tag{4.30}$$

All the dimensions of the secondary are now solved in terms of r_2 and x. For a given outside radius, r_2, the total magnet volume per pole can be plotted

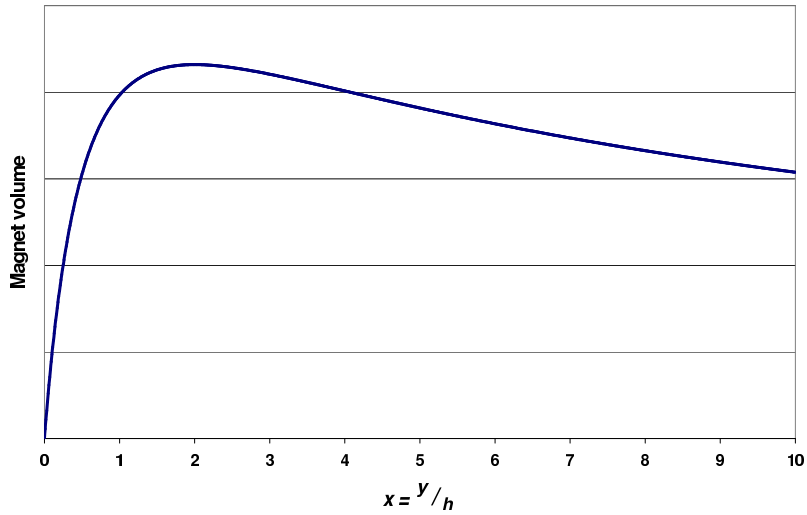


Figure 4.19: Magnet volume versus the ratio of the lengths of the surface mounted and buried magnets - with a fixed r_2 (***Design Two***)

for $0 < x < 10$. This is shown in Figure 4.19. The maximum value can be determined mathematically as follows:

The equation for the permanent magnet volume per pole is:

$$\text{Volume} \;=\; \pi r_1^2 y \;+\; (\pi r_2^2 - \pi r_1^2)h \tag{4.31}$$

Simplifying Equation 4.31 in terms of r_2 and x gives:

$$\text{Volume} \;=\; 2\pi r_2^3 x(1+x)^{-\frac{3}{2}} \tag{4.32}$$

With r_2 being a constant, Equation 4.32 can be differentiated with respect to x and made equal to zero in order to determine the value of x where the magnet volume will be a maximum. The maximum volume occurs at $x = 2$, as shown in Figure 4.19.

In the second case, if the pole pitch is a fixed value, then the parameters of the secondary can be described in terms of τ and x as follows:

Again, r_1 can be found in terms of τ and x as follows:

$$\begin{aligned} x &= \frac{y}{h} \\ x &= \frac{\tau - h}{h} \\ x &= \frac{\tau - r_1}{r_1} \\ \therefore \quad r_1 &= \frac{\tau}{(1+x)} \end{aligned} \tag{4.33}$$

From Equation 4.27:

$$\begin{aligned} r_2 &= r_1\sqrt{1+x} \\ r_2 &= \frac{\tau}{\sqrt{1+x}} \end{aligned} \tag{4.34}$$

And,

$$h = r_1 = \frac{\tau}{(1+x)} \tag{4.35}$$

$$\text{and} \quad y = xh = x\frac{\tau}{(1+x)} \tag{4.36}$$

All the dimensions of the secondary are now solved in terms of τ and x. For a given pole pitch, the total magnet volume per pole can be plotted for $0 < x < 10$. This is shown in Figure 4.20. This maximum value can be determined mathematically as follows:

The equation for the permanent magnet volume per pole is:

$$\text{Volume} = \pi r_1^2 y + (\pi r_2^2 - \pi r_1^2)h \tag{4.37}$$

Simplifying Equation 4.37 in terms of τ and x gives:

$$\text{Volume} = 2\pi\tau^3 x(1+x)^{-3} \tag{4.38}$$

With τ being a constant, Equation 4.38 can be differentiated with respect to x and made equal to zero in order to determine the value of x where the magnet volume will be a maximum. The maximum volume occurs at $x = \frac{1}{2}$, which is also shown in Figure 4.20.

Choice of Magnet Arrangement

All magnet arrangements are limited by the flux carrying capacity of the steel sections in the secondary. If all the magnet arrangements have the same dimensions (equal r_2 and τ), it is clear that the BMA has a distinct advantage in the axial plane as the cross-sectional area of the steel section is πr_2^2 where the cross-sectional area for the CMA and SMMA is πr_1^2. The ratio of the surface areas in the axial plane is $(\frac{r_2}{r_1})^2$. Thick surface mounted magnets in either the SMMA or CMA would mean that there is a large difference between r_1 and r_2. Thus, the BMA would have a bigger axial cross-sectional area for the flux compared to either the SMMA or CMA.

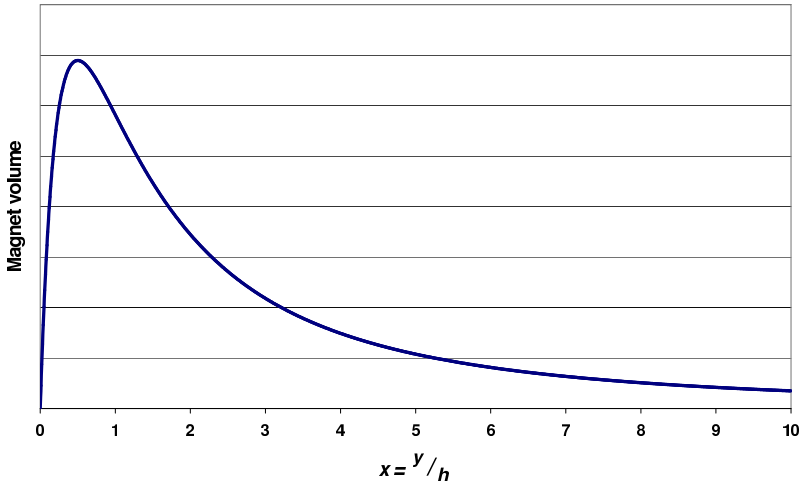


Figure 4.20: Magnet volume versus the ratio of the lengths of the surface mounted and buried magnets - with a fixed τ (***Design Two***)

For the magnet arrangements presented here, the relationships between the dimensions of the secondary are for optimal use of the steel sections in the secondary. These dimensions ensure that the flux passes through constant cross-sectional areas in the secondary section. Comparisons between the magnet arrangements has shown that the BMA design is the preferred topology as it makes more effective use of steel in the secondary section.

It must be noted that these parameter equations for the various permanent magnet arrangements are guidelines for an optimal design. If, in a tubular LSM design, more force is required and the steel sections are being under utilised in terms of flux density, then the magnet volume can be increased. FEA can be used to monitor the level of flux saturation within the steel sections of a linear motor and to determine the maximum thrust force.

4.2.2 Optimisation Approach for the Modified Tubular LSM

The optimisation approach for the modified tubular LSM is very similar. The only difference is that the equations for the outer surface on the secondary section have a factor of $\frac{5}{6}$. The factor of $\frac{5}{6}$ is due to the fact that the outer primary is not continuous, but has $\frac{1}{6}$ of its periphery missing to accommodate the mechanical connection to the secondary. This factor of $\frac{5}{6}$ does not make any major changes to the optimisation of the secondary section.

The optimisation of the modified tubular LSM focused on only the SMMA and

BMA. The SMMA was investigated for the modified tubular LSM using FEA to see if any further improvements could be made to the secondary from the first stage of the project. Using the results of the conventional tubular LSM optimisation, only the BMA was investigated and not the CMA, as the results showed the BMA to be the preferred design.

Surface Mounted Magnet Arrangement (SMMA)

In the first stage of the project, FEA was used to determine the optimum outside radius, r_2, for the secondary section using magnets with a thickness of $10mm$ and a pole pitch of $114mm$. This FEA investigation resulted in an optimal outside radius of $r_2 = 47.5mm$. If r_2 was increased further, the thrust force increased in the same proportion as the radius. But, the secondary mass increased with the square of the radius and hence the FWR decreased. If r_2 was decreased the solid steel tube on which the magnets are mounted would saturate with flux and the force would reduce. Thus, the first stage of the project, the linear motor was built with an secondary outside radius of $r_2 = 47.5mm$.

To optimise the SMMA design further, a FEA was conducted to determine the effects of increasing the thickness of the permanent magnets, while keeping the secondary outside radius set at $47.5mm$ and the pole pitch at $114mm$. The results in Figure 4.21[5] show that an increase in magnet thickness from the $10mm$ will result in marginal increase in the thrust force owing to further saturation of the steel in the secondary section (The magnet volume for a thickness of $10mm$ is $1.07 \times 10^{-3}m^2$ as indicated). Thus, the SMMA was close to optimum at a thickness of $10mm$ and the linear motor should produce a maximum thrust force of $2496N$ with a current of $12A$ per coil (150% of rated current).

[5]These results are from a FEA at a primary coil current of $12A$ (150% of rated current). This value of $12A$ was used to determine the maximum force that can be produced before the steel sections go into saturation due to the higher current. The forces produced at $12A$ still have a linear relationship with current. Saturation only occurs at currents higher than $12A$. This is shown more clearly in Chapter 8.

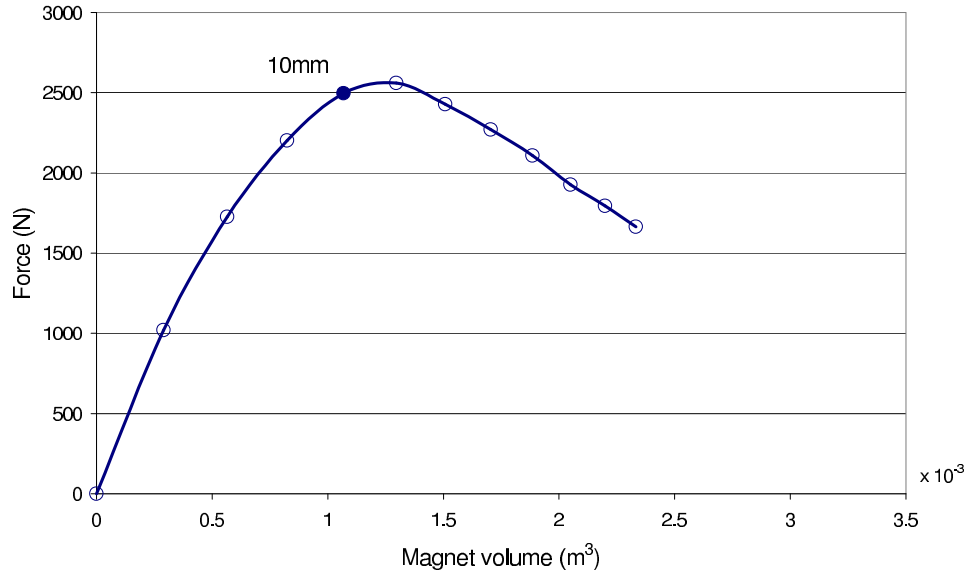


Figure 4.21: Thrust force with the change in permanent magnet volume in a surface mounted magnet arrangement (12 A per coil).

Buried Magnet Arrangement (BMA)

As discussed earlier, the BMA is the preferred magnet arrangement. For the modified tubular LSM, Equation 4.6 changes to:

$$\begin{aligned} \pi r_2^2 &= \frac{5}{6} \times 2\pi r_2 \times \frac{h}{2} \\ r_2 &= \frac{5}{6} h \end{aligned} \tag{4.39}$$

The pole pitch of this buried magnet design is:

$$\begin{aligned} \tau &= h + y \\ \tau &= \frac{6}{5} r_2 + y \end{aligned} \tag{4.40}$$

If there is a set secondary outside radius, r_2, for the linear motor, then the pole pitch, τ, depends on the length of the buried magnets, but will always be larger than $\frac{6}{5} r_2$.

Alternatively, if the pole pitch is fixed, then r_2 cannot be larger than $\frac{5}{6}\tau$:

$$r_2 = \frac{5}{6}(\tau - y) \tag{4.41}$$

For the first modified tubular LSM built with $\tau = 114mm$ and $r_2 = 47.5mm$, this buried design is suited to these dimensions. So the ideal magnet length for this buried design would be $y = 57mm$, which is $\frac{1}{2}\tau$.

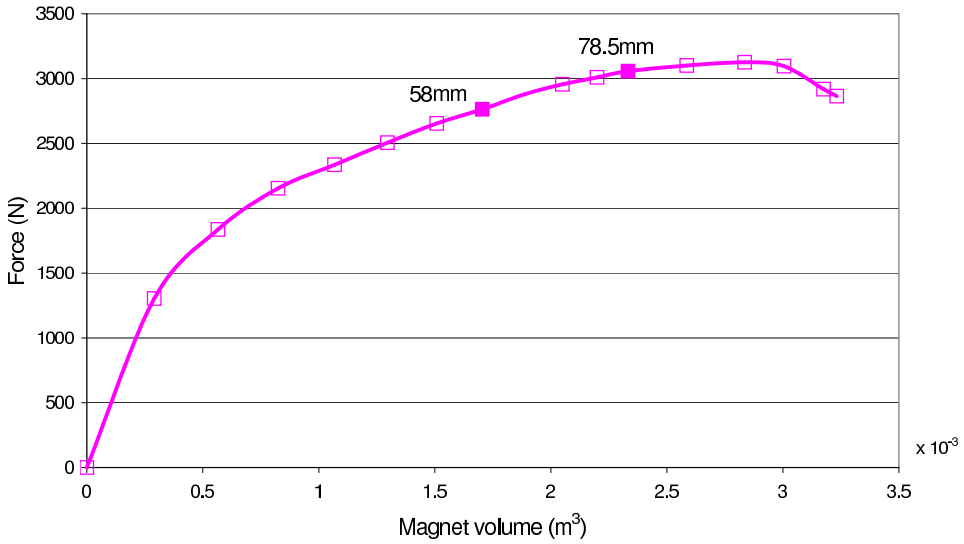


Figure 4.22: Thrust force with the change in permanent magnet volume in a buried magnet arrangement (12 A per coil).

Section 4.2.4 shows that the cogging forces produced with this design would be smallest if the magnet length was $58mm$. This is very similar to the above value.

FEA of this buried magnet design showed that the steel sections for a magnet length of $58mm$ (The magnet volume is $1.64 \times 10^{-3}m^2$ as indicated) was being under utilised (Figure 4.22). For this magnet length a maximum thrust force of $2763N$ was produced with $12A$ per coil. The next largest magnet volume was then selected, while keeping the cogging forces to a minimum as described in Section 4.2.4. This option had a magnet length of $78.5mm$ with a magnet volume of $2.23 \times 10^{-3}m^2$ as indicated in Figure 4.22. A maximum thrust force of $3057N$ was produced with this magnet length. This is approximately 10% more thrust force compared to the buried magnets which are $58mm$ in length. It is also approximately 22% more compared to the optimised SMMA. Buried magnets, which are larger than $78.5mm$ in length, were not considered as there is only a small increase in thrust force with increased magnet volume.

Comparison Between SMMA and BMA

Figure 4.23 shows a comparison between the forces produced in both the SMMA and BMA. It also indicates which magnet arrangement should be used, if magnet volume was a deciding factor. For smaller volumes, where there is

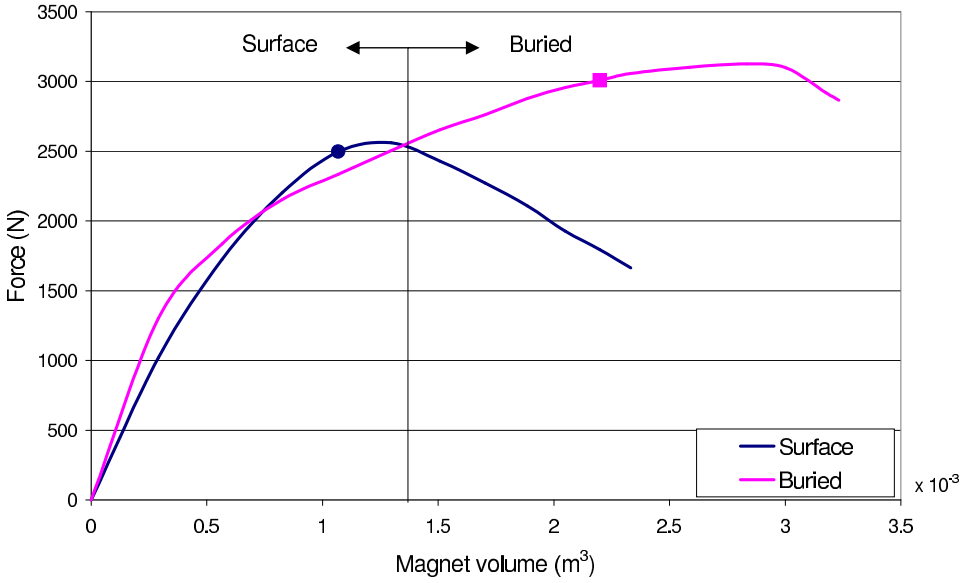


Figure 4.23: Thrust force with the change in permanent magnet volume in a surface mounted and buried magnet arrangements (12 A per coil).

no flux saturation of the steel sections for both magnet arrangements, there is little difference between the thrust forces for both SMMA and BMA. Just before the SMMA saturates with flux, it produces slightly higher forces compared to the BMA. This is similar to the results produced by Gieras et al. [47] and Jeans et al. [54] for a single-sided topology. The SMMA has the advantage as the cogging forces can be kept to a minimum for all magnet volumes (The magnet length, h, remains constant[6] and the volume is adjusted by varying the magnet thickness, $r_2 - r_1$). For larger magnet volumes, the BMA should be used as greater thrust forces are achieved.

After considering the FEA results from both the conventional and modified tubular LSM's, the final optimised design was therefore the BMA with the following dimensions listed in Table 4.3

Table 4.3: Secondary Design Parameters

Number of Poles		4
Pole Pitch	τ	$114mm$
Magnet Length	y	$78.5mm$
Steel Pole Length	h	$35.5mm$
Outer Radius of the Secondary	r_2	$47.5mm$

[6]The magnet length, h, is optimised to reduce cogging forces as described in Section 4.2.4

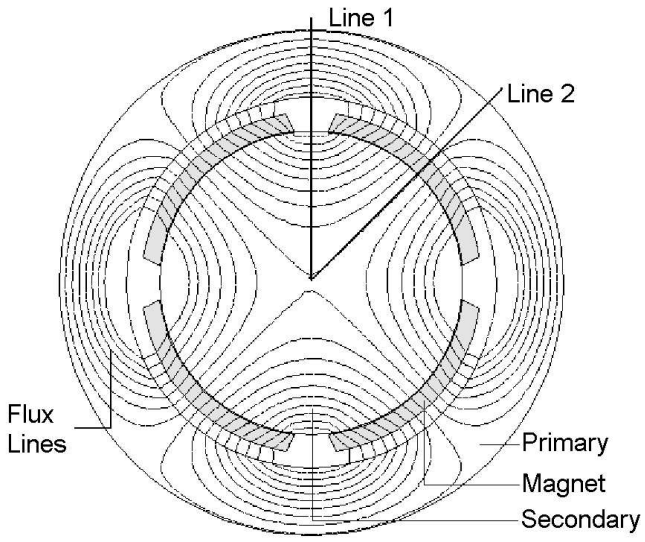


Figure 4.24: A four pole rotary motor

4.2.3 Split-Pole Surface Mounted Magnet Arrangement

The split-pole magnet arrangement can be used in the design of the secondary section for a LSM. This unique concept requires the placement of half length magnets at the two ends of a surface mounted magnet arrangement. This new arrangement produces half the amount of flux per pole in both the primary and secondary sections compared to the conventional surface mounted magnet arrangement. An electrical circuit analogy has been included in Appendix C to assist with the interpretation of the split pole magnet arrangement.

In Figure 4.24 the ordinary rotary motor is shown with the flux lines generated by the magnets. Only half the flux per pole flows through both the primary and secondary.

Traditionally, the rotary motor is conceptually cut through Line 1 to produce the linear motor in Figure 4.25. A novel approach is to conceptually cut the motor along Line 2 to give rise to the unconventional magnet arrangement in Figure 4.26.

The discussion of this section concentrates only on the surface mounted magnet configuration. These principles can be equally applied to single-sided, double-sided and tubular LSM's.

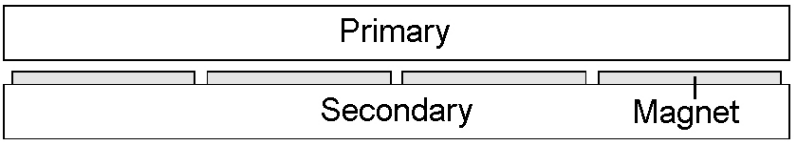


Figure 4.25: A four pole linear motor with the cut made at Line 1.

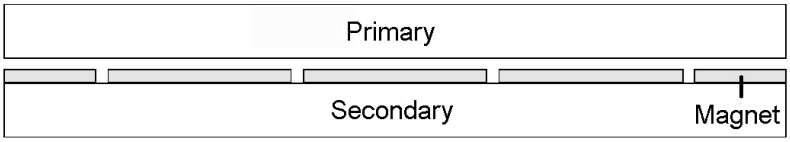


Figure 4.26: A four pole linear motor with the cut made at Line 2.

Conventional Even Pole Magnet Arrangement without Saturation Effects

The conventional magnet arrangement is shown in Figure 4.25. This is the traditional approach used for linear motors and is achieved by slicing through Line 1 in Figure 4.24, thus cutting between the magnets on the secondary.

This type of linear motor with the flux lines generated by the magnets can be seen in Figure 4.27. FEA was used to plot the flux lines. For this model, the primary section and the steel on which the magnets have been mounted have both been defined as infinitely permeable materials. This model shows that all the flux per pole flows through the steel and links with the adjacent magnet.

The reason that the flux links in pairs is that the flux generated by the outside magnets has to follow a complete path. In this arrangement, the easiest path for the flux of the outside magnets is to link with the adjacent magnets.

The major disadvantage of this arrangement is that the total flux per pole flows through both the primary and secondary. Therefore, to prevent saturation, a thick steel block is required for each section.

Conventional Even Pole Magnet Arrangement with Saturation Effects

The area most likely to saturate first is the area between two magnets, as this is the region where all of the flux from one magnet links with the adjacent magnet. If this area becomes saturated, it will limit the amount of flux passing through this region. In the FEM simulation the primary was kept as an infinitely

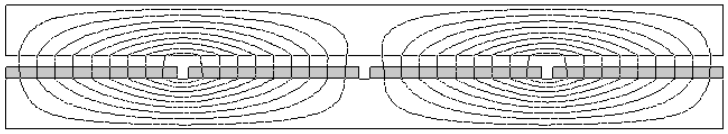


Figure 4.27: Conventional magnet arrangement with flux lines

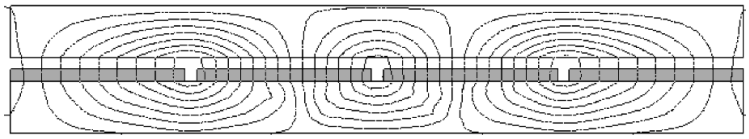


Figure 4.28: Conventional magnet arrangement with saturation effects

permeable material. To emphasis the effects of saturation, the secondary has been assigned a material that saturates at $0.6T$. In the four-pole configuration, the total flux generated by the outside magnets will not link with the total flux generated by the corresponding middle magnets. Thus, there will be some linkage between the two middle magnets, as can be seen in Figure 4.28. The consequence is that the total amount of flux generated by the magnets in the conventional magnet arrangement will be reduced due to the saturation effects caused by the greater reluctance of the magnetic circuit.

Split-Pole Magnet Arrangement

A novel approach, of the split-pole magnet arrangement, is to use two half magnets at the ends of the secondary section. It is a unique design, as it is not used in any other type of motor. It does not occur in conventional rotary motors, as the secondary is a continuous structure. Also, it is not found in any linear motors that the author is aware of.

For the split-pole arrangement, cutting along Line 2 in Figure 4.24 makes the conversion from rotary to linear topologies (Figure 4.26). This cut bisects a magnet, but not the flux, as in the case of the conventional magnet arrangement. Even though there are now five magnets, it is still an even pole magnet arrangement. The two end magnets are half the length of the other magnets and form one pole. The flux pattern for this split-pole magnet arrangement is shown in Figure 4.29.

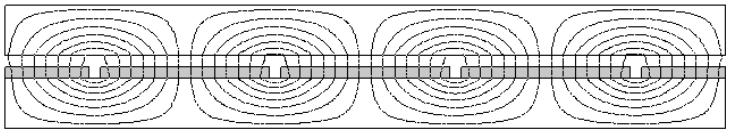


Figure 4.29: Split-pole magnet arrangement with flux lines

From the flux plot in Figure 4.29, it can be noted that at any place along the steel in the secondary, there is a maximum of half the total flux per pole flowing through the steel. There will always be a maximum of half the flux per pole irrespective of the reluctance of the primary and secondary sections.

In the split-pole magnet arrangement, the maximum amount of flux in the steel is less than that of the maximum flux in the conventional magnet arrangement. It is thus beneficial to use the split-pole magnet arrangement, as the amount of material in the primary and secondary can then be reduced. This decreases the secondary's weight and improves the performance (FWR) of the LSM.

4.2.4 Reduction of the Cogging Forces

Cogging forces are the result of the interaction between the permanent magnets and the steel teeth of the primary section. As a pole shoe edge passes the steel teeth of a primary section, a sinusoidal force is produced which has the period of one slot pitch. This occurs at both the leading and trailing edge of the pole shoe. This is represented in Figure 4.30. The combination of these two forces gives an overall cogging force for the pole shoe. This cogging force produces a slightly jerky motion during the travel of the linear motor. This jerky motion is most noticeable at low speeds. The cogging forces can also make the positioning of the linear motor tricky if exact positioning within the distance of one slot pitch is required. Various methods have been introduced to reduce the effects of the cogging forces [55].

Techniques to Reduce Cogging Forces

The most effective technique to reduce cogging forces is the use of skewed magnets on a permanent magnet LSM (Figure 4.31). However, this is not always

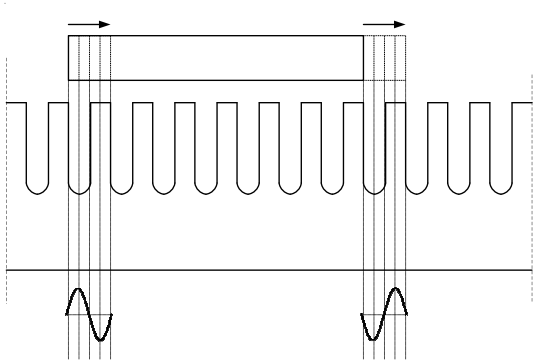


Figure 4.30: Cogging forces produced by both the leading and trailing edge of a pole shoe.

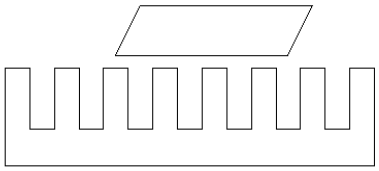


Figure 4.31: A skewed magnet for cogging force reduction

possible if the geometry of the design is complicated. This technique also results in a slight reduction of the fundamental force component, particularly in motors with a small number of teeth per pole [56].

Another technique is to skew the slots on the primary section (Figure 4.32). This has the same effect in reducing the cogging forces as the skewing of the permanent magnets. This results in the fundamental force component being slightly reduced. However, it is also not always possible if the primary design is complicated.

A further technique is to increase the air gap size. This technique reduces the fundamental force component drastically and is not a preferred method of reducing the cogging forces.

Control strategies can also be employed. A scalar control strategy has been

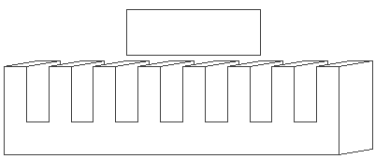


Figure 4.32: A skewed primary for cogging force reduction

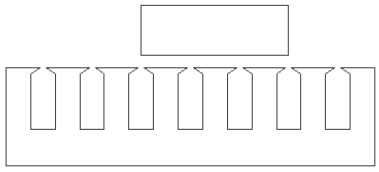


Figure 4.33: A semi-closed slots for cogging force reduction

attempted which produced a slight reduction in the cogging force [57]. A current shaping control technique has also been more successful [58]. However, using a control strategy is an expensive and complicated technique to reduce cogging forces and is not preferred when simpler options are available.

Semi-closed slots can be used in place of open slots in the primary section (Figure 4.33). This shows only a small reduction in cogging forces as the semi-closed portion of the teeth becomes saturated. It does, however, increase the fundamental component of the force, as the effective air gap is smaller. An alternative is to use magnetic slot wedges.

A technique that can be used is that of optimisation of the permanent magnet or pole shoe length on the secondary section. This technique results in a simple modification of the permanent magnet dimensions to counter cogging forces [56, 59]. If the permanent magnet dimensions are fixed, the coil carrying or primary section dimensions can be adjusted [60].

With adjustments to the permanent magnet dimensions, the length is chosen such that the generated cogging force by the leading edge of a permanent magnet effectively cancels the cogging force generated by the trailing edge of the permanent magnet. This technique was found to be effective for SMMA [33]. Further investigation has shown that this can be applied to BMA as the interaction of the pole shoes with the primary teeth create similar cogging forces.

Yoshimura et al. [59] stated that the magnet length (h in Figure 4.34), of a SMMA must be:

$$h = (2 + \frac{1}{4})\tau_s \tag{4.42}$$

- $2 = x - 1$
- $x = \frac{\tau}{\tau_s}$, the number of slot pitches per pole
- $\tau =$ pole pitch

- τ_s = slot pitch

A more general form of Equation 4.42 would be:

$$h = ((\frac{\tau}{\tau_s} - k) + \frac{1}{4})\tau_s \tag{4.43}$$

- $k = 1, 2, 3...$

For Equation 4.43, the magnet length would be at its greatest when $k = 1$.

Li et al. [56] suggests a permanent magnet length which is similar to Yoshimura et al. [59]:

$$h = (k + 0.14)\tau_s \tag{4.44}$$

Due to geometry constraints of this project and for ease of implementation, this technique of magnet length or pole shoe length optimisation was used for the modified tubular LSM.

Magnet Length Optimisation to Reduce Cogging Forces

For this investigation two different secondary designs were used, namely, a surface mounted magnet arrangement (SMMA) and a buried magnet arrangement (BMA) (Figures 4.34 and 4.35). In both designs the pole shoe is defined as the part of the secondary where the flux passes through the air gap from the secondary to the primary or vice versa. For the SMMA, the pole shoes are the permanent magnets themselves. The pole shoes for the BMA are the steel sections in the secondary.

Cruise et al. [55] found this technique to be effective for SMMA. Further investigation shows that this can be applied to BMA with a restriction. The restriction is that only discreet magnet volumes can be used. Changing the magnet volume can only be done by changing the magnet length which will affect the cogging forces. Whereas for a SMMA, the change in magnet volume does not affect the cogging forces as long as the magnet length, h, is kept constant.

Intuitively, the pole face of the secondary should be a multiple of the slot pitch. This is shown in Figure 4.30. The cogging force produced by the leading edge

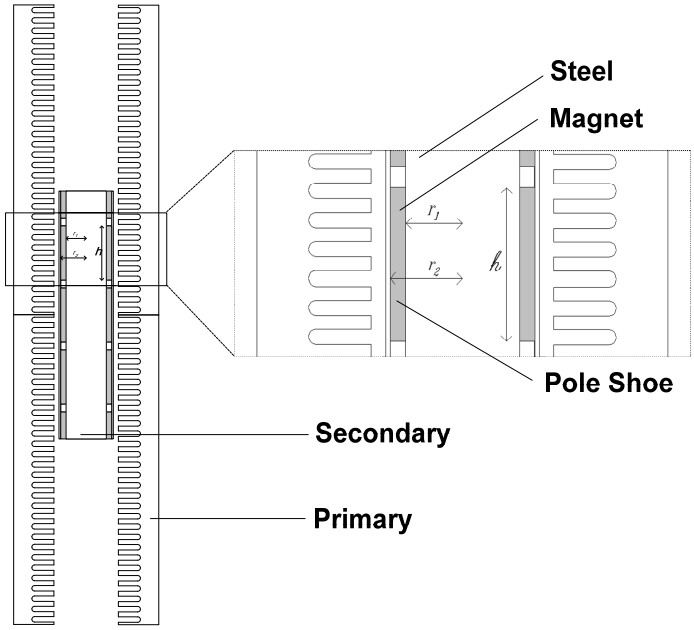


Figure 4.34: Cross-sectional view of the tubular LSM with surface mounted magnets.

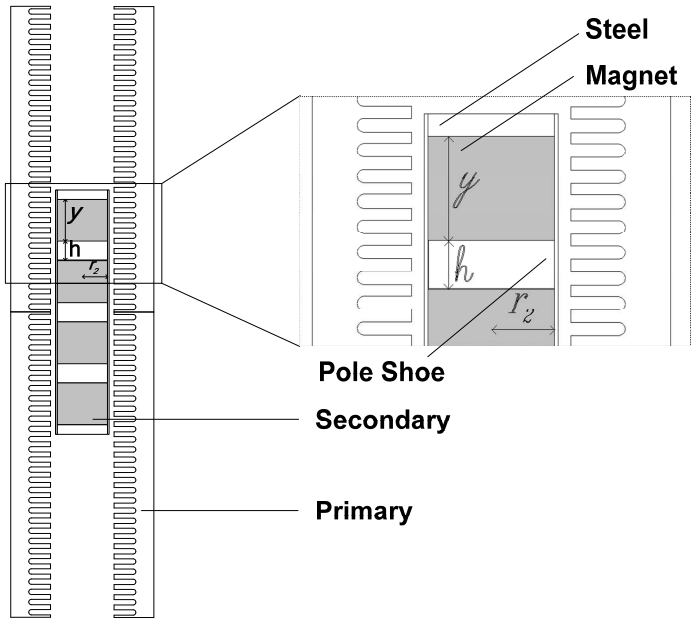


Figure 4.35: Cross-sectional view of the tubular LSM with buried magnets.

of the pole shoe cancels with the cogging force produced by the trailing edge. This simple solution is a good starting point in reducing the cogging forces. This should hold if the following are assumed:

- The cogging force for both the leading or trailing edge is a perfect sinusoidal function of distance.
- There are no fringing or leakage fluxes (the flux in the air gap is perpendicular to both the primary and secondary sections).

In reality, these assumptions do not hold and hence the development of the general equations to determine the optimised magnet length for cogging force reduction (Equations 4.43 and 4.44). However, linear motors have many different characteristics which make it difficult to use the proposed general equations for magnet length optimisation. These characteristics include:

- Different topologies. Single-sided, double-sided and tubular topologies. (Li et al. [56] proposed solution was for surface mounted magnets in rotary motors, where the principles of cogging torque reduction are similar.)
- Different ratios for tooth width verses slot pitch. The drastic changes between slot opening and the steel teeth mean that the cogging force is not a pure sinusoidal function of distance. However, the period of the cogging force is approximately equal to a slot pitch.
- The use of open or semi-closed slots. Magnetic wedges are also used in the primary sections of linear motors.
- Different air gap lengths. These variations effect the direction of the flux with the amount of fringing and leakage flux changing as the air gap changes.
- Varying degrees of flux saturation in the steel sections of the linear motor. This fact also influences the amount of fringing and leakage flux in the linear motor as well as the angle at which the flux crosses the air gap. See Figures 4.11 and 4.13 as examples.

Thus, it is suggested that for each particular linear motor design, FEA should be used to determine the extent of the cogging forces. As an example, FEM models for the BMA tubular linear motor were drawn in a two-dimensional

(2D) environment in the R-Z axes reference frame. For these simulations the air gap was reduced to $1mm$ to emphasise the effect of the cogging force. The primary coils were removed from the FEM model and only the effects of different positions of the secondary relative to the primary were investigated. These positions spanned one slot pitch.

By examining the cogging forces produced from FEA simulations, the pole shoe lengths with the least cogging forces can be selected. As the secondary travels, each pole shoe length produces a cogging force, which has a period of one slot pitch. Figures 4.36 and 4.37 are examples of simulations for the BMA.

The lengths of the buried magnets with the smallest magnitude of cogging force are $58mm$ and $78.5mm$[7]. The pole shoes lengths for these two magnet lengths are $56mm$ and $35.5mm$ respectively. These two values are approximately one slot pitch apart. These pole shoe lengths are close to multiples of a slot pitch of $57mm$ and $38mm$ respectively. The magnet length of $78.5mm$ was used in the final optimised design as detailed in Section 4.2.2.

The maximum magnitude of the cogging forces produced from Figures 4.36 and 4.37 and other pole shoe lengths are compared for varying air gap lengths and is shown in Figure 4.38. Figure 4.39 shows the maximum magnitude of the cogging forces for the SMMA.

Visual inspection of Figure 4.38 shows that, for the BMA, the minimum cogging force occurs when the pole shoe is a multiple of the slot pitch. This occurs for large pole shoes sizes or small magnet volumes. However, when the pole shoes are small and the magnet volume is very large, a distortion in the magnetic field as shown in Figure 4.40, results in the minimum cogging force occurring when the pole shoe length is slightly smaller than a multiple of the slot pitch. It is also interesting to note that a change in air gap length does not change the point at which the minimum cogging force occurs. This justifies the use of the $1mm$ air gap used in the simulations to emphasis the magnitude of the cogging forces.

Visual inspection of Figure 4.39 shows that, for the SMMA, this graph ties in closely with the general equations developed by Yoshimura et al. (Equation 4.43)[8] and Li et al. (Equation 4.44) as the optimised magnet length is

[7]The slot pitch is $19mm$ and the pole pitch is $114mm$ for the modified tubular LSM

[8]During the first stage of the modified tubular LSM, the optimised magnet length of $100mm$ was used for the SMMA. This was based on Equation 4.43 and FEA work by Cruise et al. [55].

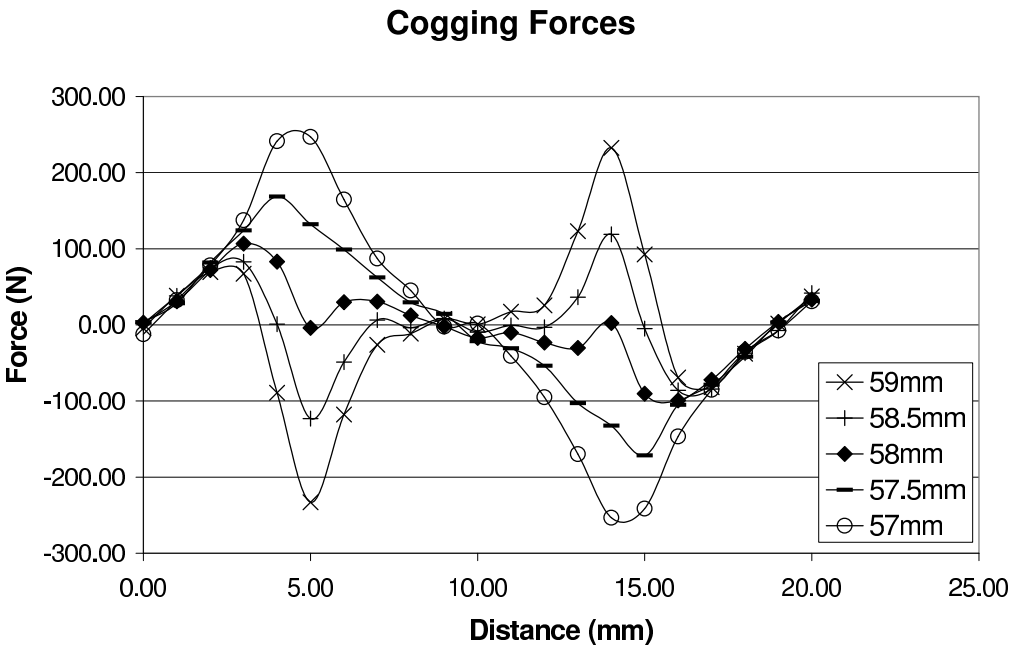


Figure 4.36: Cogging forces for a permanent magnet length of $57mm - 60mm$. This small range is used to emphasise the difference between the magnet lengths.

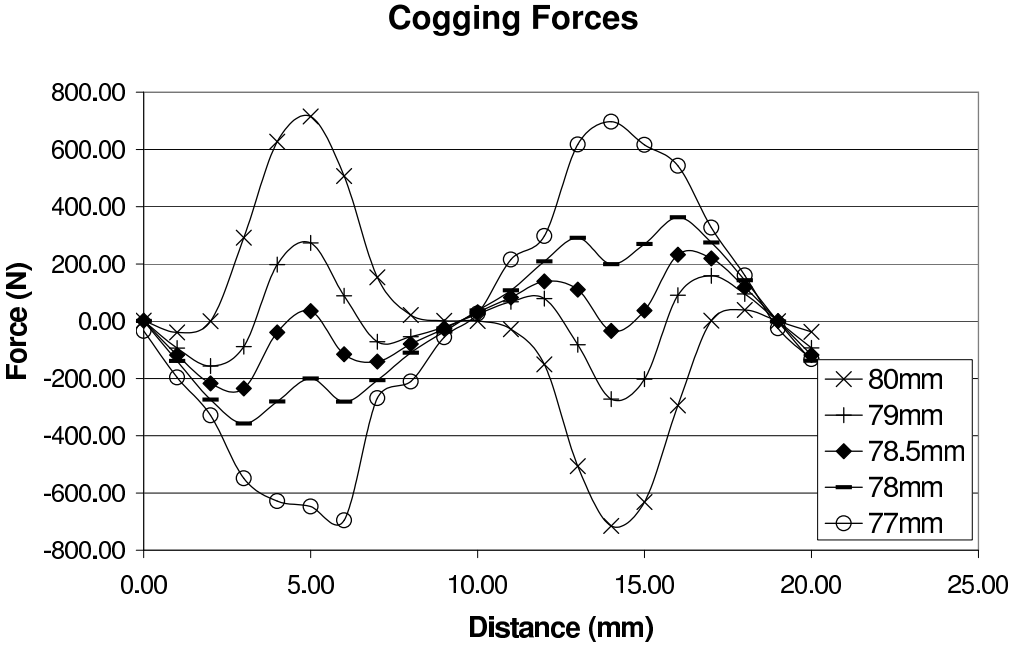


Figure 4.37: Cogging forces for a permanent magnet length of $77mm - 80mm$.

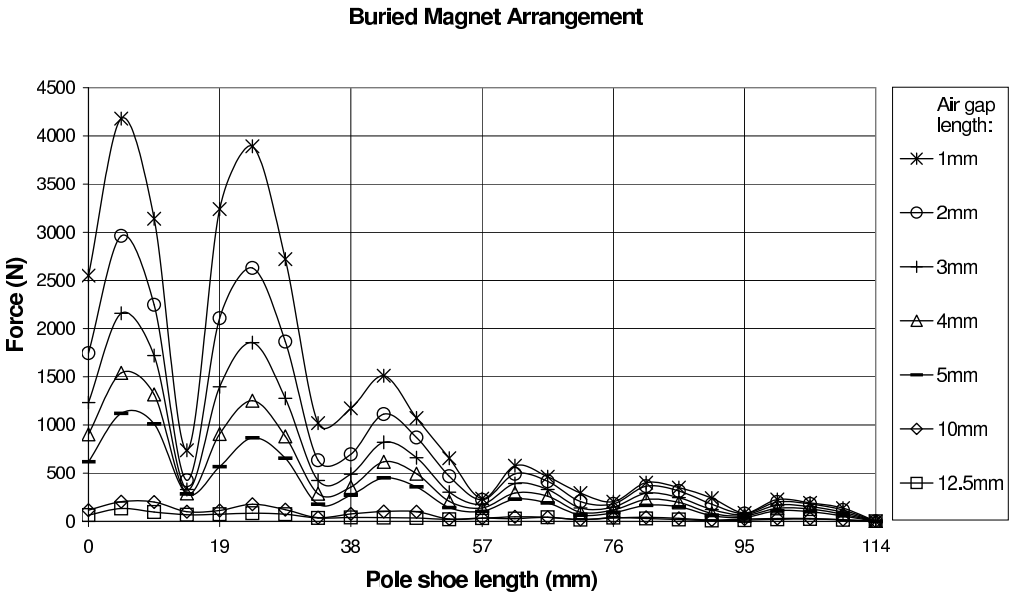


Figure 4.38: Cogging forces for a varying pole shoe lengths in a BMA.

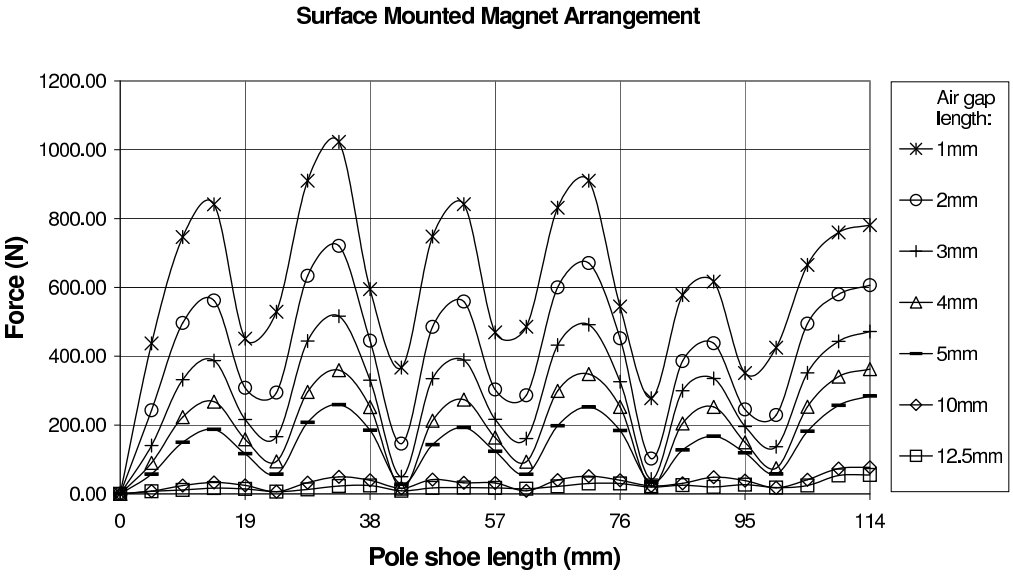


Figure 4.39: Cogging forces for a varying pole shoe lengths in a SMMA.

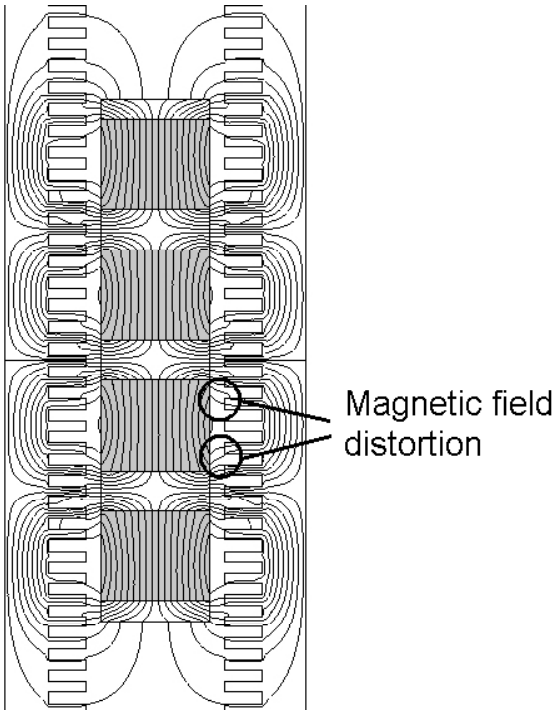


Figure 4.40: Cross-sectional view the flux in a tubular LSM with buried magnets. The areas of magnetic field distortion are highlighted. The flux is forced to enter/exit from the sides of the buried magnets.

slightly bigger than a multiple of a slot pitch. This graph also shows that the optimised magnet length is somewhat dependant on the air gap length and hence may account for the difference between Equations 4.43 and 4.44. This also means that simulations to determine the optimum magnet length or pole shoe length should be done at the required air gap length and should not be reduced to emphasis the magnitude of the cogging forces.

4.3 Summary

The focus of this Chapter was the optimisation of the secondary design and the comparison of three magnet arrangements; buried magnet arrangement, surface mounted magnet arrangement and a combination thereof. The optimisation first looked at a conventional tubular LSM and applied those results for the optimisation of the modified tubular LSM. This investigation showed that the BMA had the most optimum geometry in the axial plane as the cross-sectional area is largest by a factor of $(\frac{r_2}{r_1})^2$ compared to the other designs and thus was the preferred magnet arrangement. The dimensions of the optimised

design were given in Table 2.1 and are those used for the optimised prototype. Also, based on the properties of the permanent magnets, the BMA operates at a permeance coefficient gradient of 2.91 compared with the 0.74 for the SMMA. This means that the BMA operates at higher flux densities and out performs the SMMA at higher temperatures.

Part of the optimisation of the SMMA included the concept of using a split-pole magnet arrangement. Using this design optimisation ensured that there is a maximum of half the flux per pole flowing through the steel compared with the full flux per pole in a conventional SMMA.

The final design optimisation technique discussed in the chapter was that of cogging force reduction, which is essential for smooth travel at low speeds and precise positioning of less than one slot pitch. After various techniques were presented, magnet length optimisation was investigated and used for both the BMA and SMMA.

Chapter 5

The Design of the Mechanical System

This chapter deals with the construction of the modified tubular linear synchronous motor. It details the construction of both the primary and secondary sections of the motor. Photographs have been included to give a better visual idea of the motor's construction. The construction drawings showing most of the dimensions of the LSM can be found in Appendix D.

5.1 Primary Construction

Steel plates are used to form the basic frame of the linear motor. Round bars are used as spacers between the plates, so that there is support at the top, bottom and middle for each primary section. Small pieces of angle-iron connect the primary sections to the frame. These are welded to the frame, but could also easily have been bolted to the frame. It would be ideal to adjust the lengths of the angle-iron pieces, or the connection point on the frame, as this would allow for the minor modifications of the air gap length.

Figure 5.1 shows the basic frame of the linear motor during its construction and gives an indication of its size. Figure 5.2 shows a closeup of the motor. In this photograph four of the five primary sections can be seen. The beige tube in the centre was used as a former, so that the correct inner diameter was obtained for the primary sections. The small pieces of angle-iron used to attach the primary sections to the frame are seen loosely bolted to the frame. It was initially hoped to bolt these pieces to the frame, however, with a later adjustment to the position of the primary sections, the pieces of angle-iron were welded to both the primary sections and frame. Thus, the primary is a



Figure 5.1: The frame of the motor with primary sections only in the bottom half.

permanent construction. A schematic representation of this layout, as viewed from the top, can be seen in Figure 5.3.

Figure 5.4 shows the primary sections in the frame of the motor with the windings in place. The gap seen in Figure 5.4 allows space for the cage to be connected to the moving secondary section. Each primary section was pre-formed with the laminations stacked on a radius of $55mm$ on the inside. The width of each primary section is also $55mm$.

The next two photographs (Figures 5.5 and 5.6) show the windings inside the primary sections. These photographs were taken without the secondary section. Figure 5.6 shows a close-up of the windings.

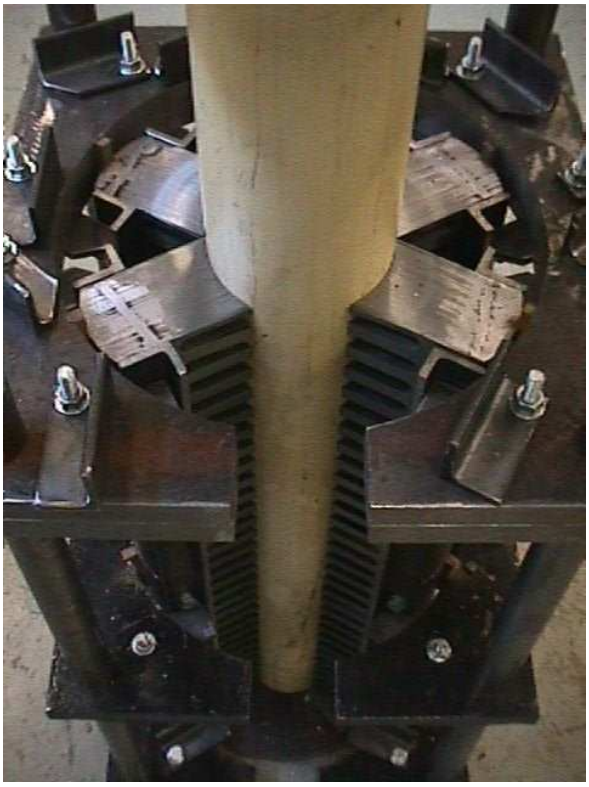


Figure 5.2: A close-up of the motor showing 4 of the 5 primary sections.

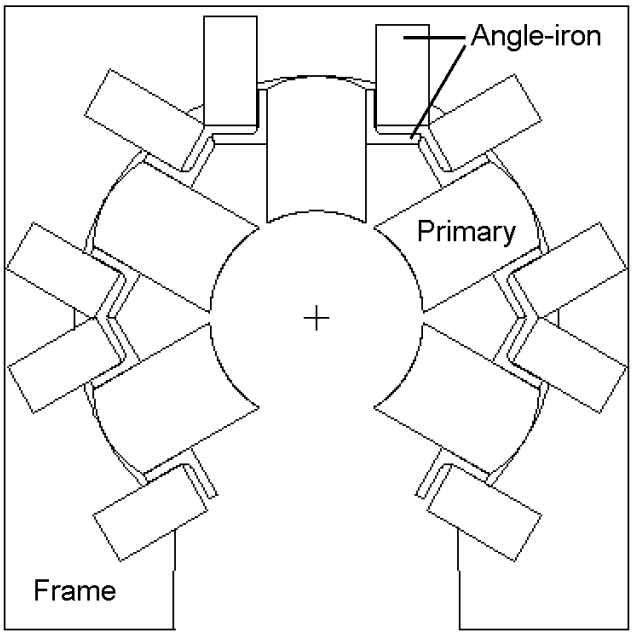


Figure 5.3: Diagram indicating the use of small pieces of angle-iron to connect the primary sections to the frame.

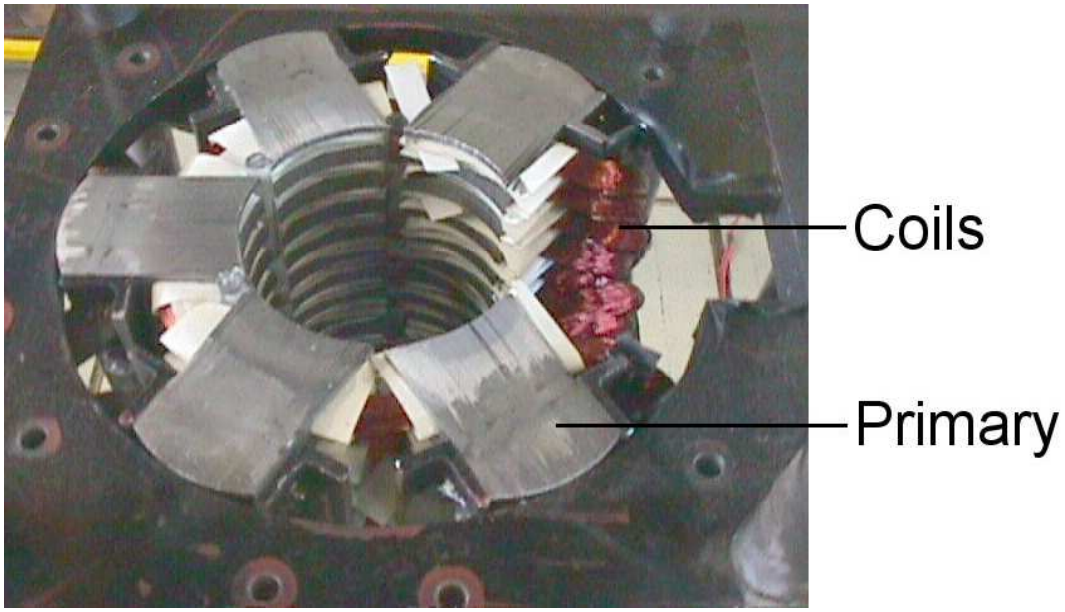


Figure 5.4: The modified tubular LSM from above showing the arrangement of the primary sections

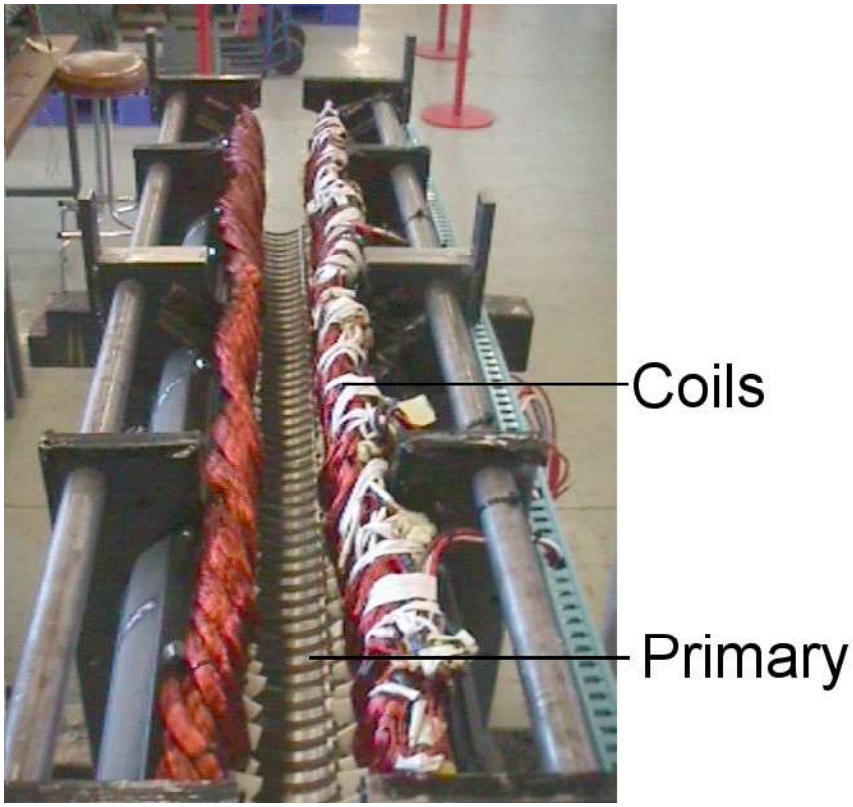


Figure 5.5: The primary section with the copper windings.



Figure 5.6: A close-up of the motor windings.

5.2 Secondary Construction

The secondary section houses the magnets for the modified tubular LSM. The construction includes an aluminium shield to protect the magnets.

For the SMMA, the steel of the secondary is a thick round bar with a diameter of $75mm$. The magnets are $10mm$ thick and are placed on the round bar as shown in Figure 5.7. The length of each magnet is $h = 100mm$. The mass of the steel and the permanent magnets (i.e. the active material as defined in section 1.1.4) is $23.62kg$. The cross-sectional view is shown in the previous chapter in Figure 4.10. Note the split-pole magnet arrangement, which is made up of the two half magnets at the top and bottom of the secondary. The length of the secondary is $456mm$, and it spans four pole pitches.

For the BMA, both the magnets and the steel round bar have a diameter of $95mm$. The magnet length of $y = 78.5mm$ is made up of 3 individual magnets as seen in Figure 5.8. The steel sections are $h = 35.5mm$ in length. The mass of the active material is $24.78kg$. A cross-sectional view of this magnet arrangement is shown in the previous chapter in Figure 4.12. Figure 5.9 shows the last set of magnets about to be placed inside the aluminium tube. The steel strips around the aluminium tube were used to aid the flux from the magnets

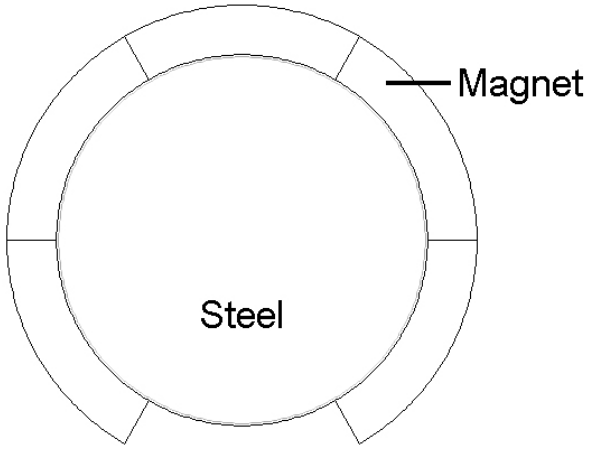


Figure 5.7: Top view of the secondary

so that the magnets and the steel round bars sections would attract to each other. The steel strips could then be easily removed. Figure 5.10 shows the completed secondary section. The bearing housings were then attached and the secondary placed inside the primary.

There is a large normal force of approximately $1200N$ within the motor. This normal force acts in a radial direction and attracts the secondary to the primary. From Figure 5.11 it can be seen that the normal force generated by primary section 1 is balanced by primary section 4. The same for primary sections 2 and 5. However, the normal force generated by primary section 3 is not balanced. The guidance system has to mechanically balance this normal force and thus forms an integral part of the whole assembly. It has to direct the secondary and prevent it making contact with the primary.

The picture in Figure 5.12 shows the attachment between the secondary and the guidance system inside the motor. There were no windings in the motor when the photograph was taken. Aluminium has been used for the guidance system so that it will not interfere magnetically with the LSM. A schematic showing the guidance system, as viewed from the top, is shown in Figure 5.13.

There are two bearing-housings shown in Figure 5.12. One on either side of the aluminium shield and they run along the two guide rails. These guide rails run the length of the motor and can be seen in the foreground of Figure 5.12. Vesconite is used as a bushing in the bearing housings. With the guide rails well oiled, the secondary moves smoothly from the one end of the linear motor to the other.



Figure 5.8: The magnet length, y, is made up of three individual magnets



Figure 5.9: Construction of the secondary section for the buried magnet arrangement



Figure 5.10: The completed secondary section for the buried magnet arrangement

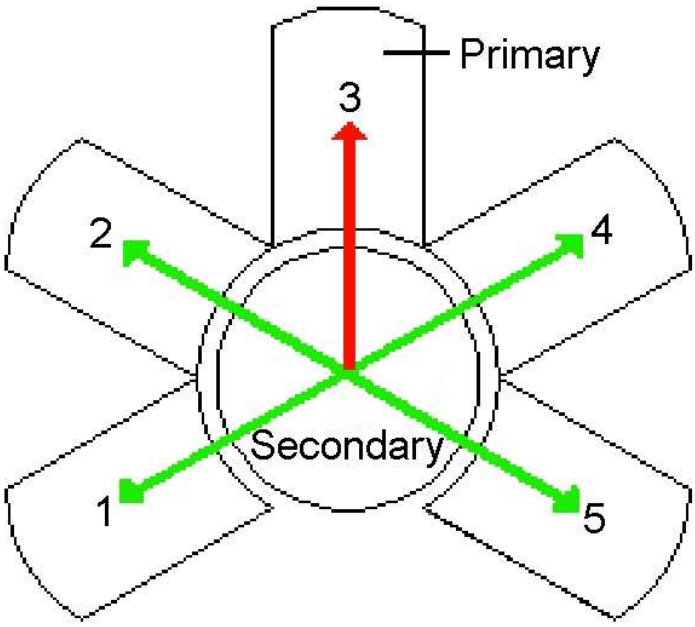


Figure 5.11: Normal forces in the modified tubular linear motor

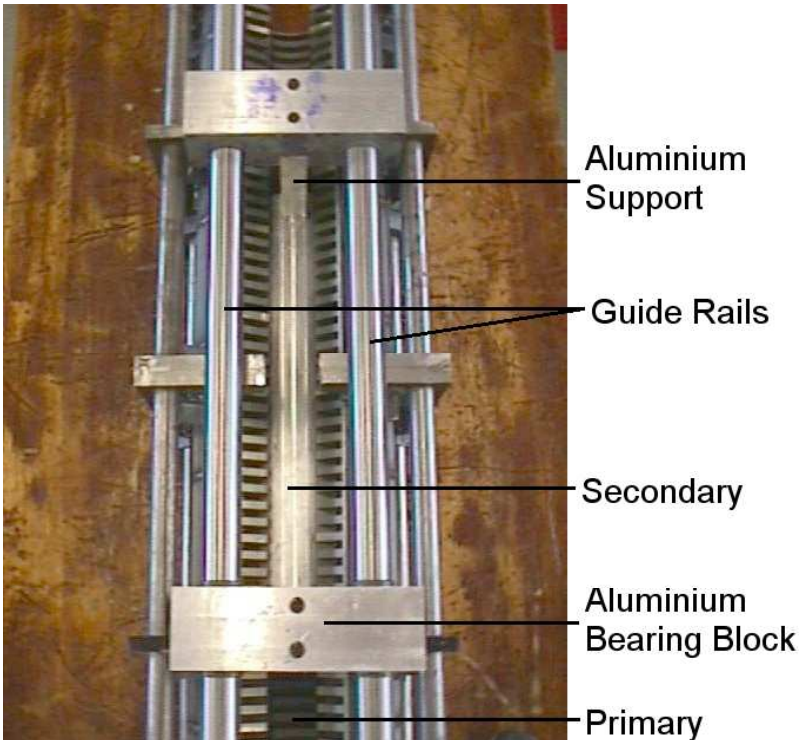


Figure 5.12: Secondary section attached to the guidance system.

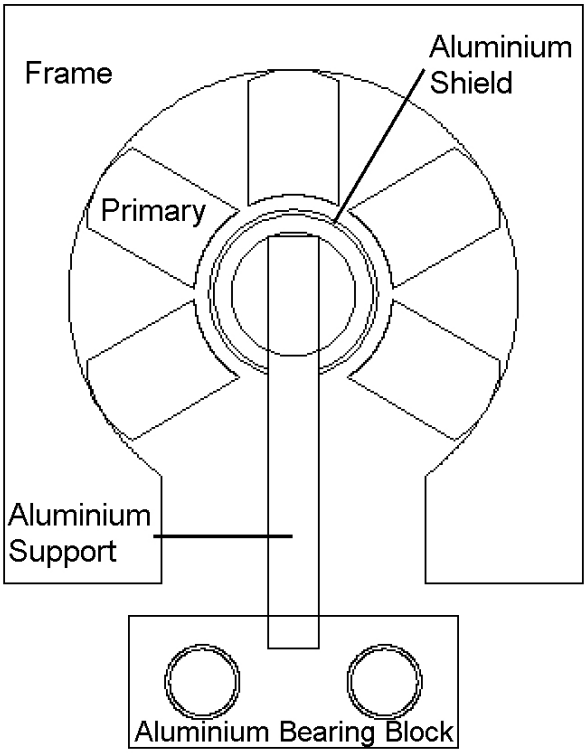


Figure 5.13: Diagram of the guidance system.



Figure 5.14: The complete model

The completed model is shown in Figure 5.14. This picture was taken from the side. The yellow frame is the cage on which a load can be placed. In the background is the Variable Speed Drive used to supply the linear motor.

5.3 Summary

This chapter gives a brief description of the construction of both the primary and secondary sections. The photographs and the construction drawings in Appendix D give a visual representation of the construction details and the process followed during the construction.

Chapter 6

Evaluation of the Thermal System

A thermal model of the primary winding in the modified tubular LSM is developed to determine the motor's operating limit. Since this LSM has been designed around a current rating rather than a voltage rating, this thermal model will determine the operating current limit. Like all electrical machines, the operating temperatures will influence the lifespan and performance of the modified tubular LSM.

Besides mechanical stability, the main area of concern for the lifespan of an electrical machine is the integrity of the electrical system. This is evaluated on the performance of the winding insulation. The lifespan of the winding insulation is dependent on its aging capability, but more so on its thermal capacity. It is around this thermal limit that the current rating will be determined using the thermal model for the primary winding.

The thermal model applies for both the SMMA and the BMA. This is because the heat source is only on the primary section. The heat produced in the linear motor is mainly in the form of copper losses and a small portion in the form of core losses. As the applied electrical supply frequency is only $0.5Hz$, the flux passing through the primary also pulsates at $0.5Hz$. This is low and the resulting eddy current and hysteresis losses produced in the primary will be minimal. It is for this reason that the core loss will be assumed to be negligible. Thus, the copper losses are the main contributing source of heat in the motor.

Due to the tubular geometry of the structure, it is assumed that all generated heat will be both stored within the LSM and will be dissipated on the outside surface of the LSM. Currents flowing through the primary heat up the copper windings. This heat dissipates into the steel section of the primary through

a process of *conduction* and also heats up the air in the air gap through a process of *radiation*. Some of the heat in the air gap is transferred into the permanent magnet secondary. For this analysis, it will be assumed that the heat in the air gap is much smaller than the heat dissipated into the primary as the process of heat conduction is a lot more efficient than the process of heat radiation. Thus, most of the generated heat will be both stored within the primary section and dissipated on the outside surface of the LSM. This stored and dissipated heat will be evaluated using a thermal model for the outside surface of the LSM. This thermal model will form the basis for the thermal model for the primary winding.

Another area of concern for the modified tubular LSM is that the linear motor must not heat up excessively such that the $NdFeB_{N-35}$ magnets exceed their maximum operating temperature[1]. If the maximum operating temperature is exceeded, the magnets may be negatively affected as discussed in Section 4.1.2. However, this is a secondary concern compared to the temperature of the winding insulation. The reason is that there is a significant thermal barrier, in the form of a large air gap, between the primary and the permanent magnet secondary. As mentioned, the heat transfer to the permanent magnet secondary is expected to be small. The effects of this small increase in temperature on the permanent magnets, will be highlighted later in this chapter when the results from practical experiments are discussed (Section 6.4).

6.1 Thermal Model for the Outside Surface of the LSM

To determine this thermal model a few assumptions are made.

- The heat generated is only the copper losses in the primary winding. The core losses in the motor are negligible.
- The material in the linear motor is homogeneous (i.e. the copper and steel are seen as one material). The material chosen is that of steel as it makes up most of the mass of the linear motor.
- The heat is evenly generated and distributed throughout the linear motor.

[1]This maximum operating temperature is dependent on the properties of the permanent magnet as well as the reluctance of the magnetic circuit as described in Section 4.1.2

- The heat can only dissipate into the air through the exposed parts of the primary section on the outside of the linear motor. There is no dissipation of heat on the inside of the linear motor.
- The heat is generated internally and is surface cooled.

It is important to note that the temperature calculated is the temperature at the exposed surface of the linear motor where the heat dissipates from the LSM into the surrounding air. The temperature of the primary winding will be determined from this model. Two heat runs at different current levels were conducted to determine the difference between the surface temperature of the LSM and the temperature of the primary winding. This model of temperature difference is combined with the model for the surface temperature to determine the temperature of the primary winding.

The temperature of the primary winding is the most important parameter to ascertain because the integrity of the winding insulation is governed by the temperature of the motor under continuous operation.

The heat equation that describes the temperature rise, θ, on the surface of the linear motor is:

$$\underbrace{qdt}_{\text{heat generated}} = \underbrace{MC_p d\theta}_{\text{heat stored}} + \underbrace{hA\theta dt}_{\text{heat dissipated}} \tag{6.1}$$

Where:

- q = heat source (W)
- M = mass (kg)
- C_p = specific heat ($\frac{J}{kg^oC}$)
- h = heat transfer coefficient ($\frac{W}{m^{2o}C}$)
- A = surface area (m^2)
- θ = temperature rise (^{o}C)

Dividing Equation 6.1 through by dt, the energy equation becomes a power equation:

$$q = MC_p\frac{d\theta}{dt} + hA\theta \tag{6.2}$$

Rearranging Equation 6.2:

$$\frac{d\theta}{dt} + \frac{hA}{MC_p}\theta = \frac{q}{MC_p} \tag{6.3}$$

Equation 6.3 is a first order differential equation. Thus, the natural or transient response is:

$$(D + \frac{hA}{MC_p})\theta = 0 \tag{6.4}$$

Therefore:

$$\begin{aligned} D &= -\frac{hA}{MC_p} \\ \theta &= Be^{-\frac{hA}{MC_p}t} \\ \theta &= Be^{-\frac{t}{T}} \end{aligned} \tag{6.5}$$

Where:

- B = constant
- T = time constant

The steady state temperature response, θ_{ss}, occurs when $\frac{d\theta}{dt} = 0$

Therefore:

$$\theta_{ss} = \frac{q}{hA} \tag{6.6}$$

The full response is the combination of Equations 6.5 and 6.6:

$$\theta = \theta_{ss} + Be^{-\frac{t}{T}} \tag{6.7}$$

To solve for B, initial conditions are taken. That is at $t = 0$ and $\theta = \theta_o$. (θ_o = ambient temperature)

Therefore: $B = \theta_o - \theta_{ss}$ So Equation 6.7 becomes:

$$\theta = \theta_{ss} + (\theta_o - \theta_{ss})e^{-\frac{t}{T}} \tag{6.8}$$

If at $t = 0$, $\theta_o = 0$, the temperature rise is:

$$\theta = \theta_{ss}(1 - e^{-\frac{t}{T}}) \tag{6.9}$$

So the overall temperature at the exposed surface ,$\theta_{surface}$, on the LSM is:

$$\theta_{surface} = \theta_o + \theta_{ss}(1 - e^{-\frac{t}{T}}) \tag{6.10}$$

6.1.1 Values for the Thermal Model

With the overall temperature at the exposed surface described in Equation 6.10, the temperature versus time characteristic can be determined by obtaining values for the variables in Equation 6.1.

Heat Source, q

The heat generated by the primary winding is:

$$\text{Coil losses for one coil} \quad = \quad I_{a1}^2 R_{a1} \tag{6.11}$$

Where:

- I_{a1} = current per coil
- R_{a1} = resistance of one coil = 0.76Ω (See Section 3.2.2)

So the heat generated by one coil is:

$$\text{Coil losses for one coil} \quad = \quad I_{a1}^2 \times 0.76 \; W$$

There are 54 coils in total, therefore the total losses heating the primary are:

$$\begin{aligned} q &= 54 \times I_{a1}^2 \times 0.76 \; W \\ &= 41.04 \; I_{a1}^2 \; W \end{aligned}$$

Mass, M

The mass used for the temperature calculation is the total mass of the primary section only. The mass of the secondary is ignored as it is not a source of heat and, as it has been assumed, it is not used to dissipate the heat generated by the primary section. The mass of the primary section includes the lamination stacks, the angle iron used to hold the stacks together and the copper of the primary winding.

Mass of the Laminations. The mass of one lamination is $154g$. There are 84 laminations in each stack. There are 10 stacks in total that make up the primary.

The mass of one stack is:

$$\begin{aligned} \text{Mass of one stack} &= 84 \times 0.154\ kg \\ &= 12.94\ kg \end{aligned}$$

So 10 stacks have a mass of 129.36 kg

Mass of the Angle Iron. The angle iron that holds the lamination stacks together is shown with its dimensions in Figure D.2. The cross-sectional area, as shown, is approximately $0.25 \times 10^{-3} m^2$. Each piece of angle iron supports the laminations for the full length of the stack ($0.57m$ in length). There are two pieces of angle iron for each stack, thus there are 20 pieces of angle iron in total. The total mass of the angle iron is:

$$\text{Mass of angle iron} = \rho_{fe} V_{fe}$$

Where:

- ρ_{fe} = mass density of iron, = $7800(kg/m^3)$ [61]
- V_{fe} = volume of angle iron (m^3) = cross-sectional area × length × number of angle iron pieces.

$$\begin{aligned} \text{Mass of angle iron} &= \rho_{fe} V_{fe} \\ &= 7800 \times 0.25 \times 10^{-3} \times 0.57 \times 20\ kg \\ &= 22.23\ kg \end{aligned}$$

Mass of the Copper. The average length of one turn in a coil from the primary winding is $1.2m$. Each turn is made of two strands. The diameter of the wire is $0.9mm$, so the cross-sectional area is $6.36 \times 10^{-7} m^2$. There are 45 turns in each coil and there are 54 coils in total in the linear motor. Thus, the mass of the copper is:

$$\text{Mass of the copper} = \rho_{cu} V_{cu}$$

Where:

- ρ_{cu} = mass density of copper, = $8900(kg/m^3)$ [61]
- V_{cu} = volume of copper (m^3) = length of each turn × number of strands × cross-sectional area × number of turns × number of coils.

$$\begin{aligned} \text{Mass of the copper} &= \rho_{cu} V_{cu} \\ &= 8900 \times 1.2 \times 2 \times 6.36 \times 10^{-7} \times 45 \times 54 \ kg \\ &= 33.01 \ kg \end{aligned}$$

Total Mass of the Primary Section. The total mass of the primary is: $129.36 \ kg + 22.23 \ kg + 33.01 \ kg = 184.60 \ kg$

Specific Heat, C_p

For the temperature calculations, the linear motor is assumed to be a homogeneous material. The material chosen is that of steel as it makes up most of the mass of the linear motor. From [48], the specific heat, C_p, of steel is $500\frac{J}{kg^oC}$.

Heat Transfer Coefficient, h

From [48], the heat transfer coefficient, h, of steel is given between 25 and 40. For a worst case scenario, 25 has been used.

Surface Area, A

As stated earlier, it is assumed that the heat will only dissipate through the outside parts of the linear motor. This is indicated by the red lines on Figure 6.1. A close up of Figure 6.1, showing the length of the outside surface, is shown in Figure 6.2[2].

From Figure 6.2, the length of the surface area for each stack is given as $0.158m$. The length of the stack is $0.570m$ and there are 10 stacks in total. Therefore, the overall surface area is $0.90m^2$.

A smaller surface area at the ends of the core stack, which can also dissipate heat and is also shown in Figure 6.2 as area BCEF. There are only ten of these

[2]The surface areas AF and DE have not been considered as they are almost completely enclosed in the linear motor. There is only a small gap between the the edges of the angle iron pieces (Point D on one stack and point A on an adjacent stack.)

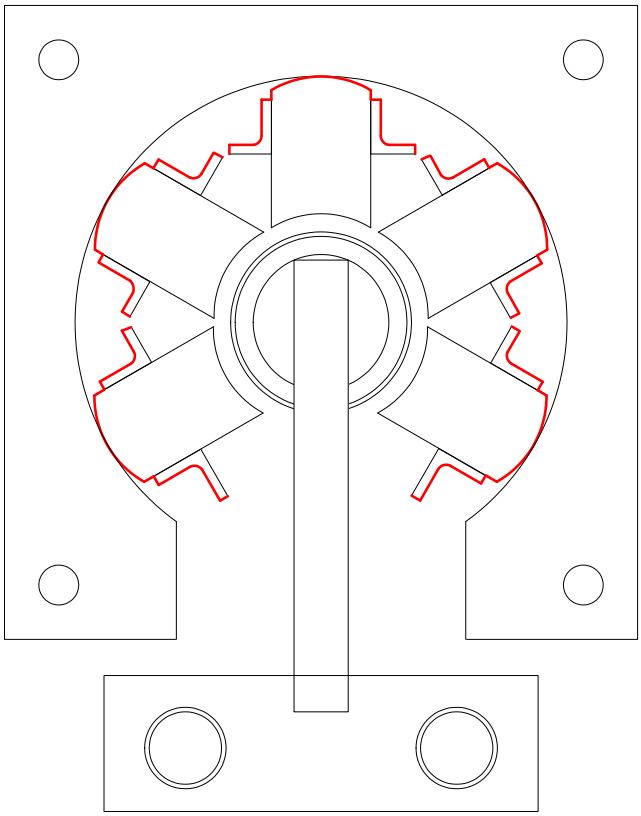


Figure 6.1: The heat generated in the primary section is dissipated through the surface area shown in red

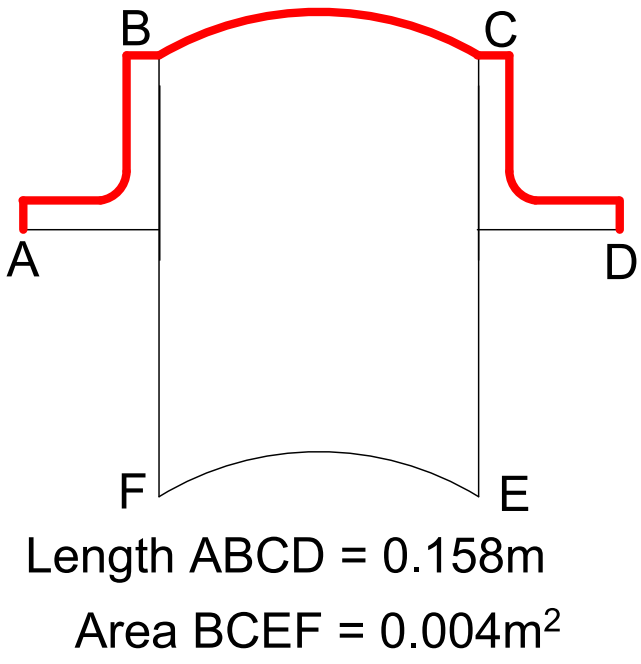


Figure 6.2: Close up of Figure 6.1

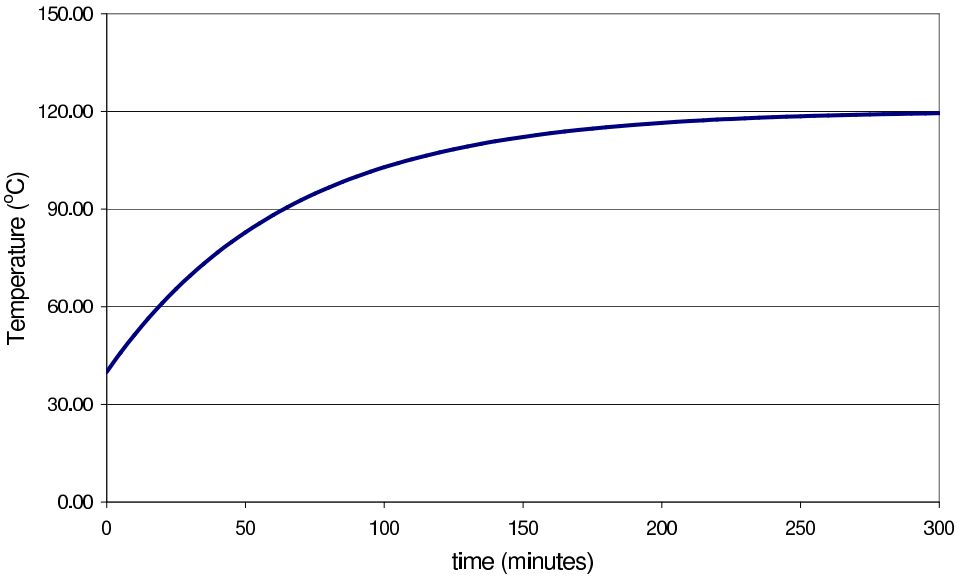


Figure 6.3: Surface temperature model.

surfaces, as the stacks of the top section are placed directly onto the stacks of the bottom section. Therefore, the overall surface area for top and bottom parts of the stacks is $0.04m^2$.

Thus, the overall surface area for the primary of the LSM dissipating heat is $0.94m^2$.

Using a rated current of $8A$ and an ambient temperature of 40^oC, Equation 6.10 for the modified tubular LSM can be represented by the graph in Figure 6.3.

6.2 Thermal Model for the Primary Winding

Equation 6.10 describes the temperature at the outside surface of the linear motor. To determine the heat transfer properties of the materials between the primary winding and the outside surface, the difference between the surface temperature and primary winding temperature was measured. This was done for the primary coil currents of $5A$ and $8A$ respectively. The respective temperature vs. time plots are shown in Figures 6.4 and 6.5.

From the graphs of Figures 6.4 and 6.5, the steady state temperature difference was found to be 18^oC and 30^oC respectively. These values are plotted in Figure 6.6 and, as expected, the relationship is linear.

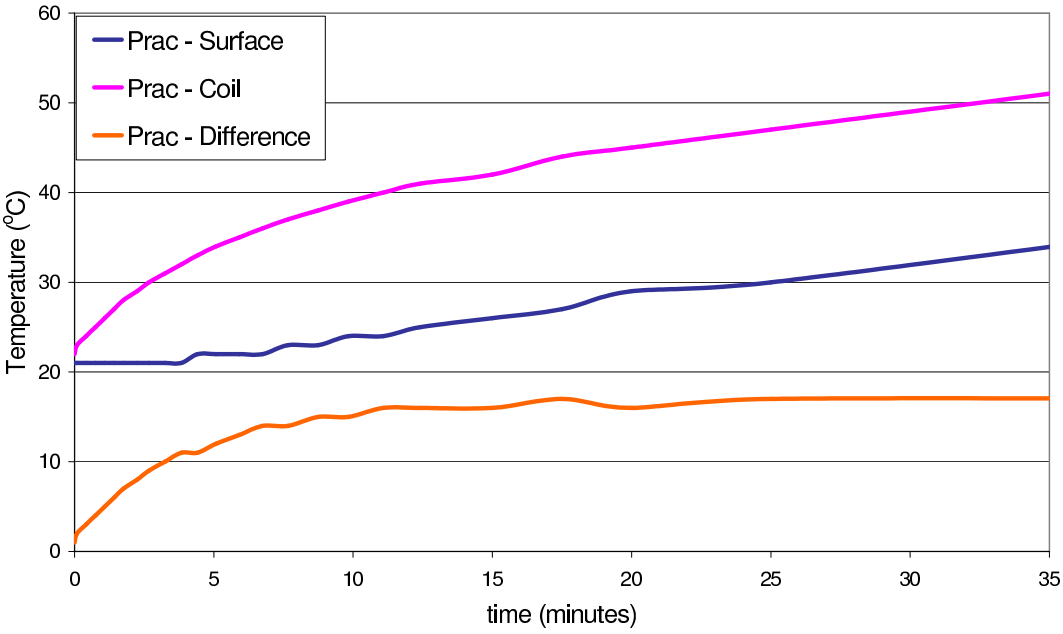


Figure 6.4: Experimental temperature curves of the surface and coil temperatures for a current of 5A per coil. The difference in the two temperatures reaches a steady state value after a short period of time.

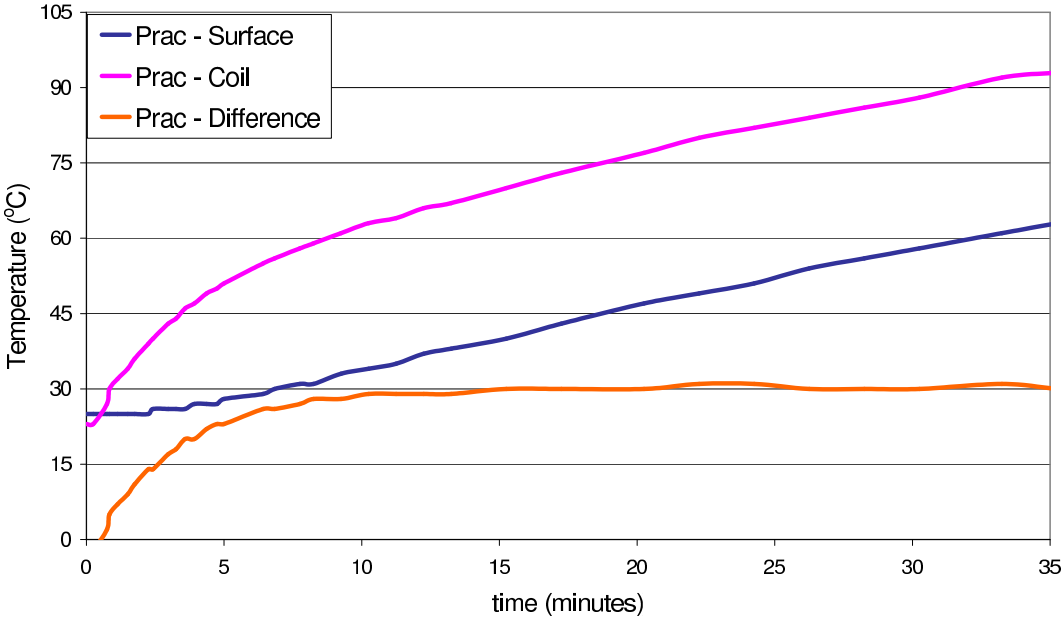


Figure 6.5: Experimental temperature curves of the surface and coil temperatures for a current of 8A per coil. The difference in the two temperatures reaches a steady state value after a short period of time.

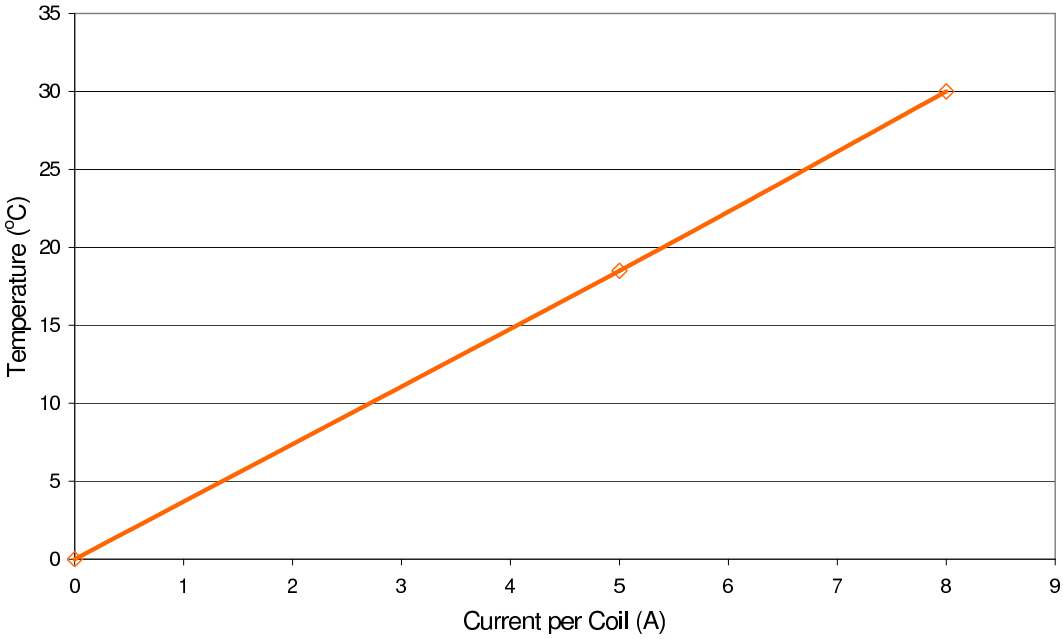


Figure 6.6: Linear model of the temperature difference between the coil temperature on the primary winding and the temperature on the surface of the linear motor

This model for the difference between the surface temperature and the coil temperature is then added to the model developed for the surface temperature in Equation 6.10. This final temperature model for the primary winding (Equation 6.12) determines the maximum continuous current rating for the linear motor depending on the properties of the coil insulation used.

$$\theta_{coil} = \underbrace{\theta_o + \theta_{ss}(1 - e^{-\frac{t}{T}})}_{\theta_{surface}} + \underbrace{\theta_k I_{a1}}_{constant} \tag{6.12}$$

Where

- θ_k = gradient of the constant slope in Figure 6.6

Table 6.1 shows the various insulation classes for the materials used for insulating copper wire [62]. This table shows the insulation class, the maximum temperature rating as well as the type of material used for the specific class of insulation. The temperature rating includes the three aspects of temperature that a copper winding would experience [63]. These are:

Ambient Temperature This is the temperature of the surrounding air. It is usually assumed to be 40^oC to allow for hot working conditions.

Table 6.1: Insulation Classes

Class	Temperature ^oC	Insulating materials
Y	90	Paper not impregnated
A	105	Paper if impregnated
E	120	Polyvinyl Formel - Polyurethane enamels
B	130	Fibre-glass impregnated - Modified polyurethane enamels
F	155	Fibre-glass impregnated in polyester and epoxy resins Modified polyurethane enamels
H	180	Polyestermide enamels Fibre-glass impregnated in class H varnishes
C	200	NOMEX* Fibre-glass impregnated in silicon resins Polyamide-imide enamels
	220	KAPTON*
*Du Pont De Nemours & Co USA trade mark		

Temperature Rise This is the actual rise or change in temperature that a material would experience if there is a source of heat. In this case the source would be the heat generated in the primary winding when the linear motor is energised.

Hot Spot Allowance Since a temperature sensor placed anywhere on a machine would give an indiction of the temperature at that point, it can not be assumed that all similar points would be at the same temperature. For instance, a temperature measurement somewhere on the primary winding would differ throughout a machine. In general, a 10^oC hot spot allowance is given for a standard machine.

With an ambient temperature of 40^oC and a hot spot allowance of 10^oC, a machine with a class B level of insulation would then allow a temperature rise of 80^oC.

Another factor that has to be taken into account is the different levels of insulation classes used on a single machine. Just like a chain is only as strong as its weakest link, the temperature rating of a machine is only as good as the lowest class insulation of all the different insulations used in a machine [63]. In the case of the linear motor the copper windings are covered with an Armoured Polyesterimide [62]. This has a class H insulation. However, the linear motor was dipped in varnish and then baked. The varnish used was Isonel 31 which

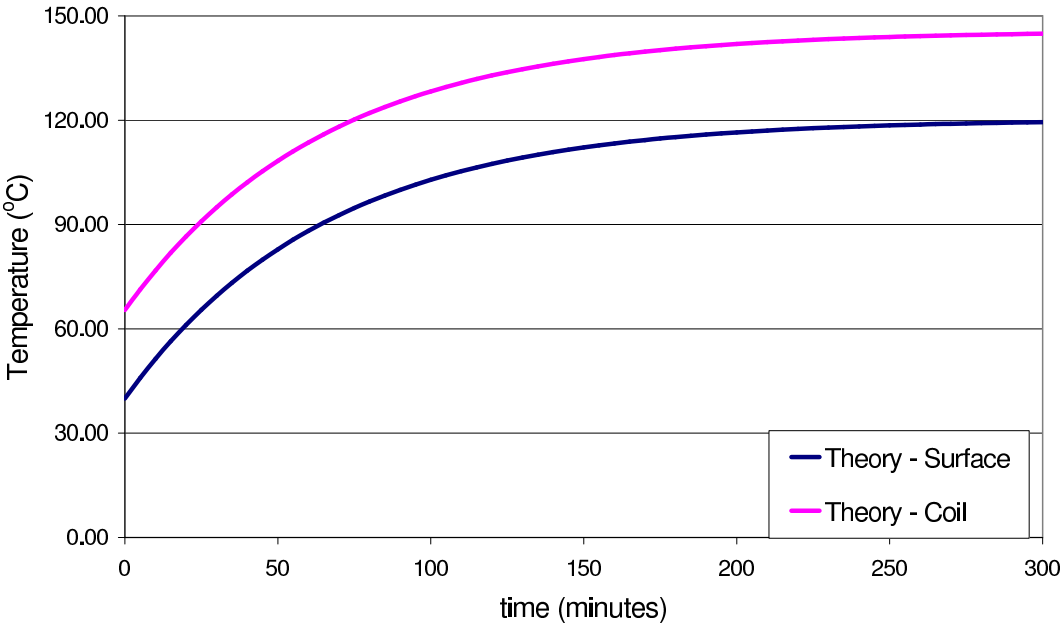


Figure 6.7: The final model of temperature rise for both the primary winding and the surface temperature. The above graphs are for the case when the linear motor has class F insulation.

has a class F insulation. So, the overall temperature rating of the linear motor is class F.

With a rating of class F, the linear motor has a maximum temperature rise of 105^oC above an ambient temperature of 40^oC. With this temperature rating, the final model for the temperature of both the primary winding and the surface of the linear motor is shown in Figure 6.7. It must be noted that a constant value for the temperature difference between the primary winding and the surface temperature has been used for the model. Thus, in Figure 6.7, the temperature of the primary winding starts above the surface temperature by a constant amount which is dependant on the value of the applied current.

The model in Figure 6.7 can be adjusted by varying the current in the primary winding. For Class F insulation, the maximum continuous allowable current that can be applied to the linear motor is $6.78A$ per coil. Alternatively, the model can be used to determine the maximum continuous current rating for each class of insulation. This is shown in Table 6.2.

Table 6.2: Continuous current ratings for each class of insulation

Class	Temperature ^oC	Current per coil (A)
Y	90	3.85
A	105	4.66
E	120	5.37
B	130	5.80
F	155	6.78
H	180	7.66
C	200	8.29

6.3 Practical Temperature Measurements

To confirm the derived model for the surface and coil temperatures, the motor was operated at two different current values. It must also be noted that the theoretical model is for constant current. During the practical tests, the current dropped slightly due to the change of the primary winding resistance with temperature. The linear motor was supplied with a constant voltage from the inverter. This was not seen as being too critical, as the current drops by a small amount of less than 8%.

For the practical tests, temperature probes connected to multimeters were placed in the primary winding and on the outer surface of the linear motor. Temperature strips were also placed on the outer surface of the linear motor to confirm the temperature reading from the temperature probe placed on the outer surface.

The following graphs are for the two heat runs conducted on the linear motor. The one test was at a current value of $5A$ (Figure 6.8) and the other at a current value of $8A$ (Figure 6.9).

The heat run for the $5A$ current level was run for five hours. It is clear from Figure 6.8 that the temperature rise measured on the outer surface of the linear motor and on the primary winding, follow that of the theoretical model.

The test at $8A$ was stopped prematurely because, owing to a previous insulation failure, it was decided not to test the linear motor near the theoretical limit of the Class F insulation. Nevertheless, the correlation achieved is good.

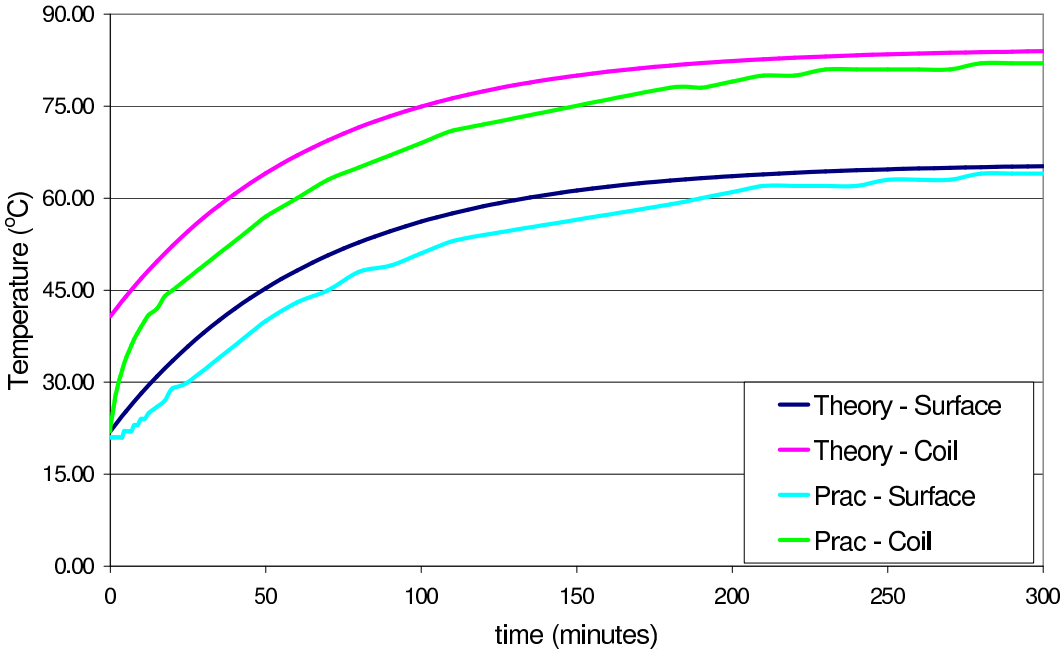


Figure 6.8: The temperature of the primary winding (coils) and the surface of the linear motor (surface) for a current level of $5A$ per coil. Both the theoretical model and practical measurements are plotted.

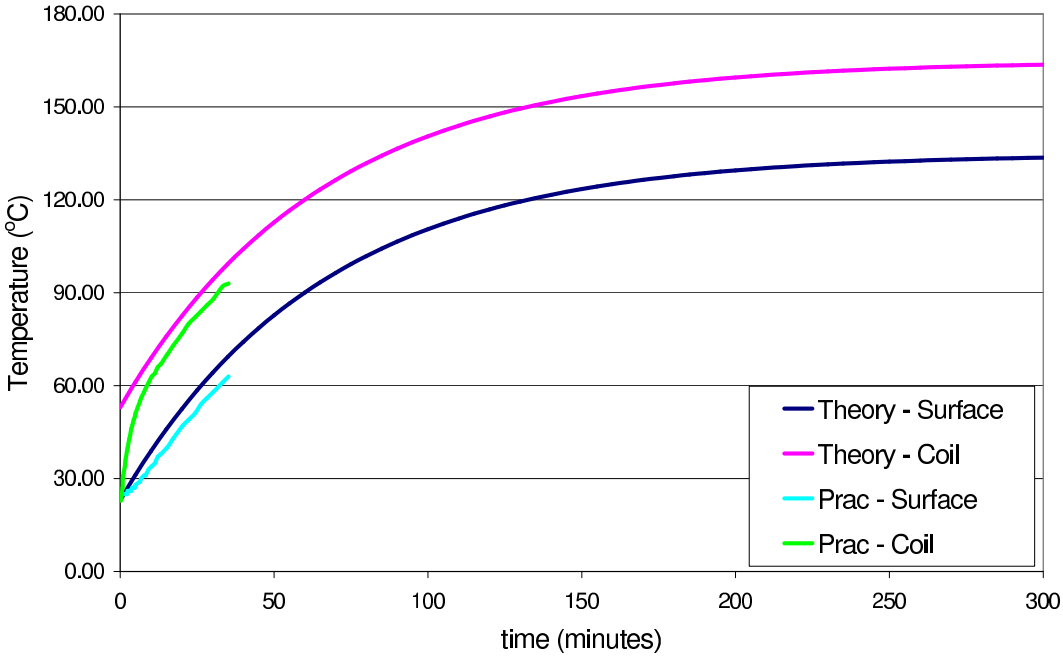


Figure 6.9: The temperature of the primary winding (coils) and the surface of the linear motor (surface) for a current level of $8A$ per coil. Both the theoretical model and practical measurements are plotted.

6.4 Temperature Effects on the $NdFeB_{N-35}$ Magnets

The temperature effects on the performance of the permanent magnets was discussed in Section 4.1.2. This section concluded that due to the location of the Pc line on the demagnetisation curves of the $NdFeB_{N-35}$ magnets, the secondary of the BMA would perform better than that of the SMMA.

For the SMMA, Figure 6.10 indicates how the force drops when the current decreases with time and the magnets heat up ('Force_Temp' are the actual points measured and 'Linear(Force_Temp)' is a linear trendline fitted to the points). The current decreases as the resistance of the primary winding increases with temperature. So the force should follow the line marked 'Force_AC_test' as these were the force measurements taken at various voltage and current levels. However, when the motor runs at a constant voltage for a period of time, the current drops due to the increase in resistance of the primary winding. Also, there is an additional drop in the thrust force due to the reduction of the flux density in the $NdFeB_{N-35}$ permanent magnets owing to the increased temperature. As discussed in Section 4.1.2 this is more severe for the SMMA.

In the BMA the problem is not as severe since the linear motor operates on a steeper Pc line on the demagnetisation curve of the $NdFeB_{N-35}$ permanent magnets. It is seen in Figure 6.11, the BMA performs better than the SMMA.

6.5 Duty Cycle

The calculations, so far, have been for the continuous operation of the linear motor. However, in a mining environment, this will not be the case. Due to the long length of the linear motor is a mine shaft, each primary section is only energised when the secondary is adjacent to it. As the lift cage will travel at a speed close to $18m/s$, each section will be energised for a few seconds at a time. The duty cycle is low, so the linear motor can be operated at higher current densities giving larger thrust forces.

Another advantage with the cage travelling at high speeds, is that an air flow will be created, providing meaningful air cooling.

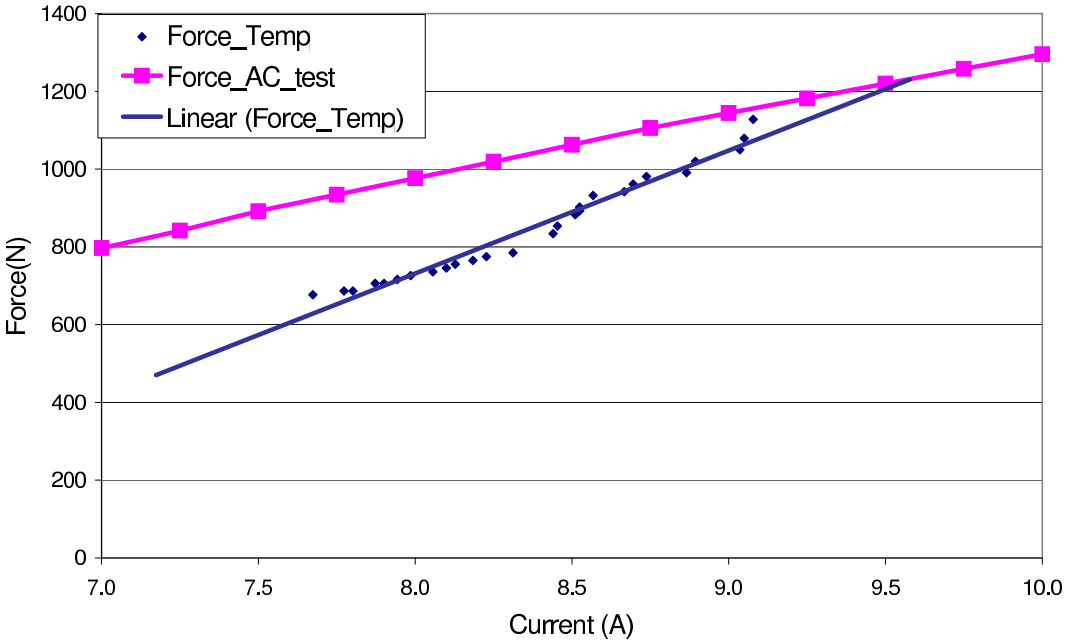


Figure 6.10: Reduction of thrust force in the SMMA due to the increase in temperature of the $NdFeB_{N-35}$ permanent magnets. The current decreases with time as the temperature of the primary winding increases.

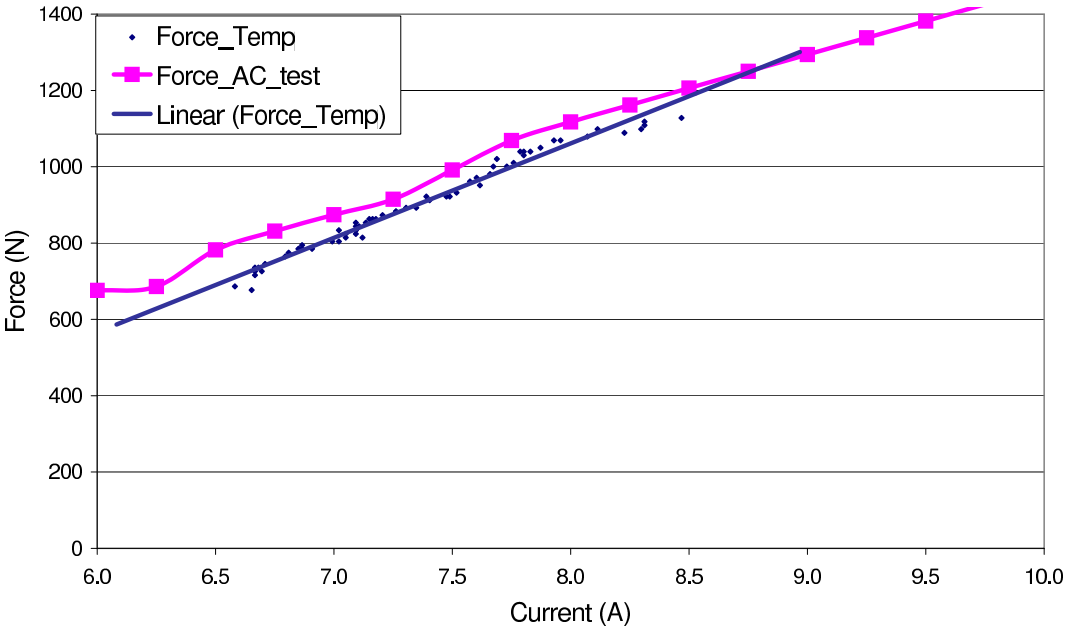


Figure 6.11: Reduction of thrust force in the BMA due to the increase in temperature of the $NdFeB_{N-35}$ permanent magnets. The current decreases with time as the temperature of the primary winding increases.

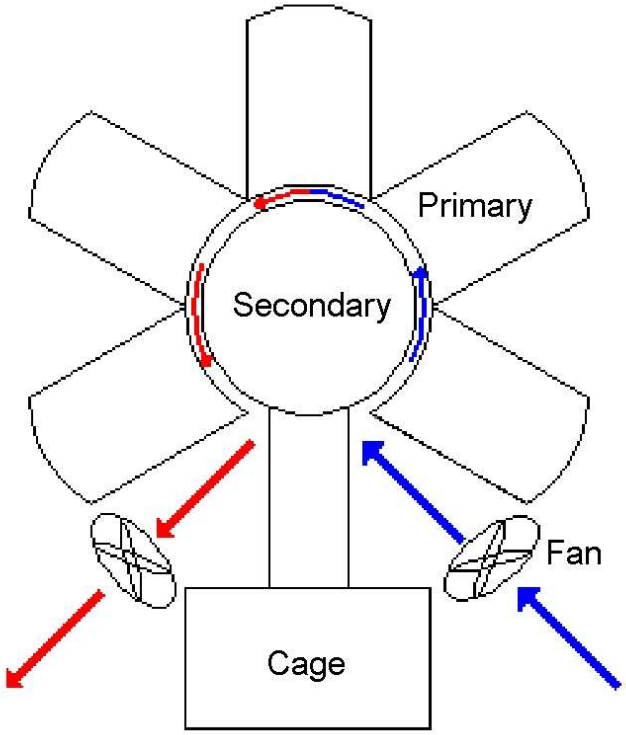


Figure 6.12: Cooling at loading bays with the use of fans.

6.6 Loading Bays

A problem could exist at the loading bays in the mine shaft, where the linear motor would have to be energised for long periods of time, while the cage is loaded or unloaded. In this case the following are possible solutions to prevent overheating of the linear motor.

1. Increase the size of the primary section at the loading bays. The primary winding diameter should be made larger to accommodate the high currents that would be necessary to produce the high holding forces required.

2. Install fans, to circulate air through the air gap (Figure 6.12). This would be essential at the loading bays as the cage is stationary and the linear motor sections are continually energised.

3. Hold the cage mechanically using kepping clamps, once it is stationary. Thus, the cage can be loaded or unloaded without having the primary sections energised.

6.7 Summary

A thermal model of the temperature on the primary winding and outer surface of the primary section was developed to determine the continuous rated current of the modified tubular LSM. Due to the low operating frequency of the LSM, the core losses were assumed to be negligible and the thermal model was developed with the primary winding as the only source of heat generation. Practical heat runs validated the thermal model and showed that the continuous rated current for the Class F insulated LSM should be $6.78A$. It was noted that for the final application that the duty cycle would be low and that the current rating could be increased, however, careful consideration must be made to cooling at the loading bays. Practical tests also showed that the performance of the permanent magnets on the BMA at higher temperatures was better compared to the SMMA. This is due to the higher permeance coefficient of the BMA as described in Chapter 4.

Chapter 7

Finite Element Modelling

In finite element modelling, the problem is broken down into very small segments instead of being solved as a whole. This allows complex problems to be split into smaller and more manageable sections. The computer package used for this project is called Maxwell, developed by Ansoft Corporation[1].

The program divides the model into a mesh of triangles. The nodes or vertices of these triangles are solved individually. If, for example, a magnetostatic problem is selected, then the program will produce magnetic field and magnetic flux density values for the nodes. The values in the area inside the triangles are solved by interpolating from the results obtained at the individual nodes. All the triangles are then combined together to give an overall result. The more triangles there are, the more accurate the solution. However, there is a trade off, as the more triangles there are, the longer it will take for the simulation to be completed.

The structure of this chapter follows the structure of the $2D$ Field Simulator of the FEM program. This is a systematic approach and the flow diagram from the $2D$ Field Simulator Manual is shown in Figure 7.1. The flow diagram shows the options and various decisions made in the set up of a general model in the FEM program.

The various models of the linear motor were simulated in a $2D$ environment. Appendix A describes how the physical model correlates with the $2D$ model drawn in FEM. This appendix verifies the use of the $2D$ FEM environment for a $3D$ object. An example of a model drawn in FEM is shown in Figure 7.2. The diagram is of a surface mounted magnet arrangement.

[1]Ansoft Corporation, Pittsburgh, USA, www.ansoft.com

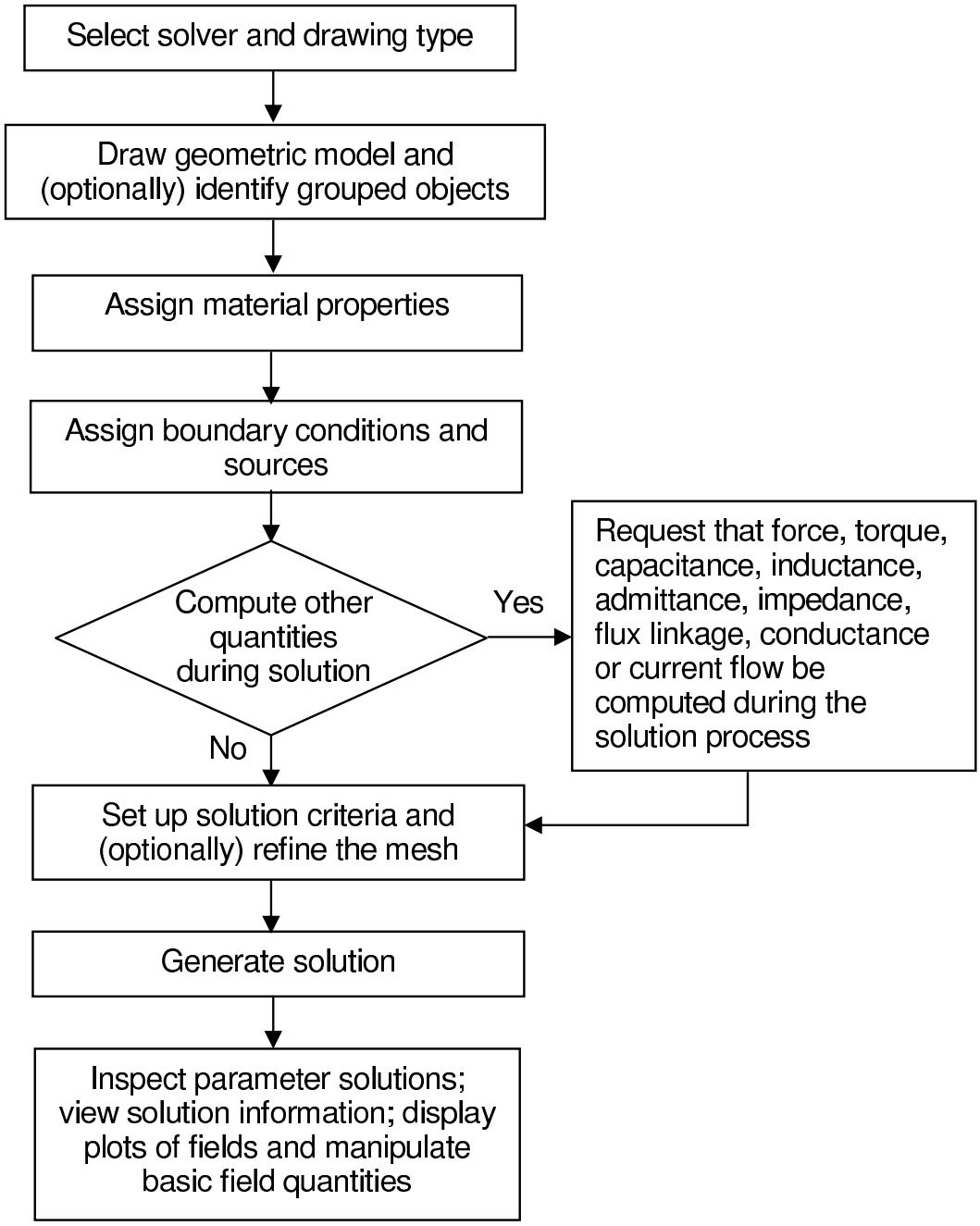


Figure 7.1: Procedure for setting up, solving and analysing a model

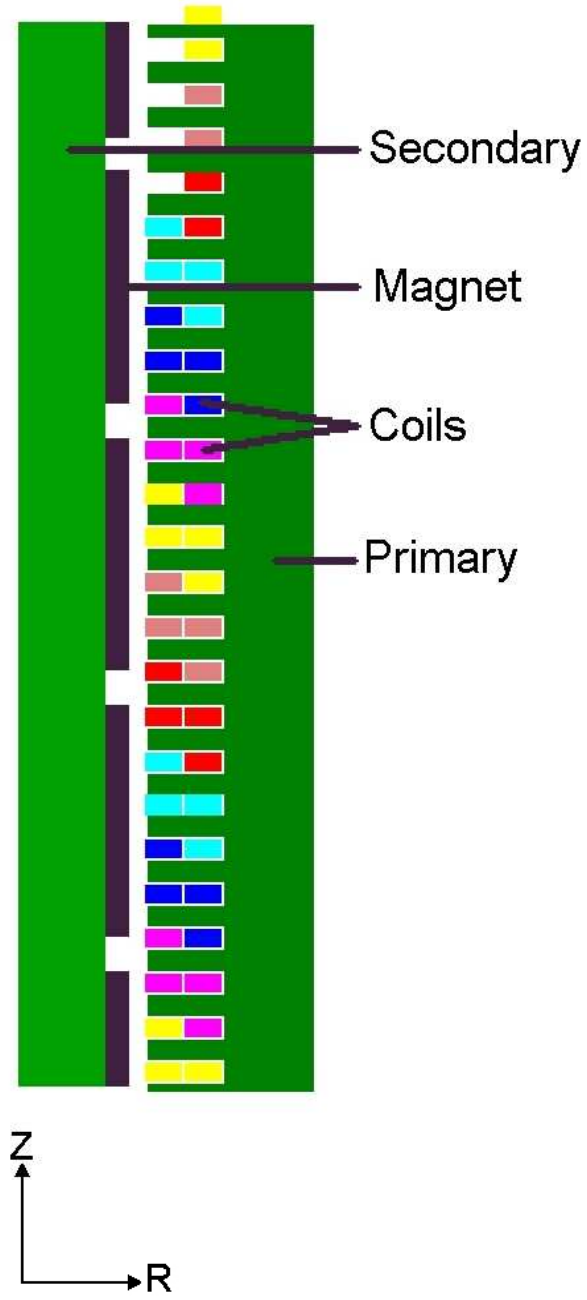


Figure 7.2: Diagram showing both the primary and secondary sections. Each set of coloured coils represents either a “go” or “return” current for one phase.

7.1 Executive Commands

In Maxwell, the Executive Commands is the main menu where the model is drawn, parameters set and the simulation is started. The menu controls the model from its inception to the point where the results can be analysed.

Solver

The solver allows the user to choose which type of simulation is required. As a force generated by the interaction of magnetic fields needs to be determined from this model, the Magnetostatic option was selected. This means that the force value calculated will be the value at one specific position at a particular time, given some current value.

Plane

The two options are the XY-plane and the RZ-plane. The required plane for this tubular motor design is the RZ-plane (See Figure 7.2). For this plane, the computer package takes the $2D$ model drawn and revolves it 360^0 around the Z-axis. This is a problem for the modified tubular design as the model is not completely cylindrical. The secondary is totally cylindrical whereas the primary is not (See Figure 1.7 and 2.1). Thus, as described in Appendix A, it was necessary to analyse the complete cylindrical LSM and then to adjust the results to account for the missing primary section.

Model Definition

There are two options for the model definition. The first is termed "Draw model" where the model geometry is defined. This is very similar to any other computer aided design (CAD) package. The model for this particular design was set up in a two dimensional plane. This simplified the drawing of the model as the modified tubular linear motor has a complex structure. The most complex part in a $3D$ model would have been to draw the windings on the primary section. With the $2D$ models the simulations times are also reduced. However, in working in the $2D$ environment, some assumptions have to be

made in the simplification of the model's geometry. Appropriate scaling of results have to be calculated and incorporated when using these assumptions. This is done in Chapter 8.

The other option is termed "Group Objects". This allows the user to group objects of similar materials as well as objects which have the same boundary or source conditions. This is done if there is a considerable number of objects which share the same properties. This then reduces the time it takes to assign materials and boundary/source conditions to various objects. The need to group objects in this way, was for the coils only. For each phase, both "go" and "return" conductor were grouped together and an appropriate name was given to that group.

Setup Materials

This allows each object or grouped object to be assigned a particular material. A library of materials is already built into the program and if a material does not appear, that material can be created by defining its properties. It was found that the material library was adequate for the purpose of the design. The magnets were assigned to be $NdFeB_{35}$, which is the same magnet material used in the practical model. The primary section and the steel part of the secondary were assigned 'Steel 1010'. This steel is not the same as the material used in the model, but its B-H characteristic is that of a general mild steel, and is sufficient for this project. The reason for this is that the reluctance of the magnetic circuit is dominated by the large air gap and the reluctance due to the steel is negligible. The B-H curve of the material 'Steel 1010' can be seen in Figure 7.3. Copper was assigned to all the coil groups. The background to the drawing and the reference block (described later and shown in Figure 7.4) were specified as a vacuum.

Setup Boundary/Sources

The user can define any boundaries and designate any value to that boundary. The value is the magnetic vector potential along that boundary and is given in Webers. Either a function or a constant value can be allocated to this boundary. Any objects or grouped objects can have a current source assigned.

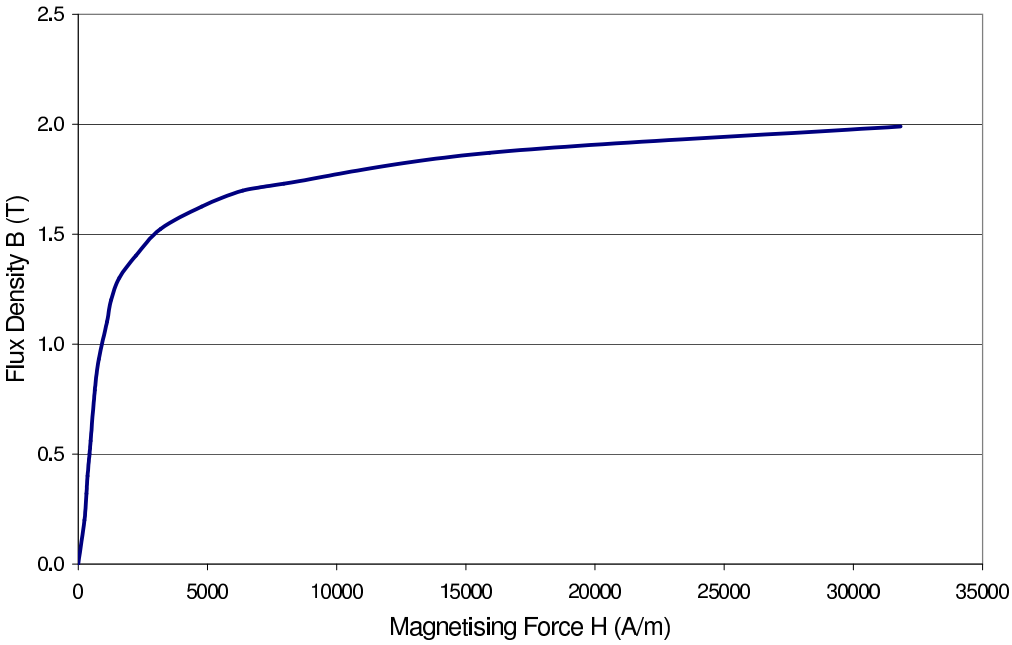


Figure 7.3: B-H curve for 'Steel 1010'.

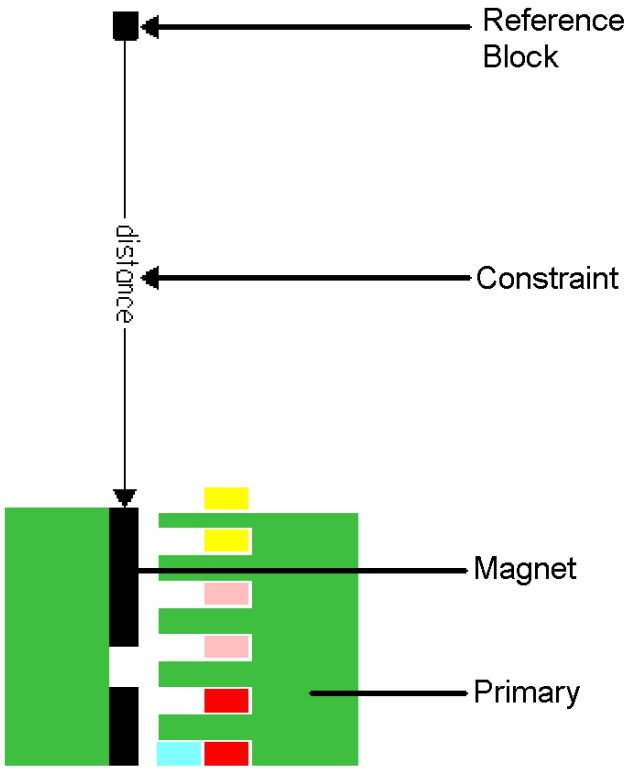


Figure 7.4: Diagram showing the reference block and constraint.

The outer limits of a drawing plane are the limits for that model. It is this boundary that has a zero vector potential assigned to it, to contain the associated energy of the model within that boundary. This means that flux is prohibited from crossing the boundary. Usually this boundary is lumped together as a "balloon" as the whole model is contained within a rectangle. However, for a model in the RZ-plane it is different. The model is revolved around the Z-axis. Even though this model will be symmetrical and theoretically will have no flux passing through the Z-axis, there is still the possibility of having an imbalance in the distribution of flux through the model. This imbalance might mean that some flux will pass through the Z-axis. It is for this reason that the Maxwell simulator ignores the "balloon" boundary on the left side. The simulator models that edge as an axis of rotational symmetry. This will allow the model to be a continuous structure. The computer package assigns the other three sides of the "balloon" boundary as having a zero vector potential.

As this is a magnetostatic problem, the current values will be set values. Essentially, a DC current will be assigned to each of the coil groups. This can be done in two ways. Firstly, the current value for the coils can be entered in as a current density. Alternatively, the current can be entered in as a total current value for the total cross-sectional area of the coil group. The latter option was chosen.

The modified tubular LSM will, however, have an AC current supplied to its windings. As this is a static model and can only be solved for the one position at that one instant in time, an instantaneous current value must be entered for each phase group. Instantaneous values at any point in time can be taken. For convenience, phase a is taken at its maximum value, so the other two phases will be half the magnitude and negative.

In the FEM models there are 14 coils for each phase. There are 14 "go" coil sides and 14 "return" coil sides. Each coil has 45 turns with two parallel wires for each turn. The value for the total current in phase a is the peak value of the sinusoidal current waveform. Thus, a factor of $\sqrt{2}$ must be included as the current value of $12A$ (150% of rated current), used for the simulations, is the rms value.

Therefore, the assigned ampere-turns per coil side for phase a is:

$$= \sqrt{2} \times 12 \times 45 = 764 \quad \text{Ampere-turns / coil side} \tag{7.1}$$

The assigned ampere-turns per coil side for phases b and c is:

$$= -\left(\frac{1}{2}\right) \times \sqrt{2} \times 12 \times 45 = -382 \quad \text{Ampere-turns / coil side} \tag{7.2}$$

The inverse or return conductors for each phase will have the same magnitudes but will be of opposite sign.

Setup Executive Parameters

In this drop-down menu, there are options for calculating various parameters of the model. Only two are relevant for this project. The first and more important is the "Force" calculation. Here the user selects the objects and/or grouped objects for which the force acting on them will be calculated.

The other is the "Flux linkage". This calculates the flux passing through a predetermined area. The user defines a line in the $2D$ environment. This line is revolved around the Z-axis to form an area (A hollow tube around the Z-axis). During the simulation the total amount of flux passing through that area is calculated. The flux value given is the total magnitude of the normal component of flux passing through the area. This is useful to determine the flux density in the air gap between the primary and secondary sections.

Setup Solution

This sets up the solution parameters for the simulation. The first consideration is that of the finite element mesh. This can either be automatically generated by the program itself or a manual mesh can be set up depending on the needs of the user. Generally, the automatically generated mesh is sufficient. However, the user must be aware of specific areas in the model that might require a greater degree of accuracy and would need a manual mesh.

The other consideration is the "Variables". This is an option which allows the model to be solved for different object positions. An example is to see the effects of the force on the secondary as it moves relative to the magnetic field generated by the primary winding. Since the program can only solve static problems, it then solves $\boldsymbol{n}$ cases for $\boldsymbol{n}$ different positions.

The Mesh

Firstly, it is necessary to understand how the mesh is created and how the computer program decides to refine the mesh in subsequent iterations. Initially, the program sets up a mesh along the lines of the model's geometry. This is a very rough mesh, and probably not close to the optimum mesh required, but it's a starting point. The program calculates the magnetic field at particular points in the geometry. These points are the nodes or vertices of the triangles in the mesh. The magnetic field in the rest of the triangle is then calculated by interpolation from the nodes. If the triangles are too big, then the magnetic field at any point inside will not be accurately interpolated. This means that the percentage energy error between triangles will be large. The magnitude of this percentage error will depend on the magnitude of the energy in that area. So areas of high energy, generally tend to have a high percentage energy error, on the first iteration. The program then refines the mesh, concentrating on these areas of high energy. The mesh is refined until the solution has converged. Convergence occurs once the percentage energy and delta errors (Delta error is the percentage error change between refinements) have dropped below their stipulated values. The defaulted percentage energy error limit is 1%, which is sufficiently accurate. If this limit is reduced for more accurate solutions, the computational time for the solution would increase.

Figure 7.5 shows the secondary and the corresponding part of the primary for a mesh of 7224 triangles for the whole model. The figure does not show the whole model and all the triangles, but just a portion of the model. More importantly is shows the density of the triangles. For the force calculations of the model during the "Variables Solution" simulation, each solution and position had between 7000 and 10000 triangles. The "Variables" will be discussed in the next section.

The problem with the iterative process of mesh refinement, is that the program may not refine the mesh sufficiently in areas of low energy, because the percentage energy error is relatively low. Another problem is areas of drastic change in magnetic field strength. These are found at boundaries where materials of different permeability meet. This commonly occurs at the air gap in electric machine models. The user must make sure that in these areas there are at least three or more triangles spanning the air gap. This should be enough to generate an accurate solution for the air gap. It was found for this project,

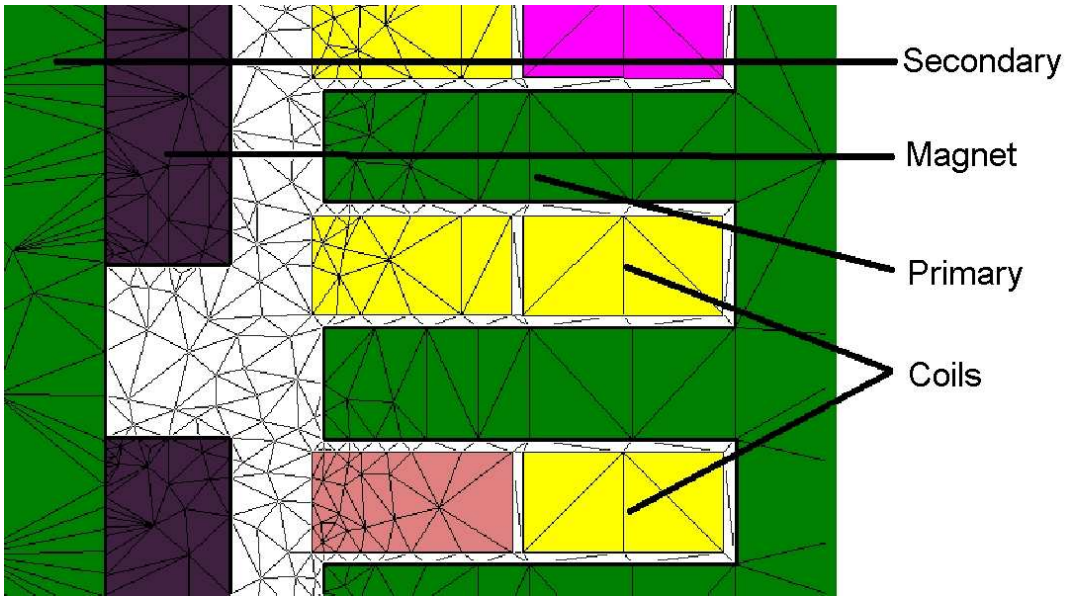


Figure 7.5: A close up showing sufficient number of triangles in the air gap for a model with 7224 triangles.

that the mesh generated automatically by the program was sufficient. The reason for this, is that this model has a relatively large air gap. The air gap in this model is $12.5mm$, which is larger than the normal air gaps for rotary motors.

Variables

In the magnetostatic option, any simulation is a static solution. Also the parameters during the setup of the model are static. The two dynamic quantities of the physical model are the current and the mobile secondary. The current setup has already been described earlier in this chapter. Now with the current values set, the associated MMF wave developed by the primary coils is also static. The unknown quantity here is the position of the secondary where the maximum force is developed for that particular MMF distribution. In order to find this position, it is necessary to run a number of simulations for different positions.

These positions are chosen by varying a constraint which has been assigned to the model. Constraints are assigned in the drawing phase. A reference block is constructed and a line is drawn from the reference block to the secondary. This line is the constraint in Figure 7.4. The reference block is then held stationary,

and the secondary is moved into different positions by changing the magnitude of the constraint. The program then produces solutions for each position as it sweeps through the variables. The line drawn must be parallel to the direction of the movement.

Once the simulation has gone through all the variables or positions, the force values can then be plotted against their respective positions. This should give a sinusoidal graph. The maximum force generated by the modified tubular LSM occurs at the peak value.

Solve

Once the model has been drawn and the parameters set, the problem can now be solved. In this menu option the simulation can begin for either the "Nominal Problem" or the "Variables". The "Nominal Problem" simulation will produce a solution for the model in the exact way that it has been drawn in the "Draw Model" phase. This is particularly useful, as for that position, the flux distribution passing through any defined line can be plotted. The "Variables" option initiates the simulation to obtain solutions for various positions as described in the previous section.

Post Processor

Finally, once the simulations have been completed the results can be analysed. There are various tools available here in the Post Processor to completely analyse any "Nominal Problem" and/or "Variables". For example, the magnetic fields and magnetic flux densities in the model can be analysed. The force plots for various positions can also be viewed.

7.2 Summary

The processes used during the finite element modelling stage of the project are described in a step by step approach through the complete setup and simulation of a model. The approach starts at the drawing of the model and the parameter setup options required for this particular model. The required

output options of force and flux quantities are chosen during the setup so that these calculations can be performed during the simulation. The meshing process was described in detail and presents the outcomes produced during the simulation part of the program.

Chapter 8

Results

For any study or investigation, there should be a practical evaluation to verify the theoretical predictions. In this case, performance testing on the modified tubular linear synchronous motor has been done to verify the FEM solutions. This chapter will describe the testing procedure and gives the correlation between the measured performance and that of the FEM evaluation for both SMMA and BMA.

8.1 Predicted Forces Using FEM

As described in Section 7.1, the predicted maximum force for a given current is determined by sweeping the secondary through a range of positions. The position of this maximum force is then recorded. This was done for both the SMMA and BMA. An example is shown in Figure 8.1 which is for the SMMA at a current of $12A$ per coil. The abscissa is the distance in millimetres between the stationary reference block and the secondary section. The starting position of the secondary is $200mm$ from the reference block. It is then swept through a range of positions until it is $400mm$ from the reference block.

From the graph in Figure 8.1, the positions of maximum force (in magnitude) are located at $275mm$ and $389mm$. These points are $114mm$ apart, the distance of one pole pitch, as expected. Once the point of maximum force is determined, simulations are then performed at this one position. A range of currents from $1A - 14A$ (rms) per coil were investigated and the corresponding forces determined.

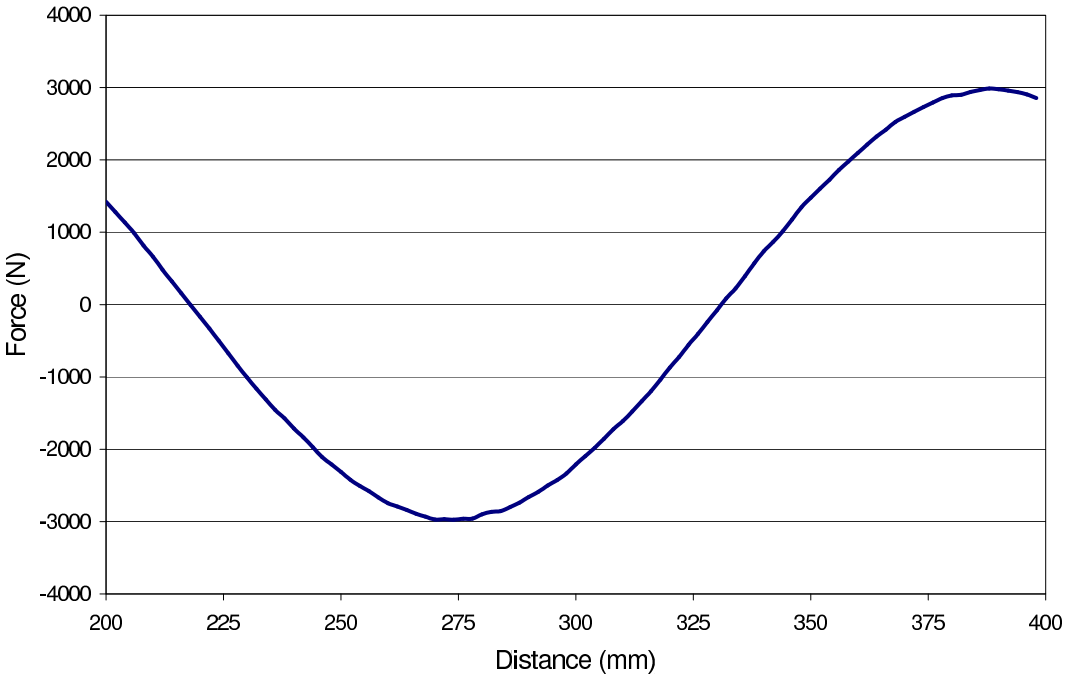


Figure 8.1: The graph of the force versus position of the secondary relative to the reference block for a current with the value of $12A(rms)$ per coil in the SMMA

The FEM solutions assume a completely tubular linear motor, therefore, the results have to be scaled accordingly. Since the actual design of the modified linear motor only covers 300^0 of a complete circle, the results have to be scaled by a factor of $\frac{5}{6}$. This is done on the assumption that there will be no fringing effects. The predicted force vs. current graphs for both the SMMA and BMA are shown in Figure 8.2. This is the theoretically predicted performance of both the secondary sections of the linear motor.

8.2 Testing Procedure

Another assumption made in the FEM solutions is that there is no friction in the guidance system. Therefore, a testing procedure had to be developed to determine the thrust force by itself without the effect of friction.

For this, two tests were performed. The one test is an AC test, the other a DC test. To ensure the same magnetic state existed for both the AC and DC tests, the magnitude of the peak flux density generated by the stator coils in the air gap for the two respective tests, had to be the same. A gaussmeter was

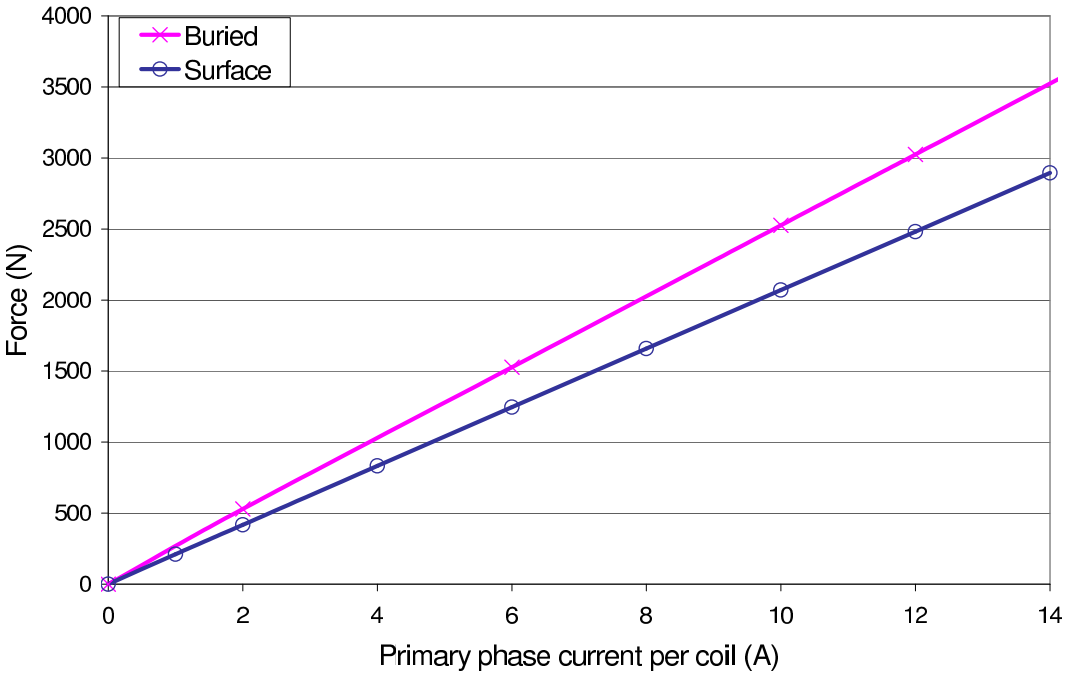


Figure 8.2: The FEM predicted force versus the rms current applied to each coil

used for this verification.

First, a DC current was supplied to the primary windings, as described in Section 7.1. A probe connected to the gaussmeter was then placed in the position of maximum air gap flux density for that particular current. This was easily found as the DC current in the primary windings produces a static magnetic flux density wave. The probe is then fixed in that position. It must be noted that this was a comparative measurement so when the corresponding AC current was supplied, the gaussmeter had to produce the same magnitude of maximum flux density.

The RMS value of the AC current used in the AC current test was the same as the value of the DC current. A frequency of $0.5Hz$ was used for the AC current test. With this low frequency, the variations on the gaussmeter could be easily monitored by the human eye. The results of this experiment are shown in Figure 8.3. These results verify that the same flux density was achieved in the AC and DC case.

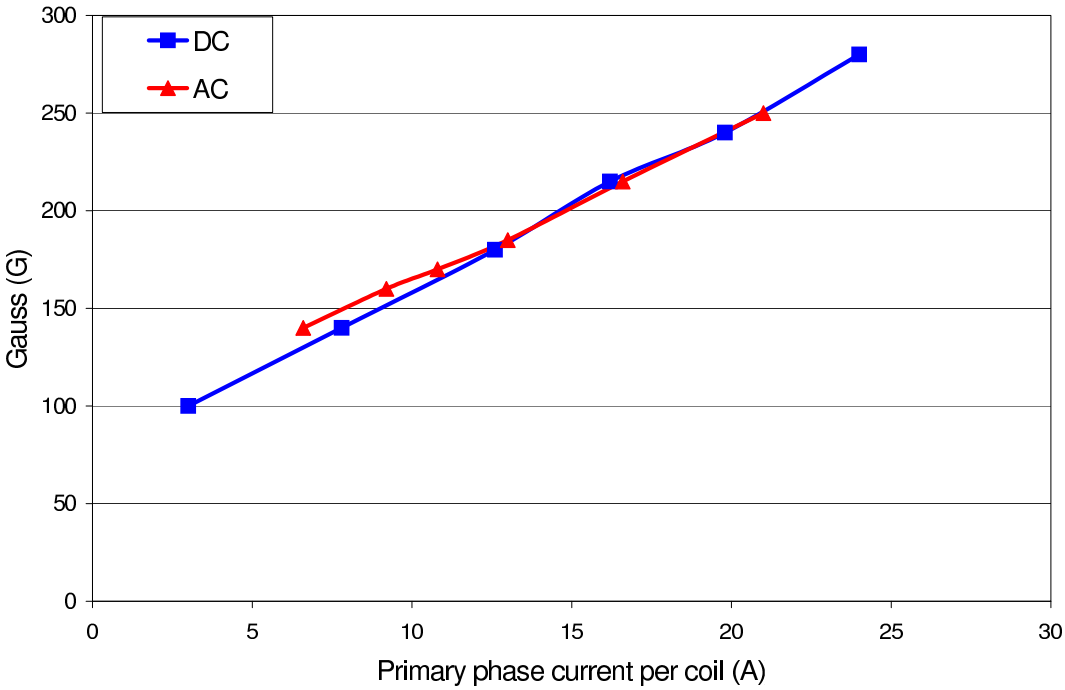


Figure 8.3: The maximum air gap flux densities for a given probe position for the AC and DC tests

8.2.1 AC test

This test determined the maximum weight the linear motor could lift with an AC current flowing through the windings. A measuring scale was attached to the moving secondary, with the other end of the scale attached via an elastic rope to the floor of the test bed (Figure 8.4).

The reason for the elastic rope is that the developed force would increase slowly as the secondary ascends. The secondary will ascend until it reaches a point of maximum force (load angle is at 90^o), where it will then slip a pole. This can be a relatively violent action and the secondary and/or measurement scale can be damaged. The elastic rope helps to dampen this effect.

The scale then measures the maximum thrust force that the linear motor can generate with the motor overcoming the weight of the secondary as well as the friction from the guidance system. The weight of the secondary includes the active material as well as the material used for the guidance of the secondary section. This is represented in Figure 8.5 and may be expressed as:



Figure 8.4: AC test with the scale attached between the secondary and the floor of the test bed

$$\text{Scale Reading (AC test)} = F_T - F_w - F_f \tag{8.1}$$

- F_T = thrust Force
- F_w = weight of Secondary
- F_f = friction (of the guidance system)

8.2.2 DC test

For the DC tests, one phase is connected to the positive terminal of the supply, and the other two phases are connected to the negative terminal. This simulates an instantaneous point in time of a three phase AC supply. In other words, phase A will be at its peak, and phases B and C will be negative and half the magnitude. This is the same principle used in section 7.1 for the FEA solutions. The DC test sets up a static MMF wave in the air gap.

As described earlier, in the FEM simulations, a DC current was supplied to the

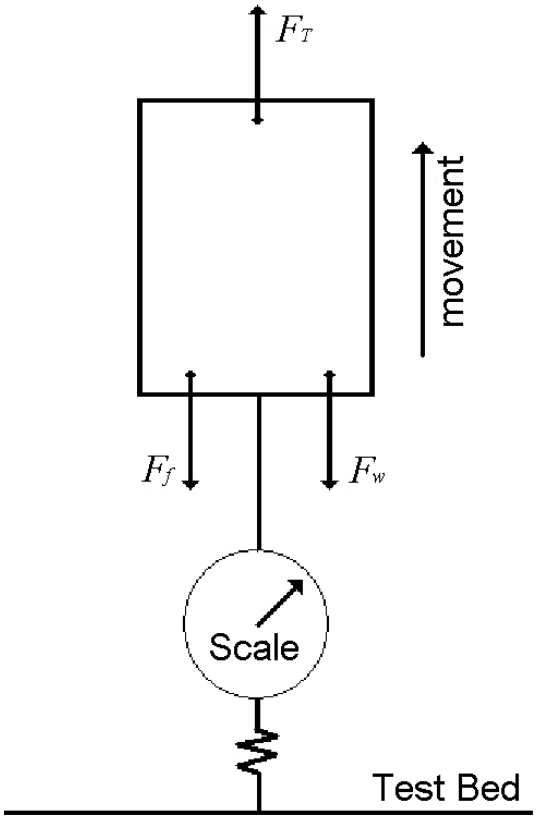


Figure 8.5: Graphical representation of the AC test

coils and the secondary was moved through a range of points to determine the position and magnitude of the maximum thrust force generated. This same principle is applied in practice for the DC tests.

In this test the scale is attached to the secondary section and suspended from an overhead crane. The DC voltage is supplied to the coils. This sets up the static MMF wave in the LSM. The scale is then lifted by the crane and the secondary is then pulled through the static MMF wave. The scale will read a maximum value when the load angle is at 90^0. The scale measures the maximum thrust force that the linear motor can generate at that position as well as the weight of the secondary and the friction from the guidance system. This is represented in Figure 8.6 and may be expressed as:

$$\text{Scale reading (DC test)} \quad = \quad F_T + F_w + F_f \tag{8.2}$$

If equations 8.1 and 8.2 are added together, the maximum thrust force that the linear motor generates is given by the simplified equation:

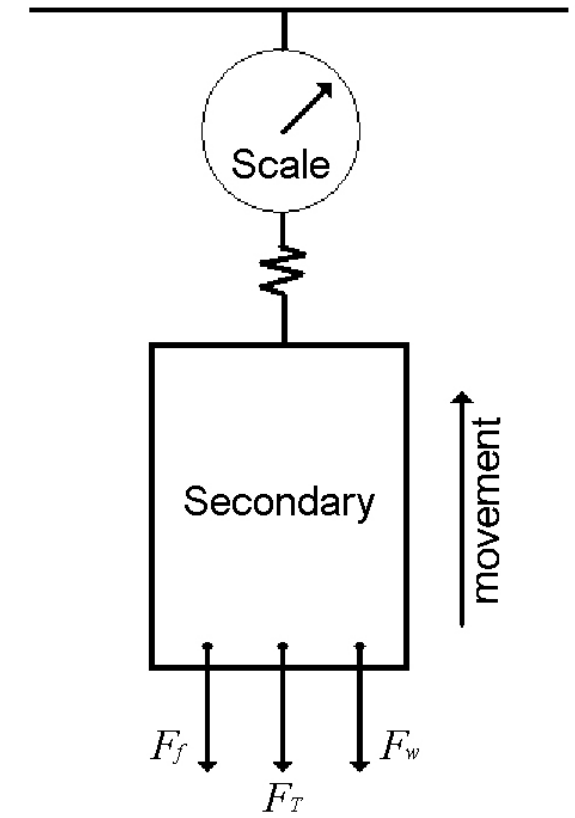


Figure 8.6: Graphical representation of the DC test

$$F_T = \frac{\text{Scale reading (AC test)} + \text{Scale reading (DC test)}}{2} \qquad (8.3)$$

8.3 Discussion of Results

Figures 8.7 and 8.8 show the results achieved for the SMMA and BMA secondaries respectively. Each set of results shows:

- The scale reading for the AC test

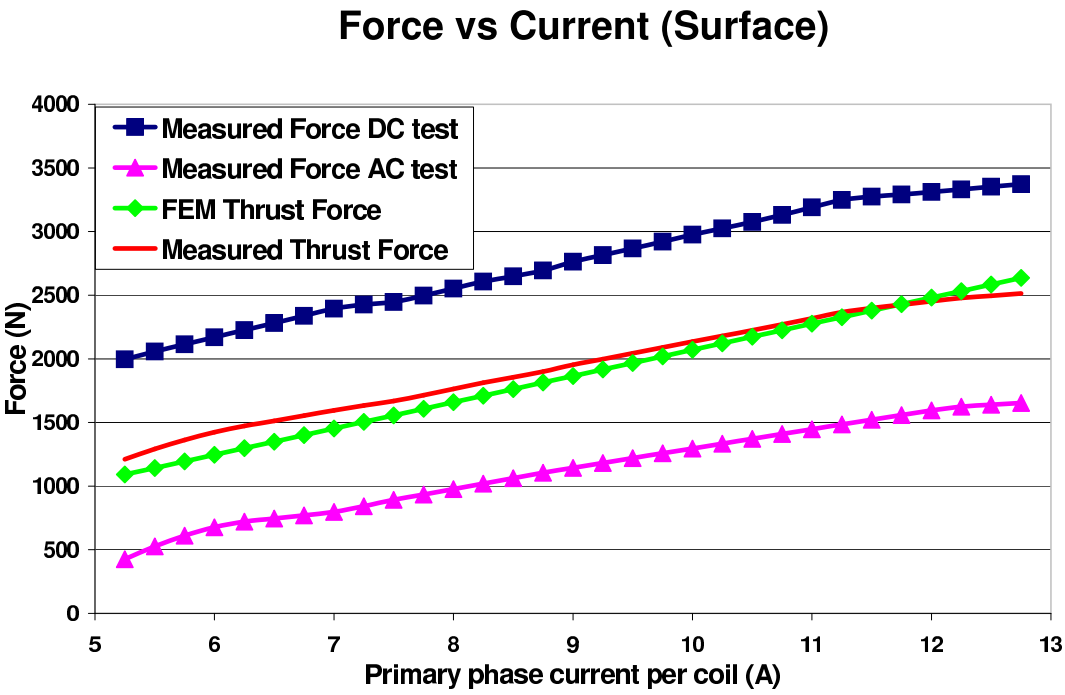


Figure 8.7: Measured and predicted forces for the surface mounted magnet arrangement

- The scale reading for the DC test
- The FEM thrust force solutions (predicted force)
- The resultant thrust force from equation 8.3 (measured force)

The correlation achieved between the predicted and measured results for the thrust force developed is very good, particularly for the BMA. For the SMMA, the measured thrust force is an average of 6.5% greater than the predicted thrust force. For the BMA, the measured thrust force is an average of 1.5% greater than the predicted thrust force. The slight discrepancies between the measured and predicted results may be due to the friction force, F_f, not being exactly the same between the DC and AC tests as described in Appendix E. (This is yet another verification that FEA can be used successfully as a design and an analytical tool.)

Further investigation of the two graphs shows that there is some saturation occurring in the practical tests for higher currents. This is due to the fact that the practical model has less steel in the primary section than the FEM model, as described in Appendix A. This is not seen as a problem, as the saturation

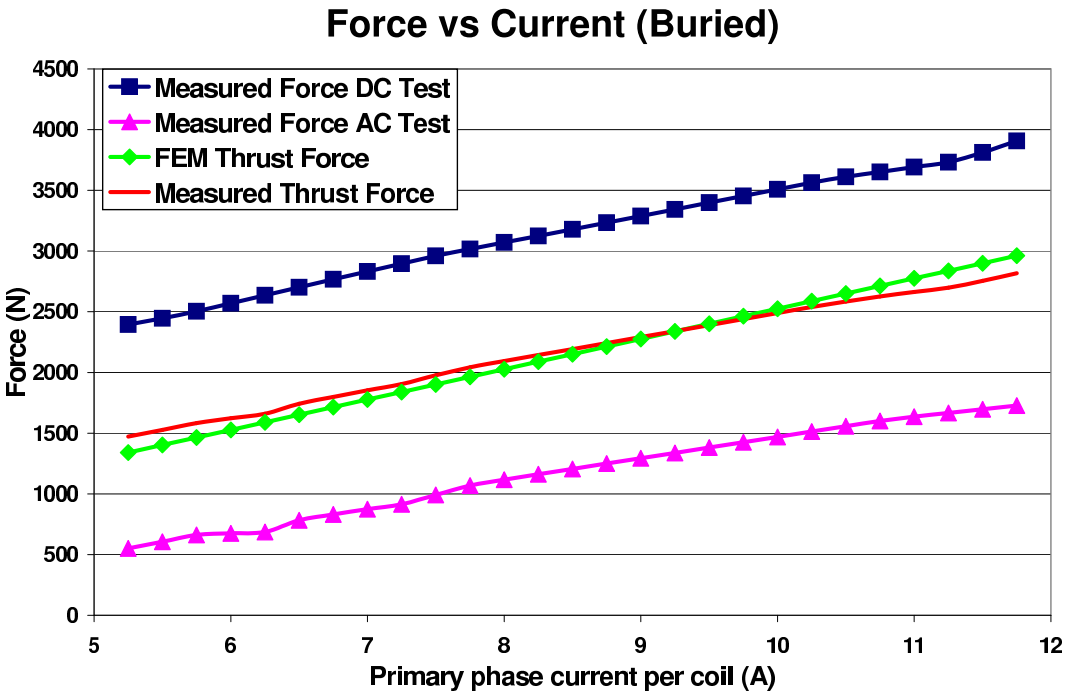


Figure 8.8: Measured and predicted forces for the buried magnet arrangement

occurs at current values approximately 50% higher than the rated value of $8A$ per coil.

The fundamental input voltage and current waveforms from the inverter were recorded during the force measurements for the AC tests. Six of these waveforms are shown for each magnet arrangement in Appendix F. The glitch in the current waveforms was due to the secondary slipping a pole once the maximum force was attained and would occur once every cycle. As the amplitude of the current is increased, the force increases and the secondary travels a little bit further each time before it slips a pole. This is indicated with the glitch occurring further down the waveform as the current is increased. The extra distance travelled each time can be determined as the speed is known and time differences can be measured.

The predicted and measured thrust force vs. current characteristics for the two magnet arrangements are shown in Figures 8.9 and 8.10 respectively. It is seen that the BMA structure produces a greater thrust force for all values of input current. For the predicted thrust force, the BMA produces an average of 22% more thrust force than the SMMA. For the measured results, the BMA produces and average of 17% more thrust force than the SMMA.

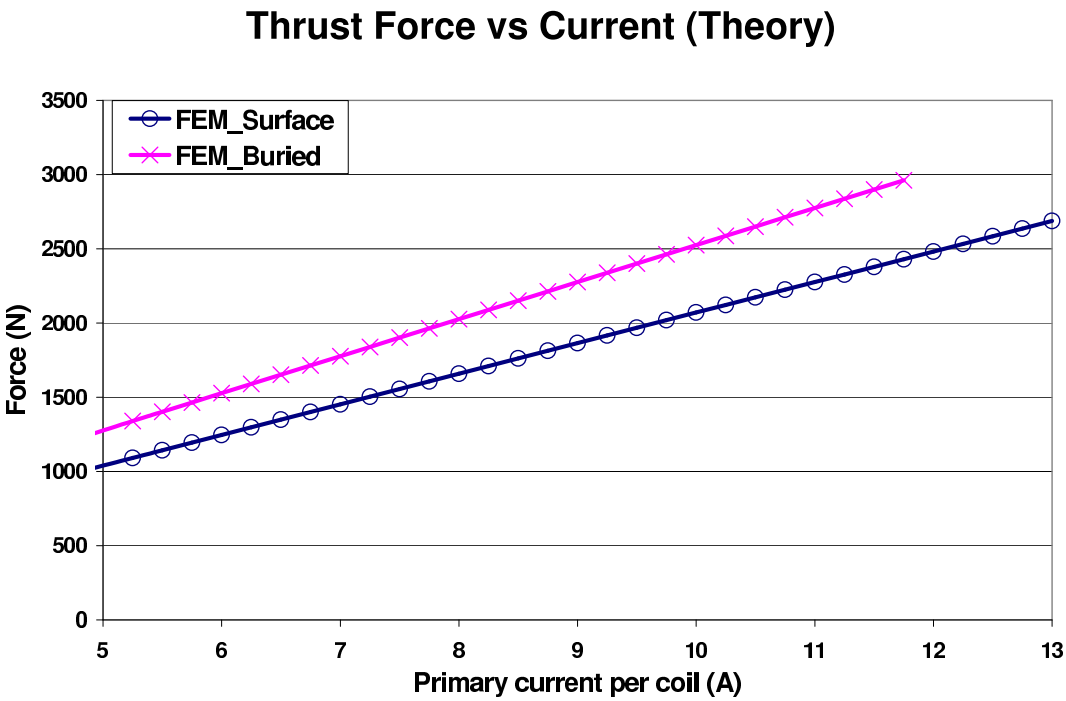


Figure 8.9: Predicted thrust forces for both magnet arrangements

Again, the 5% discrepancy may be due to the friction force not being exactly the same between the DC and AC tests as described in Appendix E. The greater thrust forces produced by the BMA was expected and verifies the conclusions drawn in Section 4.2. The Force to Weight Ratios (FWR's) described in section 1.1.4, were calculated because the mass of the active material in the secondary was known (The masses for the SMMA and BMA are $23.62kg$ and $24.78kg$ respectively.). The FWR's, as a function of the input current, are shown in Figures 8.11 and 8.12. These graphs are similar in form to Figures 8.9 and 8.10 as the two masses of the magnet arrangements are almost the same.

A comparison of the forces produced by each magnet arrangement for the AC and DC tests are shown in Figures 8.13 and 8.14. These graphs show that the forces in the AC test were similar but the forces produced by the BMA in the DC test are a lot higher. This suggests that the friction component for the BMA was a lot higher compared to the SMMA. This could be due the alignment of the BMA not being as accurate as the SMMA. Since the radial forces are uneven in the linear motor, any slight misalignment can cause greater friction with the guidance system of the secondary section. The friction also increased with current as the imbalanced radial force increases with current.

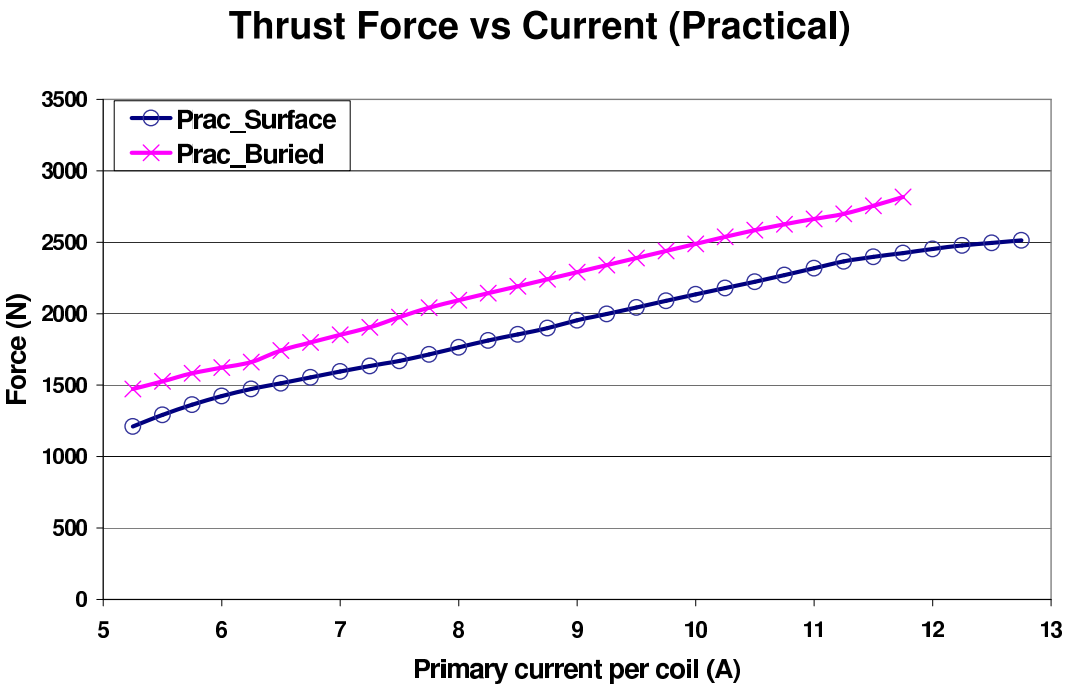


Figure 8.10: Measured thrust forces for both magnet arrangements

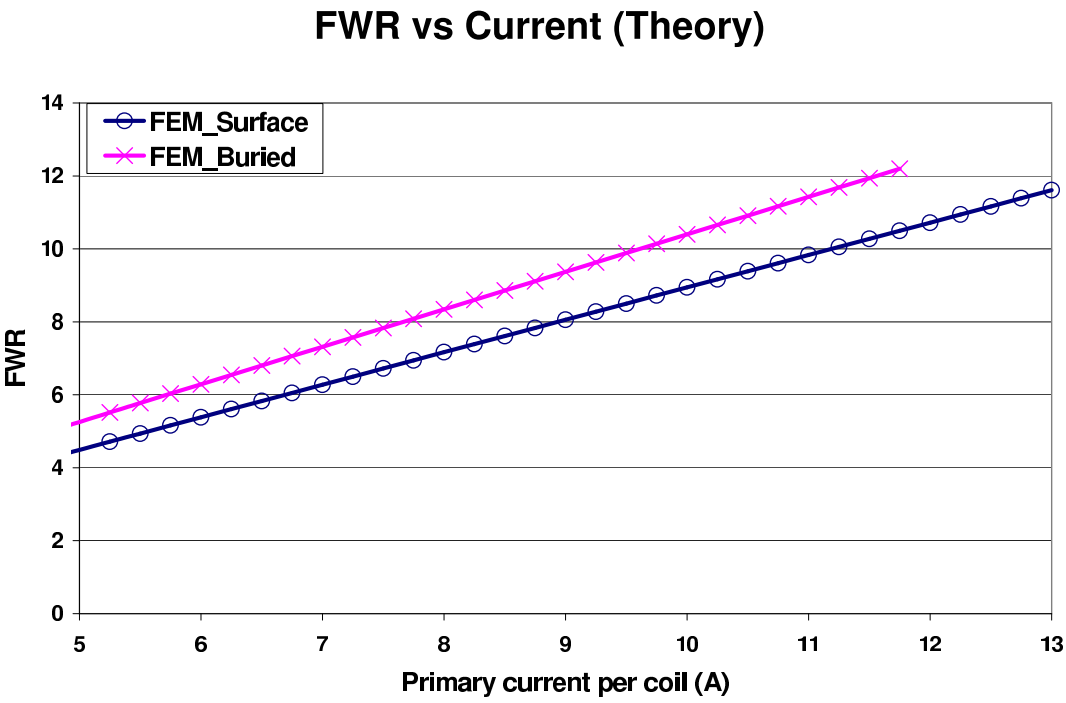


Figure 8.11: Predicted FWRs for both magnet arrangements

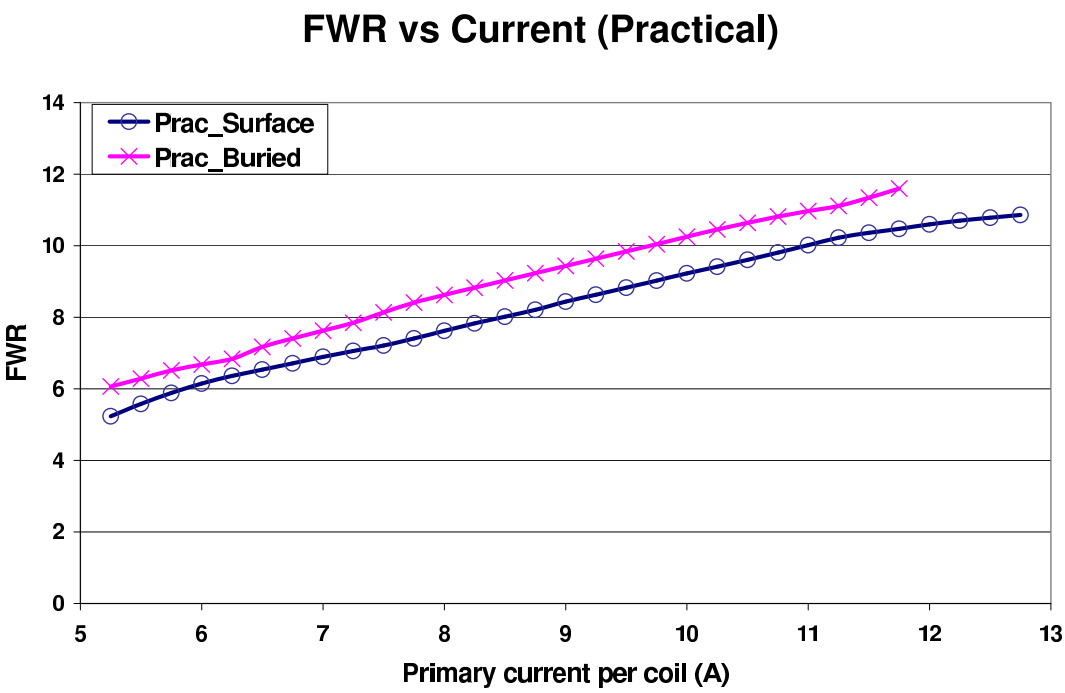


Figure 8.12: Measured FWRs for both magnet arrangements

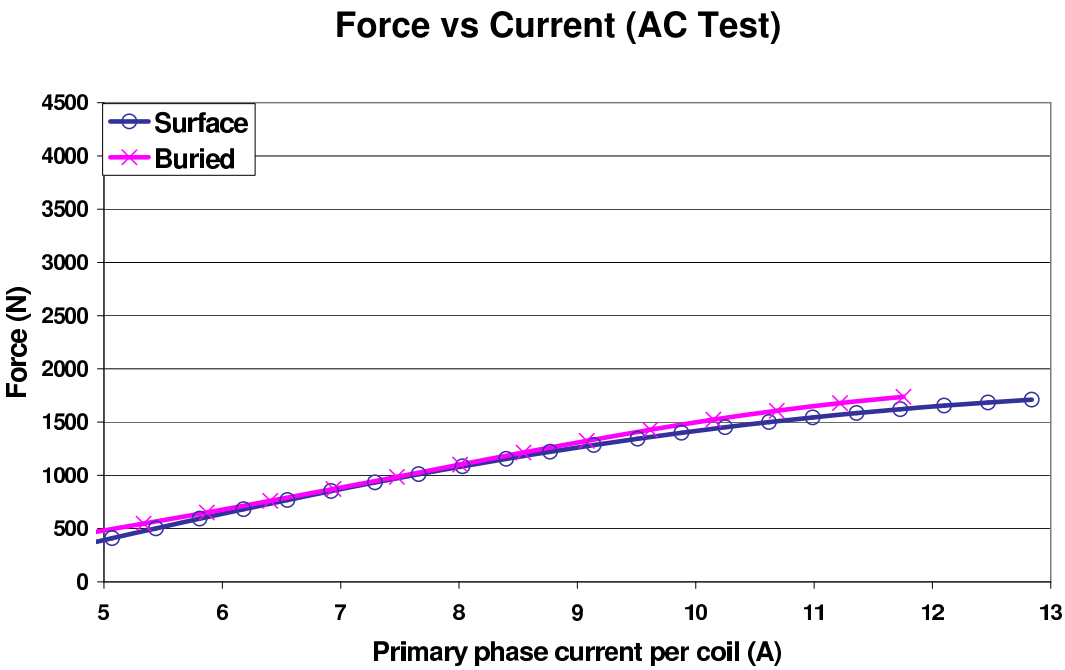


Figure 8.13: Forces measured during the AC tests for both magnet arrangements

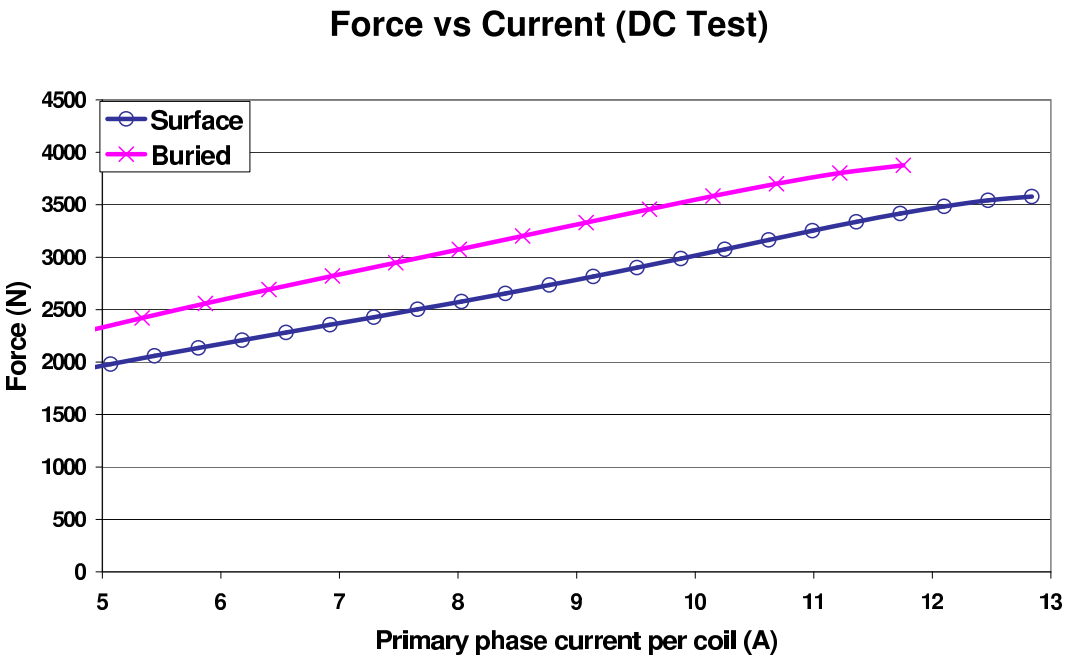


Figure 8.14: Forces measured during the DC tests for both magnet arrangements

The performance of any machine is generally evaluated in terms of its output power and efficiency. Firstly, the output power can be determined by the following equation:

$$P_{out} = force \times speed \tag{8.4}$$

The force in Equation 8.4 is the force generated by the linear motor less the weight of the conveyance and friction of the guidance system. In other words, the force measured during the AC tests. This output power is shown in Figure 8.15, while the input power is shown in Figure 8.16. The output is very low as the speed of the secondary is only $0.114m/s$. Thus, most of the input power to the linear motor is lost as heat and the overall efficiency of the linear motor is between $3\% - 5\%$. The efficiency reduces as the input current increases since the copper losses are proportional to the current squared. This trend can be seen in Figure 8.16. Figure 8.17 shows the force vs. input power graph. This graph is relatively linear with the force tapering off slightly at the higher input powers, again, due to the increase in copper losses (Current increases with increasing input power).

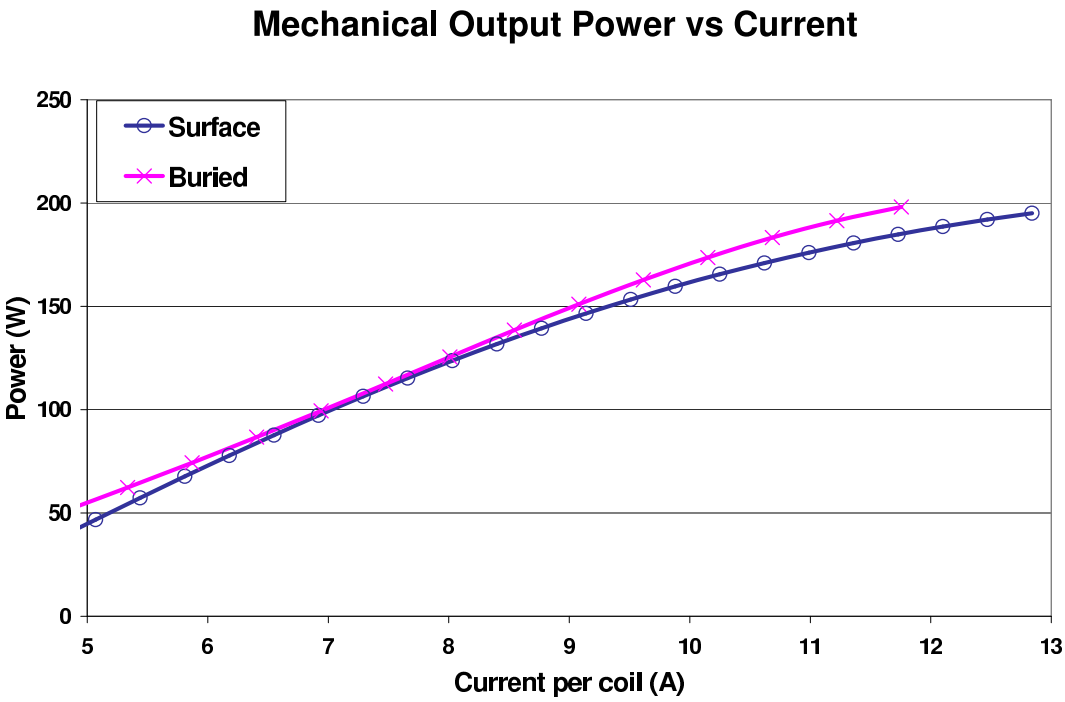


Figure 8.15: Mechanical output power of the modified tubular linear synchronous motor

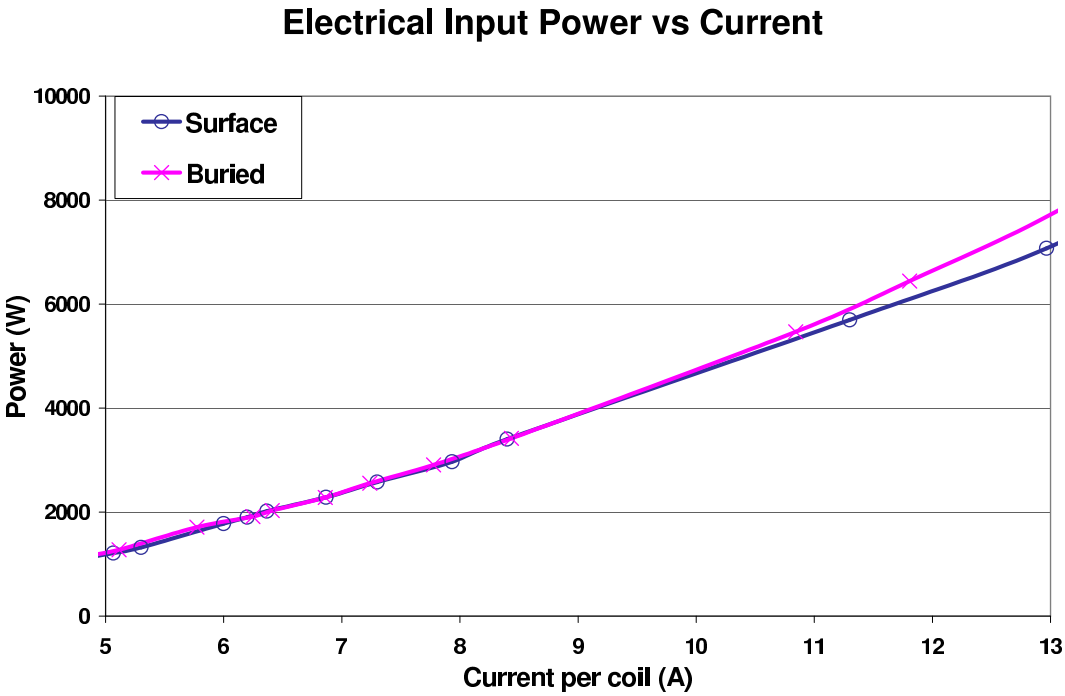


Figure 8.16: Electrical input power to the modified tubular linear synchronous motor

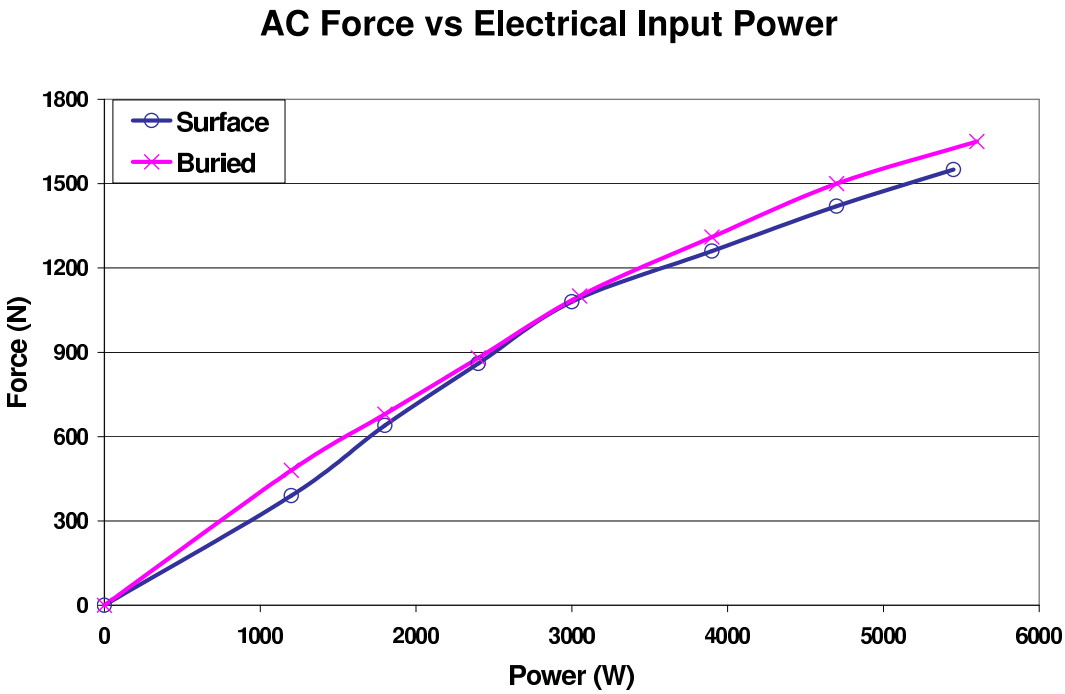


Figure 8.17: Force produced compared with the electrical input power

If the linear motor operates at speeds of approximately $18m/s$, which is the speed of a mine hoist, then the output power would increase substantially. The proportion of losses would decrease and the linear motor would be a lot more efficient. The modified linear motor would operate at an efficiency of approximately 41.5% (Calculations can be seen in Appendix G). The efficiency of a full scale modified tubular LSM is greater than the efficiencies for both man winders ($12\% - 18\%$) and rock winders ($27\% - 35\%$) (These efficiency calculations can also be seen in Appendix G). This will make a significant difference in the operating costs of a hoisting system. Also, the peak power requirement for the linear motor is approximately 25% greater than the rms power. This is much better than the conventional rope hoist, where the peak power requirements are approximately double the rms power ratings (See Table G.1).

8.4 Summary

This chapter presented the theoretical results obtained from the FEA and the practical results from tests in the laboratory for both the SMMA and BMA. These results showed that there was, at most, a 6.5% discrepancy between the theoretical and practical tests. This discrepancy could be due to the differences

in the moment of force on the bushings in the bearing housings for the AC and DC tests used to determine the thrust force. The FEA results also showed that the BMA produced 22% greater thrust forces compared to the SMMA, while the practical results showed a 17% improvement. With the mass of the two secondary sections being similar, the FWR for the BMA was greater than the SMMA. During the practical tests the BMA produced a maximum thrust force of $2800N$.

The efficiency of the modified tubular LSM was also evaluated. Due to the low operating speeds, the overall efficiency of the modified tubular LSM was between $3\% - 5\%$. The efficiency of the motor operating at full speed ($18m/s$) in a mine shaft was evaluated and the results are given in Appendix G. These results showed that a full scale model would operate at 41.5% efficiency which is greater than present man and rock winders ($12\% - 35\%$). The peak power requirement would only be 25% greater than the rms power compared to a conventional rope hoists which requires double the rms power for periods of acceleration.

Chapter 9

Conclusion

A modified tubular linear synchronous motor has been designed, constructed and fully assessed. It has proven to be a success. The research objectives have been met and therefore, the author believes that the original contributions put forward in this work are:

- the postulation and development of the motor and the extrapolation of the performance of the proposed full scale motor. The motor postulated and developed in this project retained the advantages of the tubular structure for the linear synchronous motor. However, the geometry and the windings were modified to make the secondary accessible and suitable for long distance applications like ultra deep level mining.
- the formulation and verification of the design optimisation criteria. This optimisation of the linear motor has shown that, with the correct choice of magnet arrangement using an optimal amount of permanent magnet materials, the linear motor is able to produce a maximum thrust force for a given size motor.

The four principle design aspects related to the development of this motor, namely electrical, magnetic, mechanical and thermal, have been analysed and proven. Along with these design aspects, a full finite element analysis has been performed and these results compare favourably with the measured results.

9.1 Design Aspects

Electrical System

The practical voltage and current measurements on the linear motor correlate closely with predicted results from the analytical evaluation. These predicted results were obtained from the analysis of the equivalent circuit for the modified tubular LSM, which was developed using the theory for a rotary synchronous motor as a base. This analysis was essential to make sure that the linear motor would operate within the limits of the supplied VSD.

The motor was designed with a current rating of $8A$ per coil, using a high current density of $6.3A/mm^2$. This is the same current density used on other linear motors built at the University of the Witwatersrand as it has the same winding configuration. The reason for the high current density, is that the duty cycle of the linear motors is small. These linear motors are prototypes and are not expected to be run continuously. Due to the geometry and length of each coil in this modified tubular linear motor, the voltage rating differs from the other motors. Also, the voltage rating is a function of the linear motor's speed and it was shown in Appendix B that a considerably higher voltage is required for a full scale motor with an operating speed of $18m/s$.

Magnetic System

The first phase of the project concentrated on proving the feasibility of using the modified tubular topology for a linear synchronous motor. During this phase the secondary section was built with a surface mounted magnet arrangement (SMMA). This first phase proved successful, so the second phase of the project was to optimise the design of the linear motor. With a fixed primary section, the optimisation focused on the design of the secondary. Various magnet configurations were investigated. The buried magnet arrangement (BMA) proved to be the one that produced the greatest amount of force. This was then constructed using the same grade of magnets, namely, $NdFeB_{N-35}$, as was used for the SMMA. The predicted improvement using FEA was 22% while that measured was 17%; which is still very significant. (The difference between the predicted and measured improvement was shown to be due to possible variation of the friction force between the AC and DC tests used in

the evaluation of the thrust forces.)

The optimisation also included an investigation into the reduction of the cogging forces within the linear motor for both the BMA and SMMA designs. This investigation focused on the technique of magnet length optimisation to reduce the negative effects of the cogging forces.

The split-pole magnet arrangement for the SMMA was introduced as a method to halve the maximum amount of flux flowing through any cross-sectional area in both the primary and secondary sections. This was done to prevent the saturation of either section. For a four pole secondary, the conventional arrangement has only two flux paths that contain the total amount of flux, whereas, the split-pole arrangement has four flux paths each containing the same amount of flux. Thus, each path carries half the amount of flux compared with each path of the conventional arrangement.

Mechanical System

The linear motor operated effectively as it had a solid construction and was built with fine tolerances. The major consideration in the mechanical design is that it had to account for the unbalanced attractive force developed by the powerful rare-earth $NdFeB_{N-35}$ magnets. The guidance system had to be rigid and accurate to prevent the secondary section pulling over to the primary section.

Thermal System

For the thermal system, the main area of concern was the integrity of the winding insulation used in the linear motor. Class F insulation was used for the winding of the linear motor. During the evaluation of the thermal characteristics, under continuous rated current conditions of $8A$ per coil, it was found that the temperature rise of linear motor exceeded that for the Class F insulation by 35^oC. The long effective length of copper in each coil, which would lead to greater copper losses, was the major contributor to the heat generated in the linear motor. The linear motor also heated up quickly due to its geometry, causing hot air to be trapped inside the motor.

The thermal model developed showed that for Class F insulation the continuous rated current should be $6.78A$. However, the prototype model would have a low duty cycle and would not be operated continuously for extended periods of time. Thus, the same current rating of $8A$ per coil, used in other linear motor projects, was selected as the rated current for this project. For the final application in a mine shaft, the duty cycle of the individual primary sections would be very low. In this case much higher currents could be used as these sections would only be energised for short periods of time. This is an area for further assessment so as to determine the exact duty cycle and hence current rating that could be used in a full scale motor.

The effects that the linear motor can have on the performance of the rare-earth $NdFeB_{N-35}$ magnets, used for the project, were carefully examined. This was necessary because the magnets can demagnetise if they are exposed to high temperatures combined with opposing magnetic fields. The higher the temperatures, the smaller the external magnetic field required to demagnetise these magnets. However, the air gap proved to be an effective thermal insulation barrier and the permanent magnet secondary did not heat up significantly. This investigation showed that the SMMA was only affected slightly by the increased temperature in the permanent magnets, due to its low permeance coefficient gradient, but the BMA remained largely unaffected.

9.2 Results

This linear motor produces high thrust forces and hence, owing to its size, has a good force to weight ratio (FWR) of approximately $8:1$, under rated current conditions for the BMA. For both the SMMA and BMA close correlation between the predicted FEA solutions and the measured results were achieved, verifying the use of FEA as a design tool.

The efficiency of the system was also discussed. The linear motor has a low efficiency due to its slow speed of operation. However, the efficiency was calculated for a full scale motor which showed that the linear motor would operate at higher efficiencies compared to conventional rope hoists in deep level mines.

9.3 Viability

Linear motors have numerous advantages compared to conventional rope hoisting systems (These advantages were listed in Chapter 1). With these advantages and successful operation of the prototype modified tubular LSM, the use of linear motors in vertical transportation systems is technically viable.

However, it was found during the construction phase that the linear motor was a difficult machine to put together. From an industrial point of view it would take a long time to construct and hence would turn out to be an expensive linear motor. The high forces may not justify the costs involved. If this is the case, then a double-sided construction could possibly be a better solution (Further investigation between the performance of the modified tubular LSM and other topologies is required.). But, as far as the author is aware, this is the first motor of its type ever to be built. It is the first of hopefully many prototypes. With newer models and with the experience gained from this project, the ease of construction should improve to make this type of linear motor a viable and cost effective solution for vertical or even horizontal transportation.

References

[1] Ishii T. Elevators for Skyscrapers. *IEEE Spectrum*, pages 42–46, September, 1994.

[2] Dohm M. Feasibility Study into a Linear Motor Driven Shaft Transport System. In *Mine Hoisting 2000, Fifth International Conference*, pages 177–183, Johannesburg, South Africa, September, 2000. The South African Institute of Mining and Metallurgy.

[3] Muzoriwa C.M. *Vertical Transportation of Men, Material and Mineral from Ultradeep Mining Operations - An Analysis of Options.* MSc(Eng) Thesis, University of the Witwatersrand, Johannesburg, 2000.

[4] Stewart A.T. *Hoisting Systems for Ultra Deep Vertical Shafts.* MSc(Eng) Thesis, University of the Witwatersrand, Johannesburg, 1993.

[5] Greenway M.E. An Engineering Evaluation of the Limits to Hoisting from Great Depth. In *International Deep Mining Conference: Technical Challenges in Deep Level Mining*, pages 449–481, Johannesburg, South Africa, 1990. The South African Institute of Mining and Metallurgy.

[6] Anscombe P.A. *Handbook on the Mine Health and Safety Act 29 of 1996 and the Regulations.* Juta & Co, 1st edition, 1998. ISBN: 0702127671.

[7] Ramlu M.A. *Mine Hoisting.* AA Balkema, Rotterdam / Brookfield, 1996. ISBN: 9054102985.

[8] Girodo A.M., Sparg A.N. Comparison of Hoisting Scenarios with a View to Future Trends. In *MINEMECH 94 - Mine Transport Systems for Men, Materials and Ore*, pages 1–26, Johannesburg, South Africa, September, 1994. The South African Institution of Mechanical Engineers.

[9] Gieras J.F. *Linear Induction Drives.* Oxford University Press Inc., New York, USA, 1994. ISBN: 0198593813.

[10] Laithwaite E.R. Linear Electric Machines - A Personal View. *Proceedings of the IEEE, vol 62, No.2*, pages 250–290, February 1975.

[11] McLean G.W. Review of Recent Progress in Linear Motors. *IEE Proceedings, vol. 135, Pt B, No. 6*, pages 380–416, November, 1988.

[12] Central Japan Railway Company. MLX01 Maglev eXperimental 01. Japan, 1998.

[13] Linear Drives LTD. Direct Thrust Linear Servo Motors and Systems. England, 1997.

[14] Eastham J.F. Novel Synchronous Machines: Linear and Disc. *IEE Proceedings, vol. 137, Pt. B, No. 1*, pages 49–58, January, 1990.

[15] Kikuma T., Ishiyama A. Improvement of Superconducting Cylindrical Linear Induction Motor. *IEEE Transactions on Superconductivity, vol. 11 Issue 1*, pages 2331–2334, March, 2001.

[16] Laithwaite E.R. Induction Coil Guns for Hypervelocities. *IEE Proceedings, vol. 142, Pt. B, No. 3*, pages 215–221, May, 1995.

[17] Vadher V.V., Smith I.R. Performance of a segmented rotor tubular linear induction motor. *IEEE Transactions on Magnetics, vol. 29 Issue 6*, pages 2941–2943, November, 1993.

[18] Chen D., Chen S., Yang X. A Novel Electromagnetic Hammer and its Control. In *The First International Symposium on Linear Drives for Industry Applications*, pages FA–5:187–190, Nagasaki, Japan, May, 1995. The Institute of Electrical Engineers of Japan.

[19] Ueno T., Tani J., Qiu J., Kosugo K. Dynamics of a Long-Stroke Linear Actuator Using Optimized Current Scheduling. In *The Second International Symposium on Linear Drives for Industry Applications*, pages LM–27:287–290, Tokyo, Japan, April, 1998. The Institute of Electrical Engineers of Japan.

[20] Yamada H., Kobayashi M., Watanabe M., Yamaguchi M., Karita M., Maeda M., Fukunaga S. Performance Characteristics of a Linear Motor-Driven Total Artificial Heart for the Second Step. In *The First International Symposium on Linear Drives for Industry Applications*, pages AC–12:453–456, Nagasaki, Japan, May, 1995. The Institute of Electrical Engineers of Japan.

[21] Watada M., Oishi Y., Abe K., Honda T., Ebihara D., Kasugai T., Isoyama T., Imachi K. A Basic Study of Linear Oscillatory Actuator for Artificial Heart. In *The First International Symposium on Linear Drives for Industry Applications*, pages AC–13:457–460, Nagasaki, Japan, May, 1995. The Institute of Electrical Engineers of Japan.

[22] Odajima K., Um Y., Kano Y. The Proposal of EMG Servo System of the Linear Motor for the Meal Nursing. In *The Third International Symposium on Linear Drives for Industry Applications*, pages P2–3:244–247, Nagano, Japan, October, 2001. The Institute of Electrical Engineers of Japan.

[23] Clark R.E., Howe D. Dynamic Performance Analysis of Linear Reciprocating Moving-Magnet Actuators. In *The Second International Symposium on Linear Drives for Industry Applications*, pages LM–23:271–274, Tokyo, Japan, April, 1998. The Institute of Electrical Engineers of Japan.

[24] Yatuzuka S., Takizawa K., Nara K., Hagiwara Y., Watada M., Ebihara D. Static and Kinetic Characteristics of Linear Oscillatory Actuator for Cryocooler Compressor. In *The Third International Symposium on Linear Drives for Industry Applications*, pages P1–9:140–143, Nagano, Japan, October, 2001. The Institute of Electrical Engineers of Japan.

[25] Wang J., Jewell G.W., Howe D. A General Framework for the Analysis and Design of Tubular Linear Permanent Magnet Machines. *IEEE Transactions on Magnetics, vol. 35 Issue 3*, pages 1986–2000, May, 1999.

[26] Copley Motion Systems—-TT Micro, Accessed July 2003. Available at `http://www.copleycontrols.com/motion/technologies/motor/`.

[27] Gore V., Cruise R.J., Landy C.F. Economic Considerations of Linear Synchronous Motors in the South African Mining Industry. In *The Second International Symposium on Linear Drives for Industry Applications*, pages AP–20:86–89, Tokyo, Japan, April, 1998. The Institute of Electrical Engineers of Japan.

[28] Bodika N. *Modelling of a Permanent Magnet Linear Synchronous Motor Under Regenerative Braking.* MSc(Eng) Thesis, University of the Witwatersrand, Johannesburg, 2005.

[29] Harvey T. The Calculation of Rope Sizes and Power Requirement of Winders. *International Conference on Hoisting of Men, Materials and Minerals*, pages 177–186, October, 1973.

[30] Stewart A.T. Hoisting Systems for Ultra-deep Vertical Shafts. In *Proceedings XVth CMMI Congress*, pages 39–44, Johannesburg, South Africa, September, 1994. The South African Institute of Mining and Metallurgy.

[31] Wainwright K. Some parameters to optimise shaft design. In *SAIMM Colloquium on Deep Level Mining - The Challenges*, pages 1–13, Johannesburg, South Africa, March, 1996. The South African Institute of Mining and Metallurgy.

[32] Cruise R.J. Hybrid Hoist Proposal, Accessed September 2004. Available at `http://www.texchange.co.uk/projects.htm`.

[33] Cruise R.J., Landy C.F. Design and Evaluation of a Hybrid Hoist for Ultra Deep-Level Mines. In *The 16th International Conference on Magnetically Levitated Systems and Linear Drives*, pages 417–422, Rio de Janeiro, Brazil, June, 2000. LASUP, DEE, Universidade Federal do Rio de Janeiro.

[34] Nasar S.A., Xiong G.Y., Fu Z.X. Eddy-Current Losses in a Tubular Linear Induction Motor. *IEEE Transactions on Magnetics, vol. 30 Issue 4*, pages 1437–1445, July, 1994.

[35] Roy D., Akiyama Y., Yamada S., Iwahara M., Basak B. Comparative Studies of Flux-Concentration Type and Normal Type Tubular Linear Induction Motor. In *The Third International Symposium on Linear Drives for Industry Applications*, pages A–3:21–24, Nagano, Japan, October, 2001. The Institute of Electrical Engineers of Japan.

[36] Onuki T., Iwamoto T., Watanabe H., Akita J. Improvement of Secondary Construction in the Permanent Magnet Type Linear Synchronous Motor. In *The Second International Symposium on Linear Drives for Industry Applications*, pages LM–19:256–258, Tokyo, Japan, April, 1998. The Institute of Electrical Engineers of Japan.

[37] Wang J., Jewell G.W., Howe D. Design Optimisation and Comparison of Tubular Permanent Magnet Machine Topologies. *IEE Proceedings - Electric Power Applications, vol 148, Issue 5*, pages 456–464, September, 2001.

[38] Kim W.J., Berhan M.T., Trumper D.L., Lang J.H. Analysis and Implementation of a Tubular Motor with Halbach Magnet Array. In *The 31st IEEE Industry Applications Society Conference, Vol.1*, pages 471–478, San Diego, USA, October, 1996.

[39] Schofield N., Canova A., Ottella M. A Tubular Linear Actuator for Steer-by-Wire Applications. In *The Fourth International Symposium on Linear Drives for Industry Applications*, pages AU–06:560–563, Birmingham, UK, September, 2003. The Institution of Electrical Engineers, UK and The Institute of Electrical Engineers of Japan.

[40] Laithwaite E.R. *Propulsion Without Wheels*. The English Universities Press, 1970. ISBN: 0340048360.

[41] Jeans C.G., Cruise R.J., Landy C.F. Improved Performance of a Linear Synchronous Motor by the Inclusion of an Aluminium Sheet. In *The Second International Symposium on Linear Drives for Industry Applications*, pages NA–11:392–395, Tokyo, Japan, April, 1998. The Institute of Electrical Engineers of Japan.

[42] Trumper D.L., Kim W.J., Williams M.E. Design and Analysis Framework for Linear Permanent-Magnet Machines. *IEEE Transactions on Industry Applications, vol.32, No. 2*, pages 371–379, March/April, 1996.

[43] Deng Z., Boldea I., Nasar S.A. Fields in Permanent Magnet Linear Synchronous Machines. *IEEE Transactions on Magnetics, vol. mag-22, No. 2*, pages 107–112, March, 1986.

[44] Deng Z., Boldea I., Nasar S.A. Forces and Parameters of Permanent Magnet Linear Synchronous Machines. *IEEE Transactions on Magnetics, vol. mag-23, No. 1*, pages 305–309, January, 1987.

[45] Eastham J.F., Akmese R., Lai H.C. Optimum Design of Brushless Tubular Linear Machines. *IEEE Transactions on Magnetics, vol 26, No. 5*, pages 2547–2549, September, 1990.

[46] Bianchi N. Analytical Computation of Magnetic Fields and Thrusts in a Tubular PM Linear Servo Motor. In *IEEE Industry Applications Society Conference, Vol.1*, pages 21–28, Rome, Italy, October, 2000.

[47] Gieras J.F., Piech Z.J. *Linear Synchronous Motors: Transportation and Automation Systems*. CRC Press, Boca Raton, USA, 1999. ISBN: 0849318597.

[48] Say P.C. *Alternating Current Machines*. Longman Scientific & Technical, Singapore, 5th edition, 1983. ISBN: 0582988756.

[49] Gieras J.F., Wing M. *Permanent Magnet Motor Technology, Design and Applications*. Marcel Dekker, Inc, New York, USA, 2nd edition, 2002. ISBN: 0824707397.

[50] Magnet Sales and Manufacturing, Accessed September 2000. Available at `http://www.magnetsales.com`.

[51] Strnat K.J. Modern Permanent Magnets for Applications in Electro-Technology. *Proceedings of the IEEE, vol. 78, No. 6*, pages 923–946, June, 1990.

[52] Better Elect Company Limited. $NdFeB_{N-35}$ - Magnetic and Physical Characteristics. Hong Kong, 1998.

[53] Bianchi N., Bolognani S., Dalla Corte D., Tonel F. Tubular Linear Permanent Magnet Motors: An Overall Comparison. In *IEEE Industry Applications Society Conference,* 37^{th} *IAS Annual Meeting, Vol.2*, pages 1266–1273, Pittsburgh, USA, October, 2002.

[54] Jeans C.G., Hansa A., Cruise R.J., Landy C.F. Comparison Between Surface Mounted and Buried Permanent Magnets in Linear Synchronous Motors. In *The Second International Symposium on Linear Drives for Industry Applications*, pages NA–5:371–374, Tokyo, Japan, April, 1998. The Institute of Electrical Engineers of Japan.

[55] Cruise R.J., Landy C.F. Reduction of Cogging Forces in Linear Synchronous Motors. In *IEEE Africon, Vol.2*, pages 623–626, Cape Town, South Africa, September, 1999.

[56] Li T., Siemon G. Reduction of Cogging Torque in Permanent Magnet Motors. *IEEE Transactions on Magnetics, vol. mag-24, No. 6*, pages 2901–2903, November, 1988.

[57] Bodika N., Cruise R.J., Landy C.F. Design of a Simple PI Controller for the Reduction of the Effect of Detent Forces in a Permanent Magnet Linear Synchronous Motor. In *The 8th Annual South African Universities' Power Engineering Conference*, pages 205–209, Potchefstroom, South Africa, January, 1999. The School of Electrical and Electronic Engineering, Potchefstroom University CHE.

[58] Hung J.Y., Ding Z. Design of Currents to Reduce Torque Ripple in Brushless Permanent Magnet Motors. *IEE Proceedings, vol. 140, Pt. B, No. 4*, pages 260–266, July, 1993.

[59] Yoshimura T., Watada M., Torii S., Ebihara D. Study on the Reduction of Detent Force of Permanent Magnet Linear Synchronous Motor. In *The First International Symposium on Linear Drives for Industry Applications*, pages FA–10:207–210, Nagasaki, Japan, May, 1995. The Institute of Electrical Engineers of Japan.

[60] Hor P.J., Zhu Z.Q., Howe D., Rees-Jones J. Minimization of Cogging Force in a Linear Permanent Magnet Motor. *IEEE Transactions on Magnetics, vol. mag-24, No. 5*, pages 3544–3547, September, 1998.

[61] Giancoli D.C. *Physics for Scientists and Engineers*. Prentice-Hall International, Inc., 1988. ISBN: 0136740456.

[62] Transwire (Pty) Ltd, Accessed January 2006. Available at `http://www.transwire.co.za/engineering_data.html`.

[63] Cowern E.H., Accessed April 2003. Available at `http://www.motorsanddrives.com/cowern/motorterms4.html`.

[64] Saftronics Inc., Fort Myers, USA. *FP5/GP5 Technical Manual*, 1st edition, September 1998.

[65] Chatterjee P.K., Wetherall P.J. *Winding Engine Calculations for the Mining Engineer*. E. & F.M. Spon Ltd, London, 1982. ISBN: 0419126503.

[66] Fitzgerald A.E., Kingsley C., Umans S.D. *Electric Machinery*. McGraw-Hill Companies, Inc, New York, USA, 6th edition, 2003. ISBN: 0073660094.

[67] Moll C. Modern Shaft Systems in the Republic of South Africa. *International Conference on Hoisting of Men, Materials and Minerals*, pages 85–93, October, 1973.

[68] Matsch L.W., Morgan J.D. *Electromagnetic and Electromechanical Machines*. John Wiley & Sons, Singapore, 3rd edition, 1987. ISBN: 0471613053.

[69] C.D.Wälzholz. Material data sheet: Electrical steel sheet: Grade: M 400 - 50A. Hagen, Germany, 1999.

Appendix A

Correlating the Physical Model to the Finite Element Model

The design of the modified tubular LSM was accomplished using a FEM computer package. The model was drawn and solved in the two dimensional ($2D$) environment. Using the RZ plane, a cross-sectional area of the model was drawn and the model revolved around the Z-axis by 360^0. This assumes that both the primary and secondary sections are solid $3D$ objects. However, practically this is not the case, as a block arrangement has been used. It must now be shown that the solutions from the FEM simulations can be adapted for the required shape of the modified tubular LSM. With the physical model having less material than the FEM model, the main consideration was that the material does not go into saturation.

A block arrangement can be seen in Figure A.1 [10]. For the modified tubular LSM, one block is removed to allow the cage to be attached to the secondary as in Figure A.2. This linear motor has 5 blocks that make up the primary, but any number could be used. Options for this project were 3, 5, or 7 blocks. Comparatively more active steel material can fit into the motor, with a larger number of blocks. For 3 primary blocks there is the least amount of steel used. This under utilises the space available, and the maximum axial force generated will be the smallest of the three options. Also, the normal force produced will be the greatest. For 7 and larger numbers of blocks, the gap left by the missing block decreases. From a mechanical point of view, this is a problematic, as there is a space limitation. Both the guidance system and the overhangs from the winding have to fit into this space. However, the normal forces produced will be smaller. For these reasons, 5 blocks were seen as the optimum number.

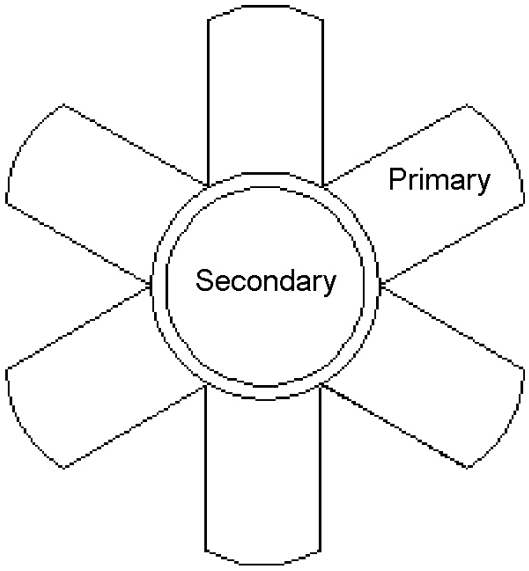


Figure A.1: Block arrangement of primary laminations for a tubular LSM.

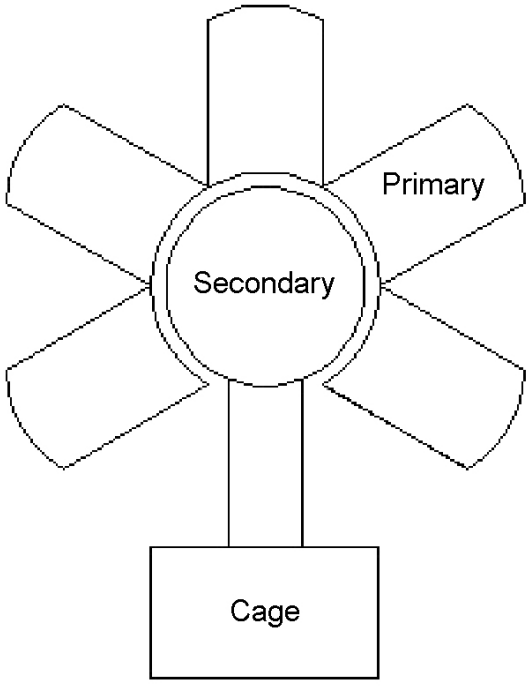


Figure A.2: Block arrangement of primary laminations for a modified tubular LSM.

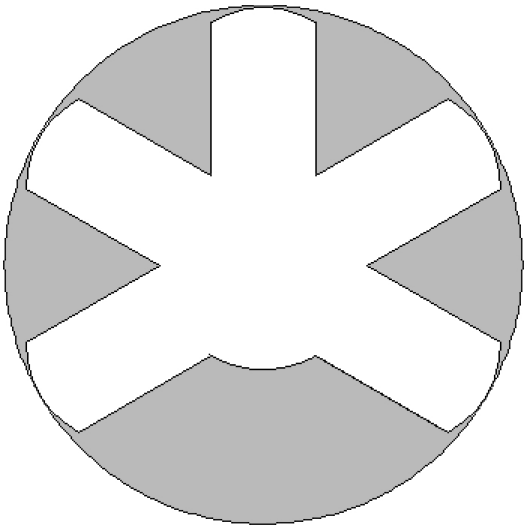


Figure A.3: The grey areas represent the difference between the FEM model and the physical model.

Table A.1: Percentages of material used

Number of sections	**3**	**5**	**7**
Angle between sections	90^o	60^o	45^o
Space used (teeth)	58%	64%	67%
Space not used (teeth)	42%	36%	33%
Space used (primary-back)	29%	32%	34%
Space not used (primary-back)	71%	68%	66%

The primary lamination has two parts. The first part is the primary teeth. The other is the rest of the lamination which will be referred to as the primary-back part. The reason for the distinction between the two parts is that the flux path changes from one effective cross-sectional area to another. Therefore, the flux densities of the two sections would differ. Thus, each part is analysed separately.

The percentage proportions of the lamination for the primary-back and tooth areas are 73% and 27% respectively. The amount of material to be used in the physical model is 41% of that used in the FEM simulations. This can be seen in Figure A.3 where the grey area is the difference between the FEM model and the physical model. Table A.1 shows the percentage area used and unused (grey areas) by each of the odd numbered configurations.

An investigation into the FEM results showed that the primary-back part had

a maximum flux density of $0.31T$. From Table A.1, the amount of material in primary-back part of the physical model compared to the FEM models is 32%. The corresponding flux density for the physical model was then calculated to be $1.0T$. For the primary teeth the FEM results showed a maximum flux density of $0.73T$ and a calculated value of $1.2T$ for the physical model. With these values, the primary sections still operate in the linear region of the B-H curve of the lamination material. If anything, the primary sections would be able to handle more flux.

The secondary section is a solid object, however magnets only cover 300^o of the object's surface. The calculated value of the maximum flux density of the secondary is $1.8T$. This occurs at the 'knee' in the B-H curve of the secondary material. It must be noted that this is for a split-pole magnet arrangement, where at any point the maximum amount of flux is half the total flux per pole. For a conventional magnet arrangement the maximum flux density would have been $2.5T$, which is well into saturation.

Appendix B

Required Applied Voltage for a Full Scale Motor

The same dimensions from the prototype model could be used for a full scale linear motor. The primary would be the length of the mine shaft and the secondary could be lengthen to accommodate the conveyances. Two modified tubular motors could be used together as shown in Figure 2.2. The resultant thrust force is then proportional to the length of the secondary. The travelling speed of the secondary would be a constant $18m/s$ (This is a similar speed to a conventional rope hoisting system).

For this analysis it will be assumed that the secondary for the full scale motor has the same length as the prototype ($0.456m$). This is so comparisons can be made between the prototype's speed ($0.114m/s$) and the speed of the full scale model ($18m/s$)[1]. The required applied voltage is calculated for the speed of the full scale model at rated current.

Required Applied Voltage at $18m/s$

The approach taken in this section is very similar to Chapter 3. The biggest difference is that the operating speed and hence frequency is larger.

[1] Theoretically, since the force is proportional to the length of the secondary, the efficiency of the full scale model should be essentially the same for any secondary length

Frequency, f

From Equation 3.4,

$$\begin{aligned} v_s &= 2\tau f \\ 18 &= 2 \times 0.114 f \\ \therefore\ f &= 78.95 Hz \end{aligned}$$

Induced Voltage for One Coil, E_{f1}

From Equation 3.2, using a frequency of $78.95Hz$, the induced voltage should be:

$$\begin{aligned} E_{f1} &= 4.44 \Phi f N_c K_e \\ &= 4.44 \times 0.01309 \times 78.95 \times 45 \times 0.966 \quad V \\ &= 199.46 \quad V \end{aligned} \tag{B.1}$$

Voltage Phasor for the Coil Resistance, R_{a1}

The voltage across one coil with resistance R_{a1} remains the same[2]:

$$I_{a1} R_{a1} = 6.04V$$

Voltage Phasor for the Coil Synchronous Reactance X_{s1}

The synchronous reactance, using a frequency of $78.95Hz$, is:

$$I_{a1} X_{s1} = 9.00V$$

Applied Voltage, V_{t1}

From the phasor diagram in Figure 3.6 and taking V_{t1} as the reference, the voltage equation is the same as Equation 3.11:

[2]Assuming no skin effects at the higher frequency.

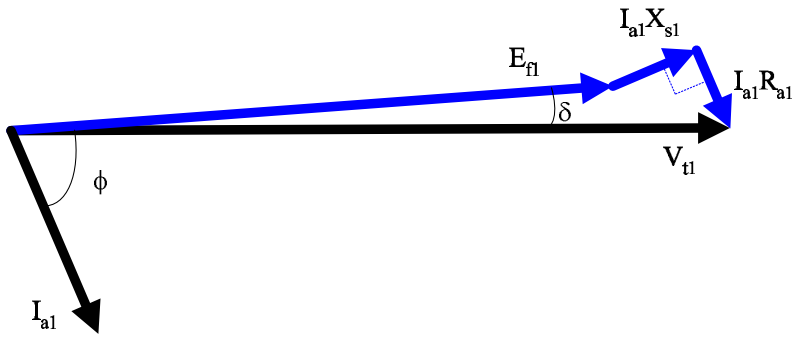


Figure B.1: The phasor diagram from Figure 3.6 with a larger E_{f1} and for $\delta > 0^o$

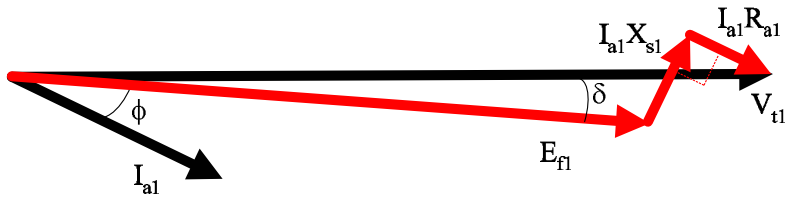


Figure B.2: The phasor diagram from Figure 3.6 with a larger E_{f1} and for $\delta < 0^o$.

$$V_{t1} \angle 0^o = E_{f1} \angle \delta + I_{a1} \angle \phi \, (R_{a1} + jX_{s1}) \tag{B.2}$$

Phasor E_{f1} is a lot larger in magnitude than phasors $I_{a1}R_{a1}$ and $I_{a1}X_{s1}$. So the phasor diagram for the LSM operating as a motor, as shown in Figure 3.6, is modified to show the larger E_{f1} phasor (Figure B.1 for $\delta > 0^o$ and Figure B.2 for $\delta < 0^o$).

With E_{f1} being the largest phasor, angle δ has a much smaller range. This is shown in Figure B.3. With a current of $8A$ per coil, angle δ must be between 3.11^o and -3.11^o. However, for $\delta = 3.11^o$ the angle ϕ will be less than -90^o. This implies that the LSM is operating as generator. Therefore, angle δ must not be greater than 1.74^o for the LSM to operate as a motor (See Figure B.4).

Phasor diagrams for $\delta = 0^o$ and $\phi = 0^o (\delta = -2.59^o)$ are shown in Figures B.5 and B.6 respectively.

Equation B.2 can be written as:

$$V_{t1}(cos(0^o)+jsin(0^o)) = E_{f1}(cos(\delta)+jsin(\delta))+I_{a1}(cos(\phi)+jsin(\phi))(R_{a1}+jX_{s1}) \tag{B.3}$$

Equating real and imaginary parts:

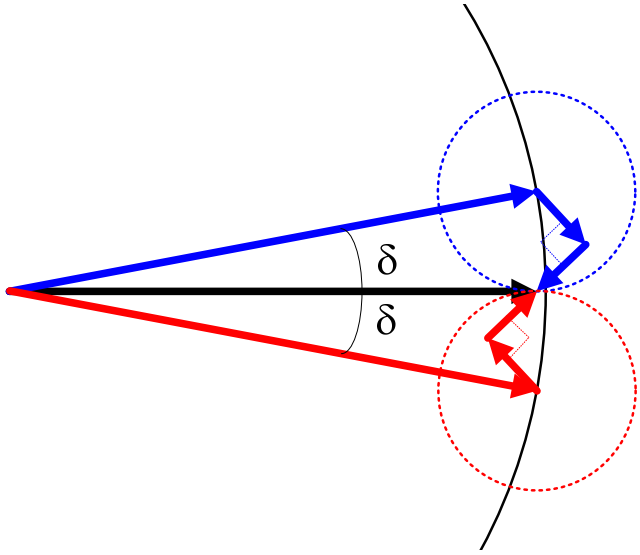


Figure B.3: The phasor diagram showing the range of angle δ.

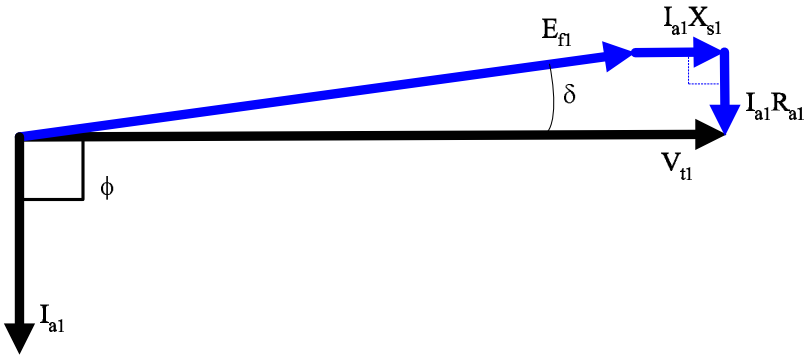


Figure B.4: The phasor diagram for maximum δ, such that the LSM will operate as a motor.

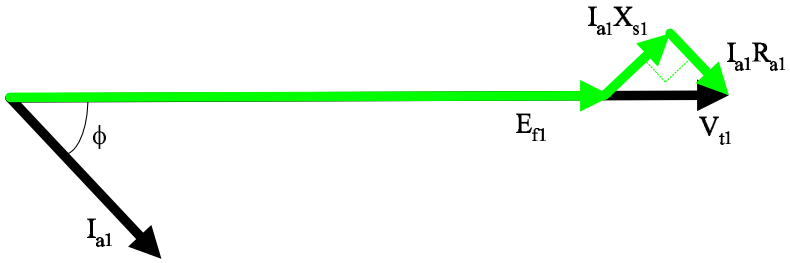


Figure B.5: The phasor diagram for $\delta = 0^o$.

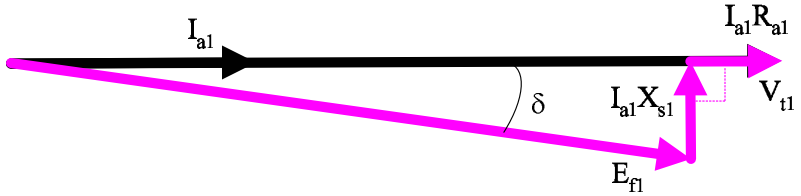


Figure B.6: The phasor diagram for unity power factor: $\phi = 0^o (\delta = -2.59^o)$.

Reals:

$$V_{t1} = E_{f1}\, cos(\delta) + I_{a1}\, cos(\phi) R_{a1} - I_{a1}\, sin(\phi) X_{s1} \quad \text{(B.4)}$$

Imaginaries:

$$0 = E_{f1}\, sin(\delta) + I_{a1}\, sin(\phi) R_{a1} + I_{a1}\, cos(\phi) X_{s1} \quad \text{(B.5)}$$

- For $\delta = 1.74^o$

  $V_{t1} = 208.37V$
  $\phi = -90.00^o$ or $cos(\phi) = 0.00$

- For $\delta = -3.11^o$

  $V_{t1} = 199.79V$
  $\phi = 30.54^o$ or $cos(\phi) = 0.86$

- For $\delta = 0^o$

  $V_{t1} = 210.30V$
  $\phi = -56.13^o$ or $cos(\phi) = 0.56$

- For $\delta = -2.59^o$

  $V_{t1} = 205.29V$
  $\phi = 0.00^o$ or $cos(\phi) = 1.00$

It must be noted that these values are for one coil only. The actual applied voltage to the linear motor will depend on winding configuration as shown in Figure 3.15. Since the same winding configuration is being used, the distribution factor, K_m, remains the same at 0.966

Thus, the required voltage per coil group is:

$$V_{t_{group}} = 2 \times V_{t1} \times K_m$$

There are three groups in series for each phase:

$$V_{t_{phase}} = 3 \times V_{t_{group}}$$

With rated current of $8A$ flowing in the primary winding, the required line voltage is in the range of $1157.98V - 1218.90V$, depending on the size of angle δ.

The power factor of the motor has a range between $0.00-1.00$; again depending on the size of angle δ. However, the $NdFeB_{N-35}$ permanent magnets dominate the magnetic field system as described in Section 3.1.1. Due to the strong field system, the full scale modified tubular LSM is expected to be *overexcited*, resulting in a leading component of current and hence a leading power factor. This would occur for $-3.11^o < \delta < -2.59^o$ and $0.00^o < \phi < 30.54^o$ (Leading power factor $0.86 < p.f. < 1.00$).

Appendix C

Electric Circuit Analogy for the Split Pole Magnet Arrangement

This is a useful analogy and has been included for ease of interpretation of the split pole magnet arrangement should this be necessary. Following the usual electric circuit analogy for magnetic circuits, the electrical analogies of the different structures can be evaluated.

Conventional Even Pole Magnet Arrangement without Saturation Effects

All of the permanent magnets are made of the same material. They each see approximately the same reluctance in the magnetic circuit and would each operate along the same P_c line as described in Section 4.1.2. Thus, each of these magnets will have the same flux density, B, and field intensity, H. These magnets have the same dimensions, so the MMF for each magnet will be the same. In the electric circuit, these magnets can be modelled by constant voltage sources.

The "resistors" in the electric circuit, represent the reluctances of the magnetic circuit. The reluctance of the air gap between the primary and secondary is represented by a large value of resistance (Figure C.1). The infinite permeability of the primary and secondary sections is characterised by the zero resistance values in the electrical circuit.

As in the case of the conventional magnet arrangement, where there is no flux linkage between the two middle magnets in Figure 4.27, there is no current flow between the two middle voltage sources in Figure C.1.

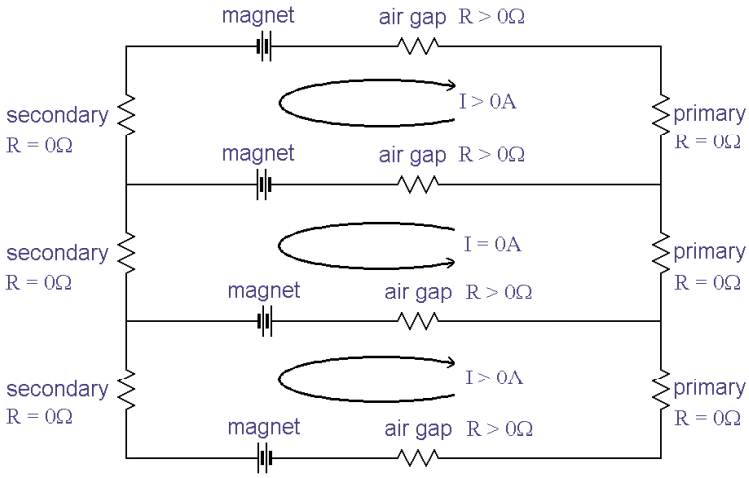


Figure C.1: Circuit analogy representing the magnetic circuit for the conventional magnet arrangement (without saturation effects).

Conventional Even Pole Magnet Arrangement with Saturation Effects

The magnetic circuit for this scenario can be represented by an electric circuit shown in Figure C.2. This time the resistances representing the secondary have been increased to simulate the extra reluctance seen by the magnetic circuit. This results in a current in the centre loop as shown in Figure C.2. This circuit is the analogy for Figure 4.28, where a certain amount of flux links the centre two magnets.

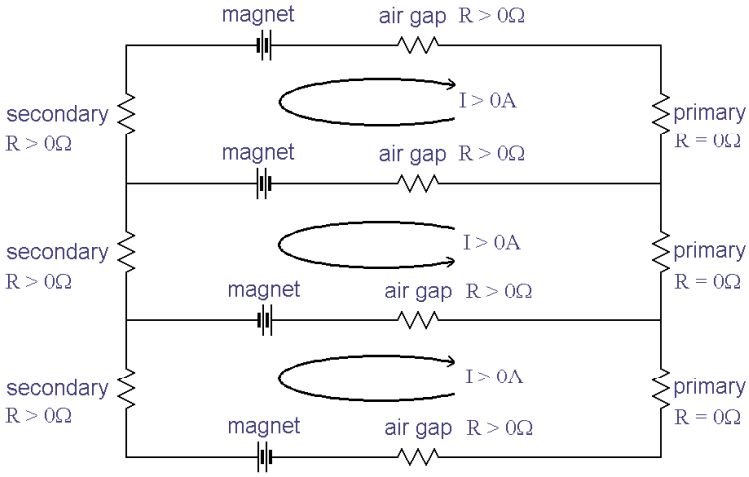


Figure C.2: Circuit analogy representing the magnetic circuit for the conventional magnet arrangement (with saturation effects).

Split-Pole Magnet Arrangement

For the split-pole magnet arrangement, an electrical circuit analogy for with no saturation is shown in Figure C.3. Each current loop in Figure C.3 is equal in magnitude. Figure C.4 is the electrical circuit analogy with saturation effects. Again, the current loops are equal in magnitude.

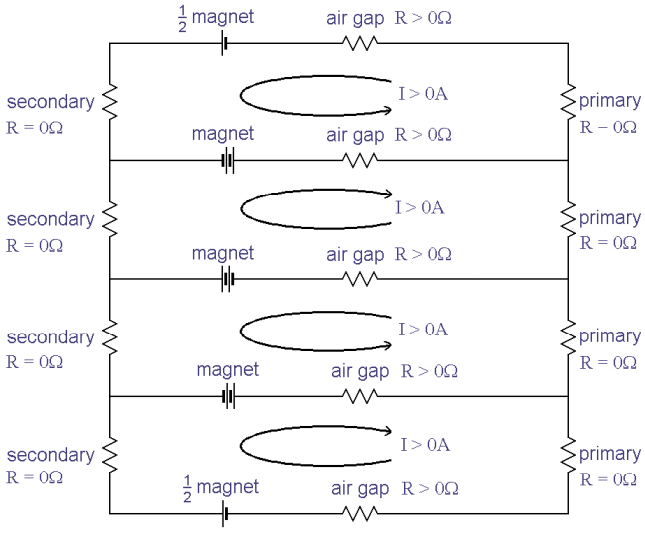


Figure C.3: Circuit analogy representing the magnetic circuit for the split-pole magnet arrangement (without saturation effects).

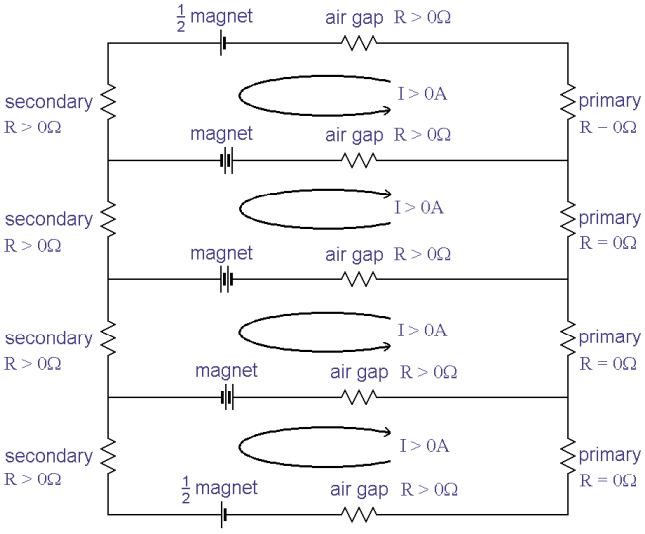


Figure C.4: Circuit analogy representing the magnetic circuit for the split-pole magnet arrangement (with saturation effects).

Appendix D

Construction Drawings

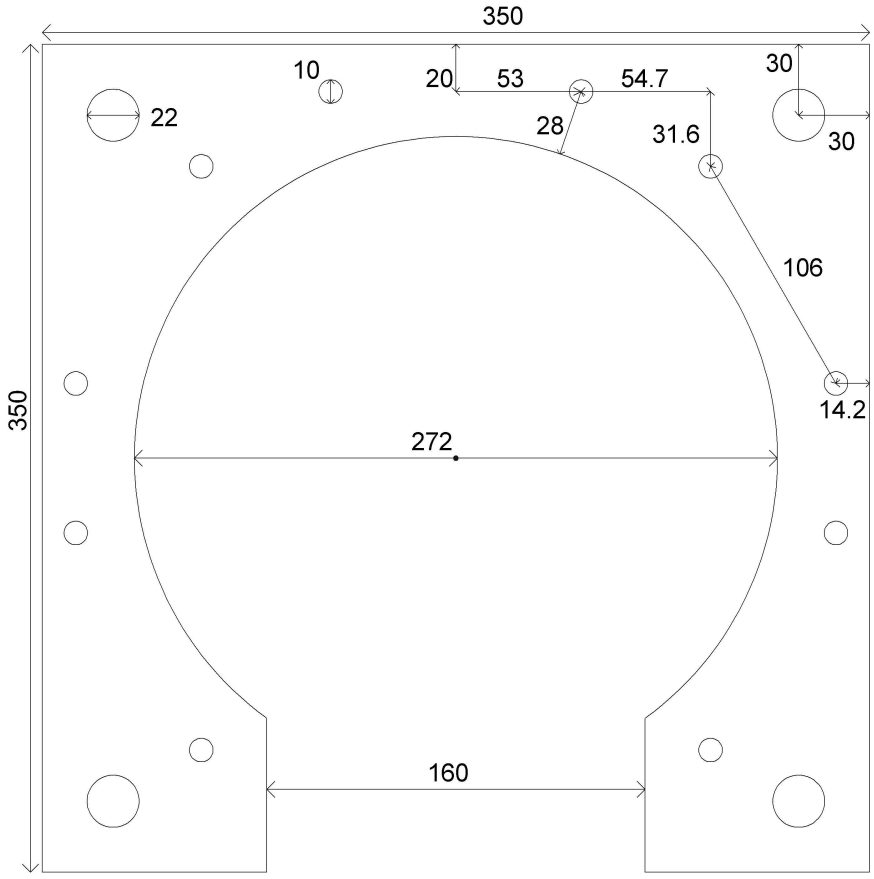


Figure D.1: The support plate

This support plate forms part of the frame to the linear motor. The four holes in the corners are there to support the rods that connect the plates. The smaller holes are there to connect the frame to the primary section with the use of angle iron pieces. The space in the support pate allows access to the secondary section of the linear motor. The support plates that form the top and bottom to the linear motor are solid rectangular plates with just the holes for the connecting rods.

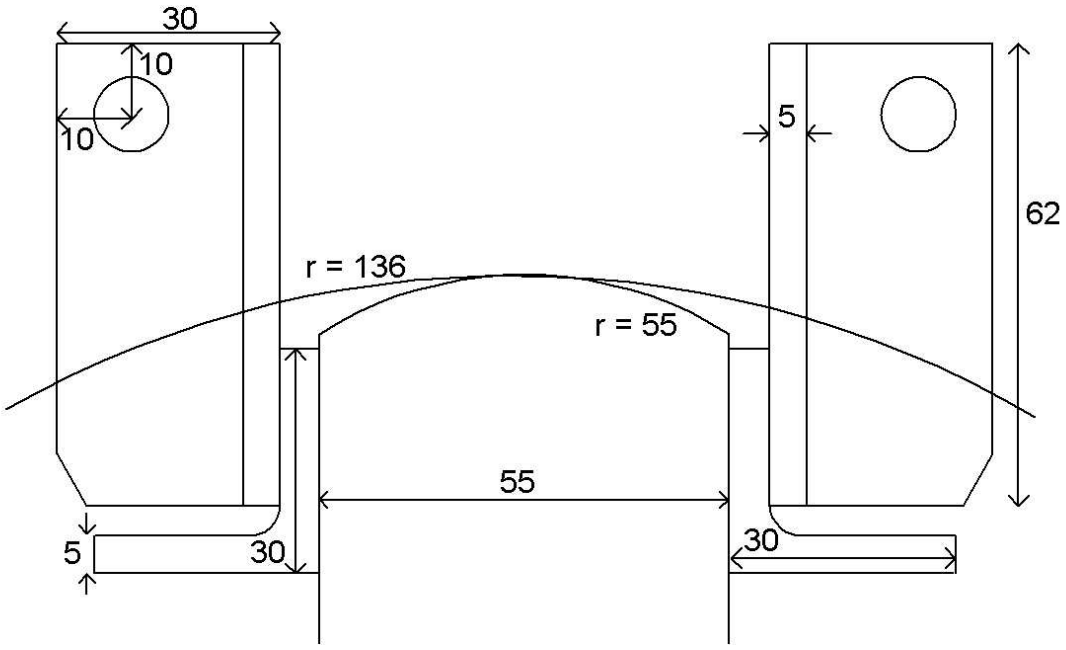


Figure D.2: Close-up of the connection between the support plate and the primary

This figure shows a close up of the connection between the support plate and the one primary stack. The primary stack has angle iron bolted to its sides along its length (Holes are drilled trough the primary stack). The small pieces of angle iron are then welded to the angle iron sections connected to the primary stack. These small pieces of angle iron are then bolted to the support frame. Due to the adjustments made to actual model, the small pieces of angle iron were welded to the support plates.

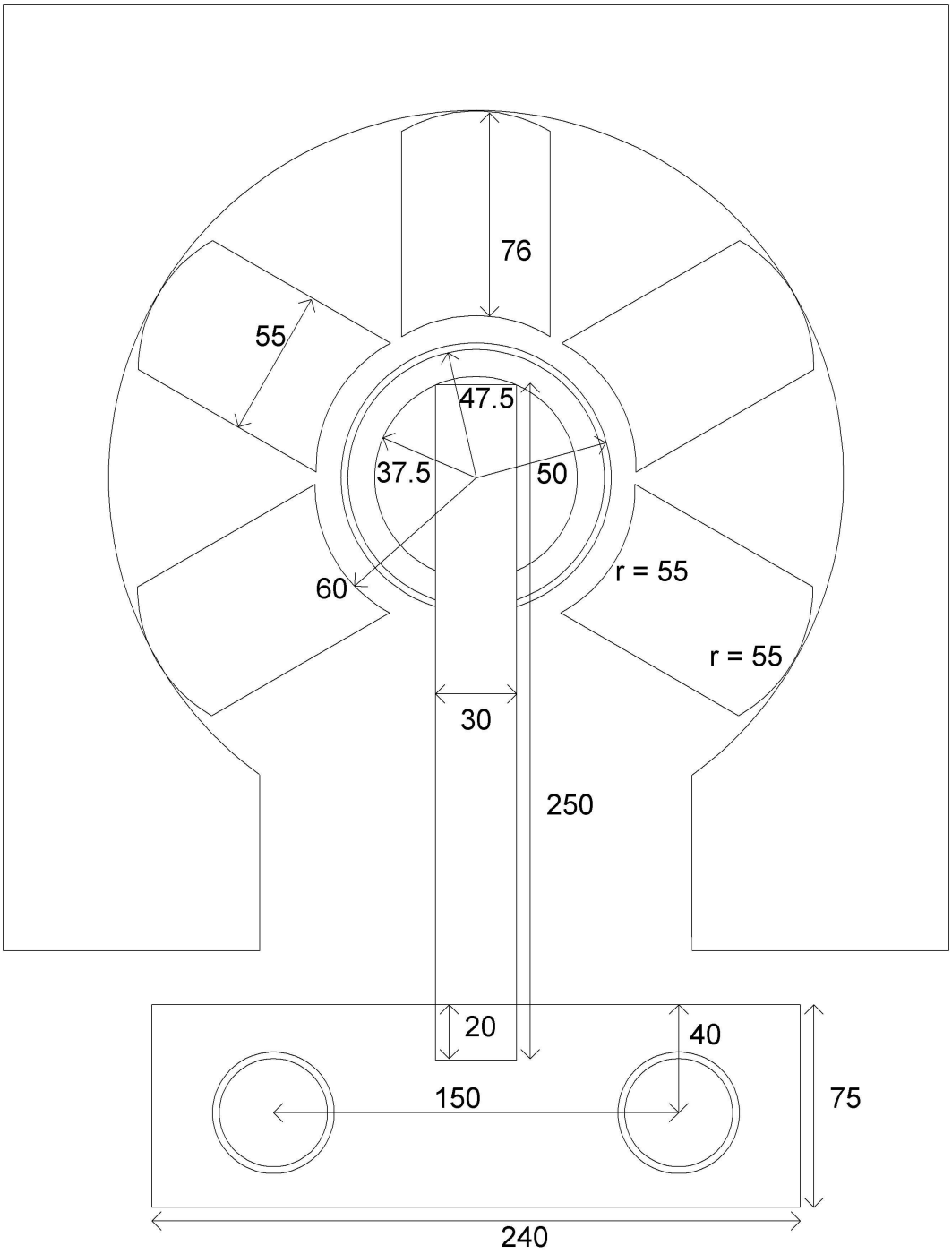


Figure D.3: Position of the guidance system

This shows the placement and dimensions of the guidance system within the linear motor. The two holes of the bearing block are there for the two guidance rods. Vesconite is used between the bearing block and the guidance rods to allow for the smooth travel of the linear motor.

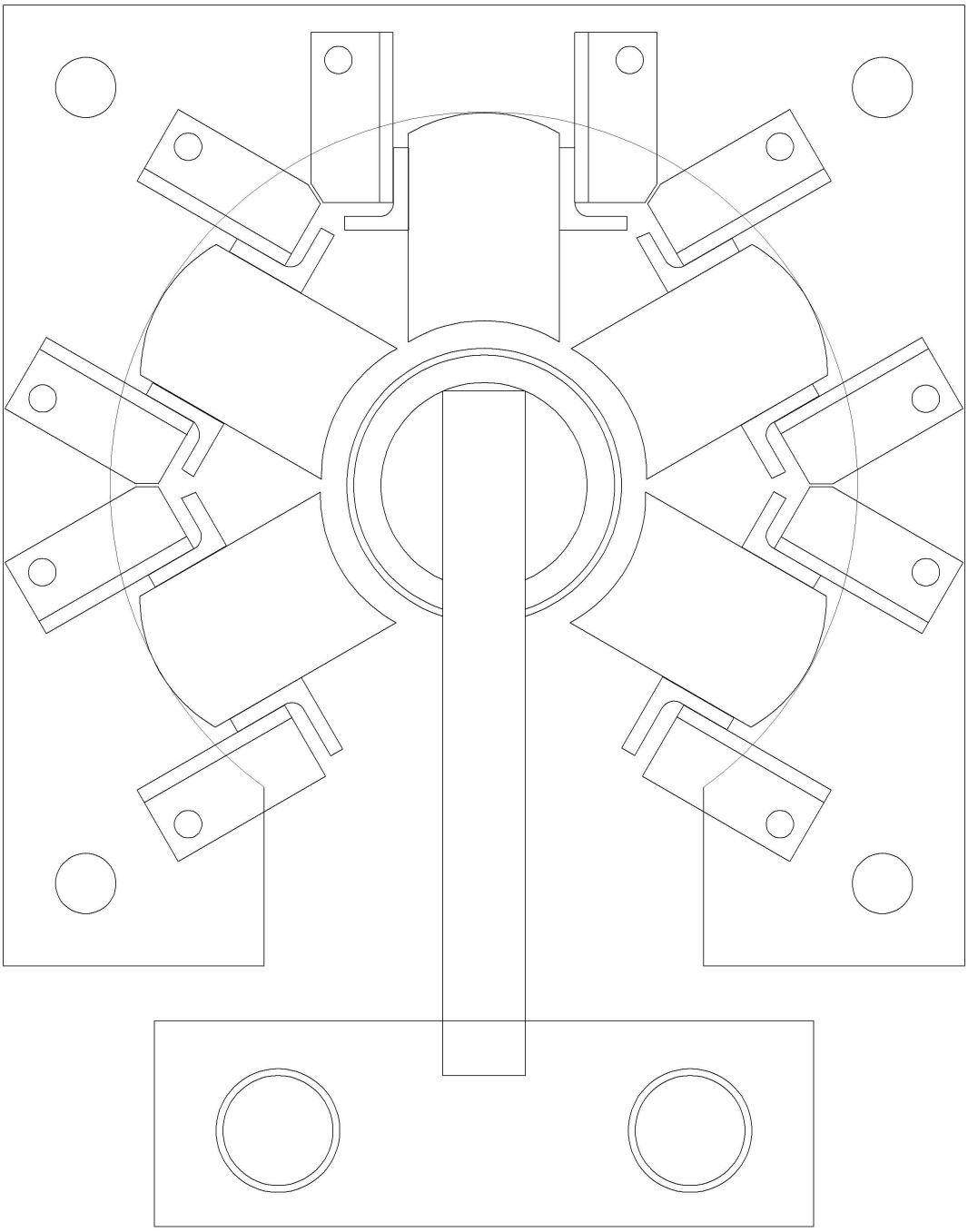


Figure D.4: The assembly of the linear motor as seen from above.

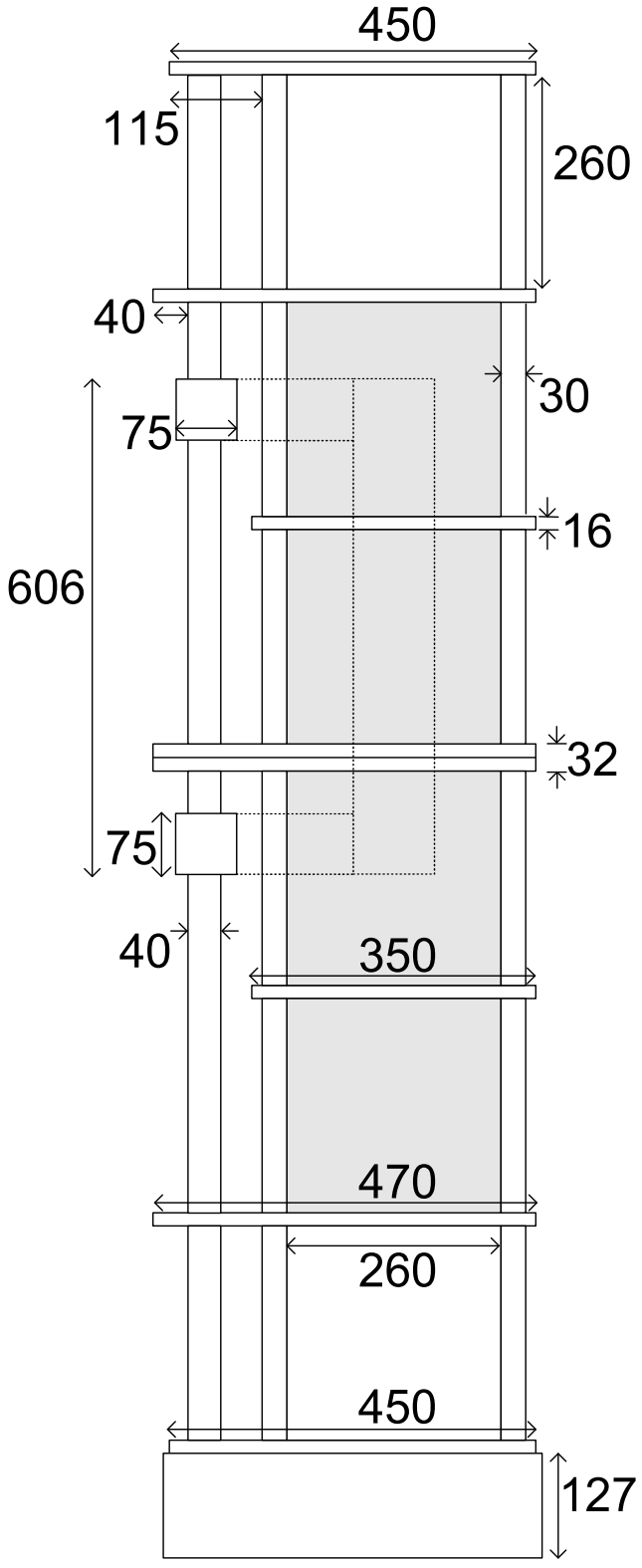


Figure D.5: Side view of the linear motor. The shaded areas show the location of the primary section. The position of the secondary section is indicated with a dashed outline

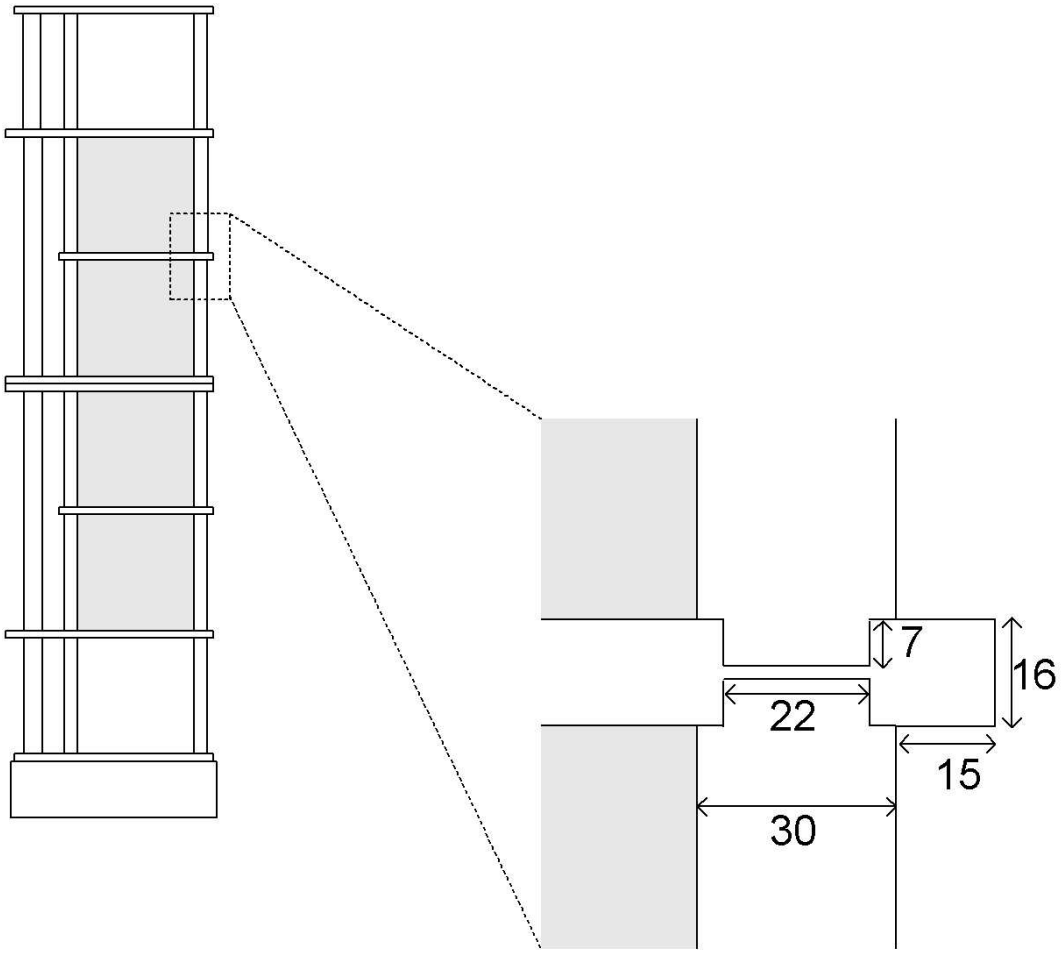


Figure D.6: Close up view of the connection between the support plates and the connecting rods.

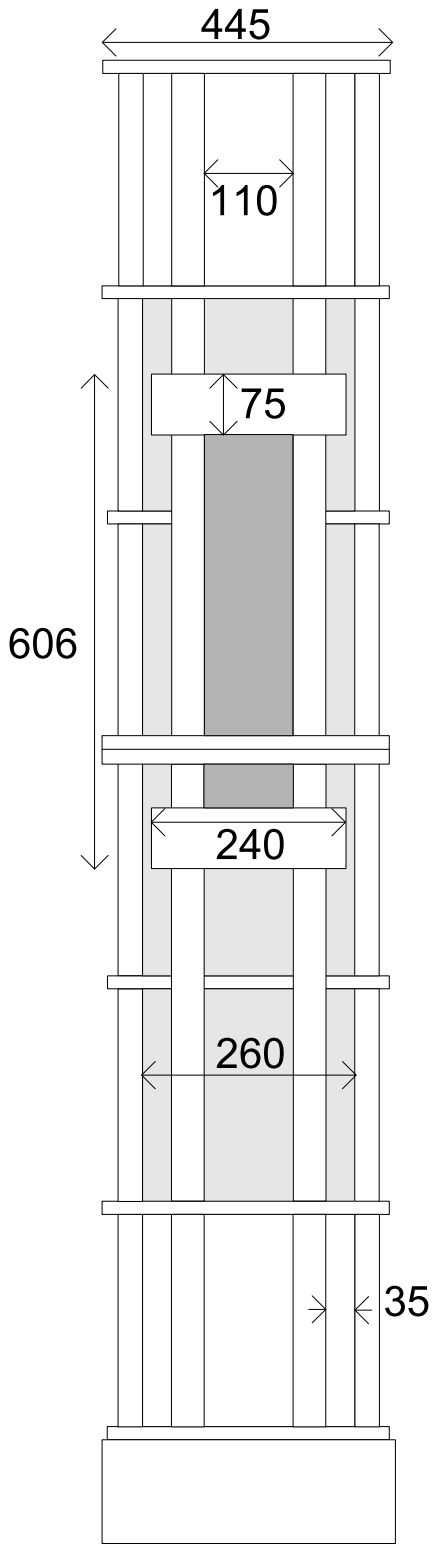


Figure D.7: Front view of the linear motor. The lighter shading shows the location of the primary section. The darker shading shows the position of the secondary section.

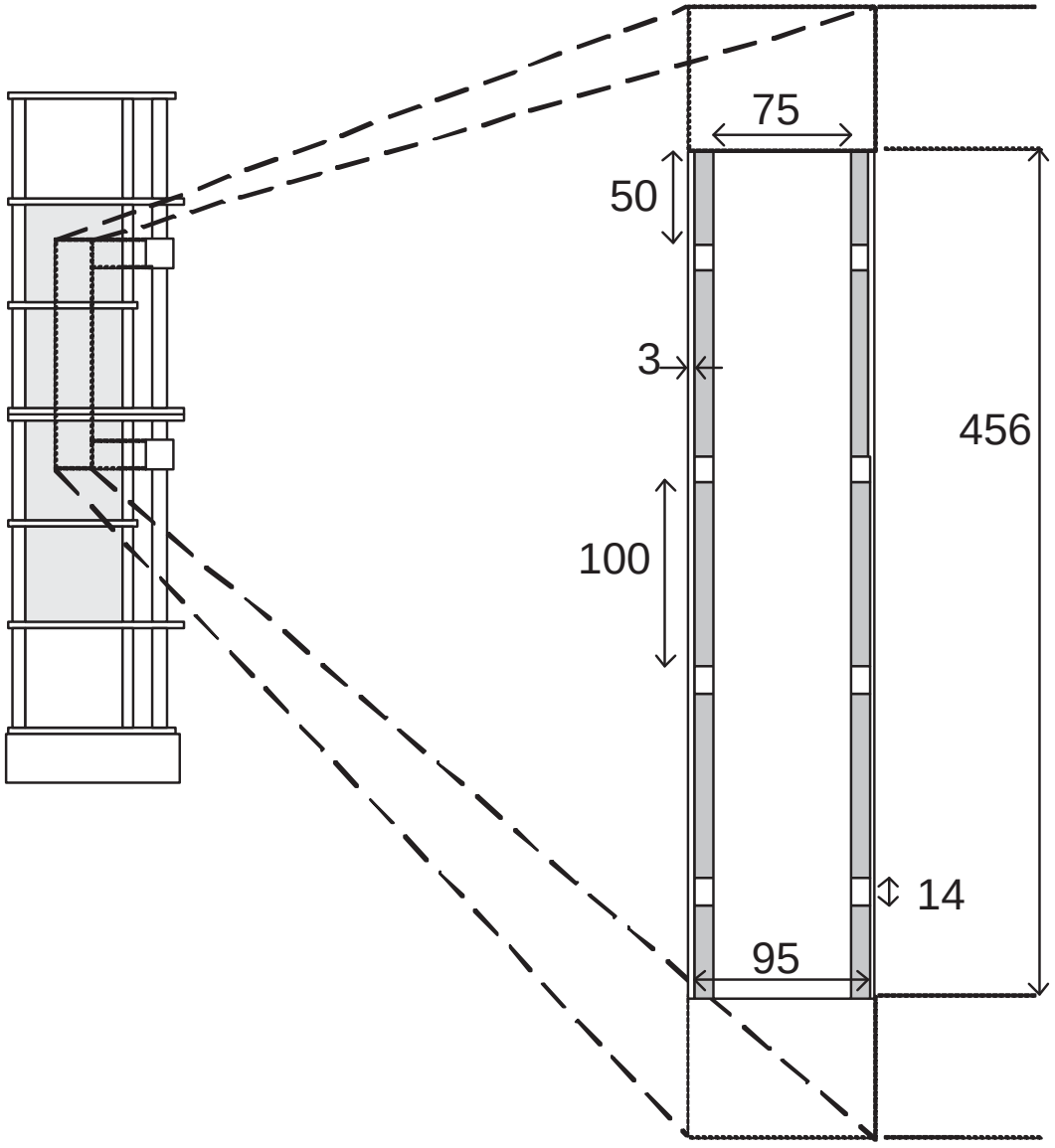


Figure D.8: Side view of the linear motor with the surface mounted magnet arrangement.

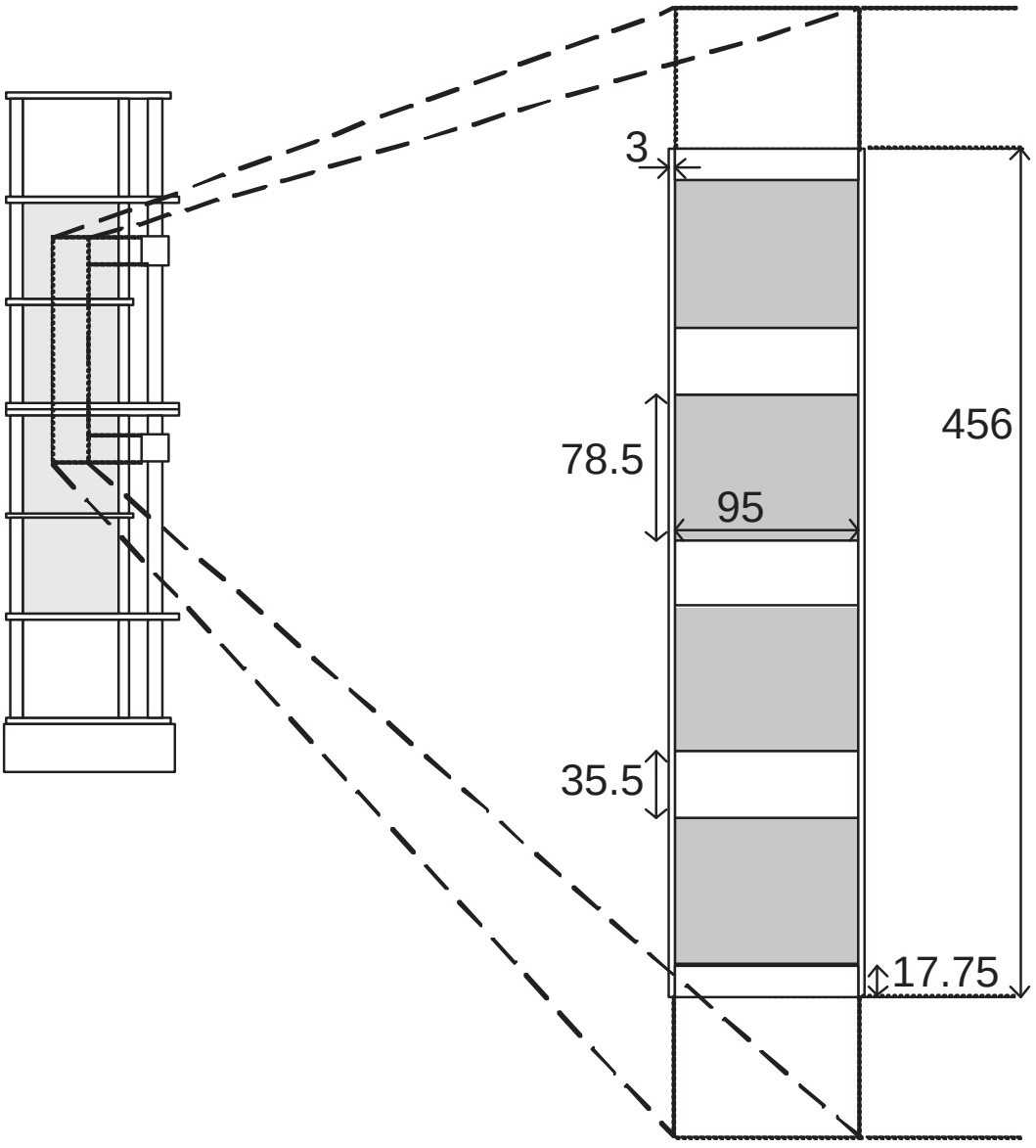


Figure D.9: Side view of the linear motor with the buried magnet arrangement.

Appendix E

Friction Force on the Guidance System

For the calculation of the thrust force (Equation 8.3), it is assumed that the component of friction, F_f, is the same for both the AC and DC tests. However, this is not completely correct. The bearing housings experience a slightly different friction force in each test due to the moment of force acting around each bearing. The surface areas between the bushings and the steel guidance rods changes for each test. The AC test produces a negative moment of force around each bearing housing as indicated in Figure E.1. The DC test produces a positive moment of force (Figure E.2).

The different friction forces created due to the two tests is the probable reason that there is a slight discrepancy between the measured and predicted thrust forces for both the SMMA and BMA. This discrepancy may be larger for the SMMA compared with the BMA and this may be the reason that there is a 5% difference between the predicted and measured thrust forces for both magnet arrangements. But, the discrepancy is small for both magnet arrangements and for the analysis of the modified tubular linear it will be assumed that the friction force, F_f, is the same for both the AC and DC tests.

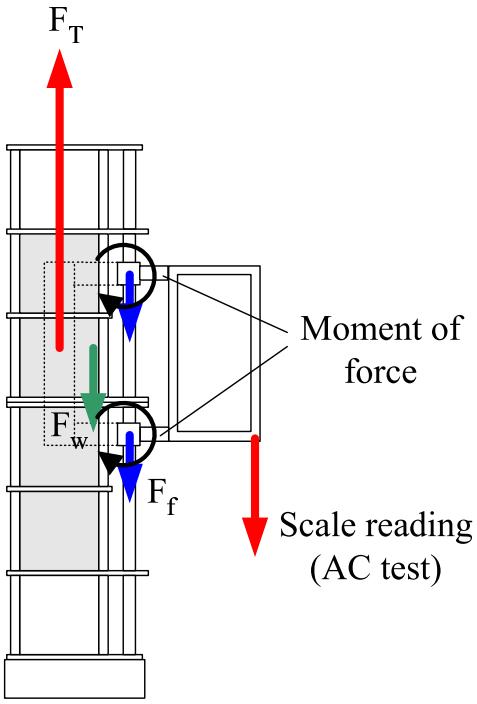


Figure E.1: Moment of force for the AC test.

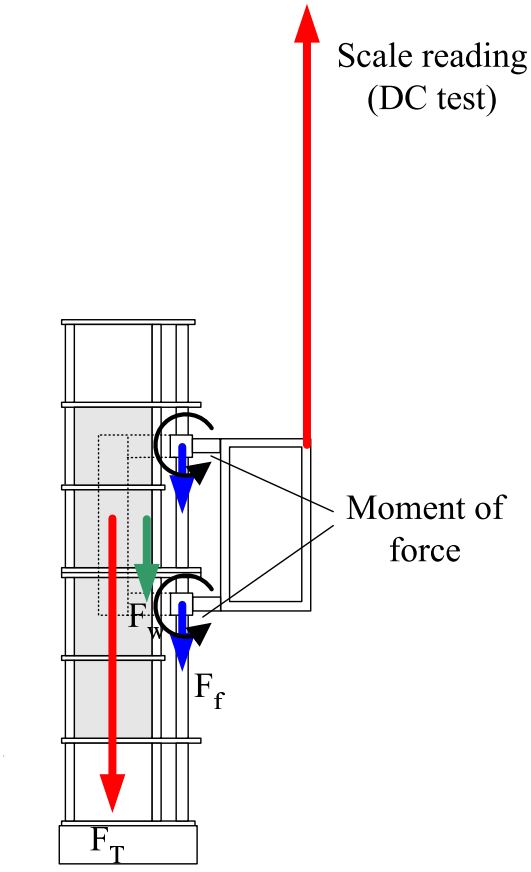


Figure E.2: Moment of force for the DC test.

Appendix F

Voltage and Current Waveforms

The voltage and current waveforms were captured during each force measurement for the AC tests. The voltage waveform has been filtered just to show the fundamental reference frequency which was kept constant at $0.5Hz$. The voltage and hence current was varied by adjusting the inverter's settings. Figure F.1 [64] shows the inverter settings in Table F.1 that were adjusted to obtain a custom $\frac{V}{f}$ pattern.

Adjustments to the output voltage of the inverter were achieved by keeping the minimum voltage (n018) and frequency (n017) constant and adjusting the base frequency (n014). The middle output voltage (n016) and frequency (n015) were set at the same levels as n018 and n017 respectively. Variations in n014 changed the $\frac{V}{f}$ characteristic and hence the output voltage of the inverter.

With hindsight, a better method would have been to set the middle output frequency (n015) to the reference frequency of $0.5Hz$. Adjustments to the output voltage of the inverter could have been changed directly by altering the middle output frequency voltage (n016).

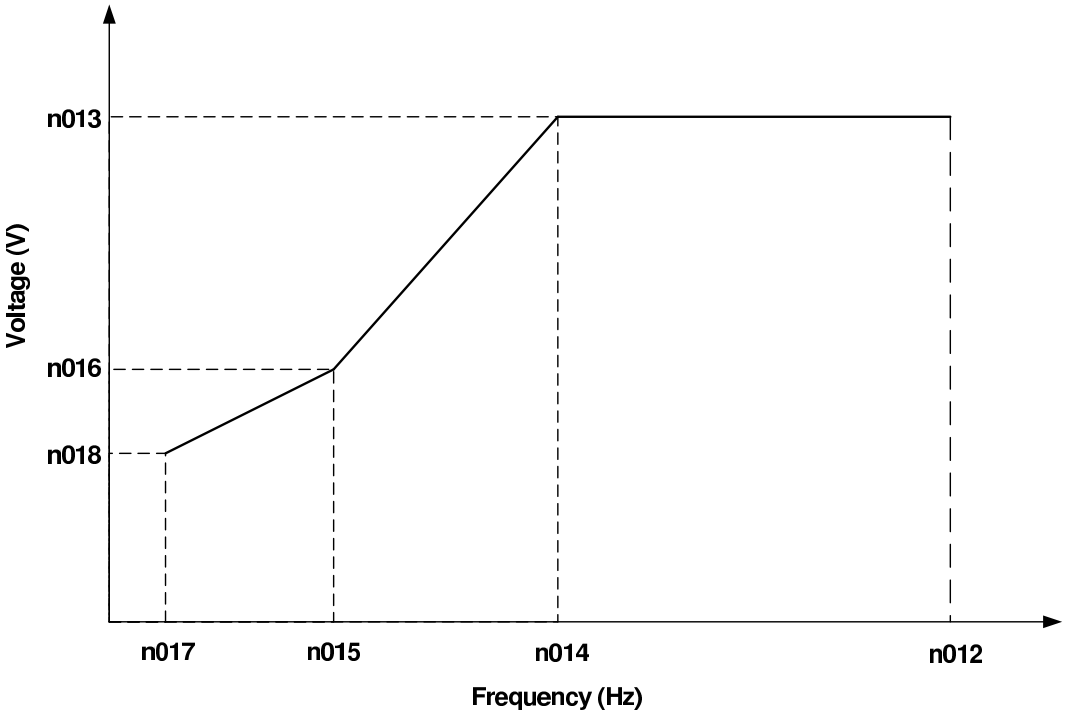


Figure F.1: Custom $\frac{V}{f}$ pattern setting

Table F.1: Descriptions of the inverter settings shown in Figure F.1

Constant No.	Name	Value
n012	Maximum output frequency	$50Hz$
n013	Maximum voltage	$380V$
n014	Maximum voltage output frequency (base frequency)	Variable
n015	Middle output frequency	$0.1Hz$
n016	Middle output frequency voltage	$50V$
n017	Minimum output frequency	$0.1Hz$
n018	Minimum output frequency voltage	$50V$

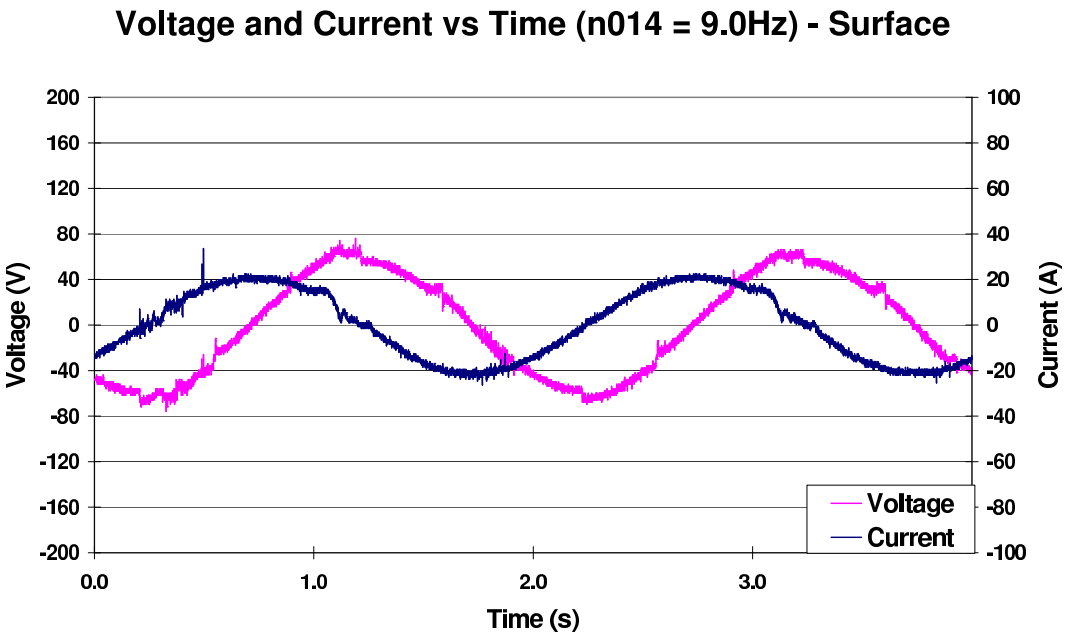


Figure F.2: Voltage and current waveforms with an inverter setting of n014 = $9.0Hz$. Surface mounted magnet arrangement.

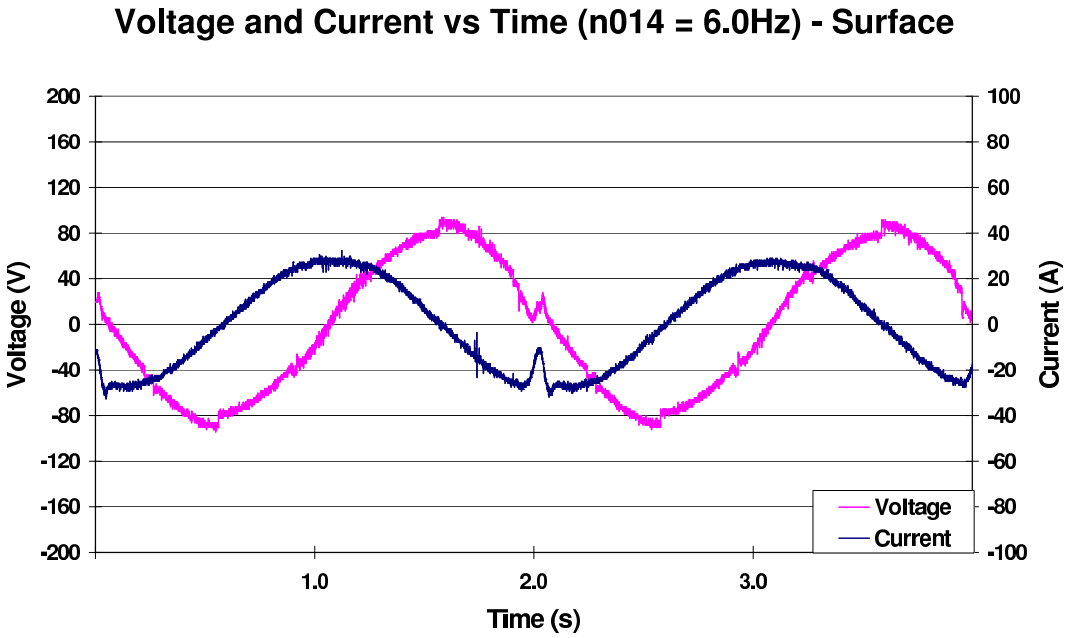


Figure F.3: Voltage and current waveforms with an inverter setting of n014 = $6.0Hz$. Surface mounted magnet arrangement.

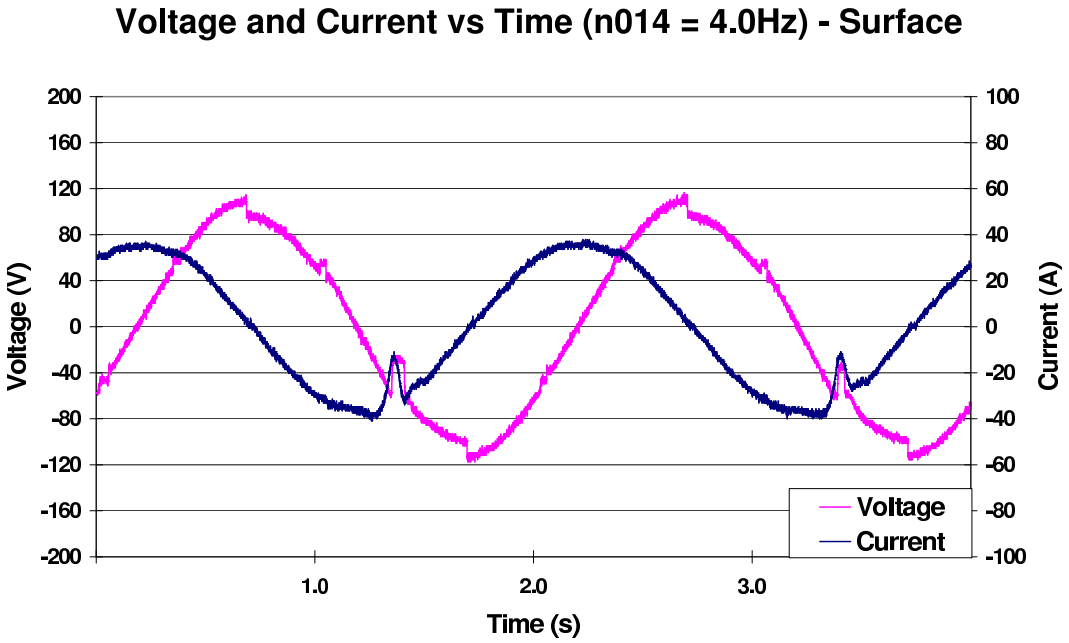


Figure F.4: Voltage and current waveforms with an inverter setting of n014 = $4.0Hz$. Surface mounted magnet arrangement.

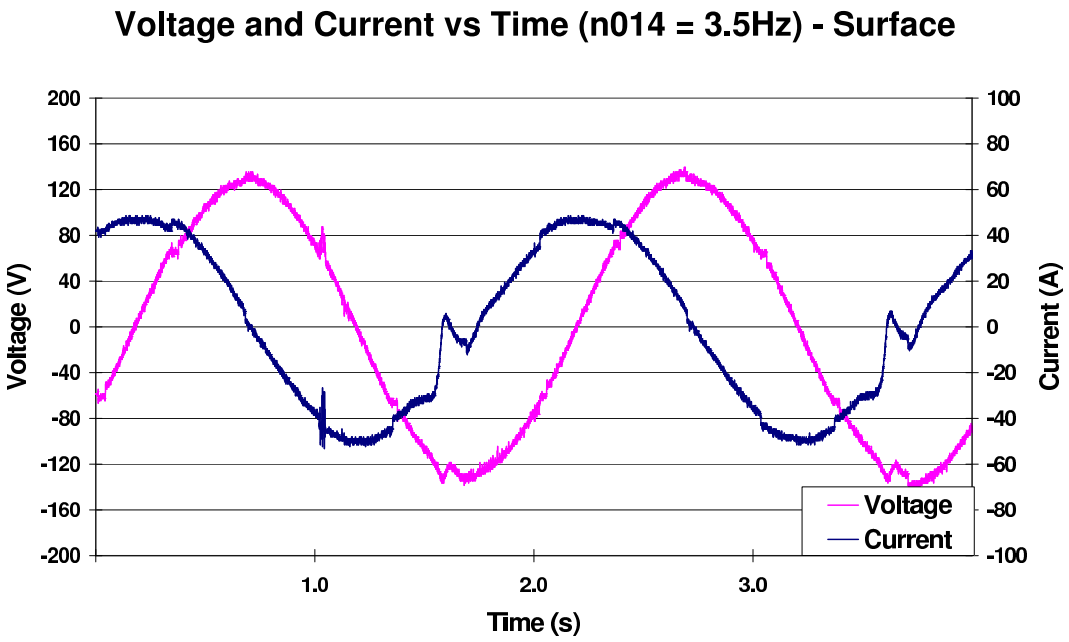


Figure F.5: Voltage and current waveforms with an inverter setting of n014 = $3.5Hz$. Surface mounted magnet arrangement.

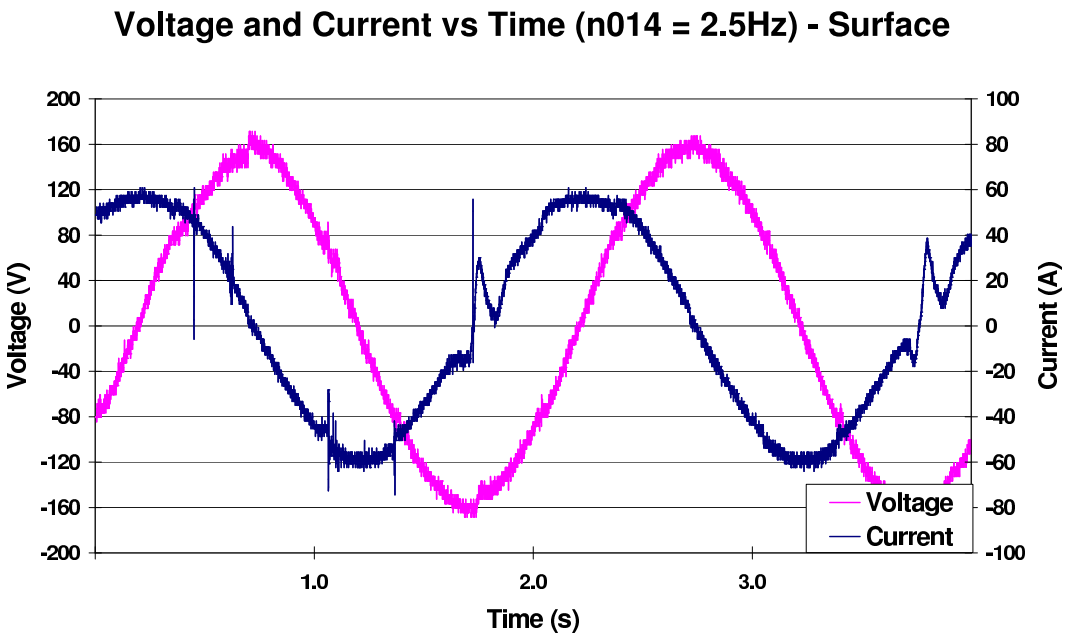


Figure F.6: Voltage and current waveforms with an inverter setting of n014 = $2.5Hz$. Surface mounted magnet arrangement.

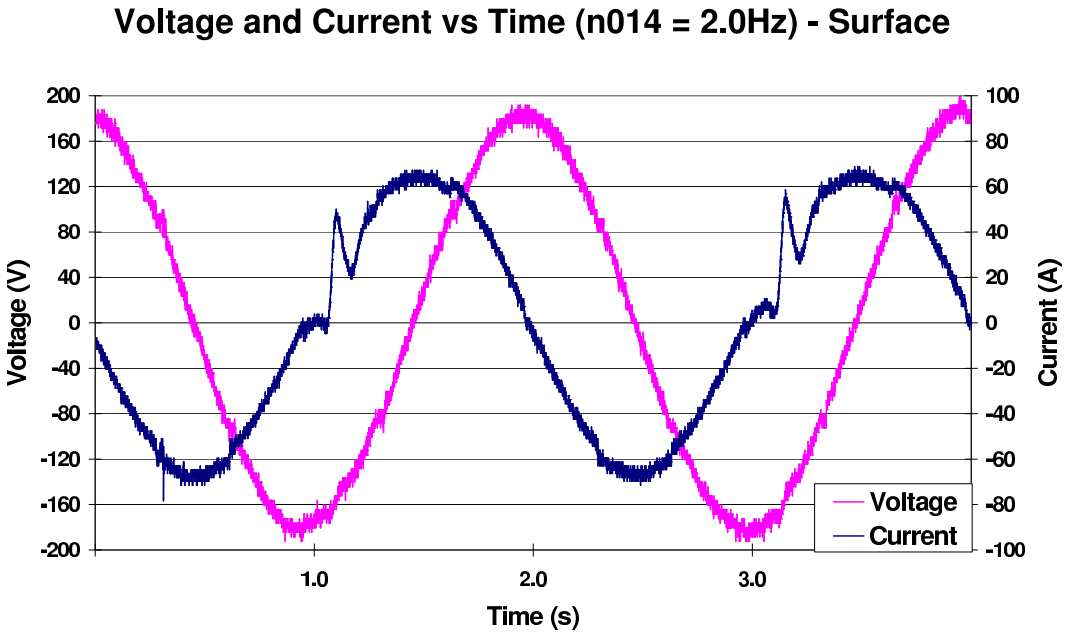


Figure F.7: Voltage and current waveforms with an inverter setting of n014 = $2.0Hz$. Surface mounted magnet arrangement.

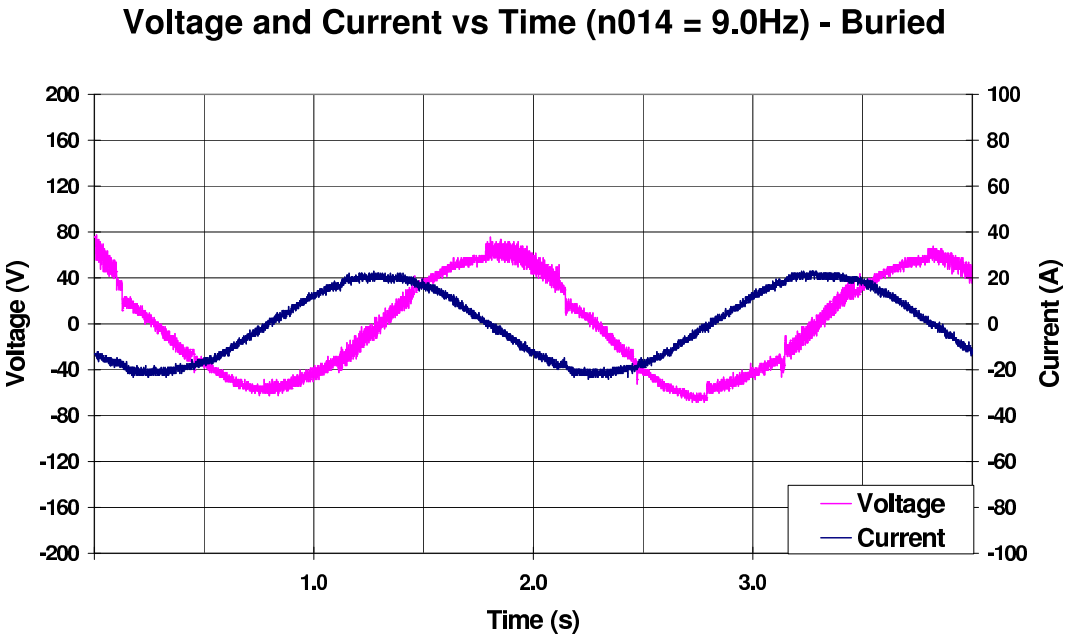


Figure F.8: Voltage and current waveforms with an inverter setting of n014 = $9.0Hz$. Buried magnet arrangement.

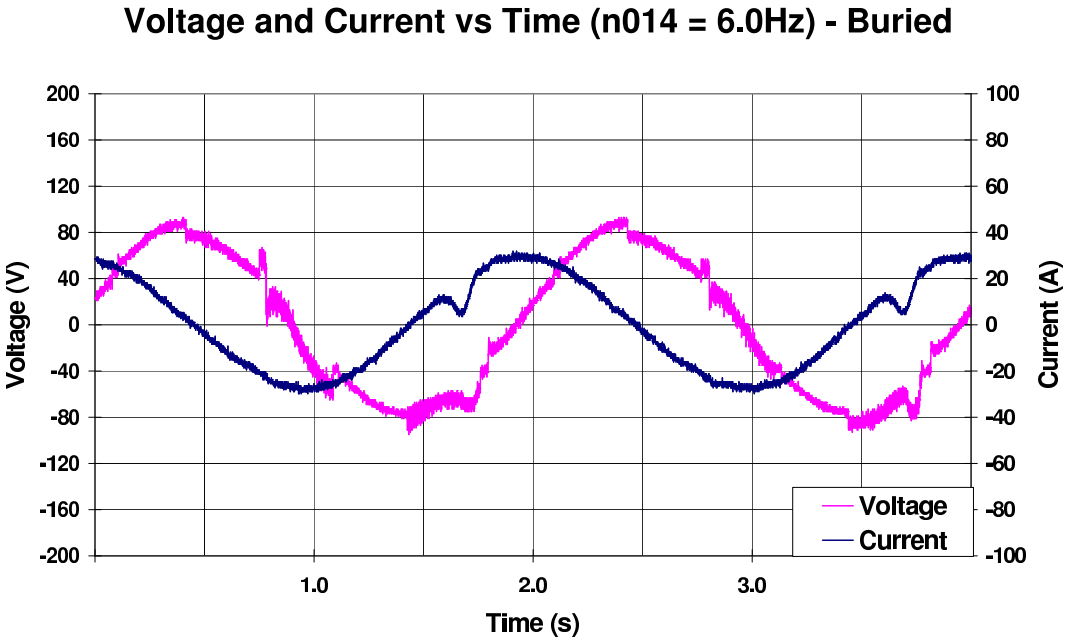


Figure F.9: Voltage and current waveforms with an inverter setting of n014 = $6.0Hz$. Buried magnet arrangement.

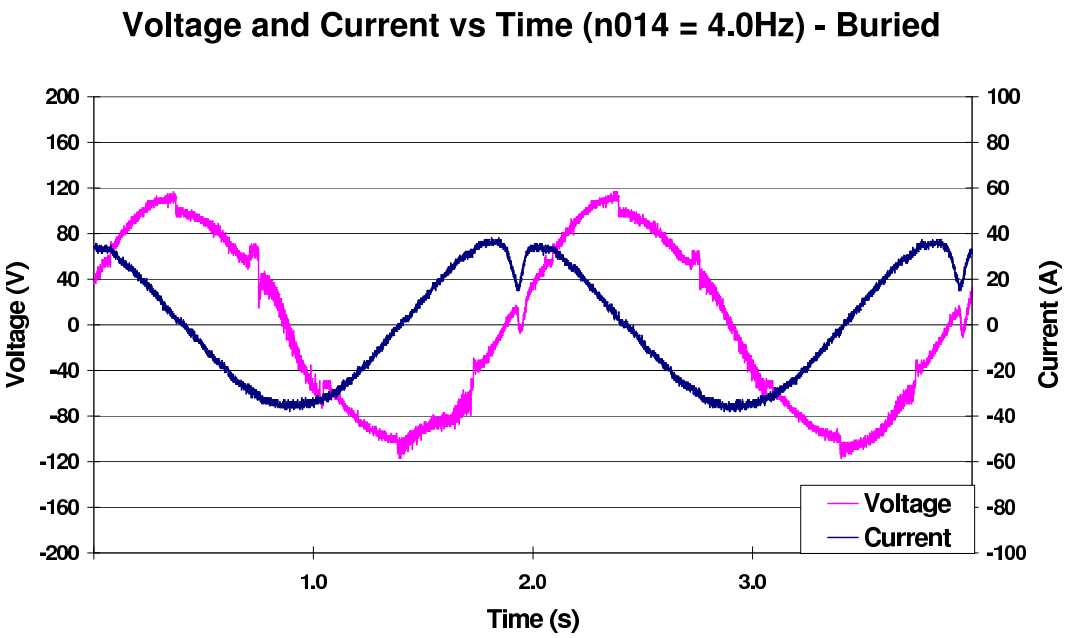


Figure F.10: Voltage and current waveforms with an inverter setting of n014 = $4.0Hz$. Buried magnet arrangement.

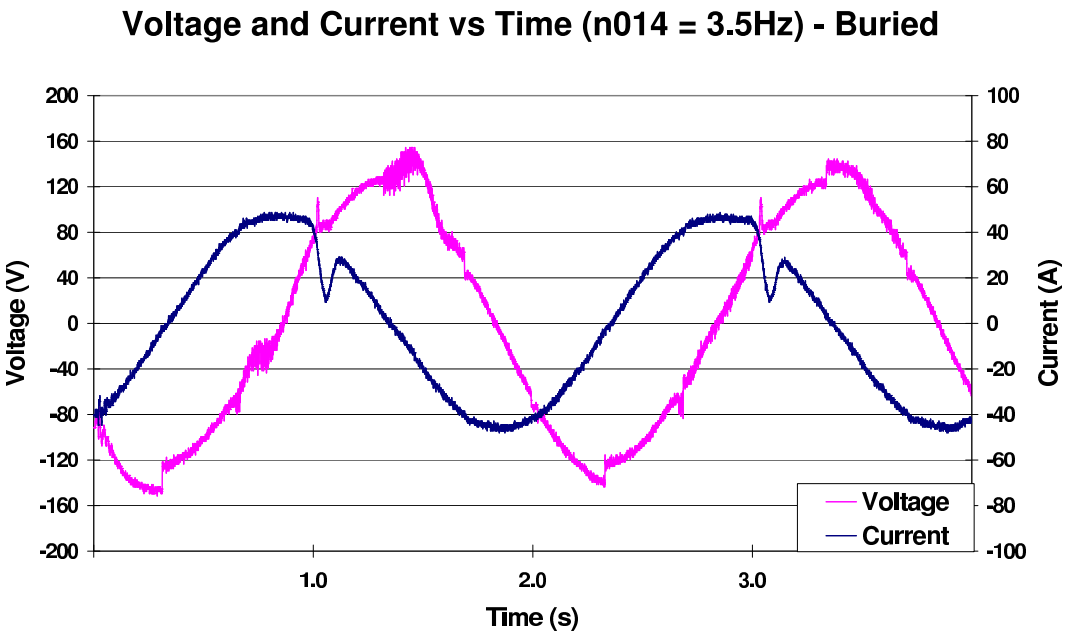


Figure F.11: Voltage and current waveforms with an inverter setting of n014 = $3.5Hz$. Buried magnet arrangement.

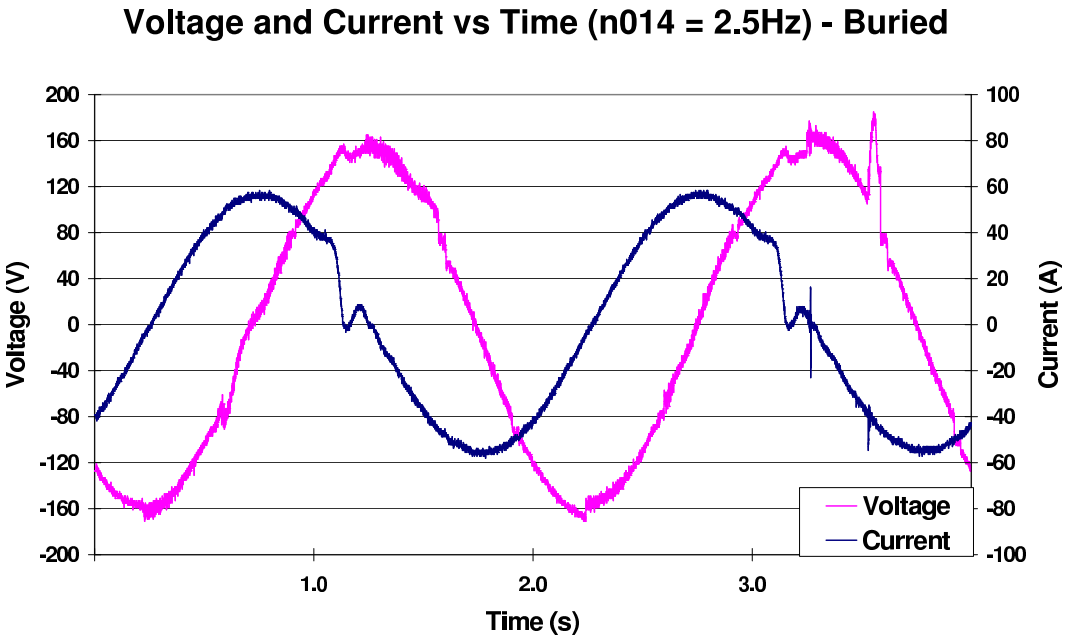


Figure F.12: Voltage and current waveforms with an inverter setting of n014 = $2.5Hz$. Buried magnet arrangement.

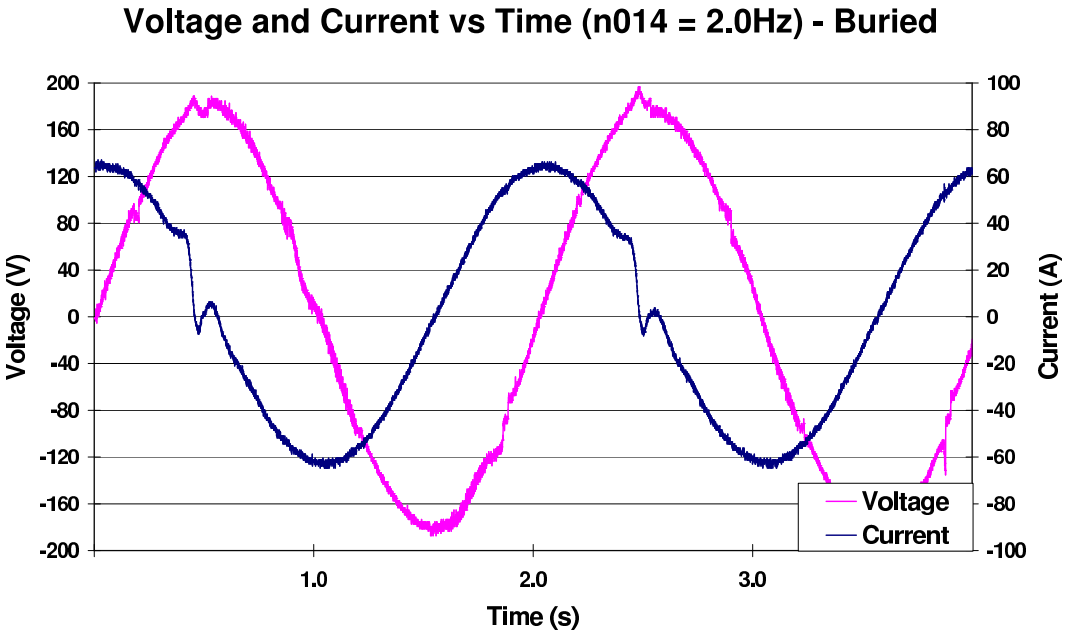


Figure F.13: Voltage and current waveforms with an inverter setting of n014 = $2.0Hz$. Buried magnet arrangement.

Appendix G

Efficiency Calculations for a Full Scale Model

This appendix compares the efficiency of a conventional rope hoisting system to that of a full scale modified tubular linear synchronous motor.

Rope Hoist Efficiency

The efficiency of a rope hoist is presented here so that comparisons can be made with the efficiency of the modified tubular LSM. The efficiency of the rope hoist is defined as follows:

$$\eta_{rope} = \frac{P_{payload}}{P_{in(rms)}} \times 100\% \tag{G.1}$$

- $P_{payload}$ = average power required to lift the payload from the bottom to the top of the shaft
- $P_{in(rms)}$ = rms input electrical power during the lifting cycle

This is similar to the efficiency calculation proposed by Ramlu [7]:

$$\eta_{rope} = \frac{\text{Energy expended in hoisting 1 tonne of payload}}{\text{Specific energy consumption per tonne}} \times 100\% \tag{G.2}$$

The average power required to lift the payload is calculated as follows:

$$P_{payload} = \frac{m_p g d}{t_t} \tag{G.3}$$

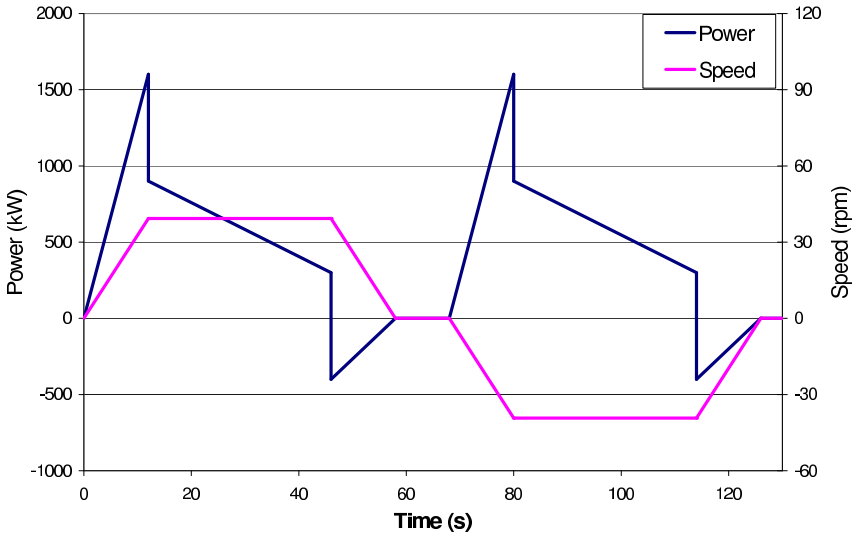


Figure G.1: Power and speed diagram for a winder cycle.

- m_p = mass of the payload
- g = gravity = $9.81 m/s^2$
- d = length of wind (depth of shaft)
- t_t = total cycle time from shaft bottom to headgear tip

The load requirements of a hoisting system vary over time and is more or less cyclic in nature. Figure G.1 shows a typical winder cycle [65]. Both the power and speed are shown in Figure G.1 and the time definitions are shown in Figure G.2 [5][1]. There are two parts to the cycle. In the first part of the cycle, the one conveyance moves from the bottom to the top of the shaft, while the other conveyance moves from the top to the bottom of the shaft. During the second part of the cycle, the direction of travel is reversed (Since it is assumed that both conveyances in a rope hoisting system are the same size, the power for both parts of the cycle is essentially the same if similar payloads are used for both parts of the cycle). The particular winder cycle in Figure G.1 is that of a coal mine shaft which has a depth of $450m$. A gold mine would have a similar form of winding cycle.

Due to this varying load, there is a need to quote the electrical power consumed over one cycle. Referring to Figure G.1, the rms input electrical power over

[1]The positive speed is with reference to the first conveyance travelling in an upward direction. Usually the counterweight in a hoisting system is another conveyance which is the same size as the first conveyance.

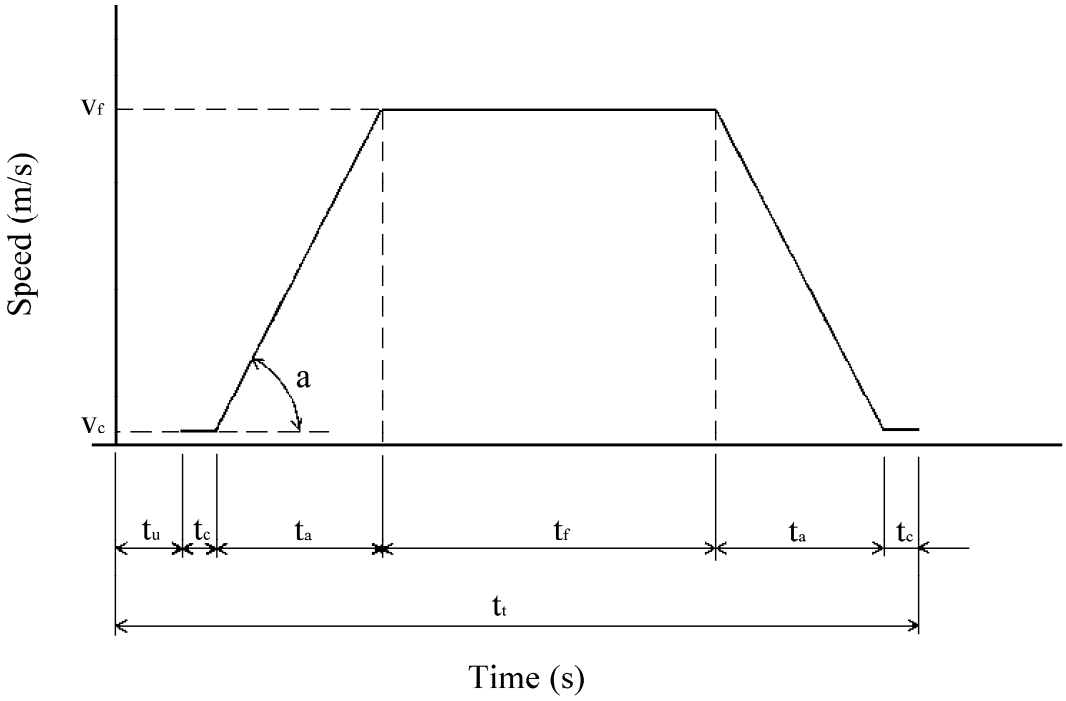


Figure G.2: Standard form of hoisting cycle

- v_f = full winding speed
- v_c = creep speed
- a = acceleration/deceleration rate (assumed to be the same)
- t_u = time to load/unload the skips when the winder is stationary
- t_c = time during creep
- t_a = time taken during acceleration and deceleration
- t_f = time at full speed

the whole cycle is the same as either the first or second part of the cycle. This rms input electrical power is described as follows [66]:

$$P_{in(rms)} = \sqrt{\frac{\sum(kW)^2 \times \text{time}}{\text{running time} + \text{standstill time}/k}} \tag{G.4}$$

- k = constant which accounts for the poorer ventilation at standstill (≈ 4)

Table G.1 gives the rms power ratings[2] and payload masses for some mine hoists in South Africa [67]. The rms input electrical power can be determined from the rms power ratings. Large electrical machines have better efficiencies than small electrical machines [68], thus, an efficiency of 94% will be assumed for the mine hoisting electrical machines given in Table G.1. The overall efficiencies can then be calculated using Equation G.1. The efficiencies for rock winders are between $27\% - 35\%$, and for man winders, the efficiencies are between $12\% - 18\%$. It is clear that the efficiencies for rock winders are greater than man winders as the skip/payload factors and rope safety factors are generally lower for rock winders [5].

The efficiency for the coal mine shaft shown in Figure G.1 is between $45.2\% - 52.0\%$, depending on the braking strategy [65]. This is for a mine shaft with a depth of $450m$. Thus, the efficiency of a rope hoisting system is dependant on the depth of wind as the hoisting capacity decreases with depth [5].

Full Scale Modified Tubular LSM Efficiency

As described, the full scale model would use two modified tubular LSM's. This would reduce the frictional force substantially as the unbalanced radial force for each individual linear motor would cancel each other out. Thus, for the efficiency calculation, it will be assumed that the friction due to the guidance system is negligible.

The corresponding power cycle for the modified tubular LSM is shown in Figure G.3. The first part of the cycle is when the conveyance travels from the bottom to the top of the shaft. The second part of the cycle is when the conveyance travels from the top to the bottom of the shaft. It is in this second

[2]This is the mechanical output power of the electrical machines used in the rope hoisting system

Table G.1: Shaft systems in South Africa

Description	Rock Winders				Man Winders			
Mine	President Steyn	President Steyn	East Driefontein	Vaal Reefs South	President Steyn	President Steyn	East Driefontein	Vaal Reefs South
	No.1	No.2	No.2	No.1	No.1	No.2	No.2	No.1
RMS rating	$5450kW$	$3185kW$	$8200kW$	$5950kW$	$5000kW$	$3800kW$	$3800kW$	$3350kW$
Peak power	$12528kW$	$6964kW$	$15200kW$	$12500kW$	$10590kW$	$7760kW$	$8650kW$	$7600kW$
Mass of Skip	$9732kg$	$7052kg$	$13022kg$	$10800kg$	$7360kg$	$7360kg$	$9600kg$	$8220kg$
Mass of payload	$17233kg$	$9000kg$	$17300kg$	$18200kg$	$8960kg$	$6720kg$	$8820kg$	$10500kg$
skip/payload	0.56	0.78	0.75	0.59	0.82	1.09	1.09	0.78
Length of wind	$2388m$	$2378m$	$2024m$	$1616m$	$2319m$	$2319m$	$1980m$	$1579m$
Winding speed	$15.21m/s$	$15.21m/s$	$18.3m/s$	$15.2m/s$	$15.24m/s$	$15.24m/s$	$18.2m/s$	$15.2m/s$
Acceleration	$0.76m/s^2$	$0.76m/s^2$	$0.76m/s^2$	$0.76m/s^2$	$0.91m/s^2$	$0.91m/s^2$	$0.76m/s^2$	$0.91m/s^2$
Deceleration	$0.91m/s^2$	$0.91m/s^2$	$0.76m/s^2$	$0.91m/s^2$	$0.91m/s^2$	$0.91m/s^2$	$0.76m/s^2$	$0.91m/s^2$
Steady state travel time	$138s$	$138s$	$95s$	$88s$	$136s$	$136s$	$83s$	$88s$
Acceleration travel time	$20s$	$20s$	$20s$	$20s$	$17s$	$17s$	$24s$	$16s$
Deceleration travel time	$16s$	$16s$	$20s$	$16s$	$17s$	$17s$	$24s$	$16s$
Creep time & load time	$26s$	$22s$	$10s$	$13s$	$130s$	$130s$	$145s$	$136s$
Cycle time	$200s$	$196s$	$145s$	$137s$	$300s$	$300s$	$276s$	$256s$
η_{rope}	35%	32%	27%	33%	13%	12%	15%	18%

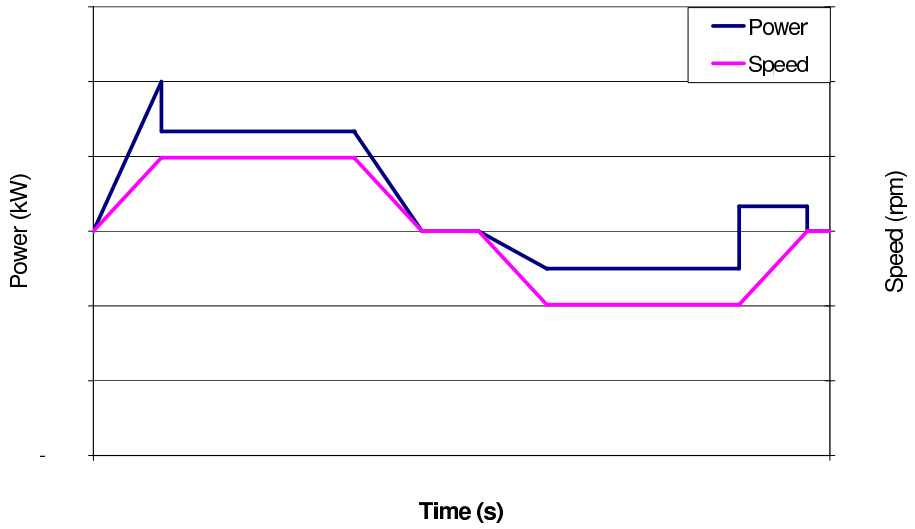


Figure G.3: Power and speed diagram for a LSM hoisting cycle.

cycle that energy can be recovered. For this analysis, the second part of the cycle will be ignored[3]. Thus, the efficiency of the modified tubular LSM will only be calculated for the first part of the cycle.

The efficiency can be described by the following equation:

$$\eta_{LSM} = \frac{P_{payload}}{P_{in(rms)}} \times 100\% \tag{G.5}$$

The input electrical power can be calculated using the subtraction of losses method (See Figure G.4):

$$P_{in} = P_m + P_{cu}$$

There are 54 coils in the 9 pole secondary, therefore the copper losses are:

$$P_{cu} = I_{a1}^2 R_{a1} \times 54 = 2609.28W$$

As stated earlier, the friction forces are assumed to be negligible. The windage losses are also assumed to be negligible. Therefore, the constant losses, P_c, are made up of only the core losses. Unlike in the case of the prototype modified tubular LSM where the core losses were ignored as the applied frequency was only $0.5Hz$, the full scale model will have an applied frequency of $78.95Hz$ and the losses need to be included.

[3]Calculation of the generated power in the second part of the cycle is complex and would need to be investigated further. So far, investigations into the regenerative braking forces has formed part of another project at the University of the Witwatersrand, Johannesburg [28]

From the core loss curves supplied by the steel manufacturer (Figure G.5 [69]), the power loss per kilogram at $78.95Hz$ is assumed to be $5W/kg$[4]. The mass of the primary stacks is $129.36kg$ (See Section 6.1.1).

$$P_c \;=\; 129.36 \times 5 \;=\; 646.8W$$

Referring to Figure G.2, the following parameters are assumed:

- Steady state speed, $v_f = 18m/s$
- Acceleration $= 0.91m/s^2$
- Deceleration $= 0.91m/s^2$
- Acceleration/Deceleration travel time, $t_a = 19.78s$
- Total distance of travel $d = 4000m$
- Distance of acceleration/deceleration travel $= 178m$
- Distance of steady state travel $= 3644m$

[4]The core loss curve supplied is for a frequency of $50Hz$. Therefore, the core loss curve should be steeper for a frequency of $78.95Hz$ than that shown in Figure G.5. But, the primary is only operating at flux densities between $0.73T - 1.2T$ (See Appendix A). So a value of $5W/kg$ will be assumed. This is accurate enough as it will be shown that the core losses are less than 2% of the rms input power.

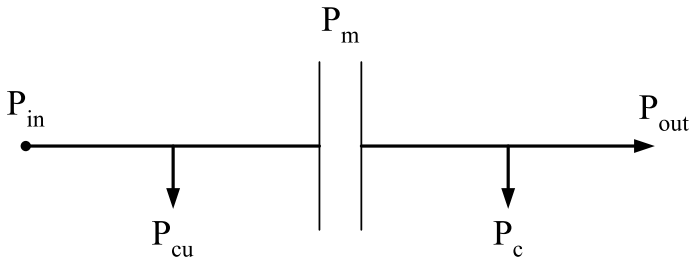


Figure G.4: Power flow in the modified tubular LSM.

- P_{in} = input electrical power
- P_{cu} = copper losses
- P_m = mechanical power converted from electrical power (thrust force)
- P_c = constant power losses (iron, friction and windage losses)
- P_{out} = output mechanical power

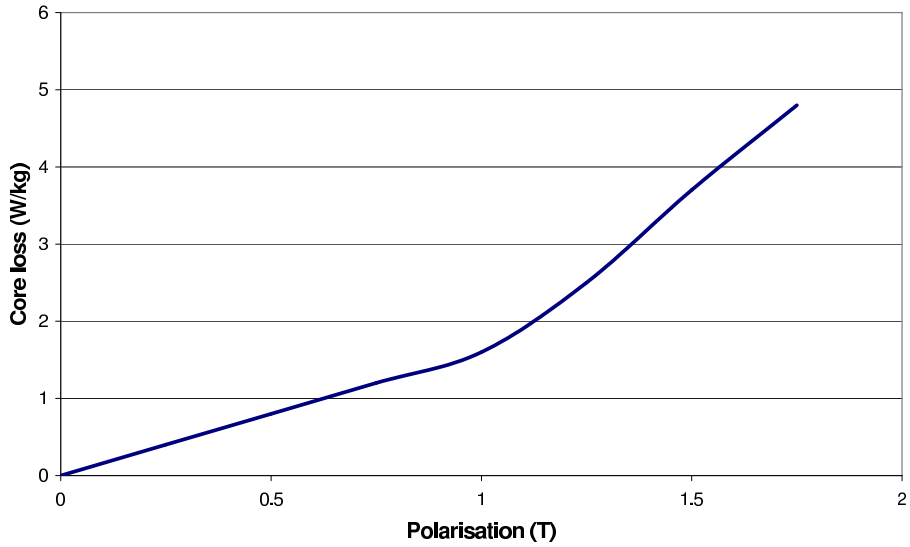


Figure G.5: Core loss curve for the steel used in the primary laminations.

- Steady state travel time, $t_f = 202.44s$
- Creep and load time, $t_c + t_u = 130s$ (man hoist)
- Total cycle time, $t_t = 372s$

Assuming a skip/payload ratio of 0.5 (a smaller skip/payload factor is being used compared to Table G.1 as there is no need for any rope attachments), P_m is broken up into three parts.

- Power to lift the skip
- Power to lift the payload
- Power to overcome the core losses, P_c = constant

Under steady state conditions, the rated current of $8A$ produces $2088N$ of thrust force. Using Equation 8.4 the power under steady state speed conditions, $P_{m(ss)}$, at $18m/s$ is[5]:

$$P_{m(ss)} = 2088 \times 18 = 37584W$$

Referring to the power flow diagram (Figure G.4), P_c will consume $646.8W$ of $P_{m(ss)}$ and the rest will be used to lift the skip and the payload. Thus, $P_{out} = 36937.2W$. At a steady state speed of $18m/s$ the output force would

[5]The subscript $_{ss}$ indicates that the quantities presented are for steady state conditions

be $2052.1N$. With a skip/payload factor of 0.5, the mass of the conveyance is $69.72kg$ and the mass of the payload is $139.46kg$. Thus, the input electrical power under steady state speed conditions is as follows:

$$\begin{aligned} P_{in(ss)} &= P_{m(ss)} + P_{cu(ss)} \\ P_{in(ss)} &= 37584.00 + 2609.28 \;=\; 40193.28W \end{aligned}$$

During acceleration from standstill, the required thrust force must be bigger than the force under steady state speed conditions. With a combined mass of $209.18kg$, the conveyance and payload require a force of $2242.41N$ at an acceleration of $0.91m/s^2$. Assuming the core losses are the same during acceleration as they are under steady state speed conditions, the required thrust force would be $2278.31N$. For this thrust force, the input current must increase to $8.85A$ per coil. The copper losses for a current of $8.85A$ per coil are[6]:

$$P_{cu(acc)} \;=\; I_{a1}^2 R_{a1} \times 54 \;=\; 3193.21W$$

At the end of the acceleration time period, the maximum required mechanical power, $P_{m(acc)}$, is:

$$P_{m(acc)} \;=\; 2278.31 \times 18 \;=\; 41010W$$

Thus, under acceleration, the maximum input peak power required is:

$$\begin{aligned} P_{in(acc)} &= P_{m(acc)} + P_{cu(acc)} \\ P_{in(acc)} &= 41010.00 + 3193.21 \;=\; 44203.21W \end{aligned}$$

Using Equation G.4 and the time values given for the modified tubular LSM hoisting cycle, the rms input electrical power, $P_{in(rms)}$ can be calculated as $35436W$. Thus, the peak power requirement for the linear motor is approximately 25% greater then the rms power.

With a known payload mass, the average power required to lift the payload is calculated from Equation G.3:

$$\begin{aligned} P_{payload} &= \frac{m_p g d}{t_t} \\ P_{payload} &= \frac{139.46 \times 9.81 \times 4000}{372} \\ P_{payload} &= 14710.78W \end{aligned}$$

[6]The subscript $_{acc}$ indicates that the quantities presented are for acceleration conditions

Finally, the efficiency can be calculated:

$$\begin{aligned} \eta_{LSM} &= \frac{P_{payload}}{P_{in(rms)}} \times 100\% \\ &= \frac{14710.78}{35436} \times 100\% \\ &= 41.51\% \end{aligned}$$

This efficiency for this modified tubular LSM is greater than the rope hoist efficiencies given in Table G.1($12\% - 35\%$), but less than the efficiencies given for the $450m$ deep coal mines [65]($45.2\% - 52.0\%$). This indicates that the linear motor has the added advantage of greater efficiencies in deep level mines compared to shallow mines or even high rise buildings.